AN ABSTRACT OF THE THESIS OF

Maxwell K. Wallace for the degree of Doctor of Philosophy in Chemistry presented on March 7, 2019.

Title: Enigmatic Quantum Materials: Novel Spin-Orbit Coupled $4d/5d$ Metal Oxides and Intermetallics

Abstract approved: _____

Munirpallam A. Subramanian

This dissertation examines unexplored $4d/5d$ metal oxides and intermetallics projected to have novel quantum states such as topologically insulating, quantum spin liquid, superconducting, and/or thermoelectric behavior. Fundamentally, the aim is to establish novel structure-property relationships of such candidates. Five projects are presented in this dissertation.

A quantum spin liquid (QSL) represents a new state of matter. Unlike conventional magnetic states, such as the ferromagnetic or the antiferromagnetic states, a QSL never enters into a long-range ordered phase with a static arrangement of spins, even at absolute zero temperature. Quantum computation is the most attractive potential application of a QSL. The demonstration by Alexei Kitaev of an exactly solvable QSL model incorporating $S = 1/2$ spins with anisotropic

interactions on a honeycomb lattice has motivated searches for its experimental realization. Whereas magnetic honeycomb-containing compounds have been extensively investigated in $3d$ and $4d$ metal oxides, the strong interaction anisotropy required by Kitaev's theory has placed a focus on $5d$ metal oxides, for which spin-orbit coupling (SOC) can be expected. Many A_2MO_3 "honeycomb" layered oxides, where A is an alkali atom and M is a $4d$ or $5d$ element, show unique electronic and magnetic properties, indicative of SOC. Known A_2MO_3, however, do not display QSL behavior. Osmium based A_2MO_3 "honeycomb" layered oxides has been of current interest within the solid state community as it is considered to be a candidate Kitaev quantum spin liquid. The first example of Os on a honeycomb structure, $Li_{2.15(3)}Os_{0.85(3)}O_3$, is presented. This compound is an off-stoichiometric version of Li_2OsO_3 with the β-Li_2SnO_3 structure ($C2/c$) (a = 5.09 Å, b = 8.81 Å, c = 9.83 Å, β = 99.3°). Neutron diffraction shows large site disorder in the honeycomb layer and X-ray absorption spectroscopy indicates a valence state of Os (+4.7 ± 0.2), consistent with the nominal concentration. A narrow transport band gap of Δ = 243 ± 23 meV, a large van Vleck susceptibility, and an effective moment of 0.85 μ_B is observed. No evidence of long range order is found above 0.10 K but a spin glass-like peak in ac-susceptibility is observed at 0.5 K. The specific heat displays an impurity spin contribution in addition to a power law $\propto T^{(0.63\pm0.06)}$. Density functional theory (DFT) applied to Li_2OsO_3 leads to a reduced moment, suggesting incipient itineracy of the valence electrons. Constrained non-collinear moment DFT is applied to an ordered version of $Li_{2.25}Os_{0.75}O_3$, finding evidence that Li over stoichiometry leads to Os(4+)-Os(5+) mixed valence. This local pic-

ture is discussed in light of the site disorder and a possible underlying quantum spin liquid state.

The interest in perovskites can be attributed to their wide array of properties, which in turn derives from their compositional and structural flexibility. The framework of the $A_2MM'O_6$ double perovskite containing $4d/5d$ elements with strong spin-orbit coupling (SOC) are of interest for the exploration of quantum magnetism. In such systems, the interplay between the electron localizing tendencies of SOC and the delocalizing effects of the large spatial extent of the $4d/5d$ orbitals has the potential to combine with electronic correlations to produce unusual states. The motivation to study $Ba_{2-x}La_xYIrO_6$ is twofold: (1) to investigate a mixed $5d^4/5d^5$ iridate perovskite with noncubic symmetry and with iridium as the sole magnetic ion, and (2) to elucidate the influence of local environment on the magnetism in such systems. As shown by the structural refinements presented, $a^0a^0a^0$ ($Fm\bar{3}m$) $\rightarrow a^0b^-b^-$ ($I2/m$) octahedral distortion of the YO_6-IrO_6 rock-salt framework occurs with increasing x to account for the incorporation of smaller La^{3+} radii. From the magnetic susceptibility measurements, deviations from the proposed mixed valence picture are observed, not only for $x = 0.2$, but also on approaching $x = 0.8$. For $x = 0.2$, χ_{VV} is larger than found for $x = 0$.

Frustrated systems populated with large spin-orbit coupled (SOC) ions are an ideal setting for the exploration of exotic states. Among the known frustrated frameworks, the spinel structure has been extensively investigated. Though many spinel systems with $3d/4d$ elements exist, to our knowledge, an Iridium based spinel oxide has not been reported. Most spinel oxides are known to be insulating

and only two, LiV_2O_4 and $LiTi_2O_4$, are reported as conducting. A frustrated mixed valence system that is metallic and exhibits large SOC is scarce, and if a metallic spinel is close to a correlation driven metal-insulator transition, a novel interplay between the charge carriers and the frustrated spin degree of freedom is anticipated. Here we present the first Iridate spinel: $Cu[Ir_{1.498(1)}Cu_{0.502(1)}]O_4$. Synchrotron XRD refinements reveal a face-centered cubic structure with space group $Fd\bar{3}m$. Electrical properties reveal a metallic state within 50~600 K range with a Kondo-effect at T<50 K.

The "phonon-glass/electron-crystal" approach has been implemented through incorporation of "rattlers" into skutterudite void sites to increase phonon scattering and thus increase the thermoelectric efficiency. Indium filled $IrSb_3$ skutterudites are reported for the first time. Polycrystalline samples of $In_xIr_4Sb_{12}$ ($0 \leq x \leq 0.2$) were prepared by solid-state reaction under a gas mixture of 5% H_2 and 95% Ar. The solubility limit of $In_xIr_4Sb_{12}$ was found to be close to 0.18. Synchrotron X-ray diffraction refinements reveal all $In_xIr_4Sb_{12}$ phases crystallized in body-centered cubic structure (space group: $Im\bar{3}$) with ~8% antimony site vacancy and with indium partially occupying the $16f$ site. Unlike known rattler filled skutterudites, under synthetic conditions employed, indium filling in $IrSb_3$ significantly increases the electrical resistivity and decreases the Seebeck coefficient (n-type) while reducing the thermal conductivity by ~30%. The resultant power factor offsets the decrease in total thermal conductivity giving rise to a substantial decrease in ZT. Principal thermoelectric properties of $In_xM_4Sb_{12}$ (M = Co, Rh, Ir) phases are compared. As iridium is a $5d$ transition metal, zero field cooled (ZFC) magnetiza-

tion were performed to unravel the effect of spin-orbit interaction on the electronic properties. These results serve to advance the understanding of filled skutterudites, and provide additional insight on the less explored smaller "rattlers" and their influence on key thermoelectric properties.

The solid solution series $Li_2Ir_{1-x}Rh_xO_3$ is synthesized for several values of x between 0 and 1. The compounds possess a monoclinic layered structure (space group $C2/m$) throughout the solid solution range with the lattice constants following Vegard's relationship. Magnetization and resistivity data below room temperature are presented. The effective magnetic moment (μ_{eff}) is reduced below the value obtained by interpolating between the end-members, presumably due to nearest neighbor charge exchange leading to non-magnetic Ir^{5+}/Rh^{3+} pairs. Surprisingly, the degree of reduction of μ_{eff} cannot be explained by a random mixture of Ir and Rh and is strongly asymmetric around $x = 0.5$. This anomalous moment reduction possibly results from the difference in on-site Coulomb repulsion between Ir and Rh ions.

Enigmatic Quantum Materials: Novel Spin-Orbit Coupled $4d/5d$
Metal Oxides and Intermetallics

by

Maxwell K. Wallace

A THESIS

submitted to

Oregon State University

in partial fulfillment of
the requirements for the
degree of

Doctor of Philosophy

Presented March 7, 2019
Commencement June 2019

Doctor of Philosophy thesis of Maxwell K. Wallace presented on March 7, 2019.

APPROVED:

_____

Major Professor, representing Chemistry

_____

Head of the Department of Chemistry

_____

Dean of the Graduate School

I understand that my thesis will become part of the permanent collection of Oregon State University libraries. My signature below authorizes release of my thesis to any reader upon request.

_____

Maxwell K. Wallace, Author

ACKNOWLEDGEMENTS

CONTRIBUTION OF AUTHORS

Chapter 6: M.A. Subramanian and A.P. Ramirez conceived the interest. M.K. Wallace designed, constructed, and carried out the synthesis. P.G. LaBarre and M.K. Wallace collected electronic and magnetic properties. M.K. Wallace and J. Li performed TOF neutron refinements and M.K. Wallace performed stacking fault modeling. S.T. Pi and W.E. Pickett performed DFT calculations. D. Haskel collected and analyzed XAS measurements. A.P. Ramirez, W.E. Pickett, D.S. Dessau, and P.G. LaBarre analyzed and discussed electronic properties and M.A. Subramanian, M.K. Wallace, and J. Li discussed structure characterization. M.K. Wallace, A.P. Ramirez, and W.E. Pickett constructed manuscript. Remaining authors provided helpful feedback on manuscript.

Chapter 7: M.K. Wallace conceived the interest. M.K. Wallace and S. Svadlenak designed, constructed, and carried out the synthesis. M.K. Wallace and S. Svadlenak collected electronic properties and P.G. LaBarre collected magnetic properties. M.K. Wallace and S. Svadlenak performed refinements on lab XRD and M.K. Wallace performed refinements on TOF neutron diffraction data. P.G. LaBarre and A.P. Ramirez interpreted magnetic properties. M.K. Wallace and A.P. Ramirez constructed manuscript. Remaining authors provided helpful feedback on manuscript.

Chapter 8: M.K. Wallace conceived the interest. M.K. Wallace designed, constructed, and carried out the synthesis. P.G. LaBarre and M.K. Wallace col-

lected electronic and magnetic properties. M.K. Wallace performed refinements on lab XRD and synchrotron XRD. A.P. Ramirez and P.G. LaBarre interpreted magnetic properties. J. Telser collected and interpreted EPR spectroscopy measurements. M.K. Wallace and A.P. Ramirez constructed manuscript. Remaining authors provided helpful feedback on manuscript.

Chapter 9: M.A. Subramanian and M.K. Wallace conceived the interest. M.K. Wallace designed, constructed, and carried out the synthesis. M.K. Wallace collected electronic and thermal properties and A.P. Ramirez collected magnetic properties. M.K. Wallace performed refinements on lab XRD and synchrotron XRD. M.A. Subramanian, M.K. Wallace, J. Li, and A. Sleight discussed structure characterization. M.K. Wallace constructed manuscript. Remaining authors provided helpful feedback on manuscript.

Appendix C: M.A. Subramanian conceived the interest. S.L. Kumari and M.K. Wallace designed, constructed, and carried out the synthesis. S.L. Kumari and M.K. Wallace collected electronic properties and J.T. Barnes and B. Tong collected magnetic properties. A.P. Ramirez interpreted electrical properties. M.K. Wallace performed refinements on lab XRD and TOF neutron diffraction data. M.K. Wallace performed stacking fault modeling. S.L. Kumari, M.K. Wallace, and A.P. Ramirez constructed manuscript. Remaining authors provided helpful feedback on manuscript.

TABLE OF CONTENTS

TABLE OF CONTENTS (Continued)

TABLE OF CONTENTS (Continued)

LIST OF FIGURES

LIST OF FIGURES (Continued)

LIST OF TABLES

LIST OF TABLES (Continued)

LIST OF APPENDIX FIGURES

LIST OF APPENDIX TABLES

Chapter 1: Fundamentals of Solid State Chemistry: Synthesis, Material Properties, and Characterization Methods

1.1 Introduction

Solid-state chemistry is the study of the synthesis, structure, and properties of solid phase materials with a focus on the synthesis of novel materials and their characterization. It therefore has a strong overlap with solid-state physics, crystallography, mineralogy, ceramics, metallurgy, and materials science. Pertinent solid state fundamentals will be exploited in this chapter. Here, a brief overview of pertinent synthesis techniques, material properties, and structural and electronic characterization methods will be introduced to provide the reader with the basic knowledge to grasp the research presented in this dissertation.

1.2 Synthesis Methods

A variety of synthesis methods were employed in this dissertation. The standard solid-state synthesis method, crystal growth flux method, hydrothermal method, sealed quartz tube method, and ion exchange method were employed. A brief overview of each method will be addressed.

1.2.1   Standard Solid-State Synthesis

The traditional standard solid-state synthesis method, also referred to as "shake-and-bake" method relies on elevated temperatures for atomic diffusion and reaction [1]. This synthesis route begins with a stoichiometric amount of powdered starting materials, typically metal oxides or metal carbonates. These are mechanically ground together in a mortar and pestle, or ball milled, and then pressed into a pellet before heat treatment. This treatment provides maximum contact between particles, enabling atomic diffusion between the starting reagents. The corresponding sample is then heated to temperatures anywhere from 300 - 1500 ° C. The target temperature is dictated by the elemental composition of the sample, and properties such as volatility, melting point, and reactivity must be taken into consideration. Subsequent grinding, pressing, and heating processes may be needed for reaction completion. The combination of kinetics and thermodynamics can explain the success of such a method and can be thermodynamically predicted through the consultation of phase diagrams. High-temperature synthesis is needed to overcome diffusion barriers and lattice enthalpies, and diffusion begins at the interfaces between particles of starting reagents, with product formation occurring at the interface. For this reason intermediate grinding between successive heating intervals are crucial for complete product formation, as it creates new interfaces of unreacted starting material for product formation.

1.2.2 Molten Salt Ion Exchange

The molten salt ion exchange method relies on the topotactic exchange of ions in a structure [1]. In such a reaction, cations from the host phase are exchanged for those from the surrounding phase. Molten salt ion exchange uses a water-soluble salt with a low melting point, such as alkali halides or nitrates. For the exchange reaction, the parent compound is combined with the alkali salt in an excess molar ratio of the salt. Once thoroughly combined and mixed, the mixture is placed in an appropriate reaction vessel and heated above the melting point of the salt. Once in a liquid state, diffusion of the alkali cations into the host structure can occur, with counter-diffusion of host structure cations into the molten liquid phase. After cooling, any excess alkali salt or salt from the exchanged host cation can be removed by washing with water and/or using mild acidic conditions.

1.2.3 Crystal Growth Flux Method

There are a wide variety of crystal synthesis techniques; the most common method is the flux method. Flux method can be achieved when the components of the desired substance are dissolved in a solvent (flux) [1]. This flux method takes place in a crucible made of highly stable, non-reactive material such as an aluminum oxide crucible or a sealed quartz ampule. By keeping the constituents of the desired crystal and the flux at a temperature slightly above the saturation temperature, an over-saturated solution can be achieved. By cooling the crucible slowly, crystal formation can begin by spontaneous nucleation. As material precipitates out of

the solution with slow cooling, the amount of solute in the flux decreases and the saturation temperature lowers. This process repeats itself as the furnace continues to cool until the solution reaches its melting point.

1.2.4   Hydrothermal Synthesis

The synthesis of single crystals can be achieved using the hydrothermal synthesis method [1]. This method depends on the solubility of minerals in hot water under high pressure. Crystal growth using this method can be achieved using an apparatus consisting of a steel pressure vessel called an autoclave, in which the reactants are supplied along with water or nonaqueous solvents as a reaction medium. If the non-aqueous solvents are utilized as reaction medium, this approach is defined as a solvothermal method; whereas, in the presence of water, it is known as hydrothermal process. A temperature gradient is achieved between the opposite ends of the growth chamber. At the hotter end the nutrient solute dissolves, while at the cooler end precipitates form, growing the desired crystal.

1.2.5   Sealed Quartz Tube Ampule Method

Solid state reactions in which air sensitivity is a major concern can be achieved using the sealed quartz tube ampule method [2]. Here, a sample is placed at the bottom of a sealed quartz tube and a vacuum using a turbo pump system is applied to evacuate the air. Pressures within the quartz tube generally are $\sim 10^{-4}$ Torr.

An H_2/O_2 torch can be used to seal/cut the quartz tube. The corresponding quartz tube can then be heated to desired temperature.

1.3 Structural Characterization

1.3.1 Introduction

A variety of diffraction methods were employed in this dissertation. Here, fundamentals of diffraction and key powder diffraction techniques will be addressed.

1.3.2 Fundamentals of Diffraction

When electromagnetic radiation passes through a crystalline lattice, the atomic positions can act as scattering centers and coherent and incoherent scattering can occur. For an incident X-ray beam with a fixed wavelength comparable to atomic spacings, the electronic cloud will distort, and the movement of these charges re-radiates waves with the same frequency. This phenomenon is known as elastic scattering [3]. Constructive interference occurs when the distance between the adjacent Miller planes, d, is an integral multiple of the wavelength, λ, and can ultimately be explained by Bragg's law (Figure 1.1) [3].

By altering the incident angle of the X-ray beam with a fixed wavelength, certain Miller planes with different d-spacing will satisfy Bragg's law, and therefore coherent diffraction will occur, resulting in a diffraction pattern. A diffraction pattern is not a direct representation of the crystal lattice. It is, however, a repre-
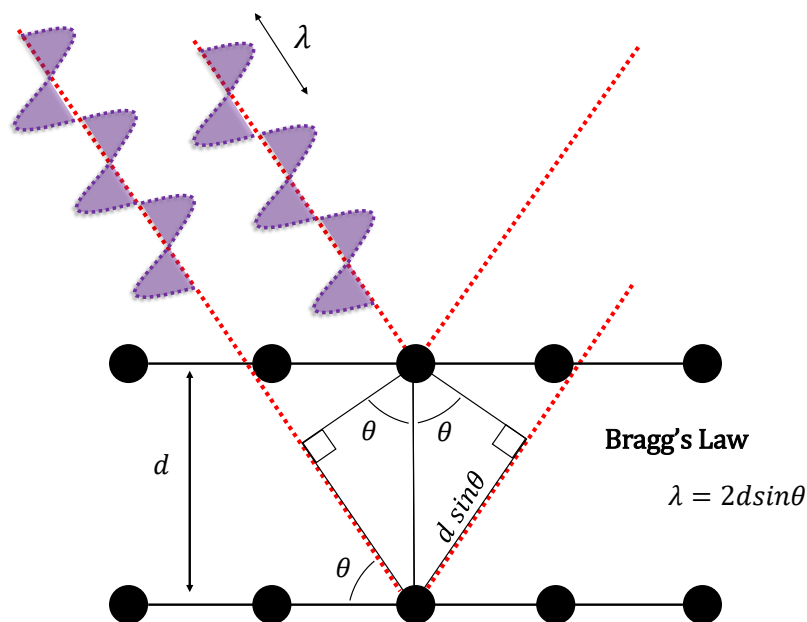
Figure 1.1: Constructive interference occurs when the waves reflected from adjacent scattering planes remain in phase. This occurs when the distance between the adjacent planes, d, is an integral multiple of the wavelength, λ, and can ultimately be explained by Bragg's law.

sentation of the reciprocal lattice. For every real lattice there is a reciprocal lattice. Therefore, the relationship between the crystal lattice and a diffraction pattern is linked by the reciprocal lattice via a Fourier transform. The families of planes in a crystal lattice can be represented by their normals, which are specified as vectors and which can be used to define a pattern of points, with each point representing a family of planes [3]. These points described by the normal vectors characterize the reciprocal lattice. Thus, the crystal axes can be defined in terms of the normal to crystal faces with each point in reciprocal space representing a set of planes within the crystal lattice.

1.3.3   Powder Diffraction Techniques

1.3.3.1   X-ray Diffraction

A popular instrument for the study of crystalline materials is powder X-ray diffraction (PXRD). For most laboratory X-ray diffraction instruments, the Bragg-Brentano focusing geometry is the most common diffractometer layout [3]. The source of X-ray radiation for PXRD is commonly an X-ray tube or a synchrotron particle accelerator at a national lab.

Laboratory X-ray diffractometers utilize an X-ray tube consisting of a metal target, which acts as the anode (typically copper), and a source of electrons (typically a tungsten filament) acts as the cathode. To generate X-rays, a large voltage potential is applied across the anode and the cathode ($\sim$30 kV), resulting in a flow of high speed electrons from the filament to the metal target [3]. Upon collision with the metal target, a continuous spectrum of X-rays is generated. This continuous spectrum of radiation is a result of the rapid changes in kinetic energy of electrons interacting with the target, and is called white radiation. For a copper anode, the incident electrons bombarding the anode surface have enough energy to ionize the $1s$ (K shell) electrons, and an electron in the $2p$ or $3p$ orbital immediately relaxes down to occupy the vacant state, resulting in a release of X-ray radiation. The $2p \rightarrow 1s$ transition has a wavelength of 1.5418 Å and is called K_{α}. The $3p \rightarrow 1s$ transition has a wavelength of 1.3922 Å and is called K_{β}. For a copper anode, nickel foil is a very effective filter as the energy required to ionize 1s electrons corresponds to a wavelength of 1.488 Å, which lies in energy between K_{α}

and K_β [3].

X-rays from synchrotron sources are emitted when charged particles (typically electrons) are traveling at near relativistic speeds and are forced to change direction on passing through a magnetic field. Such synchrotron storage rings exist at national labs such as Argonne National Lab. Synchrotron X-rays have several advantages, such as very high intensity beams that are continuous over the complete spectral range and the beams are accurately parallel, resulting in high resolution in powder diffraction data [3].

1.3.3.2 Neutron Diffraction

For both neutron and X-ray diffraction, the concept of diffraction is essentially the same, as defined by Bragg's Law. Neutron diffraction can be used to determine the structural and atomic parameters of materials that have both light and heavy atoms present [4]. Neutron diffraction is ideal to characterize most metal oxide structures as oxygen has a neutron scattering length comparable to most heavy metals [4]. Neutron diffraction can also provide contrast between atoms with similar atomic numbers, as well as contrast between different isotopes of the same atom. Neutrons exhibit a dipole moment and can therefore interact with unpaired electrons in a material. Thus, magnetic ordering will be apparent in neutron diffraction. Ferromagnetic ordering in a material results in a change in the peak intensity of peaks already present, whereas antiferromagnetic ordering results in the emergence of new peaks [4]. Neutrons can be generated through either a

spallation process or nuclear fission, and experiments can be performed at either a spallation source or reactor, respectively. Neutrons at a reactor have the advantage of better resolution at higher d-spacing due to singular monochromatic neutron wavelength. Neutrons produced at a spallation source have a higher incident flux as more neutrons with appropriate energy are released via spallation than fission. In a spallation process, a metal target is bombarded by pulses of a proton beam, and the neutrons are released in pulses with an array of kinetic energy. Recall, the de Broglie equation relates the wavelength, λ, of a system with mass (neutron) to its momentum, mv. For the spallation process, collector banks are oriented at fixed positions relative to the incoming neutron beam and the sample. Thus, by timing a neutron over a fixed path length, its velocity, and consequently its wavelength, can be measured. As such, spallation radiation is called time-of-flight (TOF). For each collector bank with a fixed position and therefore fixed angle relative to the incoming neutron beam, only certain neutrons with a kinetic energy can satisfy certain d-spacings associated to Miller planes. Thus, multiple banks of data are needed to refine the crystal structure. Fixed wavelength neutron diffraction and TOF neutron experiments were collected at National Institute of Standards and Technology (NIST) and the Spallation Neutron Source, Oakridge National Laboratory (SNS-ORNL), respectively.

1.3.4   Inductively Coupled Plasma - Optical Emission Spectrometry

Inductively coupled plasma – optical emission spectroscopy (ICP – OES) is a analytical technique that can be used to accurately determine the concentration of trace amounts of metals in a solution [5]. ICP – OES utilizes an argon plasma to excite atoms or ions which emit characteristic radiation upon relaxation. The intensity of this from the sample radiation is compared to a calibration curve of previously measured intensities obtained from solutions with known concentrations of the metal in question.

1.3.5   Thermogravimetric Analysis

Thermogravimetric analysis (TGA) can provide useful insight into the processes observed in a sample, such as the mass gained during a reaction procedure, the mass lost during a dehydration process, sample decomposition, etc. Such TGA methods delicately measure the mass of a sample as a function of temperature or time [1].

1.3.6   Iodometric Titration

Iodometric titration is a redox titration process that involves direct titration using sodium thiosulfate as the titrant [6]. This titration method can be used to determine the concentration of an oxidising agent in solution and to ultimately establish the oxidation state of a metal within a metal oxide structure (assuming

the metal oxide sample can be dissolved in a acidic solution). To a known volume of sample, an excess known amount of iodide (I^-) is added. Based on the reduction potentials, iodide will be oxidized by the oxidizing agent to produce triiodide ions (I_3^-), which produces a dark brown color in solution. The reduction reaction of I_3^- and thiosulfate are provided below [6].

$I_3^- + 2e^- \leftrightarrow 3I^-$ ($E^0 = + 0.54$ V)

$S_4O_6^{2-} + 2e^- \leftrightarrow 2S_2O_3^{2-}$ ($E^0 = + 0.08$ V)
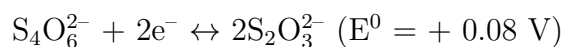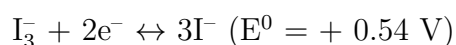
Based on the reduction potentials, thiosulfate acts as a reducing agent, thus reducing the formation of I_3^- back to iodide I^-, producing a colorless solution.

$I_3^- + 2S_2O_3^2 \leftrightarrow S_4O_6^{2-} + 3I^-$ ($E^0 = + 0.46$ V)
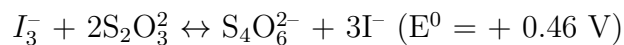
Thus, the color change represents the end-point of the reaction and from the known amount of sodium thiosulfate with a known concentration required, the concentration of an oxidising agent in solution can be determined; this will ultimately establish the oxidation state of a metal within a metal oxide structure.

1.3.7 X-ray Absorption Spectroscopy

For X-ray Absorption Spectroscopy (XAS), X-rays of a narrow energy resolution are shone on the sample and the incident and transmitted X-ray intensity is recorded as the incident X-ray energy is incremented [7]. When a beam of monochromatic X-rays passes through matter, the beam intensity decreases due to interaction with the atoms in the material. Thus, XAS is the measurement of the X-ray absorption coefficient of a material. For X-rays of sufficient energy,

an incoming photon interacts with a deep-core electron; a s electron is excited for a K-edge spectrum or a p electron is excited for a L-edge spectrum [7]. The deep-core electron is promoted to some unoccupied state above the Fermi energy, and leaves behind a core-hole. A short time later (femtoseconds), the core state is filled via one of two mechanisms: (1) a higher-energy electron decays into the core-hole and emits a photon, or (2) the energy from the higher-lying electron can be used to emit an Auger electron. Since each element has its own edge energy, an element's identity and valence can be determined within a sample using XAS methods.

1.4   Electronic Properties of Materials

All elements contain discrete electronic energy levels which are characterized by atomic wave functions. The electronic interaction between atoms within a crystal lattice produces unique delocalized electronic states. The occupied delocalized sates form an electronic energy band called the valence band (VB). The unoccupied delocalized states form an electronic energy band called the conduction band (CB). The band structure can be described from either the 'chemical approach' or the 'physical approach' [8]. The more basic 'chemical approach' is to take Molecular Orbital (MO) theory, as it is typically applied to small, finite-sized molecules, and extend it to infinite 3D structures. As shown in Figure 1.2, with an increase in atomic orbitals, the MO states become close enough in energy such that the bonding MO's form the valence state continuum and the antibonding MO's form

the conduction band continuum.
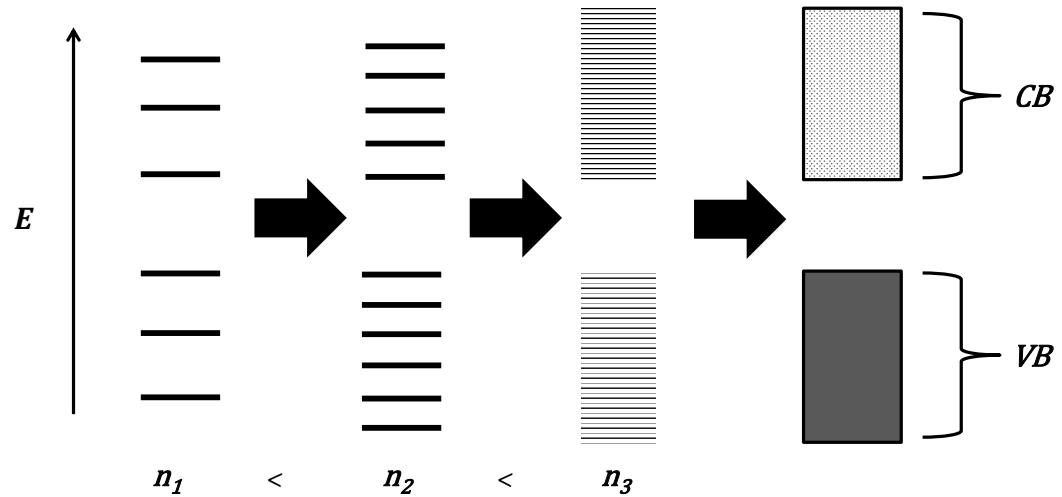
Figure 1.2: A schematic of n atomic orbitals combining to form MO states, where $n_1 < n_2 < n_3$. For n_3, the MO states are close enough in energy and occupied (VB) and unoccupied (CB) bands exist.

The 'physical approach' of band theory is to consider the energy and wavelength of electrons in a solid [8]. The analogy with the quantum mechanical problem of a particle in a box is applied where the energy levels that the electrons occupy are quantized and filled from the bottom of the well up with a total of two electrons per level. The potential within the crystal (or potential well) is periodic, in which the electrons pass through a minimum at the positions of the nuclei and a maximum between the nuclei. The Schrodinger equation that describes such a periodic potential function shows only certain bands of energies are permitted for the electrons. Such forbidden energies correspond to electron wavelengths that do not

satisfy Bragg's law and ultimately leads to discontinuities in the energy-momentum diagrams with forbidden energy levels describing the band gap [8].

1.4.1 Characterization of Metals, Semiconductors, and Insulators

If the difference in energy between the lowest unoccupied and highest occupied delocalized states (band gap, E_g) is less than $\sim$0.3 eV, the material is considered metallic (Figure 1.3 (A)) [9]. If E_g is within $\sim$0.3 to 3 eV, the material is considered a semiconductor (Figure 1.3 (B)). Thermal energy ($\sim$300 K) can promote a small portion of electrons with $k_b T$ kinetic energy to lower unoccupied states for a material. For insulating material, E_g is large enough ($>$ 3 eV) that a crystal system at $\sim$300 K does not provide enough energy to promote electrons to the CB (Figure 1.3 (C)).

The value of the electrical conductivity can, in part, characterize if the material is a metal, semiconductor, or insulator. Table 1.1 below defines the approximate electrical conductivity range for each material type [9].

Table 1.1: Typical values of electrical conductivity of metals, semiconductor, and insulators.

Material	σ ($\Omega^{-1}\ cm^{-1}$)
Metal	$10^{-1} - 10^5$
Semiconductor	$10^{-5} - 10^2$
Insulator	$<10^{-12}$

Though the conductivity values presented in Table 1.1 show a clear distinction between a metal and an insulator, establishing if a material is a metal or semicon-
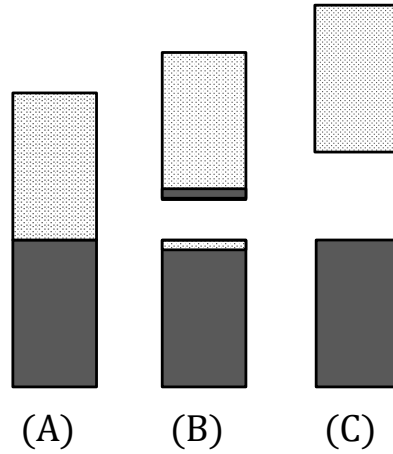
Figure 1.3: Band state schematic of a metal (A), semiconductor (B), and insulator (C).

ductor is not as straightforward. For electrical conduction in semiconductor and insulators to occur, electrons must be promoted across the band gap. In metals, however, there is no band gap. For all materials, electron–phonon collisions contribute to the overall resistivity, meaning that with an increase in temperature, an inherent increase in the electrostatic interactions between mobile electrons and lattice vibrations will occur [9]. For semiconductors and insulators, increasing the temperature means more electrons with adequate k_bT kinetic energy can occupy the conduction band, outweighing the electron–phonon collision contribution and therefore an increase in the overall electrical conductivity is observed. In metals, electron–phonon collisions dominate, thus showing a decrease in electrical conductivity with increasing temperature. Thus, the trend in electrical resistivity versus temperature can, in part, characterize if the material is a semiconductor or a metal.

1.4.2   Modeling the Electronic Properties

In a typical insulator, E_g is temperature-independent and much larger than k_bT. Therefore the Arrhenius expression (1.1) can be applied and $\ln(\rho)$ scales linearly with T^{-1} in which the slope equates to E_g [10].

$$\rho \propto e^{(E_g/k_bT)} \tag{1.1}$$

If the energy gap is temperature-dependent, a different behavior known as variable-range hopping (VRH) appears (1.2) in d dimensions [10].

$$\rho \propto exp\left(\frac{E_g}{k_bT^{1/(d+1)}}\right) \tag{1.2}$$

The dimensionality, d, describes the dimension of conductivity throughout the material. Plotting $\ln(\rho)$ versus $T^{-1/(d+1)}$ provides the "pseudogap" derived from the slope.

1.5   Thermal Transport Properties

Thermal conductivity can be described as the transport of energy in the form of heat through a body of mass with a temperature gradient [9]. Heat always flows toward the lower temperature portion of a material (second law of thermodynamics) (Figure 1.4).

$$\frac{dQ}{dt} = Q = \lambda A \frac{T_2 - T_1}{\Delta x} \tag{1.3}$$

The thermal conductivity equation (1.3), describes the relationship between transported heat per unit of time (dQ/dt or heat flow Q) and the temperature gradient ($\Delta T/\Delta x$) through area A representing the area through which the heat flows perpendicularly at a steady rate (Figure 1.4) [9].

$$\lambda = K_T = \alpha \rho C_p \tag{1.4}$$

Therefore, thermal conductivity (λ) is a material-specific property (Figure 1.5) described by the thermal diffusifity (α), density of the sample (ρ), and specific heat capacity (C_p) (Equation 1.4).
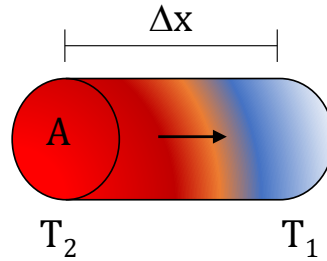
Figure 1.4: Illustration of the relationship between transported heat per unit of time (dQ/dt or heat flow Q) and the temperature gradient ($\Delta T/\Delta x$) through area A representing the area through which the heat flows perpendicularly at a steady rate.

1.6 Low Temperature Specific Heat Properties

The specific heat value is not a constant, particularly at temperatures much lower than room temperature. There are two theories to describe the behavior of the
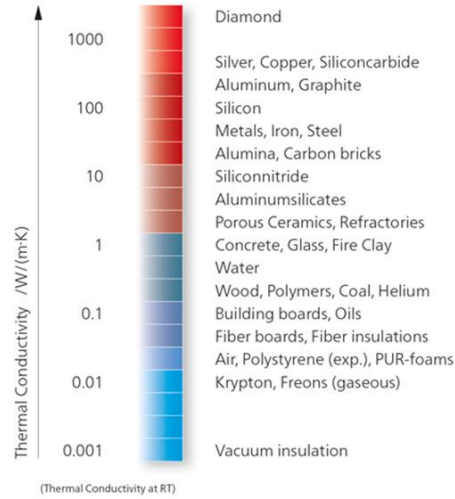
Figure 1.5: An overview of the thermal conductivity for various materials at room temperature.

specific heat of materials over the entire temperature range of interest. The first theory describes the energy contained in the lattice vibrations or phonons (Debye theory) that exist in a solid. For insulators, only the phonon contribution characterizes the specific heat. To determine the phonon specific heat, the internal energy, U, can be described by the integration of the phonon density of states, $D(\omega)$, which describes the fraction of phonons that occupy a particular energy level characterized by its frequency, ω, and the statistical distribution function, $n(\omega)$ for phonons obeying Bose-Einstein statistics (Equation 1.5) [8].

$$U = \frac{h}{2\pi} \int D(\omega)n(\omega)d(\omega) \tag{1.5}$$

By inserting the Debye density of states and distribution function (Bose-Einstein

statistics) into the integral for the internal energy of the phonons, the internal energy is given by Equation 1.6. Here, $T_D = h\omega_D/k_B$, $x = h\omega/k_BT$, and $x_D = h\omega_D/k_BT$ (where T_D is the Debye temperature and ω_D is the maximum phonon frequency representing T_D) [8]. Thus, $x_D = T_D/T$.

$$U = \frac{9Nk_bT^4}{T_D^3} \int\limits_0^{T_D/T} \frac{x^3}{e^x - 1} dx \qquad (1.6)$$

If $T \gg T_D$, $1 \gg x_D$ and therefore $e^x - 1 \approx x$. Thus, U reduces to Equation 1.7 (Dulong and Petit law) [8].

$$U = 3Nk_bT \qquad (1.7)$$

In the limit $T_D \gg T$, $x_D = \infty$, and the integral in Equation 1.6 equals $\pi^4/15$, and the internal energy expression reduces to Equation 1.8.

$$U = \frac{3\pi^4 Nk_BT^4}{5T_D^3} \qquad (1.8)$$

The specific heat is characterized by the change in the internal energy with respect to temperature. Thus, by taking the partial deriviative of Equation 1.8, the specific heat from phonon contribution is achieved (Equation 1.9).

$$C_v = \frac{\partial U}{\partial T} = \frac{12\pi^4 Nk_B}{5T_D^3}T^3 = \beta T^3 \qquad (1.9)$$

For metals and semiconductors at low temperatures (T<10 K) the energy contained in the conduction electrons also contributes to the specific heat. To deter-

mine the electronic specific heat, the internal energy, U, can be described by the integration of the electron density of states, $D(\varepsilon)$, which describes the fraction of electrons that occupy a particular energy level characterized by its frequency, ε, and the statistical distribution function, $f(\varepsilon)$ for electrons obeying Fermi-Dirac statistics (Equation 1.10) [8].

$$U = \int D(\varepsilon)f(\varepsilon)d(\varepsilon) \tag{1.10}$$

Similar to above, by inserting the density of states and distribution function (Fermi-Dirac statistics) into the integral, and by taking the partial derivative of the internal energy with respect to temperature, Equation 1.11 can be achieved.

$$C_v = \frac{\partial U}{\partial T} = \frac{\pi^2}{3}k_B^2 D(E_f)T = \gamma T \tag{1.11}$$

Combining the phonon contribution and the electronic contribution of the specic heat gives the expression defined by the Einstein-Debye model (Equation 1.12) [8].

$$C_v = \frac{\pi^2}{3}k_B^2 D(E_f)T + \frac{12\pi^4 N k_B}{5T_D^3}T^3 = \gamma T + \beta T^3 \tag{1.12}$$

Most metals and small band gap semiconductors obey the Einstein-Debye model and can be confirmed by measuring the heat capacity as a function of temperature and plotting the results as C_v/T versus T^2 at low temperature, resulting in a linear trend with β representing the slope and γ representing the y-intercept.

1.7 Magnetism

The way in which unpaired valence electrons within an inorganic solid interact describes the array of possibilities of various magnetic effects. If the unpaired electron spins are oriented at random throughout the crystal lattice, the material is considered paramagnetic (Figure 1.6 (a)). The interaction of such unpaired spins could also lead to a cooperative magnetic phenomenon. The spins could align parallel and be described as ferromagnetic (Figure 1.6 (b)), or align antiparallel and be antiferromagnetic (Figure 1.6 (c)). Other magnetic phenomenon such as spin glass behavior is possible (Figure 1.6 (d)). Here, long-range antiferromagnetic ordering throughout the lattice cannot occur as certain regions of spins are paired in a ferromagnetic fashion.

When a material is placed in a magnetic field, H, the magnetic flux density, B, (i.e. the density of lines of force in the sample) is related to H and the magnetic moment, M, by the permeability, μ_0 (Equation 1.13) [9, 11].

$$B = \mu_0 H + \mu_0 M \qquad (1.13)$$

As shown in Equation 1.13, μ_0 is the permeability of free space ($4\pi \times 10^{-7}$ H m^{-1}) with $\mu_0 H$ as the induction generated by the field alone and $\mu_0 M$ the induction by the sample. The magnetic susceptibility, χ, is the ratio of the magnetic moment to the applied magnetic field (Equation 1.14) [11].

$$\chi = M/H \qquad (1.14)$$
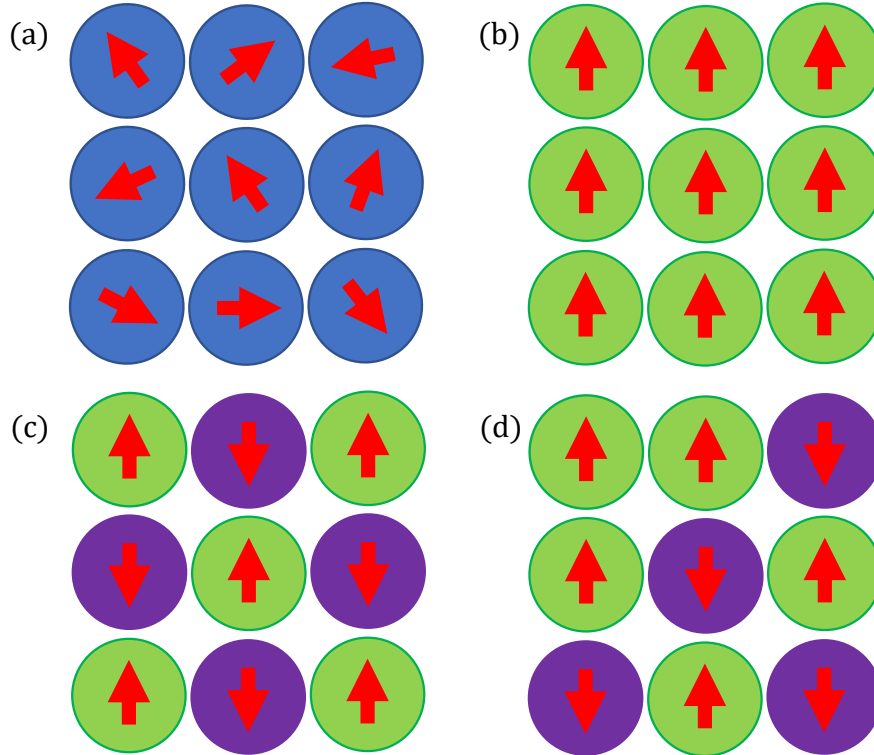
Figure 1.6: Schematic magnetic phenomena in a 2D crystal: (a) paramagnetism, (b) ferromagnetism, (c) antiferromagnetism, and (d) spin-glass.

For diamagnetic materials, the magnetic susceptibility, χ, is very small and slightly negative [11]. In the presence of a magnetic field, the small electric field generated by the orbital motion of electrons is modified and therefore alters the orbital motion of electrons slightly to give a magnetic moment that opposes the applied field, leading to a slight repulsion effect (Lenz's law of electromagnetism) [9]. Materials that exhibit paramagnetic behavior reveal a magnetic susceptibility, χ,

that is very small and positive. Type 1 superconductors expel magnetic fields completely meaning $B=0$ (perfect diamagnetism) and $H=-M$ and therefore $\chi=-1$ [9]. Magnetic structures can be distinguished by their magnetic susceptibility dependence on temperature. For ordered magnetic structures such as ferromagnets, above their respective transition temperature, thermal fluctuations with an energy scale $k_b T$ overwhelm the spin-spin exchange energy, J, causing the spins to become disordered and therefore in a paramagnetic state [11]. When the overall temperature is lowered below the transition temperature, the spins undergo a phase transition to minimize the total energy. Thus, for ferromagnetic structures, for temperatures below the transition temperature, T_c (Curie temperature), an increase in the magnetic moment, M, of the sample with respect to the applied magnetic field, H, is observed, resulting in an increase in the magnetic susceptibility, χ (Figure 1.7). For antiferromagnetic structures, at temperatures lower than the Nèel point, T_N, the electron spins align antiparallel and the magnetic moment, M, and therefore the magnetic susceptibility, χ, both decrease (Figure 1.7). For paramagnetic materials with no transition temperature, spin-spin exchange energy, J, is weak. Therefore, thermal fluctuations dominate down to low temperature.

Paramagnetic materials will obey the Curie law, which states that the magnetic susceptibility, χ, is inversely proportional to temperature, T (Equation 1.15) [11].

$$\chi = C/T \tag{1.15}$$

For systems with some spontaneous interaction between adjacent spins at low
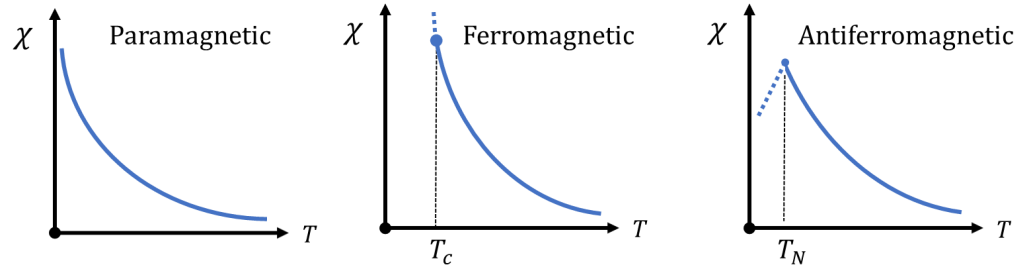
Figure 1.7: Illustrations of disordered and ordered magnetic structures and their magnetic susceptibility dependence on temperature.

temperatures such as ferromagnetic and antiferromagnetic systems, the Curie-Weiss law is obeyed, where C is the Curie constant and θ is the Weiss constant (Equation 1.16) [11].

$$\chi = C/(T - \theta) \tag{1.16}$$

For each of the magnetic structures, plotting the inverse magnetic suscepti-bility, (χ^{-1}) versus temperature, T, within the paramagnetic region will reveal a linear correlation (Figure 1.8). Thus, for paramagnetic materials, the inverse plot extrapolates to 0 K with the Weiss constant, θ, equaling 0 K. For ferromagnetic materials, 0 K $< \theta$, and for antiferromagnetic materials, $\theta <$ 0 K (Figure 1.8). Thus, by plotting the inverse magnetic susceptibility, χ^{-1} versus temperature, T, based on the Curie-Weiss law, the Curie constant, C, represents the slope and the Weiss constant, θ, represents the y-axis.

The relationship between the Curie constant, C, and the spin quantum number,
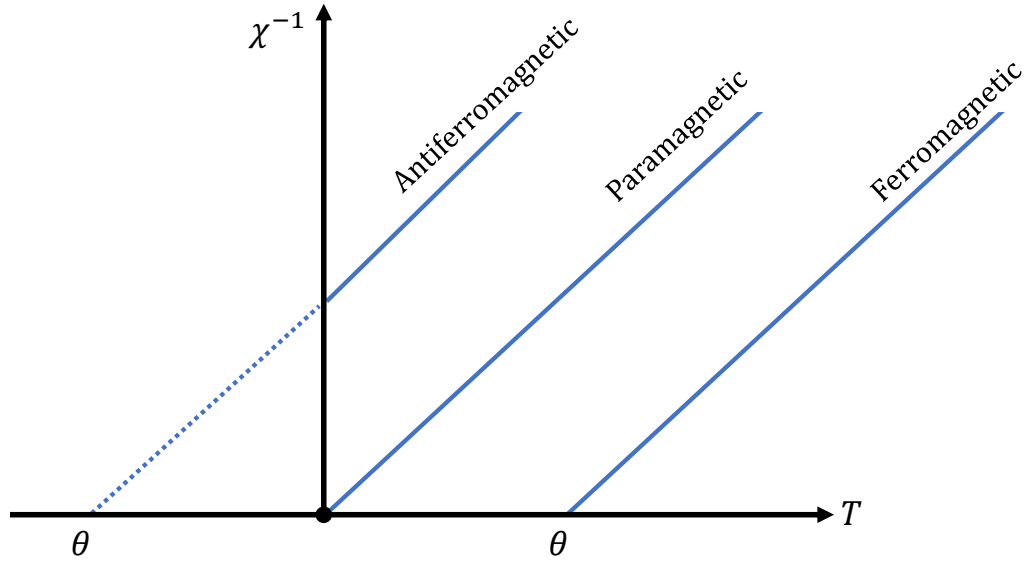
Figure 1.8: Illustration of the reciprocal of magnetic susceptibility, χ^{-1}, versus temperature, T, for paramagnetic materials that may or may not show magnetic ordering at low temperatures.

S, is represented by Equations 1.17 and 1.18, where μ_b is the Bohr magneton and the g-factor is equal to 2 [11].

$$C = \mu_b^2 \mu^2 / 3k_B \qquad (1.17)$$

$$\mu = g[S(S+1)]^{0.5} \qquad (1.18)$$

Equation 1.18 can be used to calculate the magnetic moment of a material, where S is the sum of the spin quantum numbers of the individual unpaired electrons [11]. Thus, by establishing the Curie constant, C, the effective magnetic

moment, μ can be calculated and therefore the spin quantum number can be established. Knowing these variables can corroborate with the presence of magnetic ions within the material of investigation.

1.8   Electronic/Thermal Characterization Techniques

1.8.1   Introduction

Various electrical and thermal characterization techniques were employed in this dissertation. Here, a brief introduction of such techniques will be addressed.

1.8.2   Physical Property Measurement System (PPMS) and Superconducting Quantum Interference Device-Magnetic Property Measurement System (SQUID MPMS)

1.8.2.1   Magnetism

For DC magnetic measurements, the sample is magnetized by a constant magnetic field and the magnetic moment, M, of the sample is measured, producing a DC magnetization curve $M(H)$. The moment is measured most commonly by an induction technique. Inductive measurements are performed by moving the sample relative to a set of copper pickup coils, either by vibration or one-shot extraction, where one measures the voltage induced by the moving magnetic moment

of the sample within the coils. The instrument commonly used to perform such measurements is called a Physical Property Measurement System (PPMS) [12]. A Magnetic Property Measurement System (MPMS) with a Superconducting Quantum Interference Device (SQUID) magnetometer can also be used in which a set of superconducting pickup coils is used to measure the current induced, yielding very high sensitivity to any alteration in the magnetization of the sample [13]. This process is performed over a variable temperature range. In AC magnetic measurements, a small AC drive magnetic field is superimposed on the DC field, resulting in a time-dependent magnetic moment in the sample [14]. The field of the time-dependent moment makes a current in the pickup coils, meaning measurement without sample motion can occur. Spin-glass behavior is usually characterized by AC susceptibility. This process is performed over a variable temperature range. All the magnetic measurements presented in this thesis were collected by Patrick LaBarre and Dr. Arthur Ramirez using a PPMS and SQUID MPMS at UC Santa Cruz.

1.8.2.2   Low Temperature Electrical Conductivity

The PPMS can be configured for four-terminal resistance measurements [12]. To perform four-terminal resistance measurements, the sample is mounted on a puck and four leads are attached to the sample. During the measurement the hardware will pass a current through the sample via two leads, using the other two leads to measure the electric potential drop across the sample. The current and the poten-

tial drop can be known to a high degree of accuracy because the input impedance of the voltmeter is very high. This process is performed over a variable temperature range. Most of the low temperature resistivity measurements presented in this dissertation were collected by Patrick LaBarre and Dr. Arthur Ramirez using a PPMS at UC Santa Cruz.

1.8.2.3 Low Temperature Heat Capacity

The Heat Capacity of a material can be determined using a Quantum Design PPMS [15]. For this setup, a platform thermometer and a platform heater are attached to the bottom side of the sample platform. Small wires provide the electrical connection between the platforms. The sample is mounted to the platform using a thin layer of grease or epoxy. During a measurement, a known amount of heat is applied at constant power for a fixed time. Once the heater is turned off, an exponential decay of the temperature of the sample versus time is observed, of which the decay pattern can be modeled, and the heat capacity can be extracted. This process is performed over a variable temperature range. All the heat capacity measurements presented in this thesis were collected by Patrick LaBarre and Dr. Arthur Ramirez using a PPMS at UC Santa Cruz.

1.8.3   High Temperature Thermal Transport Measurements

The ability of a material to conduct energy in the form of heat can be characterized by determining a material's thermal conductivity. This can be done by measuring the thermal diffusivity of the sample using a Laser Flash instrument [16, 17]. For this method, a Nd:YAG laser is used to provide an infrared radiation pulse normal to the sample. In carrying out a measurement, the lower surface of a plane parallel sample is first heated by a short IR energy pulse (Figure 1.9). The resulting temperature change on the upper surface of the sample is then measured with an IR detector. The higher the sample's thermal diffusivity, the steeper the signal increase. An illustration of the corresponding signal is presented in Figure 1.10.
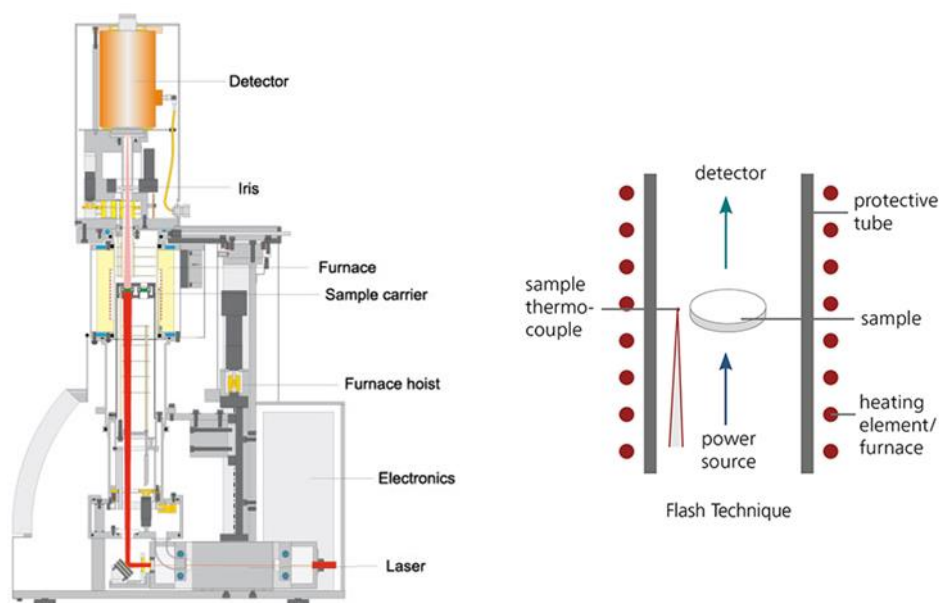
Figure 1.9: Schematic of LFA 457 MicroFlash (1100° C).

By using $1/2\Delta T_{max}$ which represents $t_{1/2}$ (Figure 1.10) and sample thickness, d, the thermal diffusivity, α, and ultimately the thermal conductivity, λ, can be calculated using Equations 1.4 and 1.19. This process is performed over a variable temperature range. To improve even heating across the sample face, a layer of graphite is applied to the sample prior to measurement.

$$\alpha = 0.1388\frac{d^2}{t_{1/2}} \tag{1.19}$$
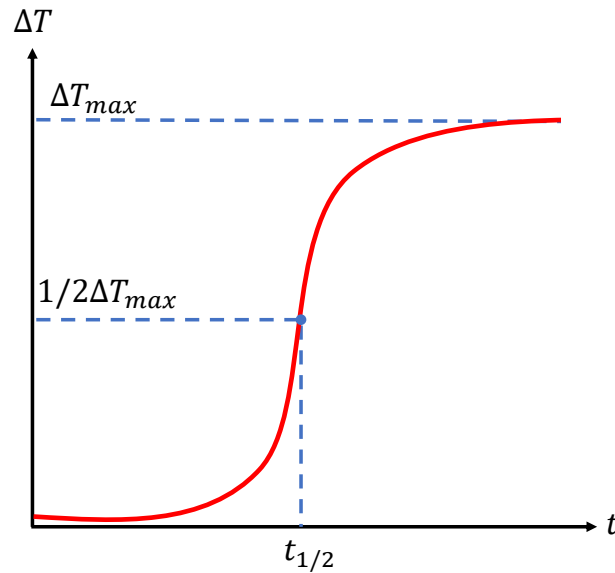
Figure 1.10: Illustration of the change in temperature versus time recorded by the IR detector due to the temperature change on the upper surface of the sample from the applied IR energy pulse.

1.8.4 High Temperature Seebeck Electric Resistivity Measurements

High temperature four-probe resistivity measurements were performed using a ZEM-3 instrument [17, 18]. Four leads are attached to a bar as shown in Figure 1.11. The Platinum wire of each of the two R-type thermocouples is used to measure the Seebeck voltage or the voltage drop between the two probes during current flow through the sample to calculate the resistivity of the sample. The resistance of the sample, R, is determined according to Ohm's law, $V = IR$, and ρ of the sample is determined by incorporating the dimensions l, w, and h (Equation 1.20) [17].

$$\rho = Rwh/l \tag{1.20}$$

The current and the potential drop can be known to a high degree of accuracy for the four-probe method because the input impedance of the voltmeter is very high.

1.9 Electron Paramagnetic Resonance Spectroscopy

Electron paramagnetic resonance (EPR) spectroscopy is used for studying paramagnetic compounds with unpaired electrons. The basic concept of EPR is analogous to nuclear magnetic resonance (NMR), the difference being excitation of the electron spins instead of the spins of atomic nuclei. The intrinsic angular momentum of an electron generates a magnetic dipole moment, μ. For a single unparied
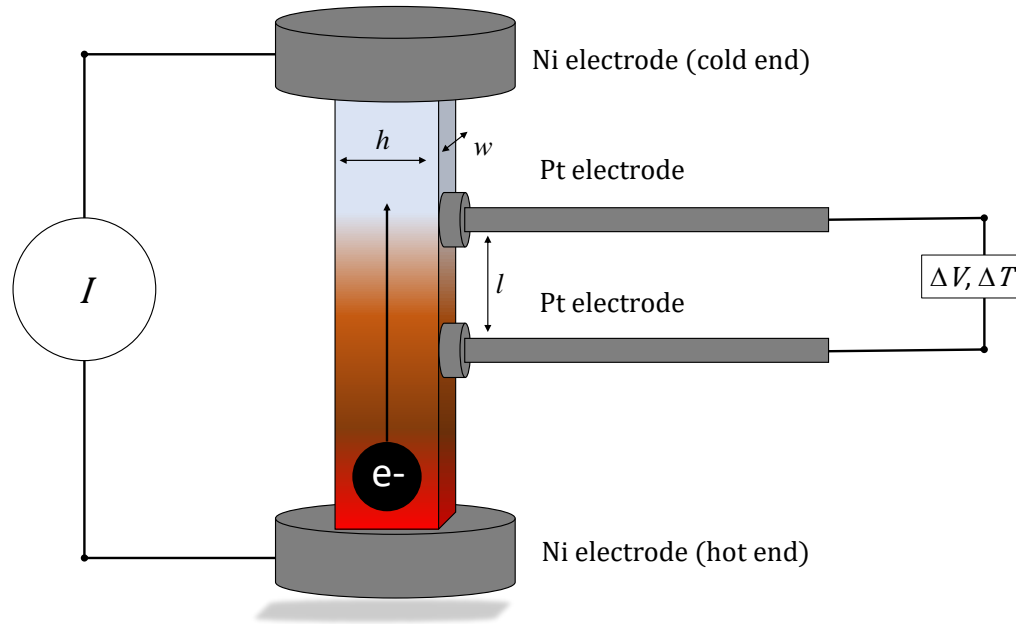
Figure 1.11: Illustration of the measurement of four-probe resistivity and Seebeck coefficient in a sintered bar sample.

electron, under the application of a magnetic field with strength B, the potential energy developed from the interaction of the magnetic dipole moment and the applied magnetic field can be represented by Equation 1.21 where θ represents the angle between the magnetic dipole vector and the applied field vector, $m_s = \pm\frac{1}{2}$, and g_e is the Landé g-factor [19, 20].

$$U = m_s g_e \mu_B B \cos\theta \tag{1.21}$$

Thus, the potential energy is dependent on the moments vector direction relative to the applied field. If the electron's magnetic moment aligns itself exactly

parallel to the field, a minimum or maximum potential energy can be achieved, depending on the moment vector direction relative to the field. The difference between U_{min} and U_{max} is expressed by Equation 1.22 (Zeeman energy splitting) [19, 20].

$$\Delta E = g_e \mu_B B \cos \theta \tag{1.22}$$

Equation 1.22 therefore states that the splitting of U_{min} and U_{max} is directly proportional to the magnetic field's strength, B. An unpaired electron can transition between the maximum/minimum energy levels by either absorbing or emitting a photon of energy, $h\nu$. Thus, Equation 1.23 is established [19, 20].

$$h\nu = g_e \mu_B B \cos \theta \tag{1.23}$$

Equation 1.23 suggests a large variety of frequency and magnetic field value combinations. EPR measurements, however, are typically conducted with magnetic fields around 0.3-0.4 Tesla and with microwaves in the 8-10 GHz region [20]. EPR measurements are usually conducted where the frequency is kept fixed with the applied magnetic field as a variable. Various information can be obtained from EPR spectroscopy, such as the identity of elements and what oxidation state is present [21]. The Zeeman energy splitting due to an applied magnetic field is related to the g-factor, which for systems that have relatively insignificant spin-orbit coupling (SOC) energies, g=2.0023 [19]. With the incorporation of large spin-orbit coupling, however, the Zeeman energy splitting results in a g-factor value

that deviates from 2.002, of which the difference is associated to the SOC. There are various perturbation theory equations that relate the observed g values to a spin-orbit coupling constant, though all are for $3d$ ions where the SOC can be treated as a perturbation, compared to the ligand-field effects [19, 22].

1.10   Computational Methods

Computational methods can provide useful information about the electronic properties of a material. The open-source package ABINIT was used to perform electronic calculations for Chapter 7 [23]. ABINIT utilizes density functional theory; implementing a plane wave basis set and pseudopotentials to compute the electronic density and derived properties of a particular system. Details of the exact model can be found in Chapter 7. All calculations were performed by Dr. Warren Pickett's research group at University of California, Davis.

Chapter 2: Enigmatic States of Matter

2.1   Abstract

Transition-metal oxides with partially filled $4d$ and $5d$ shells exhibit an intricate interplay of crystal field, spin-orbit coupling (SOC), and electronic correlations. For $3d$ compounds, the atomic interactions, crystal field, and electronic correlations can energetically compete, with the SOC remaining small. In heavy $5d$ transition metal oxides, however, SOC is significant, and all energy scales are comparable. Small changes in such effects can drastically influence the electronic properties, resulting in a variety of novel forms of quantum matter (Figure 2.1) [24, 25]. This chapter will provide a brief introduction of such effects in addition to highly sought-after enigmatic states of matter: the quantum spin liquid and the topological insulator.

2.2 d-Electron Effects

For transition metal complexes, the valence d-electrons can influence the coordination environment of the metal atom which can therefore affect electronic properties. Crystal field theory (CFT) is adequate to describe the effects that occur [26]. For a metal-ligand environment, all five valence d-orbitals on the transition metal are not degenerate. For example, in an octahedral environment, valence d-orbitals
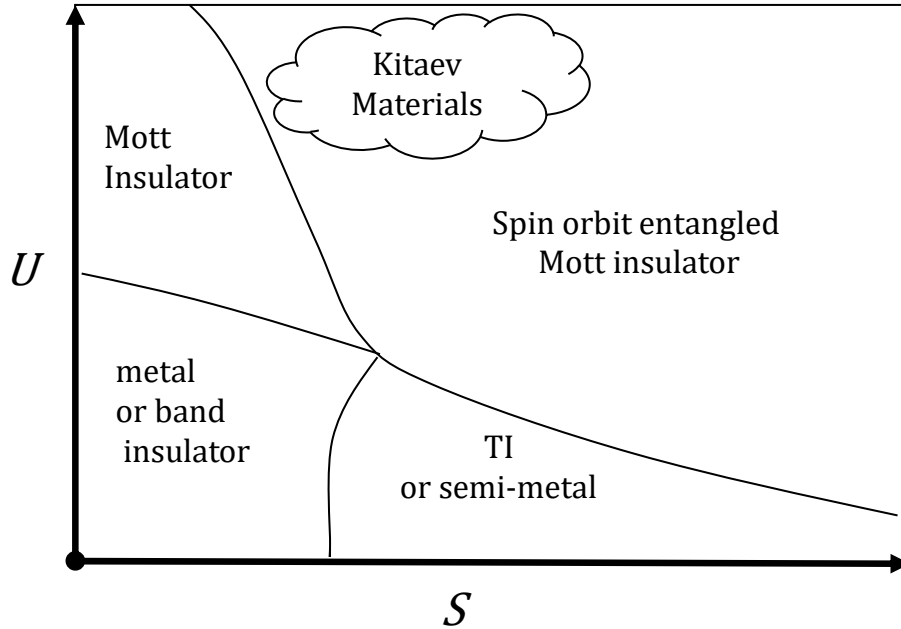
Figure 2.1: Illustration of how the electronic property of a material changes when varying the magnitudes of spin-orbit coupling, S, and electronic correlations, U. Figure adapted from review [25].

split into two groups; the t_{2g} group (3 degenerate d-orbitals) are lower in energy than the e_g group (2 degenerate d-orbitals) (Figure 2.3). If the difference in energy between the e_g and t_{2g} states, ΔO_h, is less than the pairing energy, P, of two electrons occupying a given t_{2g} orbital, Hund's rule is obeyed, forming a high-spin state. If, however, $\Delta O_h > P$, the t_{2g} states fill first, forming a low-spin state. The magnitude of ΔO_h, in part, depends on the transition metal: generally $\Delta O_h(5d)$ > $\Delta O_h(4d)$ > $\Delta O_h(3d)$ [26].

2.3 Electron Correlation

The band model (discussed in Chapter 1) is often inadequate for describing the properties of metal oxides as the bands of such compounds are typically too narrow for the effects of electron-electron interaction to be ignored [26]. For the simple band model, it is assumed that the repulsion between electrons can be represented with an independent electron orbital wavefunction to describe the average effective potentials of the electrons. For simple intermetallic systems, this approach is generally acceptable as the highly mobile electrons described by the wide bands possess good screening properties. The Hubbard U_H approximation is particularly useful to circumvent this inaccurate description for metal oxides [26]. Here, the repulsion between electrons is neglected, except when they are on the same atom. For a given metal-oxide system, unpaired electrons within the d-orbitals can effectively "hop" between trasition metal sites. The energy input required to translate between metal sites along with the energy of the now extra electron repulsion describes the Hubbard U_H energy. If $U_H>E_g$, a Mott insulator will exist. If $U_H<E_g$, a semiconductor/metallic system will exist [26].

2.4 Spin-Orbit Coupling

Spin-orbit coupling is the interaction of an electron's intrinsic angular momentum, or spin, with the orbital motion of the electrons through space [25]. This spin-orbit coupling can be better understood by examining the effect in terms of the motion of the nucleus of charge Ze (Z is the atomic number) with respect to the electron's

position. Thus, with respect to the electrons viewpoint, the nucleus circulates about the electron with the same angular momentum, l, as the electron orbiting the nucleus (Figure 2.2). This relative motion creates a current (Equation 2.1) and such a current generates a magnetic field at its centre (Equation 2.2) [27].
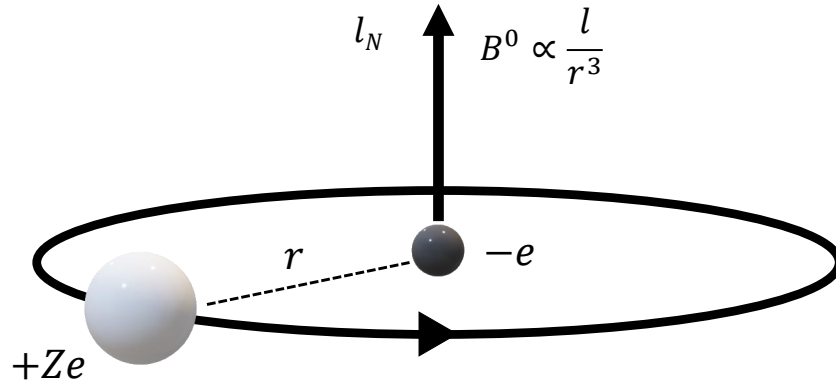
Figure 2.2: Illustration of the magnetic field at an electron produced by the relative motion of the nucleus.

$$I = \frac{Ze|l|}{2\pi m_e r^2} \tag{2.1}$$

$$B^0 = \frac{\mu_0 I}{2r} = \frac{Ze\mu_0}{4\pi m_e r^3}|l| \tag{2.2}$$

The intrinsic angular momentum, or spin, of the electron also has an associated magnetic moment (Equation 2.3) where g_e is the spin g-factor ($g_e \approx 2$) [27]. The electron spin interacts with the field B^0 resulting in potential energy expressed in

Equation 2.4 [27].

$$m^s = -g_e \frac{e}{2m_e} s \tag{2.3}$$

$$E_{so} = -m^s B^0 = \frac{\mu_0 Z e^2 g_e}{8\pi m_e^2 r^3} s \cdot l = \xi(r) s \cdot l \tag{2.4}$$

Thus the spin-orbit interaction energy, E_{so} scales with the atomic number, Z. Atoms with a high atomic number therefore have a strong spin–orbit force and electrons travelling through materials composed of such atoms therefore feel a strong spin- and momentum-dependent force that resembles a magnetic field.

Of recent interest for exotic states such as topological insulators (described in Chapter 3.7) are $4d/5d$ metal oxide systems where SOC is large enough to influence the electronic band structure. Iridates are the most widely studied with Iridium frequently in a 4+ oxidation ($5d^5$) state [25, 28, 29]. Certain frustrated systems with such $5d^5$ ground states have been predicted to possess anisotropic exchange interactions, a key ingredient of the Kitaev model of a quantum spin liquid (described in Chapter 2.6) [30].

The valence d-orbital energy level scheme of such d^5 ionic systems is illustrated in Figure 2.3. With the crystal field splitting of the valence d-orbital levels, for a $5d^5$ ionic system, the five electrons occupy the t_{2g} orbitals. The SOC acts within the t_{2g} manifold as $-\lambda$L·S, where L is an effective $l = 1$ angular momentum [31], S, is the spin, and λ is the magnitude of the SOC. Using the rules of addition of angular momenta, SOC will split the t_{2g} levels into an effective $j = 3/2$ quartet and an effective $j = 1/2$ doublet with an energy difference of $3\lambda/2$, as shown in Figure 2.3.
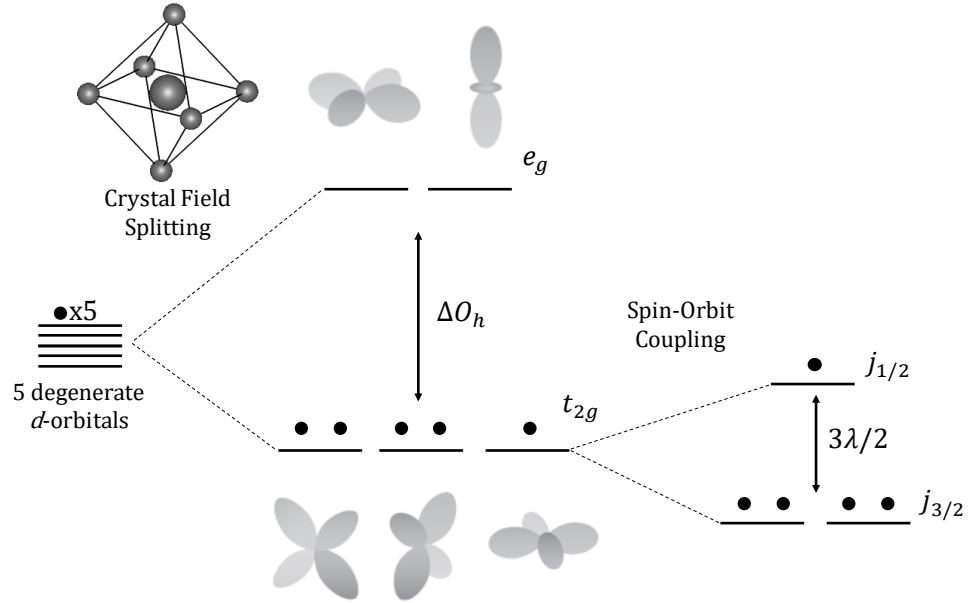
Figure 2.3: Formation of spin-orbit entangled $j = 1/2$ moments for ions in a d^5 electronic configuration.

Strong spin-orbit coupling then results in a system with a fully filled $j = 3/2$ band and a half-filled $j = 1/2$ band for a d^5 system (Figure 2.3) [25]. The magnitude of the SOC varies amongst the $4d$ and $5d$ transition metals. For example, the SOC of iridium and osmium is 540 meV and 480 meV, respectively [32]. For a small band gap semiconductor or metal, the t_{2g} splitting induced by SOC plays a significant role in the gap energy and electrical properties.

2.5 Anisotropic Nature of the Honeycomb Lattice

The framework of the honeycomb lattice enables anisotropic behavior unique to other systems [33]. The distances and angles between the three nearest edge-shared octahedral neighbors are not equivalent, resulting in orthogonal anisotropy between the three nearest-neighbor bonds. In addition, large spin-orbit coupling contributes to anistropic magnetic interactions between the three nearest neighbors [34]. Such characteristics give rise to strong magnetic frustration and therefore an ideal playground to study various exotic states such as quantum spin liquid (QSL) behavior.

2.6 Quantum Spin Liquids and the Kitaev Model

2.6.1 Introduction

A quantum spin liquid (QSL) represents a new state of matter. Unlike conventional magnetic states, such as the ferromagnetic or the antiferromagnetic states (see Chapter 1), a QSL never enters into a long-range ordered phase with a static arrangement of spins, even at absolute zero temperature [35]. For ferromagnets, above the Curie temperature T_c, thermal fluctuations with an energy scale $k_b T$ overwhelm the spin-spin exchange energy, J. When the overall temperature of a ferromagnetic system is lowered below T_c, the spins undergo a phase transition to minimize the total energy. The ground state of the ferromagnetic Heisenberg model is an eigenstate with parallel spins. The ground state of the antiferro-

magnetic Heisenberg model, however, is not a true eigenstate with antiparallel spins and can only be a linearly superposed singlet state representing the ground state [27]. This understanding is what led to the initial discussion of the existence of a QSL state. In 1973, Anderson proposed that in an edge-sharing triangular lattice, the three spins at the corners cannot be made mutually antiparallel, therefore geometrical frustration could prevent spins from undergoing magnetic long-range ordering [36]. Anderson postulated that the spins throughout a triangular lattice would form local singlet pairs and the spins would constantly alter and rearrange the pairings, resulting in a "liquid-like" state of spins [36]. Nevertheless, nearly all known frustrated lattice systems form a magnetic ordered state at some temperature above 0K [37]. The discovery of the cuprate superconductors led to the investigation of the spin-$\frac{1}{2}$ Cu^{2+} ions arranged in La_2CuO_4 square lattice as a potential QSL candidate [38]. However, La_2CuO_4 was later confirmed to possess a Nèel ordered state [39, 40].

2.6.2   Kitaev Model

A QSL state of matter has recently been demonstrated by an exactly solvable model on a 2D honeycomb lattice by Alexi Kitaev [41]. By introducing Majorana operators, Kitaev showed that the ground state of the associated Hamiltonian is a quantum spin liquid [41]. The exploration of physical proof of this model began with honeycomb layered A_2MO_3 (A = group 1 cation and M = $4d/5d$ transition metal). More specifically, iridiate A_2IrO_3 were first proposed as a candidate hon-

eycomb Kitaev model [34, 42].

Discovering a physical realization of the Kitaev model has been proven to be a challenge. All currently known A_2MO_3 honeycomb layered systems, with the potential exception of $Li_{2.15}Os_{0.85}O_3$, have been shown to not possess QSL behavior [43]. There are currently four known systems that show prominent characteristics of the Kitaev model: honeycomb layered $Li_{2.15}Os_{0.85}O_3$, Cu_2IrO_3, α-$RuCl_3$, and Herbertsmithite $ZnCu_3(OH)_6Cl_2$ [43–46].

For $Li_{2.15}Os_{0.85}O_3$, a large van Vleck susceptibility, and an effective moment of 0.85 μ_B (much lower than expected from 70% Os(+5)), and a narrow transport band gap of $\Delta = 243 \pm 23$ meV is observed [43]. No evidence of long range magnetic ordering is found above 0.10 K, however, a spin glass-like peak in ac-susceptibility is observed at 0.5 K. The specific heat displays an impurity spin contribution in addition to a power law $\propto T^{(0.63\pm0.06)}$. The magnetic susceptibility and specific heat are not easily understood using a local moment picture, which suggests that the valence electrons are close to itineracy and that spin orbit coupling of osmium is playing an important role in the collective electronic behavior of the $Li_{2.15}Os_{0.85}O_3$ honeycomb system.

Unlike Na_2IrO_3, which shows long range magnetic ordering $T_N = 15$ K [47], Cu_2IrO_3, remains disordered until 2.7 K with zero field cooling [45]. The order, however, disappears in a weak magnetic field, therefore suggesting short-range magnetic ordering [45]. In addition, unlike Na_2IrO_3 which shows a clear peak at the antiferromagnetic transition $T_N = 15$ K in the heat capacity measurements, such a peak is absent from the transition in Cu_2IrO_3 at 2.7 K. The effective magnetic

moment of 1.93 μ_B and a Curie Weiss constant of -110 K suggests, however, that the valence electrons are not in itinerate form.

When the magnetic spins throughout a lattice enter an ordered state, the low-energy excited states are defined as spin waves and the quantum of excitation is called a magnon [48]. For exotic systems in which the spins fractionalize, the allowed energies form a spinon continuum, unique from magnon dispersion. Spinons, therefore, contribute to bulk properties in ways that are distinct from magnons [49]. One of the defining properties of QSL's is that they possess a high degree of quantum entanglement, and support spinons which carry fractional quantum numbers [50]. To obtain information about such fractionalized spinon excitations requires a momentum and energy resolved technique such as inelastic neutron scattering. With inelastic neutron scattering, the magnetic neutron scattering cross section is proportional to the dynamic structure factor S(Q, ω), where Q and ω are the momentum and energy transferred to the sample, respectively. Thus the scattered neutron intensity is a measure of S(Q, ω) in reciprocal space of the spin-spin correlation function [44, 46, 50–52].

Plots of S(Q, ω) for α-RuCl$_3$ and Herbertsmithite ZnCu$_3$(OH)$_6$Cl$_2$ show scattered intensity is diffuse and covers a large fraction of the Brillouin zone, even at temperatures significantly below J/k_B, where J is the spin-spin exchange energy [44, 46]. As a comparison, the square-lattice La$_2$CuO$_4$ develops antiferromagnetic correlations for $T < 0.5$ J/k_B [39]. Though α-RuCl$_3$ shows a magnetic ordering transition at T$_N$ = 7 K, resulting inelastic neutron scattering supports scattering from the Majorana excitations, a defining characteristic of the Kitaev

model [44]. For Herbertsmithite $ZnCu_3(OH)_6Cl_2$ no magnetic ordering occurs down to temperatures near 0 K, a defining property of a QSL system [49,53].

2.7 Quantum Computation and QSL

Quantum computation is the most attractive potential application of a QSL. Quantum computers (QC's) are different from binary digital electronic computers based on transistors, as quantum bits (qubits) rely on superposition and entanglement of states [54]. A major issue of current QC's is quantum decoherence, causing the inability to store information for extended periods of time due to local perturbations from the surrounding environment [54]. One of the defining properties of QSL's is that they possess a high degree of quantum entanglement and are topologically invariant [41,50]. If a physical system has topological degrees of freedom, then information contained in those degrees of freedom would be automatically protected against errors caused by local interactions with the environment [55]. The archetypal example of a topological phase with strong electron interaction is the QSL [56]. Despite intensive experimental efforts on numerous candidate materials for the potential realization of a QSL, only a select few are proposed to have QSL behavior. It is therefore imperative to discover new QSL systems for fault-tolerant quantum computation to become a reality.

2.8 Quantum Hall Effect and Topological Insulators

2.8.1 Introduction

The quantum hall state (QHS) is an example of a quantum state that is topologically invariant [57]. Topology deals with objects that are robust against small local perturbations and is a branch of mathematics concerned with those properties of geometric configurations that are unaltered by elastic deformation [55]. Topological insulators (TI) are analogous to the quantum Hall state in that they exhibit topological order. Quantum information contained in such topological degrees of freedom would be automatically protected against errors caused by local interactions with the environment [55]. Thus, such materials may be useful for applications like spintronics and quantum computation [57].

2.8.2 Quantum Hall Effect

For a 2D xy insulating surface, the quantum hall effect can be achieved when a strong magnetic field is applied in the z-direction [58]. The applied magnetic field causes the electrons to experience a perpendicular Lorentz force, which causes their motion to curve into xy circular orbits (Figure 2.4 (a)). The quantization of the electrons circular orbits with orbital frequency creates quantized Landau levels. Electrons near the xy edges, however, undergo a different kind of motion, and lead to electronic states that propagate along the edge and do not have quantized energies, meaning these states can conduct (Figure 2.4 (a,b)) [57,58].
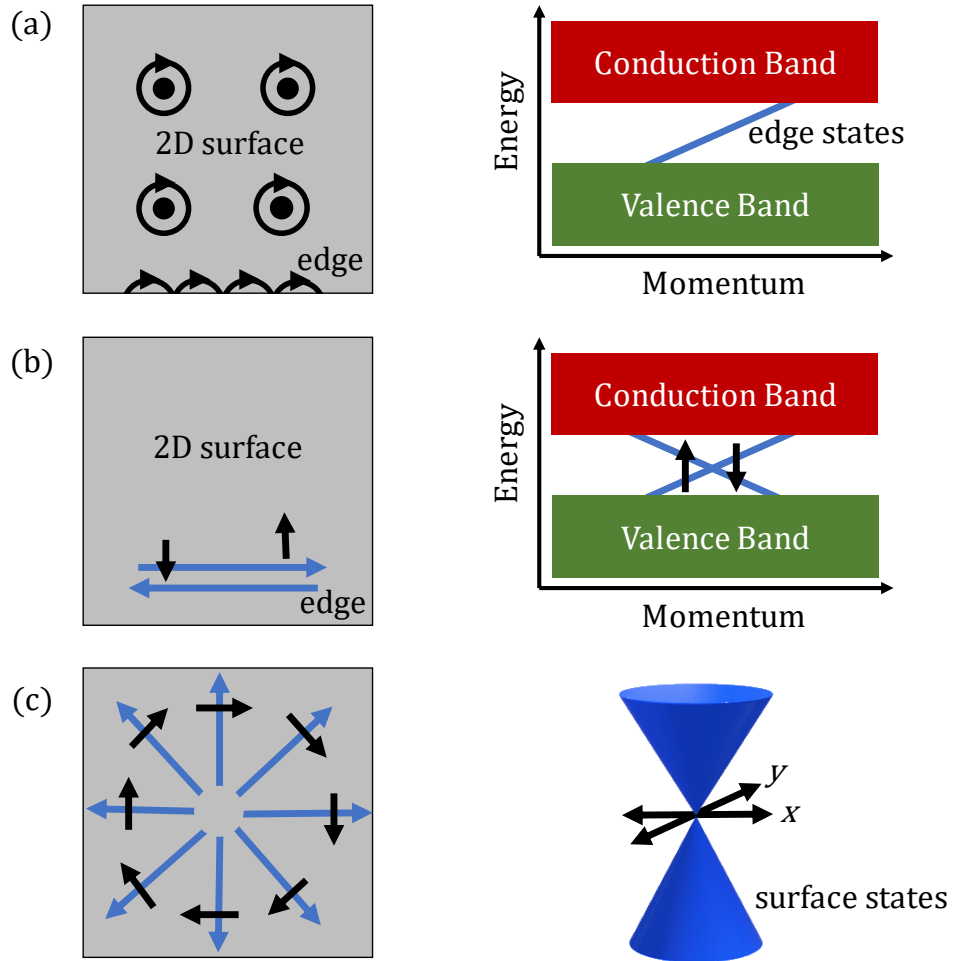
Figure 2.4: In the quantum Hall effect, the applied magnetic field in the z-direction causes the electrons to experience a perpendicular Lorentz force, which causes their motion to curve into xy circular orbits (a). For electrons on the edge states, there are two directions of propagation with opposite spins (b). Electrons on the surface of a 3D topological insulator do resemble the edge states of a 2D topological insulator where the spin direction is locked to the direction of propagation. The surface bands intersect at a "Dirac point" and form a Dirac cone in reciprical space (c).

2.8.3 Topological Insulator

The topological insulator is closely related to the QHS except for the required large magnetic field. The role of the magnetic field is played by spin-orbit coupling and is commonly known as the quantum *spin* Hall state [57]. With the combination of strong spin-orbit interactions and time-reversal symmetry, the observed properties are unlike any other known electronic systems. For electrons on the edge states, there are two directions of propagation with opposite spins (Figure 2.4). Upon a time reversal operation, the direction of propagation is reversed and (because of time-reversal symmetry) the spin direction is also reversed, interchanging the two counter-propagating modes [55, 57–59]. This leads to what is known as dissipationless transport: immune to any back-scattering from defects or impurities. The surface states of a 3D topological insulator do resemble the edge states of a 2D topological insulator, in that the direction of electron motion along the surface of a 3D topological insulator is determined by the spin direction where the spin direction is locked to the direction of propagation (Figure 2.4 (c)) [59]. The surface bands intersect at a Dirac point and form a Dirac cone in reciprical space (Figure 2.4 (c)).

The first experimental proof of the 2D TI was made by placing a thin layer of mercury telluride (HgTe) between layers of mercury cadmium telluride ($Hg_xCd_{1-x}Te$) [59,60]. The first 3D TI was the semiconducting alloy bismuth antimonide (Bi_xSb_{1-x}) [61]. Measurements of electrical transport are ideal for probing the 2D quantum spin Hall effect are more problematic for 3D topological insulators, as even for a

bulk insulator, small bulk conductivity still exists. It is therefore hard to separate the bulk and surface contributions to the current. Angle-resolved photo-emission spectroscopy (ARPES) couples only to the surface and is therefore the preferred route when establishing the existence of a 3D quantum spin Hall state [59, 61]. By analyzing the energy, momentum and spin of the electrons emitted from the sample (photoelectric effect), the electronic structure of the surface states can be directly measured.

The quantum Hall Effect of a two-dimensional honeycomb net model was first theoretically investigated by F.D.M. Haldane [62]. From the model presented, a nonzero quantization of the Hall conductance could be achieved in the absence of an external magnetic field. The band structure of 2D honeycomb graphene reveals the difference in energy of the conduction and valence band becoming zero at two distinct points in the Brillouin zone. Near these points, the electronic dispersion resembles the linear dispersion of massless relativistic particles, which can be described by the Dirac equation. From this, the quantum spin Hall Effect was theoretically predicted for the honeycomb layered Na_2IrO_3 with large spin-orbit interaction and the electron correlation playing crucial roles [63, 64]. The interest toward fundamental investigations of heavy metal honeycomb layered metal oxide systems for possible TI based applications has since grown.

2.9   Conclusion

It is well established that the interplay between crystal field, spin-orbit coupling, and electron correlation energies within various transition metal oxide and inter-metallic systems generates a wide variety of novel forms of quantum matter. Only a select few of such novel quantum states were discussed in this chapter. Other notable states are Weyl and Dirac semi-metals [65]. The theorized topological superconductor is projected to support topologically protected room temperature superconductivity [66]. It is therefore crucial to synthesize new heavy metal oxide and intermetallic systems where large spin-orbit coupling will play an influential role in the electronic properties.

Chapter 3: Introduction to Thermoelectric Materials and Applications

3.1 Introduction

Over the past few decades, a lot of attention has been focused on alternative energy sources to relieve our dependence on fossil fuels and to reduce greenhouse gas emissions [67]. Approximately 70% of energy consumed is ultimately wasted in the form of heat [67]. Thermoelectric generators (TEGs) are power-generation devices that are designed to convert waste heat into electrical energy. They can also be used as solid-state refrigeration devices, eliminating the need for CFC chemicals. The advantages of using TEGs are that they can collect waste heat covering a very wide temperature range without any vibration, noise, or gas emissions, and with no refueling or maintenance requirements [68–70]. Unfortunately, "good" TE materials possess 10-20% energy conversion efficiency [67, 68, 71]. Thus, there has been considerable interest in TEGs, driven by the desire for more efficient materials for electronic power generation and refrigeration [67, 68, 70, 72].

There are a wide array of technological applications that use thermoelectric (TE) materials. For example, TE applications are currently in use by the automotive industry to develop electrical power from waste engine heat from the radiator and exhaust systems for use in next-generation vehicles [67, 68]. In addi-

tion, TE refrigeration applications include seat coolers for comfort and electronic component cooling [67, 73]. Several deep space NASA missions have used TE materials; NASA's Voyager, Cassini, and Mars Rover missions have used radioisotope thermoelectric generators [74–76].

3.2   Thermoelectric Circuit

A thermoelectric circuit is composed of p-type and n-type semiconductors configured in parallel as a thermoelectric generator (Figure 3.2). For thermoelectric power generation to occur, the hot ends of the n-type and p-type material must be electrically connected with a load connected across the cold ends. By applying a temperature gradient across the junctions, a voltage gradent develops that is proportional to the temperature gradient. The resulting voltage produced by the Seebeck effect will cause current to flow through the load, generating electrical power (Figure 3.1). Thus, the electrical power produced is the product of the electrical current and voltage across the load. By applying an external electric potential across the load, heat can be forced to flow from one end to the other via heat carrying charges and enable what is known as Peltier cooling effect (Figure 3.1).
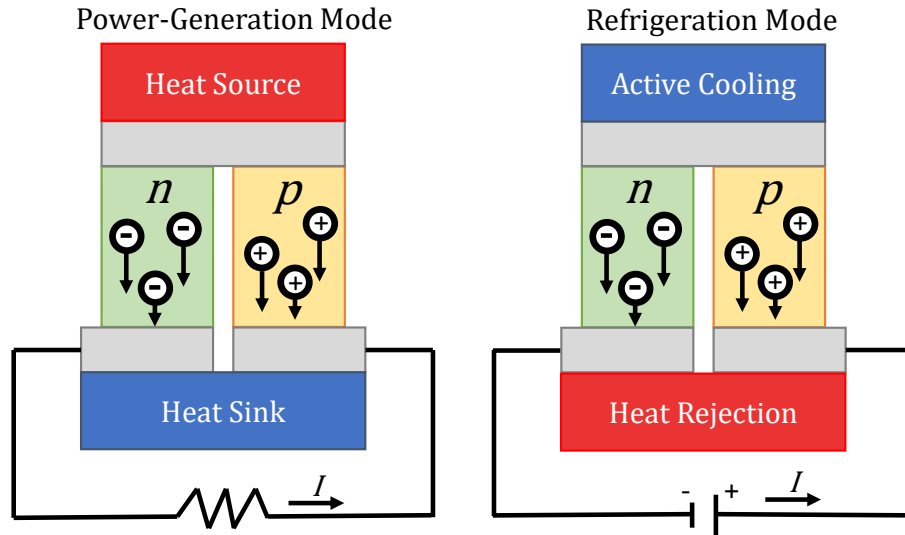
Figure 3.1: A thermoelectric cooling/heating device is composed of a series of connected semiconductor junctions (n- and p-type).

3.3 Quantifying Thermoelectric Performance

The thermoelectric performance of a material is characterized by the thermoelectric figure of merit, expressed in Equation 3.1, where S is the Seebeck coefficient, σ is the electrical conductivity, T is the effective temperature, and K is the summation of the lattice and electronic components of the total thermal conductivity ($K_L + K_e$) [67, 68, 70, 72].

$$ZT = \frac{\sigma S^2 T}{K} \tag{3.1}$$

The efficiency of a power generation device, η, is proportional to $\sqrt{(1 + Z\bar{T})}$
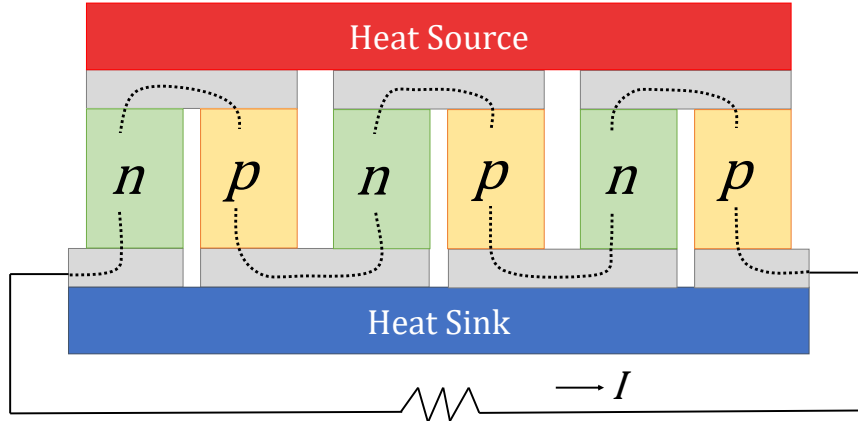
Figure 3.2: A thermoelectric cooling/heating device composed of a series of connected semiconductor junctions (n- and p-type).

and is expressed in Equation 3.2, where $\bar{T}$ is the average temperature of the hot-end temperature (T_h) and the cold-end temperature (T_c) [71].

$$\eta = \frac{T_h - T_c}{T_h} \frac{\sqrt{(1 + Z\bar{T})} - 1}{\sqrt{(1 + Z\bar{T})} - \frac{T_c}{T_h}} \tag{3.2}$$

From this, the efficiency will approach the Carnot efficiency when ZT approaches infinity. For $ZT = 1$, the efficiency η is approximately 10% [67].

Considered to be "good" thermoelectric materials have a $ZT \geq 1$ [67,68]. Well established low temperature (300 – 400 K) thermoelectric materials with ZT $\geq$ 1 are Bi_2Te_3 and $Bi_2Te_{3-x}Se_x$ alloys [77]. For operating temperatures ~900 K, SnSe has a recorded ZT of ~2.7 [78]. Figure 3.3 shows the relation between T, η, and ΔT of materials with different ZT values (inset) and ZT as a function of temperature for typical high-efficiency thermoelectric materials [67].
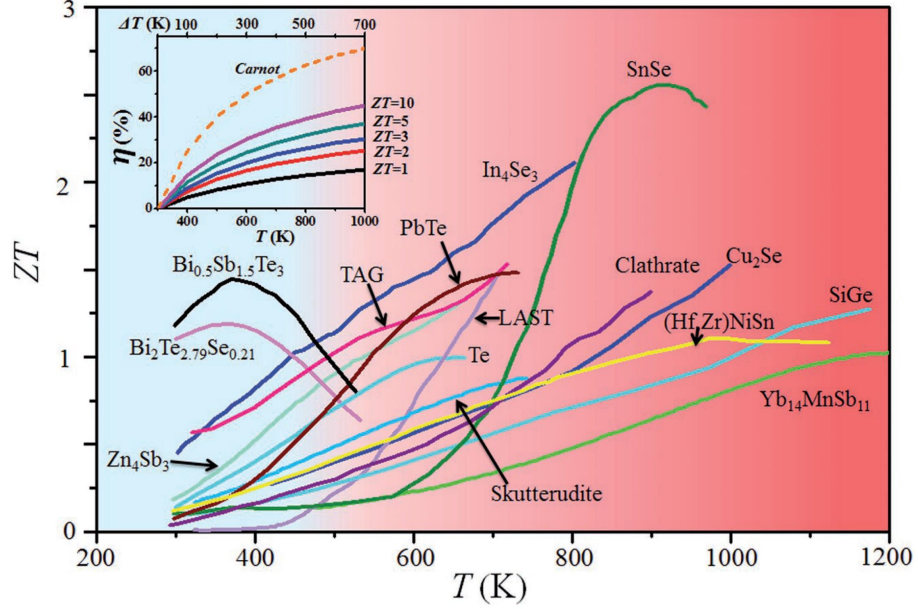
Figure 3.3: Illustration of the relation between T, η, and ΔT of materials with different ZT values (inset) and ZT as a function of temperature for typical high-efficiency thermoelectric materials (figure adapted from Yang et al [67]).

The Seebeck coefficient, S, is an intrinsic property representing the ratio of the voltage developed to the temperature gradient $(\Delta V/\Delta T)$ across a material. An increase in thermoelectric performance corresponds to an increase in the ZT value. Since $S=\Delta V/\Delta T$, the ability to maintain a potential gradient will in general diminish with the increase in the majority e^-/h^+ mobility and carrier concentration [67]. Thus, as illustrated in Figure 3.4, the conductivity, σ, will increase with an increase in charge carrier concentration, however, the magnitude of the Seebeck coefficient, S will decrease. Thus, S, σ, and k_e directly relate with the carrier
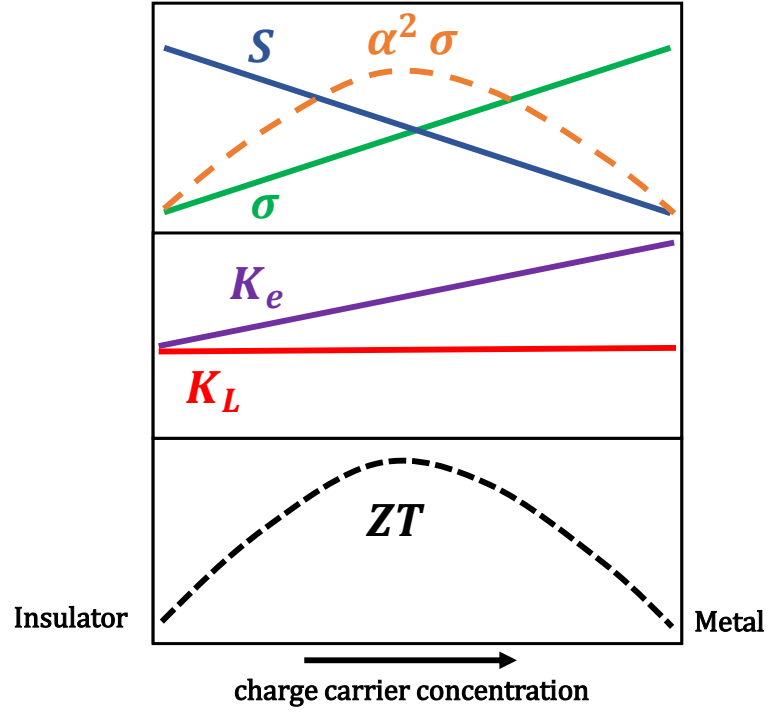
Figure 3.4: Illustration of how the Seebeck coefficient, S, electrical conductivity σ, lattice, K_L, and electronic, K_e, portions of the thermal conductivity change with charge carrier concentration.

concentration through the following relationships [67, 71].

$$S = \frac{8\pi k_B^2}{3eh^2}m^*T\left(\frac{\pi}{3n}\right)^{\frac{2}{3}} \tag{3.3}$$

$$\frac{1}{\rho} = ne\mu \tag{3.4}$$

$$K_e = L\sigma T = ne\mu LT \tag{3.5}$$

As shown in Equations $3.3 - 3.5$, m^* is the effective mass of the carrier, ρ is the electrical resistivity, e is the charge of an electron, k_B is the Boltzmann constant, μ is the carrier mobility, n is the carrier concentration, and L is the Lorenz number. Because $\mu \propto 1/m^*$, if m^* increases, the Seebeck, S, increases. The conductivity, however, will inherently decrease. With an increase in n, the electrical conductivity increases, however, S decreases. Therefore, the power factor $S^2 \sigma T$, can be optimized typically in narrow-gap semiconducting materials as a function of carrier concentration ($\sim 10^{19}$ carriers/cm^3), to give the largest ZT [67, 68, 71]. To obtain good TE performance, ideal Seebeck values on the order of ~ 200 V/K or greater and electrical conductivity close to $\sim 10^3$ Ω^{-1} cm^{-1} must be achieved [67, 68, 71].

The total thermal conductivity does increase with increasing carrier concentration and consequentially decreases the overall ZT. The electrical conductivity and the thermal conductivity are interrelated, in that σ is proportional to k_e through the Wiedemann–Franz relationship represented in Equation 3.5 (Lorentz number $L = 2.45 \times 10^{-8}$ WΩ/K^2) [67].

The lattice thermal conductivity K_L is independent of the carrier concentration and is represented in Equation 3.6, with ν_s representing the effective velocity of sound through the material, C as the heat capacity, and L_{ph} as the mean free path of the phonons [68].

$$K_L \propto \nu_s C L_{ph} \tag{3.6}$$

At higher temperatures (T > 300 K), the sound velocity and the heat capacity become temperature-independent. Therefore, the magnitude of K_L is determined by the mean free path of the phonons. Thus, when the phonons have a mean free path almost equal to the interatomic spacing of the constituent atoms, a minimum lattice thermal conductivity can be achieved. If K_L is equal to 0 $Wm^{-1}K^{-1}$, $K_T=K_e$. From this and incorporating Wiedemann-Franz relationship (Equation 3.5) to Equation 3.1, $ZT=S^2/L_0$. Thus, to obtain a $ZT = 1$, $S=$ 157 V/K. The concept "phonon-glass/electron-crystal" is of interest in which the phonon scattering properties behave as an amorphous material and the electrical properties behave as a crystalline material [79]. A variety of approaches have been explored to reduce the lattice part of the thermal conductivity while still maintaining desired electrical properties.

3.4   Methods to Improve ZT

Various strategies have been applied to improve ZT. Optimizing the carrier concentration and various band engineering approaches have been investigated to decouple σ and S and achieve a high power factor [71, 80–82]. Nano-structure engineering has been shown to effectively reduce the total thermal conductivity, K_T, without sacrificing the electrical transport of TE materials [82–84]. Other approaches to optimize ZT are alloying and transition metal/pnictogen-site doping [70, 72, 85–87]. Another method to maximize ZT is by filling the unoccupied large empty cages within M cube skutterudite framework with an ion [88–90]. The

size difference between the corresponding filler atom and void site enables the filler atom to act as an independent oscillator and thus dampen the thermal phonon conductivity.

3.4.1   Skutterudites: Strong Thermoelectric Candidates

Because of the unique structure and recognized ability to tune key transport properties, skutterudites are known to be strong thermoelectric candidates. The skutterudites are one well known class of Zintl compounds. As shown in Figure 3.5, the skutterudite crystal structure can be described as a repeated corner-sharing MX_6 arrangement with two M_4X_{12} formula units and two large empty cages per unit cell, where M is a transition metal atom (M = Fe, Co, Rh, or Ir) and X is a pnictogen atom (X = P, As or Sb).

The general formula is MX_3 with cubic space group $Im\bar{3}$. Because of the large size difference between the corresponding filler atom and void site, the filler atom can conceivably act as an independent oscillator and thus dampen the thermal phonon conductivity and decrease the total thermal conductivity [88–92]. Filling skuterudite voids can also influence the electrical conductivity, albeit the effect is usually negligible with respect to the decrease in total thermal conductivity [72, 88, 90, 92].
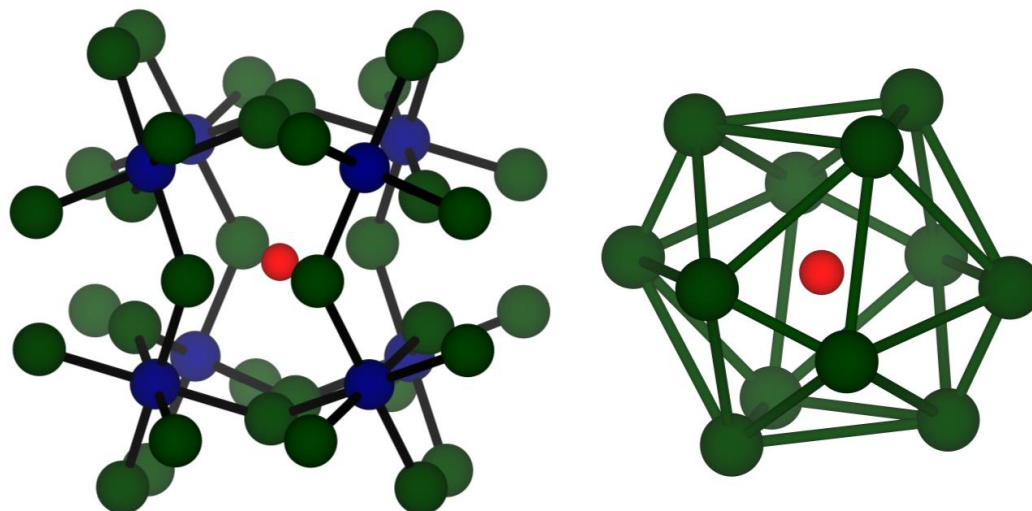
Figure 3.5: Skutterudite crystal structure shown as a repeated corner-sharing MX_6 arrangement (left), and the resulting icosahedron cage site (right). M is a transition metal atom (M = Fe, Co, Rh, or Ir) represented as blue spheres, and X is a pnictogen atom (X = P, As or Sb) represented as green spheres. The red sphere represents the "rattler" element within the icosahedron void cage.

3.5   Conclusion

Thermoelectric generators (TEGs) are power-generation devices that are designed to convert waste heat into electrical energy. They can also be used as solid-state refrigeration devices, eliminating the need for CFC chemicals. There are several advantages to use TEGs; TEGs can collect waste heat covering a very wide temperature range without any vibration, noise, or gas emissions, and with very little maintenance requirements. Unfortunately, "good" TE materials possess 10-20% energy conversion efficiency. Various strategies have been applied to improve TE efficiency. Such methods have been by optimizing the carrier concentration and

band engineering approaches. Nano-structure engineering has also been shown to effectively reduce the total thermal conductivity, K_T, without sacrificing the electrical transport of TE materials. Other approaches to optimize ZT are alloying and transition metal/pnictogen-site doping. The concept "phonon-glass/electron-crystal" is of interest in which the phonon scattering properties behave as an amorphous material and the electrical properties behave as a crystalline material. A variety of approaches have been explored to reduce the lattice part of the thermal conductivity while still maintaining desired electrical properties. Filling the unoccupied large empty cages within M cube skutterudite framework with an ion to enhance phonon scattering and to increase the overall efficiency of the TE material is discussed.

Chapter 4: Introduction to Pertinent Structure Types: Geometric and Structural Principles

4.1 Introduction

A variety of metal oxide and intermetallic structures were investigated. In this chapter, the geometric and structural principles of honeycomb layered A_2MO_3, spinel, perovskite, and the skutterudite structure will be discussed. Frustrated systems such as the honeycomb and spinel lattices have the potential to harbor exotic states such as quantum spin liquid behavior. Of recent interest for topological materials are perovskites where spin-orbit coupling is large enough to influence the electronic band structure. Because of the unique structure and recognized ability to tune key transport properties, skutterudites are known to be strong thermoelectric candidates. Understanding the structure is critical to establish a better understanding of the observed and/or predicted properties.

4.2 Honeycomb Layered Metal Oxide

The demonstration by Kitaev of an exactly solvable quantum spin liquid (QSL) model incorporating S = 1/2 spins with anisotropic interactions on a honeycomb lattice [41] has motivated searches for its experimental realization. Honeycomb

layered A_2MO_3 can be described as a rock salt ordered arrangement with 2/3 of the octahedral sites filled with A-cations and the remaining 1/3 filled with M-cations. All octahedral sites are edge shared. Figure 4.1 reveals the A_2MO_3 (A = Na^+ or Li^+ and M = $3d$, $4d$ or $5d$ element) structure as alternating A and AM_2 layers along the c-axis (left) and a single AM_2 layer, where MO_6 edge-sharing octahedra form the honeycomb framework (right). The A-AM_2 close packed stacking arrangement can vary, resulting in a variety of possible space groups.
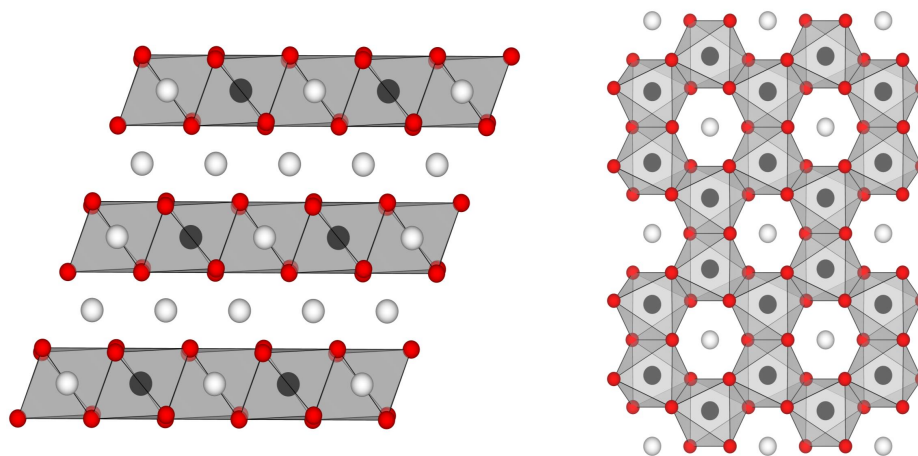
Figure 4.1: Left: A_2MO_3 (A = Na^+ or Li^+ and M = $3d$, $4d$ or $5d$ element) structure as alternating A and AM_2 layers. Right: Viewed along the c-axis the AM_2 layer, where MO_6 edge-sharing octahedra form the honeycomb lattice. White, black, and red spheres represent A, M, and oxygen atoms, respectively.

4.2.1 Stacking Sequences of the AM_2 Parallel Layers

The particular stacking arrangement between the AM_2 parallel layers will only be taken into consideration as the close packing arrangement between a single A and AM_2 layer remains unchanged. For representative AM_2 layers defined as A, B, and C, there are multiple ABC stacking sequences of the equidistant, parallel layers. Starting with the A layer, the second B layer may be placed above the A layer with the A_1 cation residing in the B_1 void site to produce the A_1B_1 stacking sequence (Figure 4.2). Though A_1B_2 and A_1B_3 are possible, they are related to A_1B_1 by a 120^0 rotation and so are not unique. There are then two possibilities for the addition of a third layer, generating either $A_1B_1C_1$ or $A_1B_1C_2$ stacking, where repeating $A_1B_1C_1$ blocks represent $C2/m$ or $C2/c$ and repeating $A_1B_1C_2$ blocks represents $P3_112$ (Figure 4.2) [93].

More complicated stacking arrangements are possible if the 3-layer blocks are combined in different manners. For example, repeating $A_1B_1C_2$-$A_2B_3C_1$ blocks are possible (Figure 4.2). Clearly there are many stacking schemes for A_2MO_3 based structures. Because the AM_2 layers are separated by oxygen and lithium layers, the relative differences in energies between such possible 3-layer blocks are not significantly different, as long as close packing arrangement is achieved, therefore enabling a reasonable percentage of stacking fault imperfections (discussed in Chapter 5).
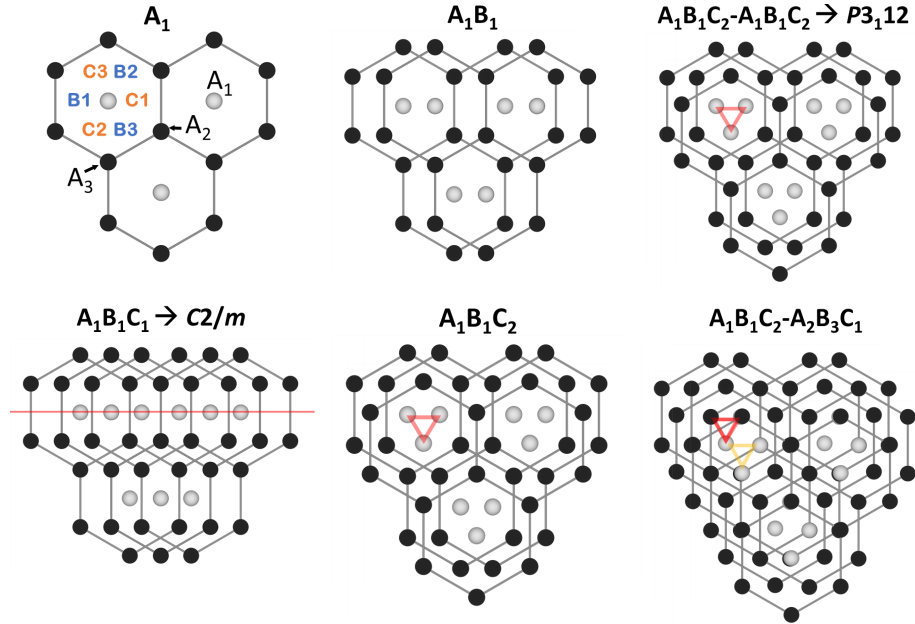
Figure 4.2: Illustrations generated by stacking AM_2 (A = Na^+ or Li^+ and M = $3d$, $4d$ or $5d$ element) "honeycomb" layers with B_x and C_x (x= 1, 2, or 3) representing the locations in the ab-planes of the B and C holes in a close-packed array. The M and A ions are denoted by white and black (smaller) circles, respectively.

4.2.2 Honeycomb Framework: Edge Shared Frustration

The A_2MO_3 honeycomb structure is unique in that the slight variations in the M-M distances and angles of the three nearest MO_6 edge sharing sites enables anisotropic behaviour unique to other systems (Figure 4.3) [33]. The magnetic superexchange between two adjacent M sites can occur via two exchange pathways as these octahedra are edge-sharing. Thus, destructive interference between the two Ir-O-Ir exchange pathways occurs, amplifying the electron correlation energy

and enhances spin frustration [33]. A honeycomb layer populated with heavy metals with large SOC enhances the electron correlation energy and the magnetic frustration [33]. It is therefore a balance between the degree of variation between the M-M distances and respective angles, orbital overlap, and the magnitude of SOC which tunes the electrical properties.
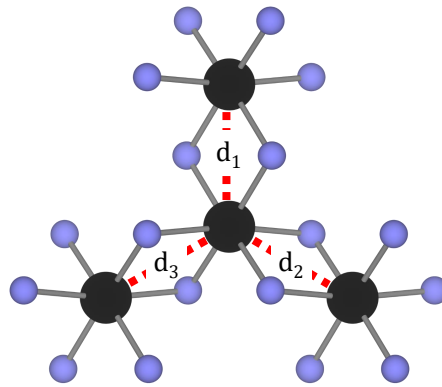
Figure 4.3: Illustration of the three MO_6 edge shared octahedra describing the honeycomb framework. The M-M distances (d_1, d_2, d_3) are not equivalent and respective angles are not equal to 120^0. Here, black and purple spheres represent M cations and oxygen, respectively.

4.3   Spinel Structure

4.3.1   Introduction

The frustrated spinel structure populated with large spin-orbit coupled (SOC) ions are an ideal setting for the exploration of exotic states. The general formula for a normal spinel is AB_2O_4, where the A-cation occupies tetrahedral sites and the B-

cation occupies octahedral sites (Figure 4.4) [94]. The B_2O_4 network forms a rock salt structure with cubic close packed O^{2-} ions where only alternate octahedral sites are occupied by the B-cations (1/2 of the octahedral sites are occupied). The A-cation occupies 1/8 of the tetrahedral sites. Only tetrahedral sites with all four neighboring empty octahedral sites are filled (Figure 4.5). If all tetrahedral and/or all octahedral sites were filled, polyhedral face sharing would occur. Thus, cation-cation repulsion's do not allow adjacent octahedral and tetrahedral sites to be occupied simultaneously.

Tetrahedral
A sites (8*a*)

Octahedral
M sites (16*d*)
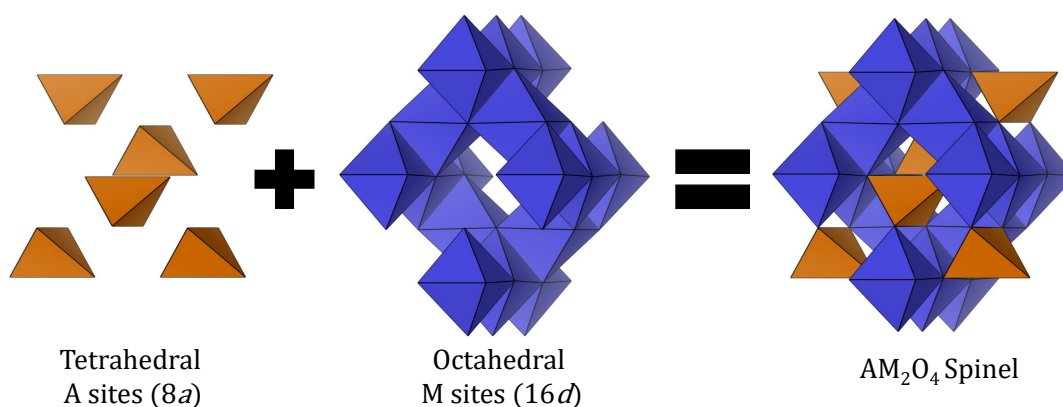
AM_2O_4 Spinel

Figure 4.4: Illustration of the AB_2O_4 spinel structure: isolated A-cation tetrahedral sites and the B_2O_4 rock salt network where 1/2 of the octahedral sites are occupied.

One of the unique features of the spinel structure is that the B ions form a sublattice of corner-shared tetrahedra (Figure 4.6). This tetrahedral sub-lattice gives rise to strong magnetic frustration, if the B cations are magnetic and the magnetic coupling is antiferromagnetic. The A-ions also form a diamond sub-

lattice (Figure 4.6) and can also lead to strong magnetic frustration, if the A cations are magnetic and the magnetic coupling is antiferromagnetic.
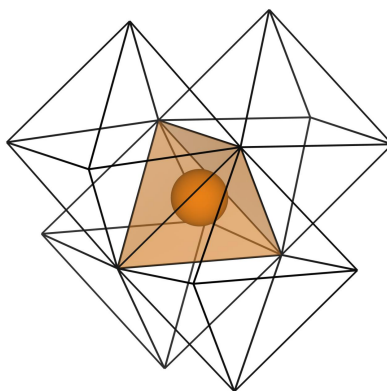
Figure 4.5: Illustration of an A-cation tetrahedral site with all four neighboring octahedral sites empty.

4.3.2   Cation Distribution in Spinels

The cation distribution between the A and B site may vary. In inverse spinels, half of the B ions occupy the tetrahedral sites, leaving all of the A ions and the remaining B ions occupying the octahedral sites, typically in a disordered arrangement. A complete range between normal and inverse spinels are possible. The cation distribution between the A and B sites can be quantified using the parameter γ, $[B_\gamma A_{1-\gamma}]^{tet}[A_\gamma B_{2-\gamma}]^{oct}O_4$ which represents the fraction of A ions on the octahedral sites [94]. Table 4.1 represents the stoichiometric identity of normal, inverse and random spinel systems.

A-ion diamond sublattice   B-ion corner-shared
                                tetrahedra sublattice
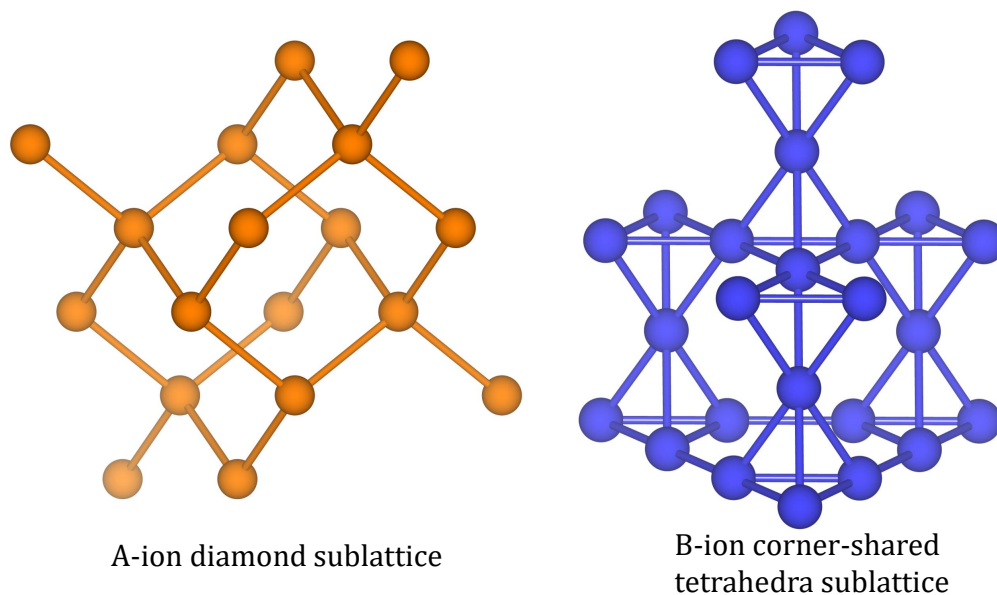
Figure 4.6: The A-ions form a diamond sublattice and the B-ions form a sublattice of corner-shared tetrahedra within the spinel structure.

Table 4.1: Classification of cation distribution in spinels

normal	$[A]^{tet}[B_2]^{oct}O_4$	$\gamma = 0$
random	$[B_\gamma A_{1-\gamma}]^{tet}[A_\gamma B_{2-\gamma}]^{oct}O_4$	$0 < \gamma < 1$
inverse	$[B]^{tet}[A, B]^{oct}O_4$	$\gamma = 1$

Several factors influence γ, such as covalent bonding effects, crystal field stabilization energy (CFSE), and cation size [10, 94]. For example, Fe_3O_4 forms an inverse spinel. Here, Fe^{3+} is d^5 and therefore has no preference for an octahedral site or tetrahedral site. Fe^{2+}, however, is d^6 and from CFSE would prefer an

octahedral environment, thus forming $[\text{Fe}^{3+}]^{tet}[\text{Fe}^{2+}, \text{Fe}^{3+}]^{oct}\text{O}_4$ [10].

4.4   Single and Double Perovskite Structures

4.4.1   Introduction

The perovskite structure class covers an enormous variety of compounds. Most of the ions in the periodic table can be incorporated into the perovskite structure with many different combinations of cations and anions. Because of this inherent flexibility, an array of properties are reported, with numerous examples where substitution of one or more of the cations can considerably impact structure and properties [95–101]. Of recent interest for topological materials are perovskites where SOC is large enough to influence the electronic band structure [102–104]. This review will encompass an introduction to the perovskite structure types, discussions on A- and B-site cation ordering within the AA'BB'X$_6$ double perovskite framework, geometric and structural principles, and on ideal diffraction techniques for correct crystal structure determination of distorted perovskites.

4.4.2   Introduction to Perovskite Structure Types

The ideal cubic perovskite structure has an ABX$_3$ stoichiometry and belongs to the space group $Pm\bar{3}m$ [97]. The A-cation is surrounded by 12 X-anions forming a dodecahedral environment, the B-cation is octahedrally coordinated by six X-anions, and the X-anions are coordinated by two B-cations and four A-cations

(Figure 4.7 (a)). There are two ways to visualize the structure. The perovskite structure is more commonly described as a three-dimensional cubic network of corner-sharing BX_6 octahedra, with the A-cation residing in the center of a cube defined by eight corner-sharing octahedral units (Figure 4.7 (b)). An alternative description is in terms of a cubic close-packed array of X-anions where one fourth of the X-anions are replaced with an A-cation in an ordered way to obtain a cubic close-packed AX_3 arrangement. One fourth of the octahedral holes in the AX_3 lattice are filled with B-cations, explicitly octahedral holes that do not border an A-cation (Figure 4.7 (c)).

The number of possible compounds is significantly expanded when multiple ions are replaced for one or more of the original ions in ABX_3. Substitution typically occurs on the cation sites, resulting in a large class of compounds known as double perovskites, $AA'BB'X_6$ (Figure 4.7 (d)). When such substitutions are made, the cations can occupy the corresponding original site in either a random or an ordered fashion, resulting in a wide variety of lower symmetry systems. The electronegativity, charge, and size difference of the substituted cations can cause structural modifications such as cation ordering, octahedral distortion, and Jahn-Teller distortion [97, 98].

Replacing one or more of the original ions in ABX_3 can result in stoichiometric identities other than $A_2BB'X_6$. For example, 1:2 ordering of the B-cations can occur along [111] for an ideal 1:2 double perovskite, identified as $A_3BB'_2X_9$ (Figure 4.8). There are many examples of perovskite-like systems. Perovskite-rock salt intergrowth structures such as the Ruddlesden-Popper phases are well estab-
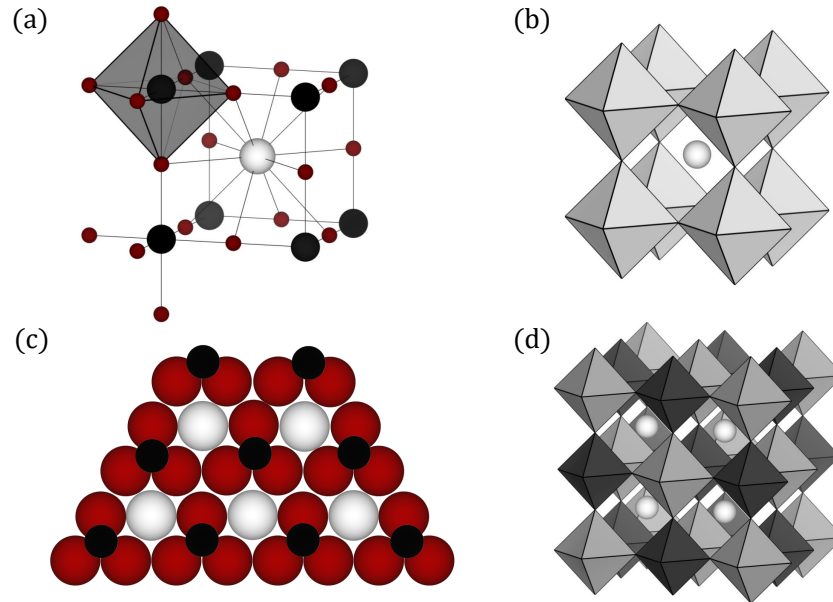
Figure 4.7: Illustrations of (a) the ideal cubic ABX_3 perovskite framework with B-cations (black spheres) residing in octahedral sites and A-cations (white spheres) residing in a 12-coordinated dodecahedral environment, (b) three-dimensional cubic network of corner-sharing BX_6 octahedra, with the A-cation residing in the center of a cube defined by eight corner-sharing octahedral units, (c) cubic close-packed AX_3 arrangement with 1/4 of the octahedral holes filled with B-cations, and (d) double perovskite 1:1 rock salt ordered $A_2BB'X_6$

lished [97]. Layered cuprates and related materials, such as La_2CuO_4 are known superconductors [105–107], and Sr_2IrO_4 is considered an ideal platform for exploring the quantum effects of magnetism in low-dimensional systems as the singular spin-$\frac{1}{2}$ Ir^{4+} ions are arranged neatly in a square lattice [108]. For the context of this thesis, attention will be focused on the $AA'BB'X_6$ structural framework for this chapter.
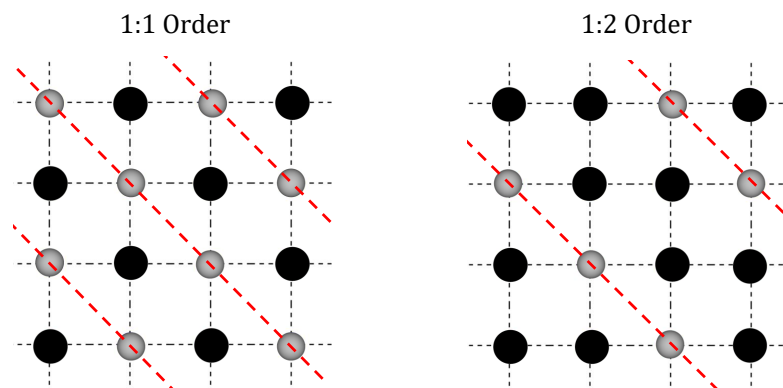
Figure 4.8: Illustration of 1:1 and 1:2 B-site cation ordering sequence in AA'BB'X$_6$ (A-cations and X-anions are removed for clarity).

4.4.3   A and B Site Cation Ordering in AA'BB'X$_6$

There are three types of ordering for both A and B-site cations within the double perovskite framework (Figure 4.9). For a double perovskite AA'BB'X$_6$, both A- and B-sites can order in rocksalt, layered, or columnar fashion with B-site ordering more common than A-site cation ordering [97, 98]. For the B-site rock-salt arrangement, all B'X$_6$ octahedra are isolated from BX$_6$ sites (Figure 4.9). For B-site layered arrangement, connectivity of B(B')X$_6$ exists in two dimensional corner shared layers. For B-site columnar arrangement, connectivity of B(B')X$_6$ exists in 1-dimensional corner shared chains (Figure 4.9). Rock-salt ordering is the most common. This can be explained in terms of electrostatic differences between the corresponding cations [97, 98]. Because all B'X$_6$ octahedra are isolated from BX$_6$ sites for the rock-salt arrangement, the more highly charged B' cations are separate

with six B cations as its nearest neighbor. Columnar ordering is the second most favorable with each B' cation having two B' cation and four B cation neighbors. Layered ordering is the least energetically favorable as each B' cation has four B' cation and two B cation neighbors. Relative to rock-salt ordering, only a few examples of layered and columnar ordering exist for $A_2BB'X_6$, systems [97]. For example, B-site layered ordering exists for La_2CuSnO_6, even though each Sn^{6+} has four Sn^{6+} neighbors [109]. It has been proposed Jahn-Teller distortion of Cu^{2+} plays an important role with stabilizing the system [97].

Most B-site columnar ordering exists with B/B' as the same element, but with mixed valency. For example, B-site columnar ordering exists in $LaCaMn^{3+}Mn^{4+}O_6$ where Jahn-Teller distortion of Mn^{3+} also plays an important role with stability [110]. There are very few examples of A-site ordering in the double perovskite $AA'BB'X_6$. This, in part, can be explained by the restricted oxidation differences between A and A' cations. Unlike B/B' cations which can have an oxidation difference of up to seven [111], A/A' cations, in all known cases, have a maximum oxidation difference of only two. Most A-site cation ordering prefers layered ordering. To understand the preference of layered ordering, the anion nearest neighbor environment must be considered [98]. For a perovskite system, each anion has six nearest neighbor cations: two B-site cations and four A-site cations (Figure 4.10).

For B-site rock salt ordering, each anion environment is equivalent. Each anion is surrounded by one B-cation and B'-cation. Layered B-site ordering, however, creates three distinct anion environments, violating Pauling's fifth rule [112]. One of the distinct anion sites resides between two higher valent B' cations, causing
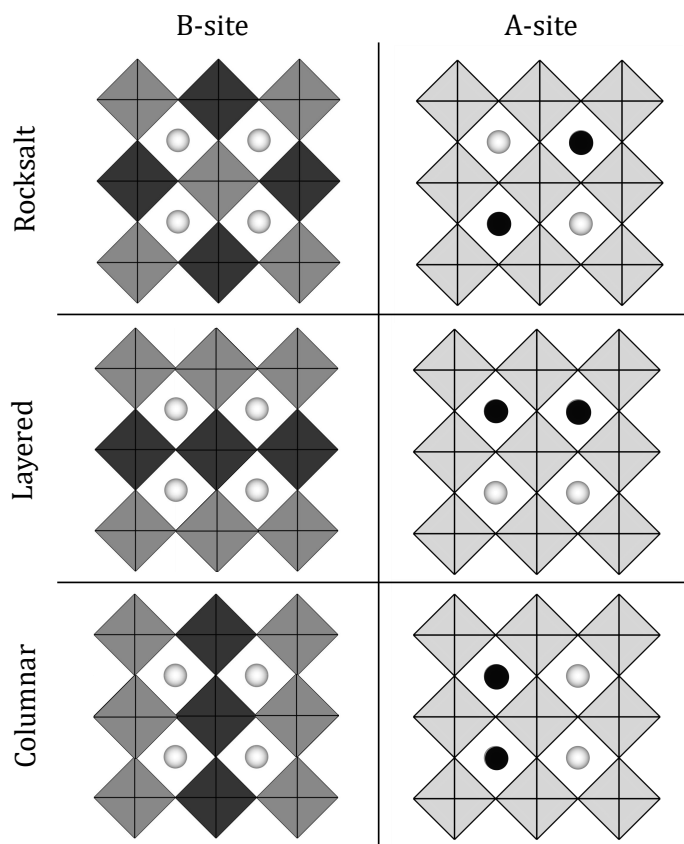
Figure 4.9: Cation ordering schemes in perovskites. From top to bottom rock salt, layered ordering, and columnar ordering are shown for B-site ordering in $A_2BB'X_6$ perovskites (left) and for A-site ordering in $AA'B_2X_6$ (right) perovskites.

over-bonding of the anion site (Pauling bond valence sum analysis [112]). The second anion site is between two lower valent B-cations, causing under-bonding of the anion site. The third anion site resides between B and B' cations, like the B-site rock salt ordering. Though A-site rock salt ordering does result in a single environment for all anions, the A-cations reside in a trans configuration (Figure 4.10), forcing A-X and A'-X bonds to be of equal length, even if A and
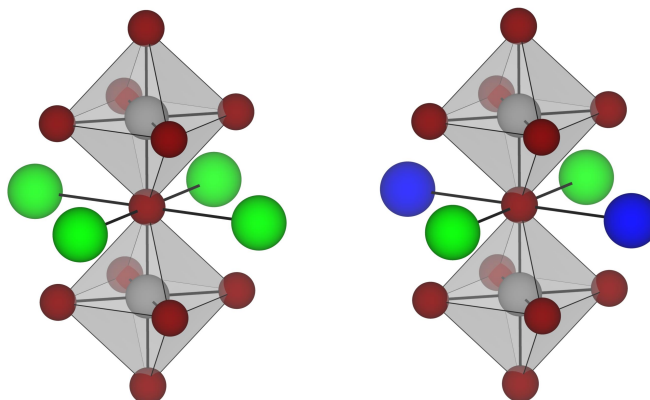
Figure 4.10: The anion environment in a primitive ABX$_3$ perovskite and in a rock salt ordered AA'B$_2$X$_6$ perovskite, where AA', B, and X are green/blue, grey, and red, respectively.

A' cations are of different size [98]. Just like with layered B-site ordering, layered A- site ordering creates three distinct anion environments. However, because two thirds of the anions are surrounded by two A and two A' cations in a cis fashion, the anions can displace if there is a significant size difference between the A/A' cations. Regardless, the remaining one sixth of the anions are surrounded by four A-cations and the other one sixth are surrounded by four A'-cations, resulting in slight over- and under-bonding. To relieve such bonding instability, octahedral tilting and/or Jahn-Teller distortion of the B-site is needed in order for A-site ordering to occur [97, 98].

4.4.4 Distorted Perovskites: Geometric and Structural Principles

For the perovskite ABX_3, structural distortions can occur depending on the size distribution between the A- and B-cations. For a cubic perovskite structure, the atomic radii are related to the unit cell dimension, a, by Equation 4.1.

$$a = \sqrt{2}(r_B + r_X) = r_A + r_X \tag{4.1}$$

The degree to which the cation sizes depart from Equation 4.1 is provided by the tolerance factor, τ (Equation 4.2) [97].

$$\tau = \frac{r_A + r_X}{\sqrt{2}(r_B + r_X)} \tag{4.2}$$

The tolerance factor (τ) for a 1:1 ordered $A_2BB'X_6$ perovskite [97] is represented in Equation 4.3.

$$\tau = \frac{r_A + r_X}{\sqrt{2(0.5r_B + 0.5r_{B'}) + r_X}} \tag{4.3}$$

For a cubic double perovskite system, if the tolerance factor (τ) is equal to 1.0, the A-X and B-X bonds can adopt their ideal lengths in the cubic structure. For τ less than 1, the A-cation is too small for the 12-coordinated site and the perovskite structure can compensate for the cation size mismatch by tilting the BX_6 octahedra and/or by distorting the ideal bond lengths [95–97].

If octahedral distortions occur to account for the cation size mismatch, the exact mechanism of octahedral distortion throughout the corner sharing $B/B'X_6$
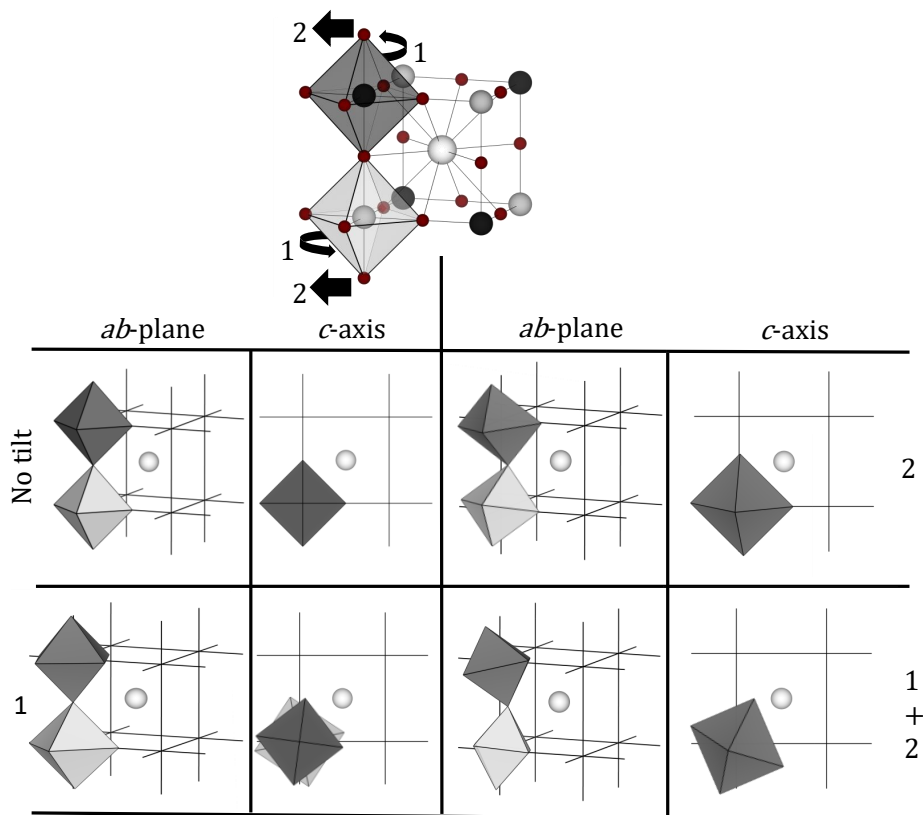
Figure 4.11: Mechanisms of octahedral distortion throughout the corner sharing B/B'X$_6$ framework.

framework can vary (Figure 4.11). If we consider a single octahedral B/B'X$_6$ site within the A$_2$BB'X$_6$ framework, distortion can occur along the ab-plane in a clockwise or counterclockwise manner (Figure 4.11 – mechanism 1), can tilt along the c-axis (Figure 4.11 – mechanism 2), or via both mechanisms (Figure 4.11 – mechanisms 1 and 2) [97]. Throughout the corner sharing B/B'X$_6$ framework, the rotation/tilting can be the same between adjacent plains of octahedra, therefore

in-phase, or the rotation/tilting between adjacent plains of octahedra is opposite, and therefore out of phase. A classification scheme has been developed and is known as the Galzer tilt method [113].

For this method, possible rotation about the three axes of the octahedron is indicated by three letters a, b, and c. If the degree of rotation about all three axes is the same, each letter will be the same, i.e. aaa, and if the degree of rotation is different for one of the axis, i.e. aac. To characterize if there is no rotation about an axis, the superscript "0" is provided for the letter. If rotation will be in-phase, the superscript "+" is provided, and for out of phase, the superscript "-" is provided. For the examples shown in Figure 4.12, rotation of octahedra about only one axis is shown. The difference between $a^o a^o c^-$ and $a^o a^o c^+$ is out of phase and in-phase between adjacent plains of octahedra, respectively. A list of Glazer tilt systems for ABX_3 and $A_2BB'X_6$ with no order, 1:1 order, and 1:2 order can be found elsewhere [97, 113–115].

4.4.5 Ideal Diffraction Techniques for Correct Crystal Structure Determination

Knowing the correct crystal structure for a given compound is essential for understanding its properties. It is very common in literature where incorrect structures are determined mostly due to the limitations of the diffraction method used. Most $A_2BB'X_6$ perovskites exhibit a high degree of pseudosymmetry, meaning slight deviations that characterize a non-ideal perovskite are subtle in these compounds.
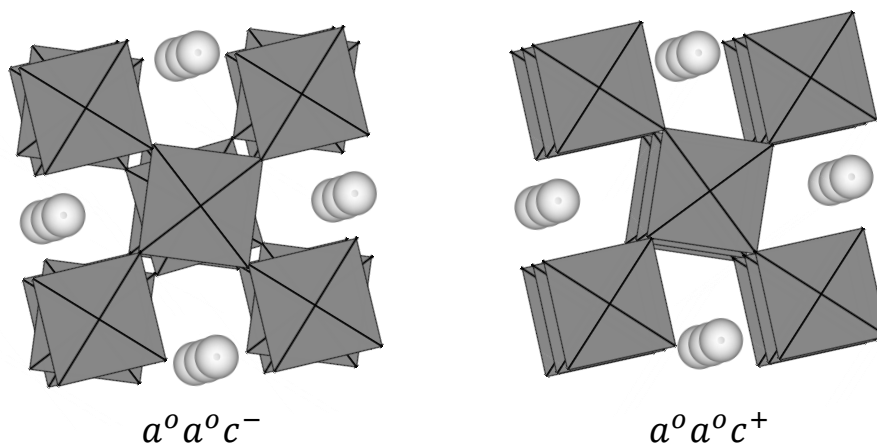
$a^o a^o c^-$ $a^o a^o c^+$

Figure 4.12: View looking down the c-axis of $a^o a^o c^-$- and $a^o a^o c^+$ with the B-site cations located at the center of the grey octahedral sites and A-site cations shown as white spheres.

Comparing compounds with the A-cation as Ba^{2+} or Ca^{2+} for $A_2BB'X_6$, the presence or lack of reflection splitting due to octahedral tilting distortions is often easily evident [95–97]. Most double perovskites containing Ba^{2+} do not distort from cubic symmetry and are therefore assigned to the $a^o a^o a^o$ tilt system. For Ca^{2+} double perovskites, well-defined peak splitting with XRPD is observed and is commonly assigned to one of the 3-tilt Glazer systems [95–97]. For Sr^{2+} double perovskites, though octahedral distortion does occur to accommodate the smaller A-cation, XRPD peak splitting is not observed due to their high degree of pseudosymmetry. Therefore, space group assignment is challenging with XRPD methods. Because of its relatively small atomic number, oxygen has a poor X-ray scattering coefficient. Oxygen, however, has a coherent neutron scattering length comparable to heavier

atoms [116]. Therefore, neutron diffraction techniques are ideal to establish the right space group due to slight octahedral distortions.

4.5 Skutterudite

The skutterudites are one well known class of Zintl compounds. The Zintl concept is important in solid-state chemistry to explain how compounds that combine main group and electropositive elements can be stable for formulas that essentially do not make any sense [117]. For example, the stability of most ionic systems such as NaCl can easily be explained by fundamental concepts through which an electropositive ion donates electrons to an electronegative ion to achieve closed shell electron configurations. For Zintil phases, fundamental concepts of electron-counting and stability rules are not as straightforward. For such compounds, to obey fundamental electron counting, the electronegative elements form a poly-atomic electron-accepting molecule inside the solid called a polyanion that fills its available energy states with electrons from the electropositive elements. For BX_3 skutterudites with B a group 6 metal such as Co, Rh or Ir and X a pnictogen atom such as P, As or Sb, Zintl electron count of 24 valence electrons per formula unit must be followed [91]. Group 6 metals with 3+ oxidation state have the electron configuration nd^6. In octahedral coordination and low spin, they thus have a filled t_{2g} band and an empty e_g band. Square X_4 Zintl polyanions form with a formal charge of 4-. Thus, $M_4^{3+}(X_4)_3^{4-}$ is achieved [91]. As shown in Figure 4.13, the skutterudite crystal structure can be described in two ways: (left) a repeated

corner-sharing MX_6 arrangement with two M_4X_{12} formula units and two large empty cages per unit cell, or (right) an open cage like structure of cube-connecting M atoms with three fourths of the void sites filled with X_4 Zintl polyanions, where M is a transition metal atom (M = Fe, Co, Rh, or Ir) and X is a pnictogen atom (X = P, As or Sb). The general formula is MX_3 with cubic space group $Im\bar{3}$. The M cations occupy the $8c$ (1/4, 1/4, 1/4) site and the X anions occupy the $24g$ (0, y, z) site with y~0.15 and z~0.34.
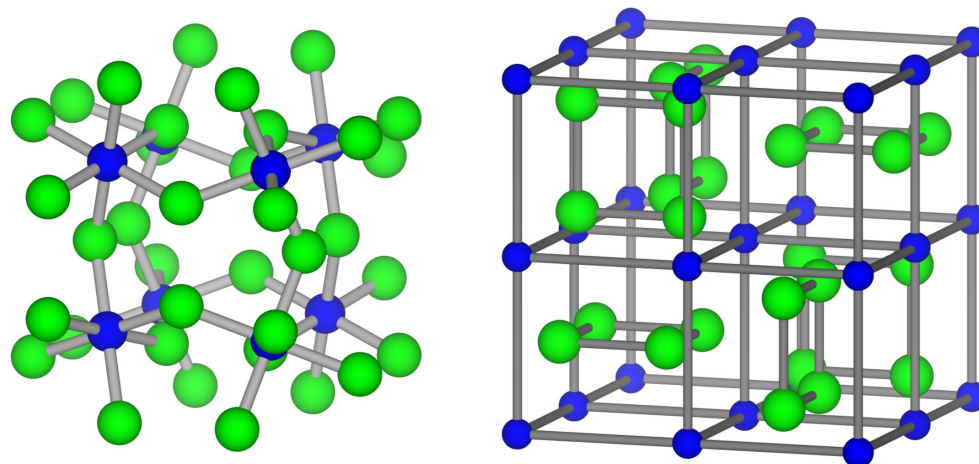
Figure 4.13: Skutterudite crystal structure shown as (a) a repeated corner-sharing MX_6 arrangement and (b) cube-forming M atoms with three fourths of the void sites filled with X_4 Zintl polyanions.

The empty cages can be filled by an ion A, leading to the formula $A_yM_4X_{12}$ with $y \leq 1$. A filled AB_4X_{12} skutterudite is expected to be with an electron precise valence electron count of 96 (4 x 24) per formula unit [91], because $M_4^{3+}(X_4)_3^{4-}$ with group-6 B metal and a p^6 X atom configuration without any filler atom

has an electron count of 96. Therefore, only small amounts of the filler ion, A, can be incorporated, with the solubility limit of y in $A_yM_4X_{12}$ typically close to 0.15 [88, 89, 91].

4.6   Conclusion

This review provides an introduction to the geometric and structural principles of honeycomb layered, spinel, perovskite, and skutterudite structures. Frustrated lattice systems such as the honeycomb or spinel structures have the potential to harbor novel enigmatic quantum states. For example, the demonstration by Kitaev of an exactly solvable quantum spin liquid (QSL) model incorporating S = 1/2 spins with anisotropic interactions on a honeycomb lattice has motivated searches for its experimental realization as a potential quantum spin liquid system. Understanding the structure is critical to establish a better understanding of the observed and/or predicted properties.

Chapter 5: Modeling Stacking Faults of Honeycomb Layered A_2MO_3 Metal Oxide Systems

5.1 Introduction

It is well known the presence of imperfections in the crystal lattice can influence the electrical properties of polycrystalline systems. A stacking fault is one such imperfection, which occurs within systems that consist of parallel layers that allow for translations parallel to the layers and rotations about the layer normal [93]. Honeycomb layered A_2MO_3 metal oxide systems are known to possess such stacking faults [43, 93, 118, 119]. A review of the honeycomb layered A_2MO_3 structure is provided in Chapter 4.

5.2 Stacking Sequences of the AM_2 Parallel Layers

As discussed in Chapter 4, for AM_2 layers defined as A, B, and C, there are two ABC stacking sequences of the equidistant, parallel layers. Starting with the A_1 layer, a second layer may be placed above this to produce A_1B_1. Though A_1B_2 and A_1B_3 are possible, they are related to A_1B_1 by a 120^0 rotation and so are not unique. There are then two possibilities for the addition of a third layer, generating either $A_1B_1C_1$ or $A_1B_1C_2$ stacking, where repeating $A_1B_1C_1$ blocks represent $C2/m$

and repeating $A_1B_1C_2$ blocks represents $P3_112$ [93]. More complicated stacking arrangements are possible if the 3-layer blocks are combined in different manners. Therefore, there are many stacking schemes for A_2MO_3 based structures. Because the AM_2 layers are separated by oxygen and lithium layers, the relative differences in coulomb repulsion energy between these possible 3-layer blocks are not significantly different, therefore enabling the possibility of a reasonable percentage of stacking fault imperfections.

5.3   Modeling Stacking Faults

Current refinement software, such as GSAS, cannot refine stacking fault contribution, as shifting AM_2 layers will not equate to the corresponding assigned space group. To model stacking fault contribution, the DIFFaX software or FAULTS software must be used. Both DIFFaX and FAULTS software require a text file of which instrumental parameters, unit cell and atomic information, and transition vectors describing interlayer connections are provided. Example input files for both software's are provided in Appendix C and D.

5.3.1   DIFFaX Program

The DIFFaX software requires the cell axes to be defined such that the c-axis is perpendicular to the fault direction, resulting with a new idealized unit cell. As an example, for a monoclinic system with space group $C2/m$, a hexagonal

unit cell with $a=a_{(C2/m)}$ and $c_{hex}=c_{(C2/m)}\times\cos(\beta_{(C2/m)}\text{-}90)$ can be implemented (Figure 5.1). For this example, only AM_2 layers are taken into consideration, with oxygen and A-cation interlayers omitted for simplicity. By repeating the hexagonal unit cell along the a-b plane, the atomic positions for the three atoms within the hexagonal unit cell (Figure 5.1) can replicate the honeycomb framework. For this example, two equidistant and parallel AM_2 layers characterize ideal monoclinic $C2/m$ system with one layer perpendicular to the c-axis origin and the second layer equating to the c-axis. For the defined DIFFaX unit cell, only a single AM_2 layer will be demarcated and perpendicular to the c-axis origin (Figure 5.1). Table 5.1 provides an example of atomic coordinates within the DIFFaX hexagonal unit cell representing A_2MO_3.
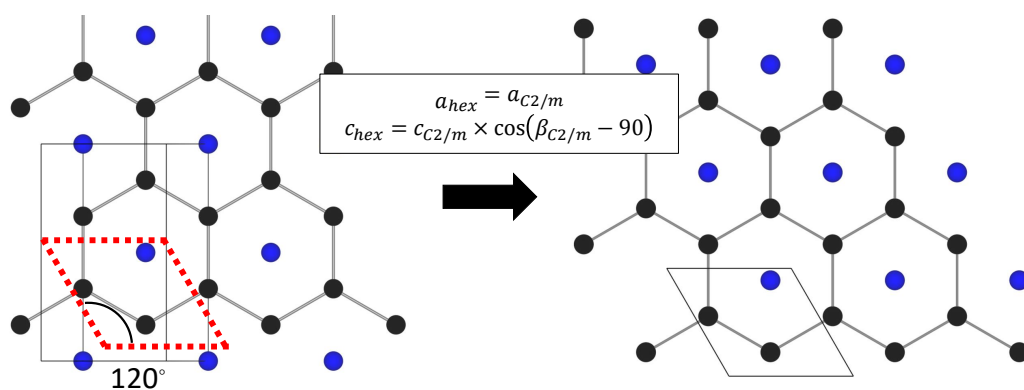
Figure 5.1: Schematic of a AM_2 "honeycomb" layer along the $a-b$ plain $(C2/m$ unit cell) and the new idealized DIFFaX hexagonal unit cell (red dash) with black and blue representing the M transition metal and the A-cation, respectively.

Table 5.1: Atomic coordinates of A_2MO_3 of the DIFFaX hexagonal unit cell.[a]

Atom	x	y	z	occupancy
M	1/9	5/9	0	0.9
A	1/9	5/9	0	0.1
M	4/9	2/9	0	0.9
A	4/9	2/9	0	0.1
A	7/9	8/9	0	0.9
M	7/9	8/9	0	0.1
O	1/9	8/9	1/4	1.0
O	4/9	5/9	1/4	1.0
O	7/9	2/9	1/4	1.0
A	1/9	2/9	1/2	1.0
A	4/9	8/9	1/2	1.0
A	7/9	5/9	1/2	1.0
O	1/9	5/9	3/4	1.0
O	4/9	2/9	3/4	1.0
O	7/9	8/9	3/4	1.0

a) unit cell dimensions: $a=b=5.18$ Å, $c=4.80$ Å, $\alpha = \beta = 90.0^o$, and $\gamma = 120.0^o$.

To determine the vectors associated with the interlayer stacking sequence, the close packing arrangement must be taken into consideration. As illustrated in Figure 5.2, the stacking sequence begins with a single AM_2 layer, and based on the close packing arrangement of oxygen, the A-cation layer and subsequently the next AM_2 layer are placed accordingly. Thus, to replicate the ideal $A_1B_1C_1$ stacking sequence of A_2MO_3 ($C2/m$), for the given DIFFaX unit cell, the layer sequencing must be characterized by the $[\frac{1}{3},0,1]$ transition vector (R_1) (Figure 5.3). To replicate stacking fault contribution, transition vectors $[\frac{1}{3},\frac{1}{3},1]$ and $[0,\frac{1}{3},1]$ (R_2 and R_3) can be used (Figure 5.3).

Illustrations representing the influence of varying the vector assignment between three AM_2 layers are shown in Figure 5.3. Figure 5.3 (b) illustrates the
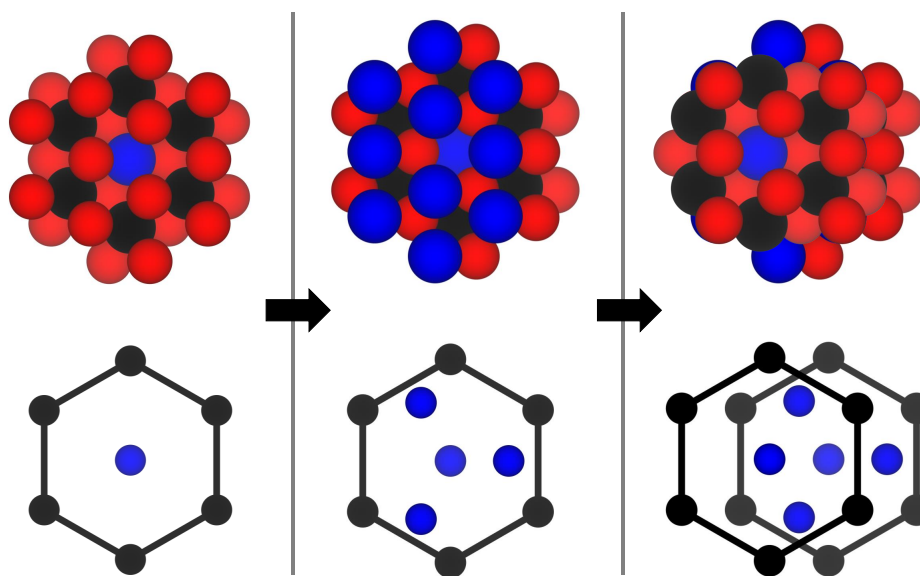
Figure 5.2: Illustration of the close packing stacking arrangement of oxygen (red), A-cations (blue), and M-cations (black) for a honeycomb A_2MO_3 down the c-axis. Top illustrations represent all atoms in space-filling form with the bottom illustrations representing only the A- and M-cations for a single honeycomb ring.

ideal $A_1B_1C_1$ stacking sequence of monoclinic A_2MO_3 ($C2/m$). For each transition vector (R_x) that describes the transition from one DIFFaX unit cell to another, a probability (α_x) must be assigned. For the example provided, probabilities must be assigned to each of the three transition vectors, with $\alpha_1+\alpha_2+\alpha_3=1$ for each layer.

Figure 5.4 shows a comparison of XRPD of Li_2IrO_3 ($C2/m$) and the calculated XRPD of Li_2IrO_3 DIFFaX model with $\alpha_1= 0.98$ and $\alpha_2=\alpha_3$. For the model presented, Li-Ir site disorder within the $LiIr_2$ layers was implemented with $Ir(4g)/Li(2a)$ occupancies set to 0.85. Calculated XRPD of Li_2IrO_3 DIFFaX model
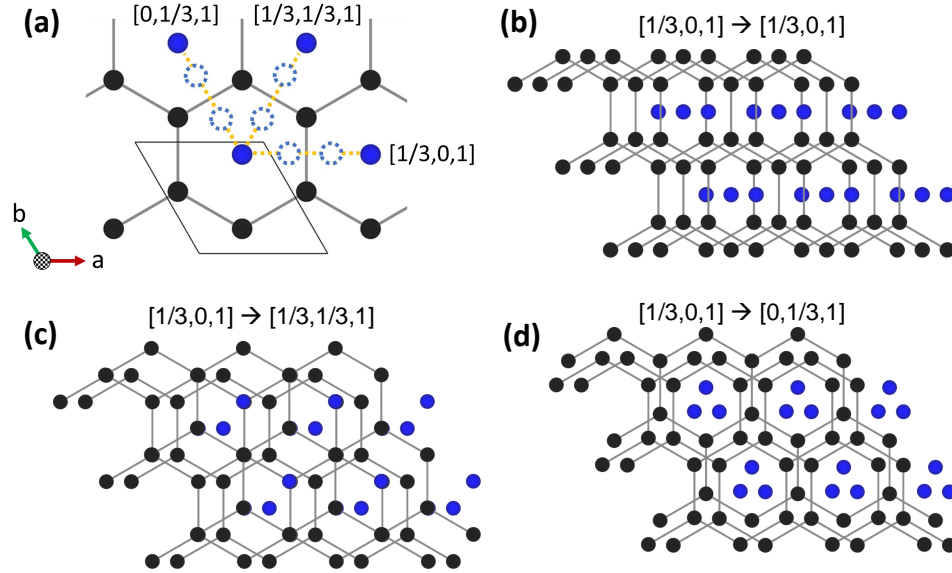
Figure 5.3: Possible stacking sequences between AM_2 layers, based on the given DIFFaX unit cell described in the text, with $[\frac{1}{3},0,1]$ transition vector (R_1) representing the ideal $A_1B_1C_1$ stacking sequence of A_2MO_3 ($C2/m$), and transition vectors $[\frac{1}{3},\frac{1}{3},1]$ and $[0,\frac{1}{3},1]$ (R_2 and R_3) describing stacking fault contribution (a). Illustrations representing the influence of varying the vector assignment between three DIFFaX unit cells are shown (b-d), with (b) representing the ideal $A_1B_1C_1$ stacking sequence of monoclinic A_2MO_3 ($C2/m$).

with α_1 ranging from 1 to 0.5 are shown in Figure 5.5. For the model presented, $\alpha_2=\alpha_3$ and Li-Ir site disorder within the LiIr$_2$ layers was implemented with Ir($4g$)/Li($2a$) occupancies set to 0.85.

With incorporation of stacking faults, only (002) and (020) peaks within 17 – 35 2θ range do not broaden (Figure 5.5). Similar observations for other DIFFaX modeled Li$_2$MO$_3$ systems exist [43, 93, 118, 119]. The absence of the (020) peak is therefore attributed to Li-Ir site disorder within the LiIr$_2$ layers.
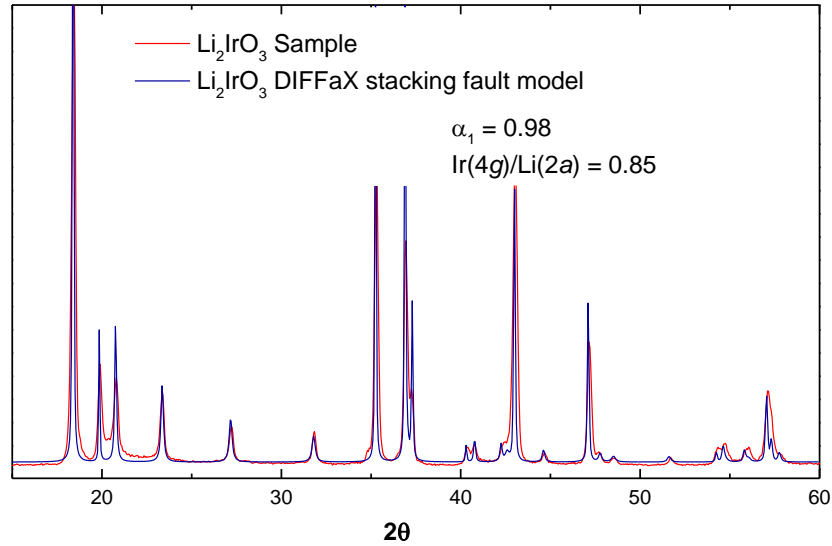
Figure 5.4: A comparison of XRPD of Li_2IrO_3 ($C2/m$) and the calculated XRPD of Li_2IrO_3 DIFFaX model with $\alpha_1 = 0.98$ and $\alpha_2 = \alpha_3$. For the model presented, Li-Ir site disorder within the $LiIr_2$ layers was implemented with $Ir(4g)/Li(2a)$ occupancies set to 0.85.

5.3.2 FAULTS Program

The FAULTS program also requires the cell axes to be defined with the c-axis perpendicular to the fault direction. A new unit cell for each individual layer must therefore be established. As an example, for a monoclinic system A_2MO_3 with space group $C2/c$, the new hexagonal unit cell can be defined as $a_{hex}=a_{(C2/c)}$ and $c_{hex}=[c_{(C2/c)}\times\cos(\beta_{(C2/c)}\text{-}90)/2](z)$, with z as the number of hexagonal layers used for the model. Division of 2 is based on the number of repeating $Li\text{-}LiM_2$ layers within $C2/c$ unit cell. The single layer used and $A\text{-}AM_2$ $C2/c$ layer are
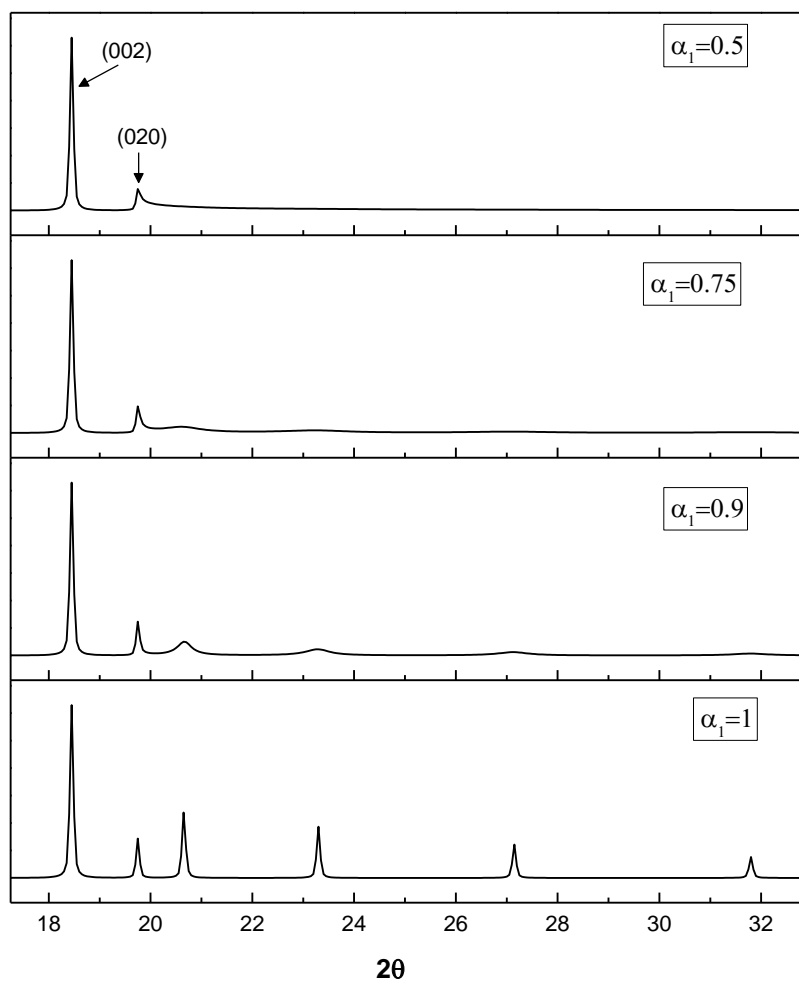
Figure 5.5: Calculated XRPD of Li_2IrO_3 DIFFaX model with α_1 from 1 to 0.5 and $\alpha_2=\alpha_3$. For the model presented, Li-Ir site disorder within the $LiIr_2$ layers was implemented with $Ir(4g)/Li(2a)$ occupancies set to 0.85.

illustrated in Figure 5.6. Table 5.2 provides the atomic coordinates within the FAULTS hexagonal unit cell represented in Figure 5.6. To replicate the ideal

stacking sequence of A_2MO_3 ($C2/c$), layer sequencing can be characterized by $[\frac{1}{3},0,\frac{1}{z}]$ transition vector (R_1). To replicate stacking fault contribution, transition vectors $[0,\frac{1}{3},\frac{1}{z}]$ and $[\frac{2}{3},0,\frac{1}{z}]$ (R_2 and R_3) must be incorporated. Probabilities must be assigned to each of the three transition vectors, with $\alpha_1+\alpha_2+\alpha_3=1$ for each layer.
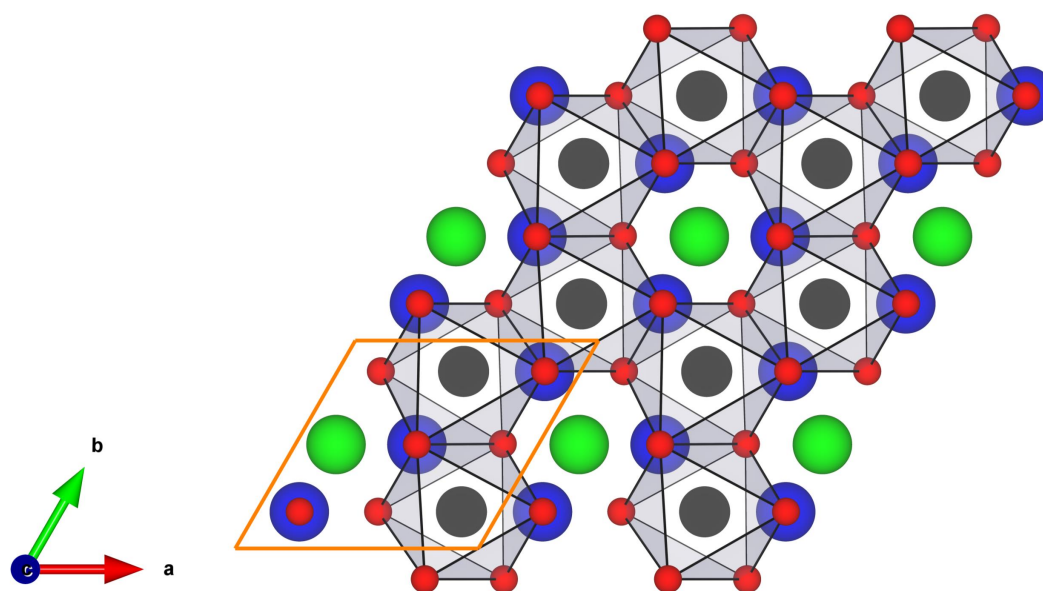
Figure 5.6: Illustration of the FAULTS single layer down the c-axis. The M-cation and oxygen are represented as black and red spheres, respectively. Lithium residing within the honeycomb rings are represented as green spheres and lithium beneath the honeycomb layers as blue spheres.

Table 5.2: Atomic coordinates of A_2MO_3 of the FAULTS hexagonal unit cell.[a]

Atom	x	y	z	occupancy
A	0.85	0.85	0	1
A	0.176	0.176	0	1
O	0.177	0.85	0.083	1
O	0.50	0.177	0.083	1
O	0.85	0.50	0.083	1
M	0.518	0.85	0.154	0.9
A	0.518	0.85	0.154	0.1
M	0.843	0.176	0.154	0.9
A	0.843	0.176	0.154	0.1
A	0.167	0.500	0.154	0.9
M	0.167	0.500	0.154	0.1
O	0.50	0.50	0.249	1
O	0.177	0.177	0.249	1
O	0.85	0.85	0.249	1

a) unit cell dimensions: a=5.14 Å, b=5.07 Å, c=14.35 Å, $\alpha = \beta = 90.0^o$, and $\gamma = 60.0^o$.

Chapter 6: Local Moment Instability of Os in Honeycomb $Li_{2.15}Os_{0.85}O_3$

6.1 Abstract

Compounds with honeycomb structures occupied by strong spin orbit coupled (SOC) moments are considered to be candidate Kitaev quantum spin liquids. Here we present the first example of Os on a honeycomb structure, $Li_{2.15(3)}Os_{0.85(3)}O_3$ ($C2/c$, $a = 5.09$ Å , $b = 8.81$ Å , $c = 9.83$ Å , $\beta = 99.3°$). Neutron diffraction shows large site disorder in the honeycomb layer and X-ray absorption spectroscopy indicates a valence state of Os (4.7 ± 0.2), consistent with the nominal concentration. We observe a transport band gap of $\Delta = 243 \pm 23$ meV, a large van Vleck susceptibility, and an effective moment of 0.85 μ_B, much lower than expected from 70% Os(+5). No evidence of long range order is found above 0.10 K but a spin glass-like peak in ac-susceptibility is observed at 0.5 K. The specific heat displays an impurity spin contribution in addition to a power law $\propto T^{(0.63\pm0.06)}$. Applied density functional theory (DFT) leads to a reduced moment, suggesting incipient itineracy of the valence electrons, and finding evidence that Li over stoichiometry leads to Os(4+)-Os(5+) mixed valence. This local picture is discussed in light of the site disorder and a possible underlying quantum spin liquid state.

Publication based on this chapter:

1. M.K. Wallace, P.G. LaBarre, J. Li, S.-T. Pi, W.E. Pickett, D.S. Dessau, D. Haskel, A.P. Ramirez, M.A. Subramanian, Local Moment Instability of Os in Honeycomb $Li_{2.15}Os_{0.85}O_3$, *Scientific Reports - Nature*, 8:6605, 2018.

6.2   Introduction

The demonstration by Kitaev of an exactly solvable quantum spin liquid (QSL) model incorporating $S = \frac{1}{2}$ spins with anisotropic interactions on a honeycomb lattice [120, 121] has motivated searches for its experimental realization. Whereas magnetic honeycomb-containing compounds have been extensively investigated in 3d and 4d metal oxides [122–130], the strong interaction anisotropy required by Kitaev's theory has placed a focus on 5d metal oxides, for which strong spin-orbit coupling (SOC), the origin of spatial anisotropy, can be expected [131–137]. In the A_2MO_3 honeycomb structure, where A is an alkali element and M a 4d or 5d element, the AM_2 layers form a hexagonal network of edge sharing MO_6 octahedra with a single A^+ ion at the centers of the hexagons (Figure 1).

Examples such as α-Na_2IrO_3 and α-Li_2IrO_3 with effective spin $J_{eff} = \frac{1}{2}$, have recently emerged as possible examples of Kitaev physics. These compounds possess antiferromagnetic (AF) Weiss temperatures of 125(6) K and 33(3) K and undergo AF order at 15.5 K and 14.5 K for Na_2IrO_3 and Li_2IrO_3 respectively [138, 139]. The 3D hyper-honeycomb lattice compound β-Li_2IrO_3, however, demonstrates a ferromagnetic (FM) Weiss temperature of 40 K and weak ordering signatures at 38 K among $J_{eff} = \frac{1}{2}$ moments [140]. Among non-oxide materials, the layered compound α-$RuCl_3$ has also been discussed as a possible Kitaev system, though it too undergoes long range order at 7.5 K [141]. Since the suppression of classical order via geometrical frustration is a requirement for creating a QSL state, the above systems, while possessing important attributes, fall short of the Kitaev
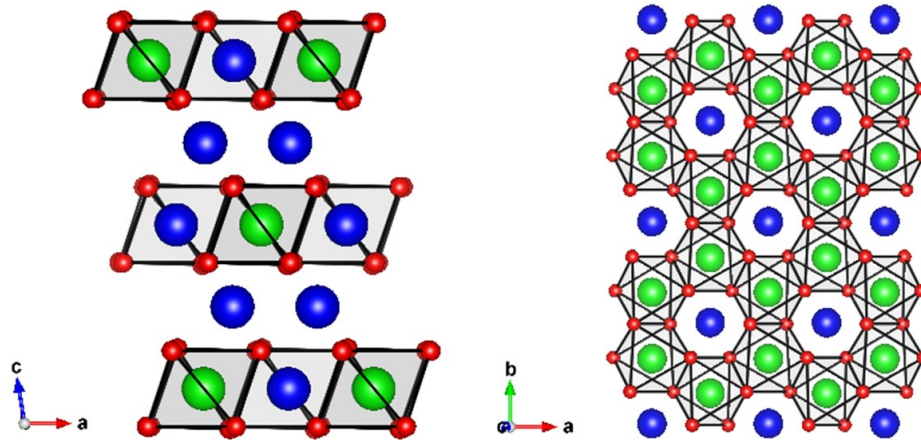
Figure 6.1: Left: Li_2MO_3 (M= 4d or 5d element) structure as alternating Li and LiM_2 layers. Right: Viewed along the c axis the LiM_2 layer, where MO_6 edge-sharing octahedra form the honeycomb lattice. Blue, green, and red spheres represent lithium, metal, and oxygen atoms respectively.

criteria [142]. Due to the ordering seen in other honeycomb compounds and because the specific materials conditions required to produce a QSL are ill-defined at present, it is important to study other honeycomb-containing compounds with sizable SOC.

Here, we ask what would be the result of *reducing* the SOC from that of 540 meV in Ir to 480 meV in Os [143]. In the present work we report on the synthesis, structure, and properties of $Li_{2.15(3)}Os_{0.85(3)}O_3$ which is isostructural to the Ir honeycomb compounds mentioned above. For the stoichiometric compound, Li_2OsO_3, the Os ion is expected to be in the $4+ = d^4$, $J_{eff} = 0$ state to maintain charge-neutrality. In our work, we find, in contrast to other honeycomb systems, a lack of

long range order above 0.1K. While this might be due to a frustrated lattice, it also might be due to site disorder among the Os ions. For each crystallographic site representing the $LiOs_2$ layer, an average of 43% of the sites (compared to the expected 33% of these sites) are occupied by lithium and thus the average valence of Os is $+4.5 \pm 0.1$ ($d^{3.5}$), a value consistent with our X-ray absorption spectroscopy (XAS) measurements, which yield $+4.7 \pm 0.2$. From a local moment perspective and using the XAS-determined valence state, our system might be comprised of 30% d^4 ($J_{eff} = 0$) and 70% d^3 ($J_{eff} = \frac{3}{2}$) but its physical properties are not easily understood. We find a transport gap of 243 meV, an effective magnetic moment of 0.85 μ_B, which is much less than the effective moment of 3.24 μ_B expected if 70% of the ions possessed $J_{eff} = \frac{3}{2}$. No magnetic order is observed above 0.10 K, and the specific heat obeys a fractional power law in temperature and is only weakly magnetic field-dependent. We discuss the constraints on the local physics of Os from a band structure perspective and their implications for collective behavior en route to a possible QSL in SOC honeycomb systems.

6.3   Results and Discussion

6.3.1   Structure

Common space groups assigned to honeycomb-structure compounds Li_2MO_3 (M = Mo, Mn, Rh, Ir, Ru, Pt, and Sn) are $C2/m$, $C2/c$, and $R\bar{3}m$ [123, 126–128, 130, 136, 144–151]. Figure 6.2 represents Li_2MO_3 $C2/m$, $C2/c$, and $R\bar{3}m$ unit

cells illustrated down the b-axis (top) and corresponding portion of the Li-M layer representing a single hexagon configuration (bottom) with lithium and metal occupying their ideal Wyckoff positions [123, 130, 136, 147, 148, 151]. For all three space groups, edge sharing octahedral LiM_2 layers alternate with edge sharing octahedral Li layers. The difference in space groups and their associated symmetries can in part be ascribed to stacking of the LiM_2 layers, with $R\bar{3}m$ as the highest in symmetry. The space group assignments of some Li_2MO_3 systems has been controversial. For example, Li_2MnO_3 was first refined to be $C2/c$, but later found to be $C2/m$ on the basis of electron diffraction and transmission electron microscopy [145, 146].
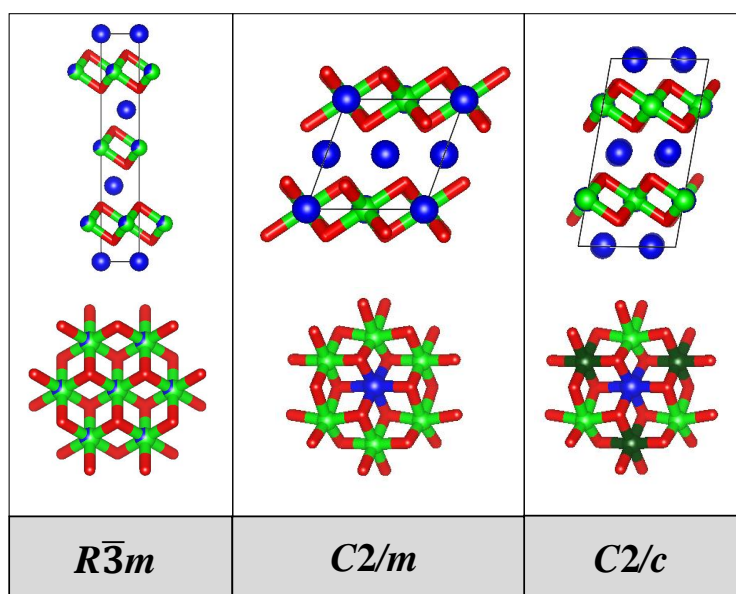
Figure 6.2: Li_2MO_3 $R\bar{3}m$, $C2/m$, and $C2/c$ unit cells illustrated down the b-axis (top) and corresponding portion of the Li-M layer representing a single hexagonal configuration (bottom) with lithium and metal occupying their ideal Wyckoff positions (lithium and metal labeled blue and green respectively). For $C2/c$ there are two unique atomic positions to describe M sites within the LiM_2 layer, represented as the two different shades of green.

$R\bar{3}m$

	Wyckoff	x	y	z
Li	3b	0	0	0.5
Os	3b	0	0	0.5
Li	3a	0	y (~0.88)	0.5
O	6c	0	0	z (~0.24)

$C2/m$

	Wyckoff	x	y	z
Li	2a	0	0	0
Os	4g	0	y (~0.33)	0
Li	2d	0	0.5	0.5
Li	4h	0	y (~0.88)	0.5
O	8j	x (~0.24)	y	z
O	4i	x (~0.26)	0	z (~0.78)

$C2/c$

	Wyckoff	x	y	z
Li	8f	x (~0.24)	y (~0.089)	z (~0.01)
Li	4d	0.25	0.25	0.5
Li	4e	0	y (~0.76)	0.25
Os	4e	0	y (~0.08)	0.25
Os	4e	0	y (~0.41)	0.25
O	8f	x (~0.13)	y (~0.24)	z (~0.13)
O	8f	x (~0.13)	y (~0.56)	z (~0.14)
O	8f	x (~0.14)	y (~0.91)	z (~0.13)
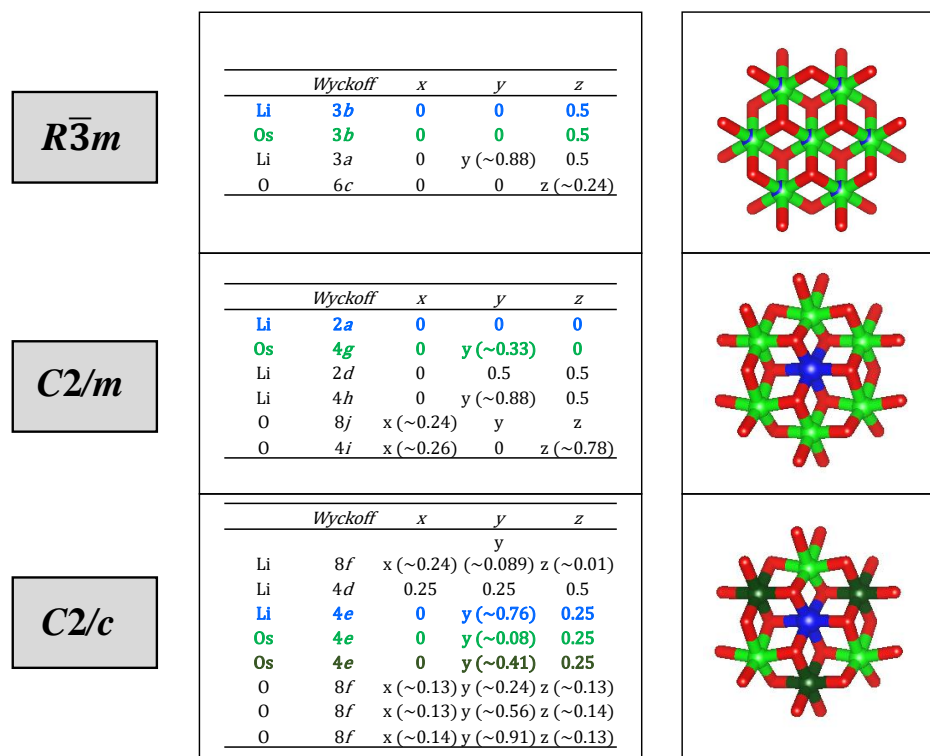
Figure 6.3: A_2MO_3 $R\bar{3}m$, $C2/m$, and $C2/c$ space groups and corresponding Wyckoff positions.

Another example is Li_2MoO_3, which was reported as both $C2/c$ and $R\bar{3}m$ [123,147]. When comparing literature on polycrystalline Li_2IrO_3 synthesized under standard solid state conditions, discrepancies in $C2/c$ and $C2/m$ space groups exist. Recent work supports the higher symmetry $C2/m$ as the appropriate space group for polycrystalline Li_2IrO_3 [136, 148, 151]. The powder X-ray diffraction pattern of Li_2OsO_3 is shown in Figure 6.4 (top black line).

At first glance, the X-ray pattern pointed to a more symmetric space group, $R\bar{3}m$, however, close examination of the pattern showed weak and broad diffraction
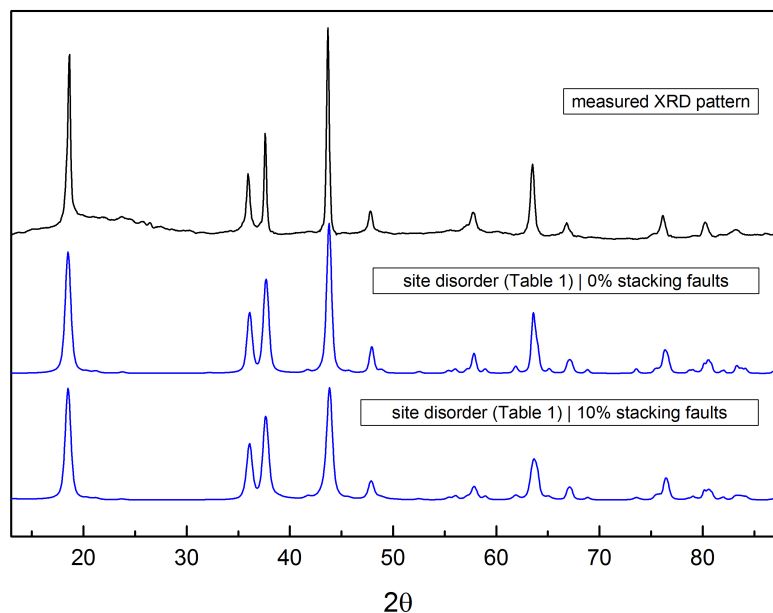
Figure 6.4: A comparison of the measured XRD pattern (top black line) (λ= 1.514 Angstroms), along with 43% site disorder (Table 1) | 0% stacking fault and 43% site disorder (Table 1) | 10% stacking fault simulated DIFFaX patterns (blue lines).

peaks in the 2θ region of 19º to 33º. It is known that for both $C2/m$ and $C2/c$ systems, with no Li-M site exchange within the LiM_2 layers, sharp peaks exist within the 19º to 33º range. However, introducing Li-M site exchange within the LiM_2 layers decreases the relative intensities of these peaks, leading to virtually no peak presence at approximately 30% Li-M site exchange [149]. Such a reduction in diffraction peak intensity is also found for (hk0) reflections past 38º [149]. Disorder among Li-M sites is commonly reported for honeycomb layered metal oxides since all corresponding crystallographic sites are octahedral and similar in size [123, 128,
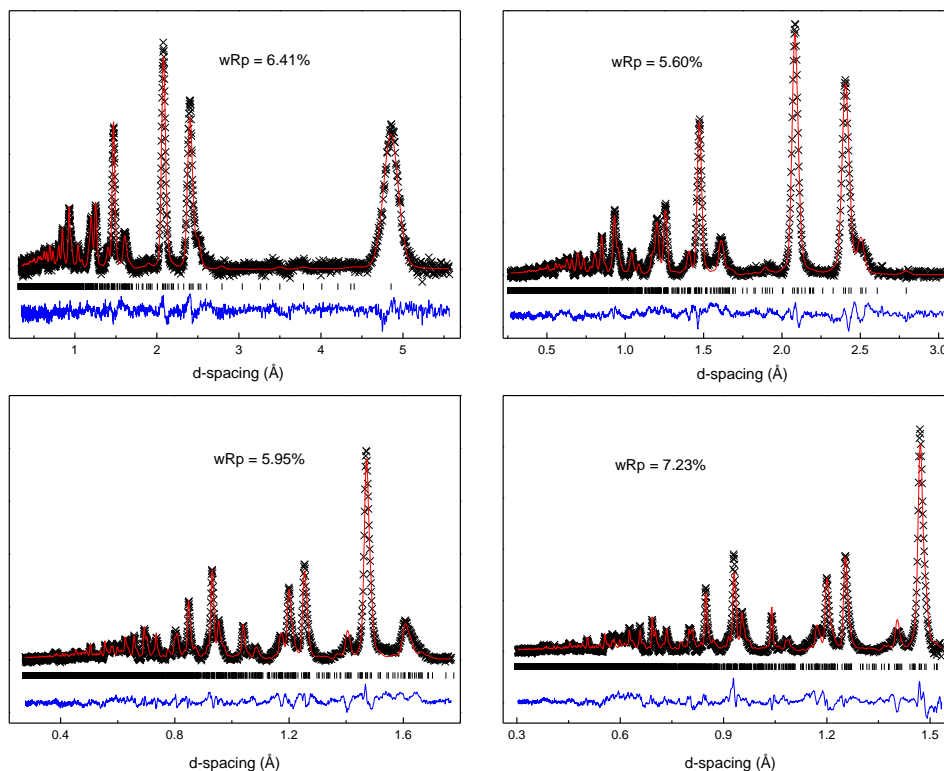
Figure 6.5: Rietveld refinement of TOF Neutron (Oak Ridge NOMAD BL-1B) diffraction data. The collected data (black cross), Rietveld refinement (red line), and difference (blue line) are presented for all four collected banks. Resulting cumulative $wR_{\mathrm{p}} = 6.4\%$.

130, 136, 137, 145–147]. The presence of stacking faults associated with a shift between successive LiM_2 layers will cause the peaks in the region from 19º to 33º to further broaden asymmetrically [126–128, 137, 149]. Thus, with the existence of Li-M site disorder and stacking faults, it is difficult to distinguish between the corresponding space groups using powder X-ray diffraction. The x-ray scattering length for lithium and oxygen are also small due to their low Z. Because of the

	Wyckoff	x	y	z	occ	U_{iso}
Li1	$8f$	0.2543(2)	0.0840(1)	0.0044(9)	1	0.25(8)
Li2	$4d$	0.25	0.25	0.5	1	0.037(4)
Li3	$4e$	0	0.7531(8)	0.25	0.32(4)	0.20(7)
Os3	$4e$	0	0.7531(8)	0.25	0.68(4)	0.20(7)
Os4	$4e$	0	0.0777(7)	0.25	0.46(2)	0.0043(2)
Li4	$4e$	0	0.0777(7)	0.25	0.54(2)	0.0043(2)
Os5	$4e$	0	0.4026(6)	0.25	0.56(2)	0.0082(2)
Li5	$4e$	0	0.4026(6)	0.25	0.44(2)	0.0082(2)
O1	$8f$	0.1335(7)	0.2414(5)	0.1344(4)	1	0.029(3)
O2	$8f$	0.1269(8)	0.5770(5)	0.1414(4)	1	0.0085(3)
O3	$8f$	0.1387(8)	0.9181(5)	0.1332(5)	1	0.0082(8)

Table 6.1: Atomic coordinates, occupancies and isotropic displacement parameters obtained from Rietveld refinement ($C2/c$) of TOF Neutron (Oak Ridge NOMAD BL-1B) diffraction data.

neutron scattering lengths of lithium, osmium, and oxygen, neutron diffraction is ideal to characterize the Li_2OsO_3 structure.

To determine the crystal structure, Rietveld refinements were performed on room temperature neutron diffraction data using the GSAS program (Figure 6.5) [152, 153]. The current synthesis procedure restricted diffraction measurements to the Oak Ridge NOMAD TOF Neutron beamline, which is well-suited for small sample sizes. A pseudo-Voigt peak shape profile was chosen and parameters refined to obtain the best fit to the collected data. The space group was refined to be $C2/c$, with lattice dimensions $a = 5.09$ Å, $b = 8.81$ Å, $c = 9.83$ Å, and $\beta = 99.3°$. Rietveld refinements for all collected banks show cumulative $wR_p = 6.40\%$. The atomic coordinates, occupancies, and isotropic displacement parameters are represented in Table 6.1.

Table 6.2: Bond lengths (Å) and angles (deg)

Li1 - O1	2.106(9)	Os4(Li4) - O1 x 2	2.020(4)
Li1 - O1'	2.136(9)	Os4(Li4) - O2 x 2	2.023(4)
Li1 - O2	2.187(9)	Os4(Li4) - O3 x 2	2.014(4)
Li1 - O2'	2.110(9)	Os5(Li5) - O1 x 2	2.005(4)
Li1 - O3	2.138(9)	Os5(Li5) - O2 x 2	2.035(4)
Li1 - O3'	2.188(9)	Os5(Li5) - O3 x 2	2.010(4)
Li2 - O1 x 2	2.175(4)	O1 - Os3(Li3) - O2	90.50(2)
Li2 - O2 x 2	2.220(4)	O2 - Os3(Li3) - O3	175.92(3)
Li2 - O3 x 2	2.113(4)	O1 - Os4(Li4) - O2	94.46(2)
Os3(Li3) - Os4(Li4) x 2	2.978(5)	O2 - Os4(Li4) - O3	178.67(3)
Os3(Li3) - Os5(Li5) x 2	2.866(4)	O1 - Os5(Li5) - O2	94.15(2)
Os3(Li3) - Os5(Li5)	3.088(9)	O2 - Os5(Li5) - O3	176.06(3)
Os3(Li3) - O1 x 2	2.025(4)		
Os3(Li3) - O2 x 2	2.046(4)		
Os3(Li3) - O3 x 2	2.047(4)		

Interatomic distances and angles are given in Table 6.2. No osmium is detected in the lithium-only layers. For $C2/c$ there are three unique atomic positions to describe the Li and Os sites within the $LiOs_2$ layer. Shown in Table 6.1, corresponding sites are labeled as Li/Os 3, 4, and 5. If no Li-Os site disorder existed within the $LiOs_2$ layer, only Li3, Os4, and Os5 would exist (each with an occupancy of 1), with Os4 and Os5 sites describing the honeycomb rings. As shown from Table 6.1 occupancies, a large percentage of Li-Os site disorder exists within the $LiOs_2$ layer. For each of the three respective crystallographic sites, an average of 43% is occupied by lithium. The stoichiometry derived from occupancy refinements of Li, Os, and O is $Li_{2.15(3)}Os_{0.85(3)}O_3$ suggesting an average osmium oxidation state of 4.5 ± 0.1. It is important to note that oxygen occupancy refinements indicate

that the oxygen sites are fully occupied and no detectable vacancies are observed. Though 2:1 stoichiometric amounts of Li:Os were used in the synthesis, the refined stoichiometric ratio is considered reasonable as the presence of a small amount of osmium impurity is formed during the synthesis and was removed by heating the sample in air at 300 °C as OsO_4 through sublimation.
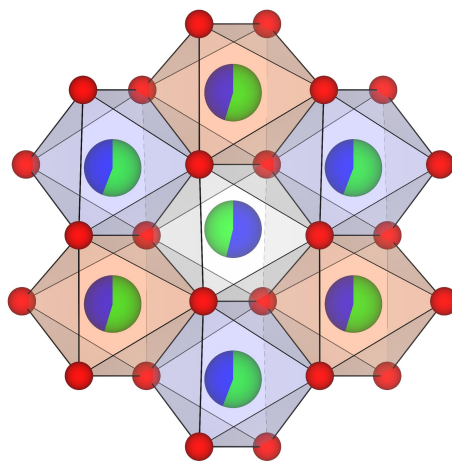
Figure 6.6: Illustration of the $C2/c$ honeycomb ring with lithium and osmium sites labeled according to Table 6.1 with Os3/Li3, Os4/Li4, and Os5/Li5 octahedral sites as grey, purple, and orange (osmium and lithium labeled green and blue respectively).

Stacking faults were modeled using the FAULTS program [154] and the description of the model and analogous XRD patterns are discussed in Chapter 6. The FAULTS program requires the cell axes to be defined with the c-axis perpendicular to the fault direction. For a monoclinic space group a new idealized unit cell for each individual layer must therefore be established. The new hexagonal unit cell was defined as $a_{hex}=a_{(C_2/c)}$ and $c_{hex}=[(c_{(C2/c)}\cos(\beta_{(C2/c)}\text{-}90))/2](z)$, with z as

the number of hexagonal layers used for the model. Division of 2 is based on the number of repeating Li-LiM$_2$ layers within $C2/c$ unit cell. Layer extension in a- and b- direction was set to infinite. The single layer used in DIFFaX and Li-LiOs$_2$ $C2/c$ layer are illustrated in Figure 6.7.
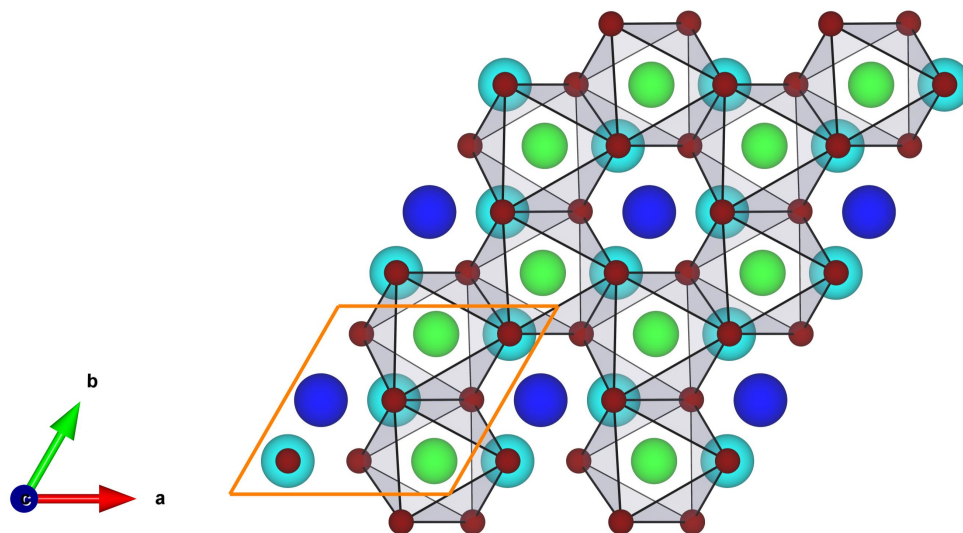
Figure 6.7: Illustration of the FAULTS single layer down the c-axis for Li$_2$OsO$_3$ with no Li-Os site disorder. Here, Osmium and oxygen are represented as green and red spheres, respectively. Lithium residing within the honeycomb rings are represented as dark blue spheres and lithium beneath the honeycomb layers as lighter blue spheres.

To replicate the ideal stacking sequence of Li$_2$OsO$_3$ ($C2/c$), layer sequencing was characterized by $[1/3,0,1/z]$ transition vector (R$_1$). To replicate stacking fault contribution, transition vectors $[0,1/3,1/z]$ and $[2/3,0,1/z]$ (R$_2$ and R$_3$) were incorporated. Probabilities were assigned to each of the three transition vectors, with $\alpha_1+\alpha_2+\alpha_3=1$ for each layer. For the latter two transition vectors, there was no

tangible difference in the model when varying the contribution for a given total stacking fault probability. Thus for the models presented, the assumption $\alpha_2=\alpha_3$ was implemented. Figure 6.8 shows a comparison of the measured XRD pattern (top black line), along with 0% site disorder — 0% stacking fault, 0% site disorder — 30% stacking fault, and 50% site disorder — 0% stacking fault simulated patterns (blue lines) within 17-35 2θ region. With incorporation of stacking faults, only (002) and (020) peaks within $17 - 35$ 2θ range do not broaden (Figure 6.9).
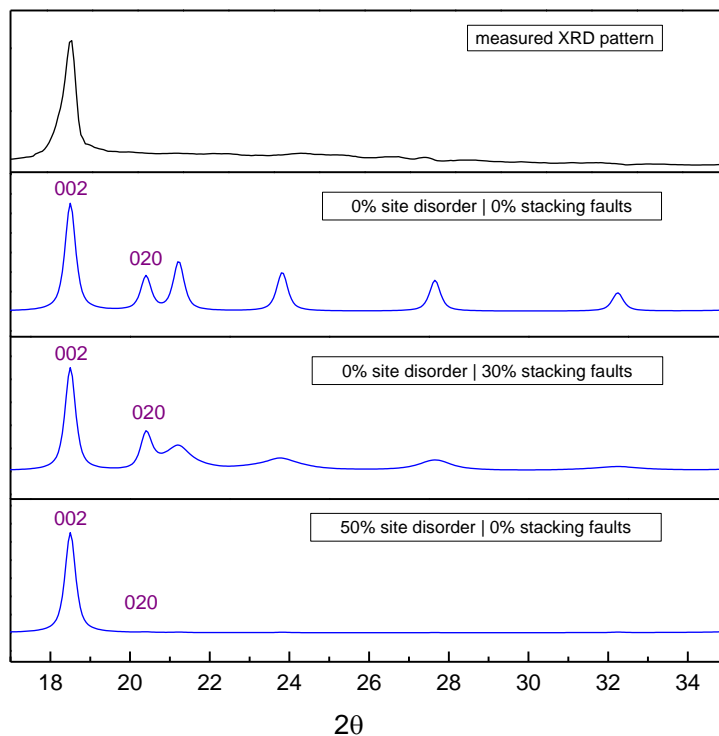
Figure 6.8: Measured XRD-pattern (black) and simulated FAULTS patterns of stacking faulted without site disorder and 50% site disorder of Li_2OsO_3 within 17 $- 35$ 2θ range.

Similar observations for other DIFFaX modeled Li_2MO_3 systems exist [126,128, 137,155–157]. Calculated XRD patterns with site disorder equivalent to Table 6.1 without and with 10% stacking faults are shown in Figure 6.4. The absence of the (020) peak is therefore attributed to Li-Os site disorder within the $LiOs_2$ layers. From the discussion presented, the absence of the (020) peak can only be attributed to Li-Os site disorder within the $LiOs_2$ layers and not from stacking faults, consistent with the neutron refinement. As shown in Figure 6.4, the measured XRD pattern is compared to simulated DIFFaX patterns with site disorder representing Table 6.1 refined Wyckoff site occupancies with and without 10% stacking faults (blue lines).

XAS measurements at the Os $L_{2,3}$ absorption edges ($2p_{\frac{1}{2},\frac{3}{2}} \to$ 5d resonant excitation) were used to provide an additional estimate of Os valence (Figure 6.10). The enhanced X-ray absorption above the leading edge ("white line") is a result of large density of empty 5d states near the Fermi level. This peak grows in intensity and shifts to higher energy with increasing Os oxidation state. Interpolating the XAS peak position in the honeycomb sample onto those of the reference compounds yields an oxidation state of $+4.7 \pm 0.2$, within errors of results from structure refinements.

The ratio of L_3 to L_2 white line intensity, also known as the isotropic branching ratio (BR), provides a measure of the relevance of SOC interactions in the 5d band [158,159]. In the absence of sizable SOC interactions, the isotropic branching ratio equals 2 reflecting the different occupancies of the core levels at L_3 and L_2 edges. We measured BR=2.9(1) which significantly differs from the statistical
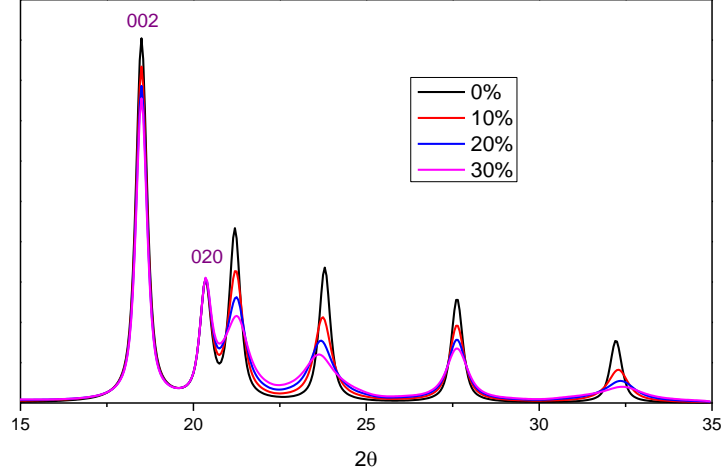
Figure 6.9: Simulated FAULTS XRD patterns with 0% - 30% staking faults and no site disorder within 15 – 35 2θ range .

value of 2 and indicates that SOC interactions need to be included in order to describe the 5d electronic structure of this compound.

6.3.2   Thermodynamic and Transport Properties

Temperature dependent resistivity and Seebeck measurements from $300 – 600$ Kelvin are shown in Figure 6.11. The gap energy (E_g) for the sample was extracted using $\rho = \rho_o \exp(E_g/2k_B T)$ with $E_g = 220$ meV and 266 meV obtained from low- and high-temperature transport measurements respectively, thus indicating a small band gap insulator (Figure 6.11 - bottom).

The magnetic susceptibility, χ_{dc}, for $H = 0.5$ T (Figure 6.12) suggests the
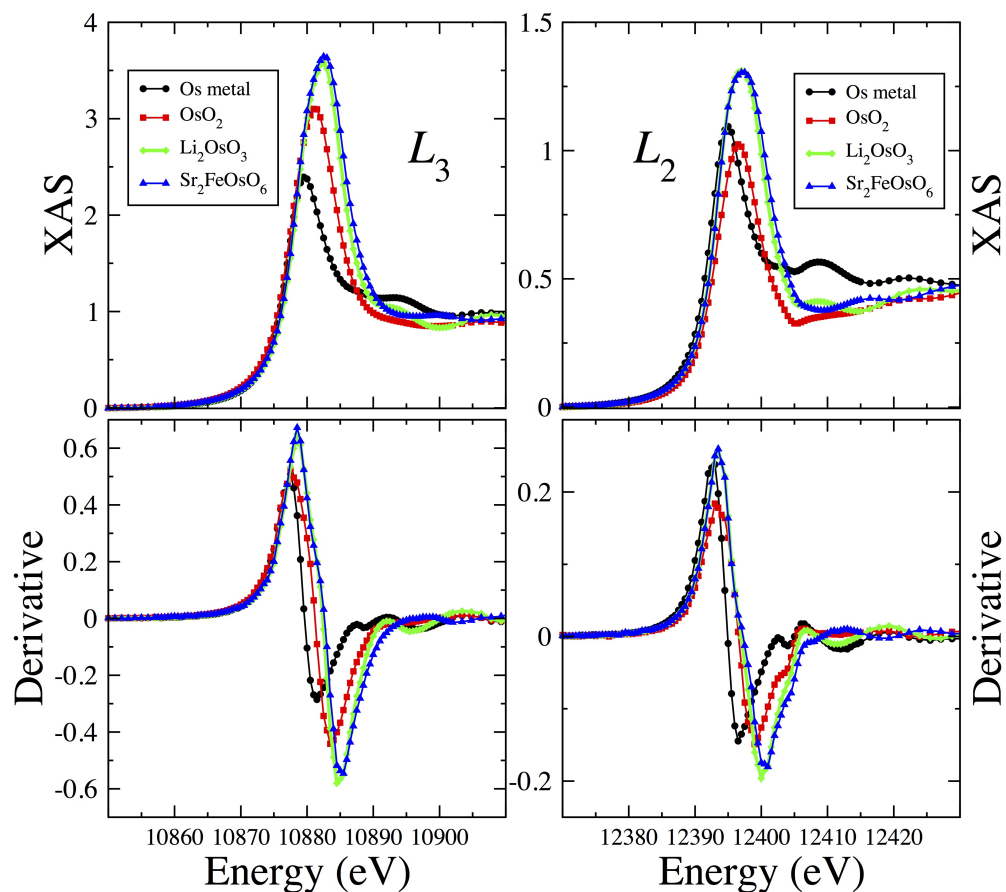
Figure 6.10: XAS measurements at the Os $L_{2,3}$ absorption edges on $Li_{2.15}Os_{0.85}O_3$ and three reference compounds with known oxidation state.

combined effects of Curie-Weiss as well as van Vleck temperature independent paramagnetism over the entire measurement range above 2 K. Within this assumption, we varied the magnitude of the van Vleck term, χ_{VV}, to produce a pure Curie-Weiss contribution. We found that subtracting $\chi_{VV} = 0.00135$ emu/mole from the measured $\chi(T)$ produces the straightest $1/\chi(T)$, resulting in a good fit to the Curie-Weiss form, $\chi = C/(T\text{-}\theta)$, where C is the Curie constant and, θ is
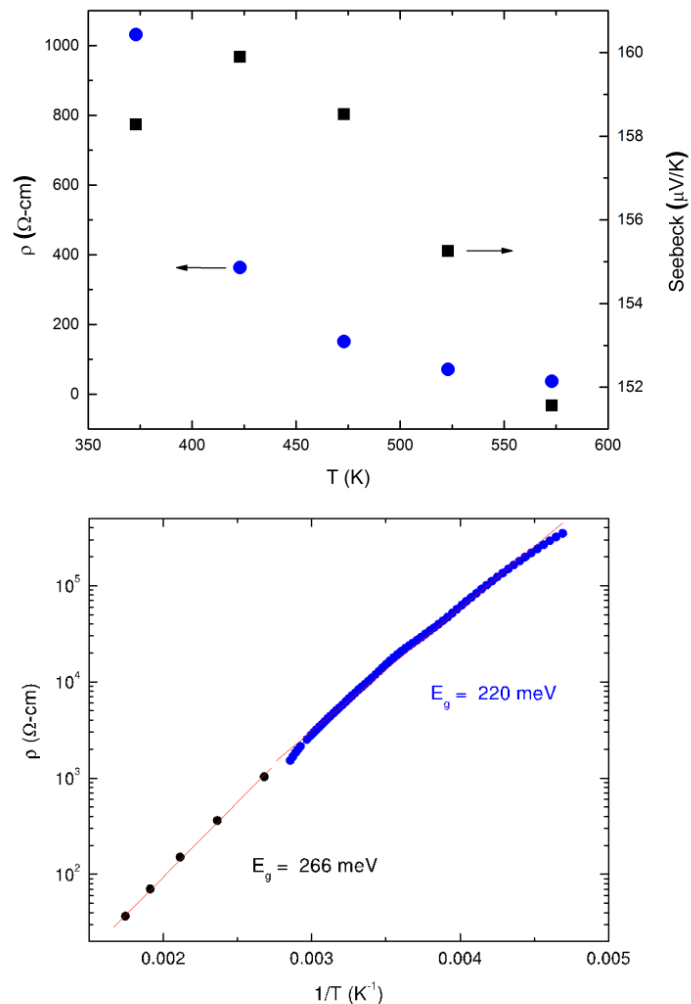
Figure 6.11: Top: High temperature resistivity and Seebeck coefficient data of $Li_{2.15}Os_{0.85}O_3$ sample from 350 to 600 K. Bottom: Resistivity versus temperature for $Li_{2.15}Os_{0.85}O_3$ in the range 200 – 600 K versus inverse temperature. The low and high temperature measurements were performed in different apparatuses on samples from the same growth run. To assure continuity at T = 300 K, the data have been rescaled for the low temperature measurement due to its greater uncertainty in the geometric factor.

the Weiss constant.

Fitting the data between 50 and 200 K yields a Weiss constant of θ = -11.5 K and a finite effective moment μ_{eff} = 0.85 μ_B, significantly greater than expected for the J_{eff} = 0 state of Os(+4). Given the above XAS and neutron scattering refinement results showing that the average Os valence is 4.7, however, an alternate ionic scenario is for 70% of the Os ions to be in the +5 state ($J_{eff} = \frac{3}{2}$) and 30% in the +4 state ($J_{eff} = 0$). This analysis yields $\mu_{\text{eff}} = 1.01\mu_B$ (θ = -11.8 K) for the magnetic (+5) ions, which is now significantly less than the expected moment.

We discuss possible sources of this discrepancy below. These χ_{dc} data were augmented with ac-susceptibility (χ_{ac}) data down to 0.1 K, which were calibrated to the χ_{dc} data in the overlapping temperature range 2.0 – 2.5 K. A peak in χ_{ac} is observed at 0.5 K, but is rapidly suppressed by magnetic fields far less than 0.1T. Given the usual relationship between H and T for a g-factor of two, one expects suppression of an antiferromagnetic ordering feature at 0.5 K for H values an order of magnitude larger than observed. Alternatively, such a cusp in χ_{ac} can be attributed to spin glass freezing, a scenario consistent with the high degree of disorder in this spin system. The spins involved in such freezing may not represent the bulk of the Os(+5) spin population, as we argue below.

The existence of a small subset of spins that are interacting at a mean field energy scale of k_BT for T = 0.5 K, as suggested by the χ_{ac} peak, is also supported by $C(T,H)$, shown in Figure 6.13.

For semiconductors, the Einstein - Debye theory of specific heat can be applied to model the change in specific heat at low temperatures. The Einstein - Debye
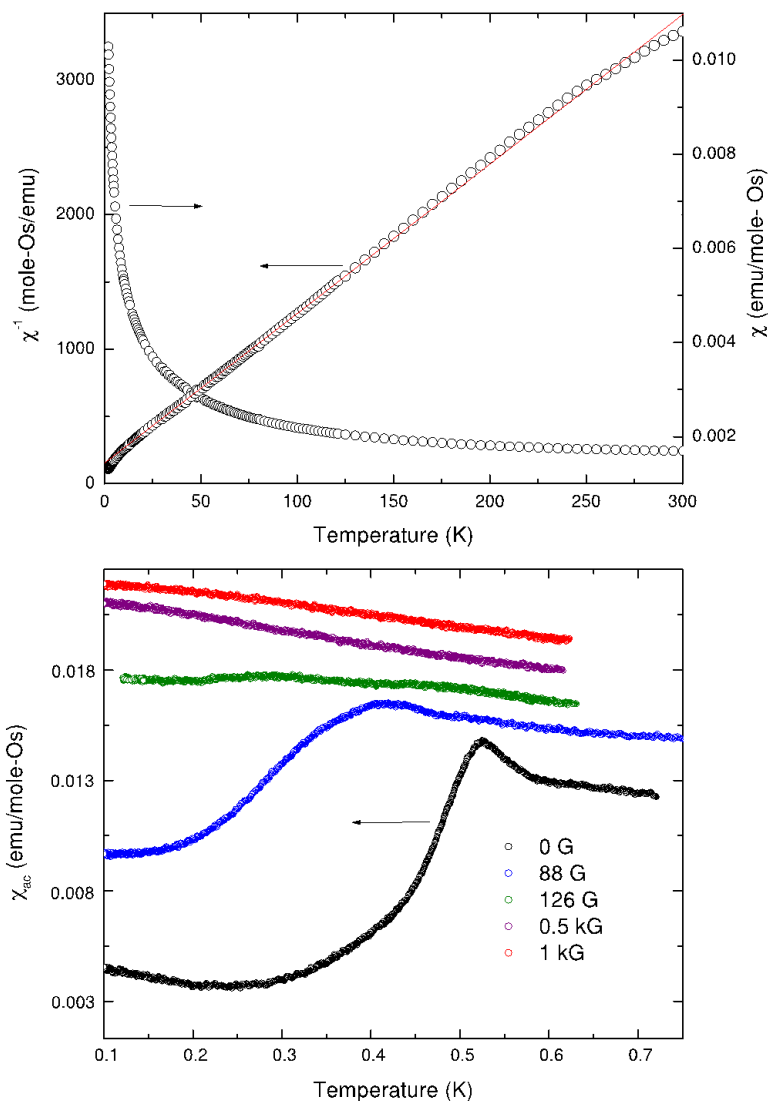
Figure 6.12: Top: DC-Susceptibility $Li_{2.15}Os_{0.85}O_3$ versus temperature. Also shown is the inverse susceptibility after subtracting a van Vleck term as described in the text. Bottom: ac-susceptibility versus temperature at different values of applied magnetic field. The curves have been offset vertically by 0.0020, 0.0032, 0.0044, and 0.0056 emu for $H = 88$, 126, 500, and 1000 G respectively, for clarity.
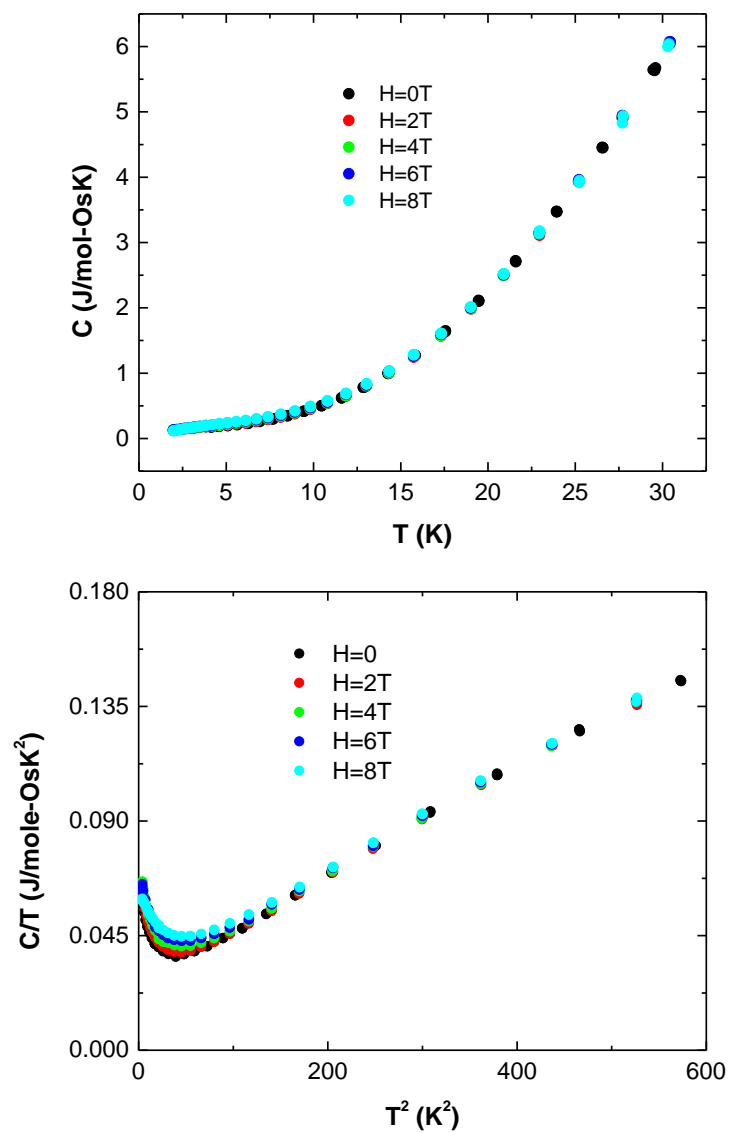
Figure 6.13: The specific heat C(T) of $Li_{2.15}Os_{0.85}O_3$ in various applied fields, measured using a Physical Property Measurement System. Bottom: Plotting C/T vs. T^2 from the Einstein-Debye model should result in a linear correlation if no phase/electronic transition occurs.

theory is calculated theoretically by taking the partial derivative of the internal energy with respect to temperature (discussed in Chapter 2). From the Einstein - Debye equation, the electronic contribution to the specific heat is proportional to T and the vibrational contribution to the specific heat is proportional to T^3. For any sort of physical state transition-phase, magnetic ordering, and/or transition to a superconducting state, an increase in the specific heat will be observed at the corresponding transition temperature. Thus, by plotting C/T versus T^2, from the Einstein - Debye expression, a linear trend will be observed as long as a physical/electronic transition does not occur within the temperature region. As shown in Figure 6.13, C/T exhibits an upturn below its minimum at T = 6 K. This upturn is only moderately affected by fields up to 8 T, so we model this as $C = C_1(T) + C_2(T,H)$. Here C_1 is a combination of the lattice specific heat and an H-independent electronic contribution and C_2 is a combination of the lattice specific heat and an H- dependent electronic contribution. Taking the difference between $C(H = 8T)$ and $C(H = 0)$, the H-dependent electronic contribution ("spin impurities") can be shown in terms of a Schottky trend, where $C_2(T,H=8T)$ resembles a broadened Schottky anomaly (Figure 6.14). Recall, the existence of a small subset of spins suggested by the χ_{ac} peak. This observation is also supported by the specific heat. We can fit this contribution to either a single $J_{eff} = \frac{3}{2}$ (g = 1.3) Schottky anomaly or a pair of $J_{eff} = \frac{1}{2}$ (g = 2.6 and 7.4) Schottky anomalies with molar concentrations of 4.1% and 9.6% (total for the pair) respectively (Assuming 70% of the spins are magnetic, these fractions become 5.9% and 13.7%). By subtracting C (H=8T) from $C_{schottky}$ trends (i.e. subtracting out the contribution

of the "spin impurities"), the resulting lattice specific heat and an H-independent electronic contribution can be plotted as a power plot (Figure 6.14). A resulting power law $T^{0.63}$ is therefore obtained. Thus, it is not unlikely that the spins undergoing spin-glass-like freezing are the same spins responsible for the Curie-tail susceptibility. We now turn to the $C_1(T)$ term, which is calculated using the two different Schottky approximations mentioned above and plotted Figure 6.14. We note that, below 8 K, $C_1(T) \propto T^\alpha$, where $\alpha = 0.69$ and 0.57 for the $J_{eff} = \frac{3}{2}$ and $\frac{1}{2}$ Schottky analyses respectively. Such a sublinear form cannot persist down to the lowest temperatures, and importantly is clearly distinct from the phonon contribution visible above 8 K. At the same time, it appears that, among the 70% of Os ions that are in a +5 state (within an ionic picture) and thus possibly magnetic, less than 15% are accounted for in either susceptibility or field-dependent specific heat. All known spin frustrated systems possess a resulting power law with $\alpha=2$. The only known systems that possess $\alpha < 1$ are quantum spin liquid candidates [160]. If the sublinear low-T contribution is due to these unaccounted for, but nevertheless magnetic, Os(+5) ions, then they must be in a type of singlet state due to exchange interactions with a strength greater than the Zeeman energy of an 8 Tesla field, but of a type that invalidates the effective moment approximation below room temperature.
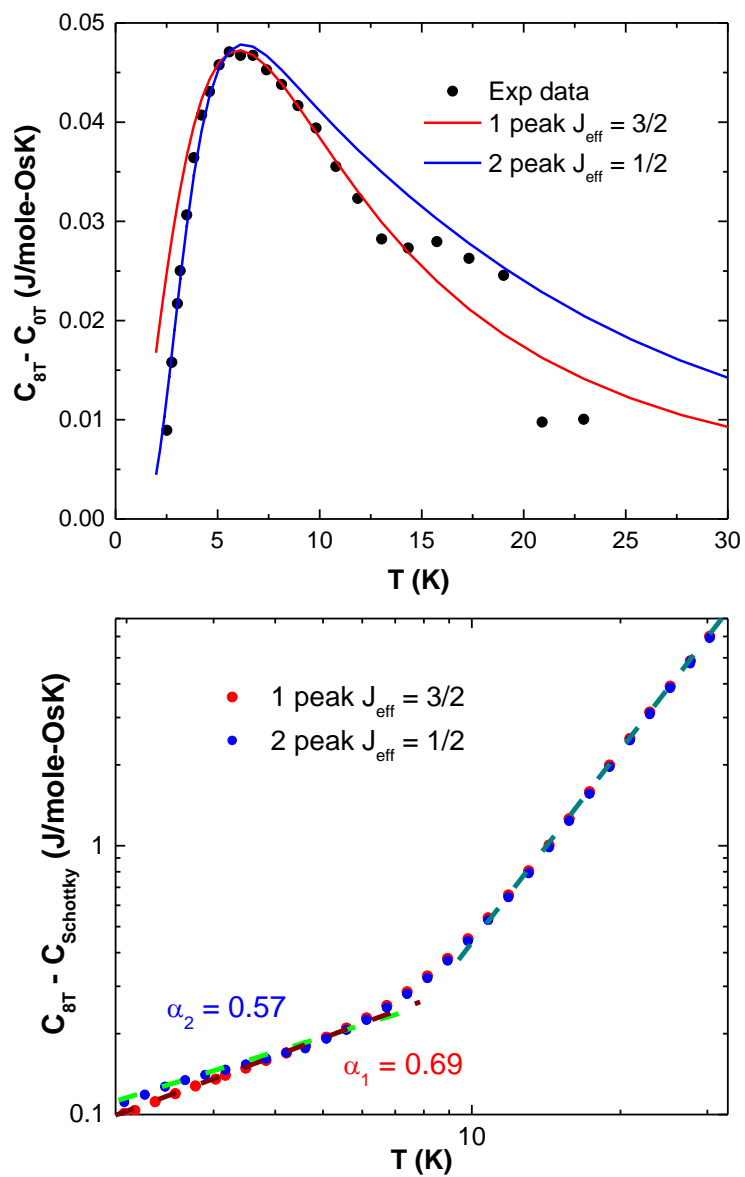
Figure 6.14: Top: Impurity spins modeled with a Schottky anomaly. Bottom: Specific heat after removing the impurity contribution.

6.3.3 Electronic Structure

Early model treatments of 5d oxides on honeycomb lattices built on the ionic description of crystal field splitting, additionally with strong SOC among orbitals, focused attention on the t_{2g} subshell $J_{eff} = \frac{1}{2}$ and $\frac{3}{2}$ subspaces. The relevant energy scales of individual bandwidth W, Hubbard U, Hund's J_H, and SOC strength ξ, all lie in the 0.5-1.5 eV range, and studies of the electronic structure and especially the exchange coupling have concluded that the ionic picture provides a challenging starting point at best. The electronic structure of octahedral osmates is complicated by several features. First, the active t_{2g} orbitals are strongly hybridized with the oxygen 2p orbitals, resulting in strongly coupled Os 5d – O 2p states as the fundamental chemical unit. Osmates in the Ba_2NaOsO_6 family, for example, have half of the spin density residing on the O octahedron [161, 162]. Iridates behave similarly, leading to their characterization as *molecular orbital compounds*, which can lead to longer range exchange coupling parameters compared to more localized moments [163]. Second, SOC also affects the electronic structure, creating both single-ion as well as exchange anisotropy, the relative effects of which are difficult to disentangle. Third, the distortion from ideal rhombohedral symmetry introduces new lower symmetry Fourier components of the potential that causes band anti-crossings. These in turn result in very narrow, 0.3 eV, individual bandwidths and the likelihood of small gaps, as shown below.

Several theoretical studies of honeycomb iridates have concluded that magnetic interactions beyond the Heisenberg-Kitaev model are important, suggesting a more

itinerant picture of the electronic structure [164–170]. Many of the general findings for iridates carry over to osmates. Our compound presents the additional complication of Os possessing a nominal valence of +4.7, so one must consider a mixture of d^3 with d^4 ions. The ionic picture of d^4 begins with a non-magnetic $J_{eff} = 0$ ion and for d^3 the ionic value is $J_{eff} = \frac{3}{2}$, and the insulating nature suggests these different ionic states reside on distinct lattice sites, as opposed to the intermediate valence picture. In this ionic picture, the measured $\mu_{eff} = 0.85\mu_B$ is challenging to account for, as mentioned above, which leads us to consider the general question of moment formation in nearly itinerant systems.

In an effort to reconcile the valence state measurements with the magneto-thermal measurements, we have applied density functional theory (DFT) methods including SOC, correlation effects, and a fixed atomic spin moment method in our study of Li_2OsO_3 (see Methods for the description) [171–176]. Without magnetism, SOC is strong enough to provide a pseudogap but no gap, within the Os t_{2g} bands. This SOC-driven separation is compromised by crystal subfield splittings, bandwidth effects, and anti-crossings arising from structural distortion away from rhombohedral symmetry leaving two inequivalent Os sites. The resulting band structure (not shown) is that of a very narrow, essentially zero (indirect) gap semiconductor. Due to the molecular orbital nature of the t_{2g} band complex, intra-atomic repulsion effects as treated by the Hubbard U repulsion are ineffective in opening a gap, for reasonable values of U (2 eV or less). Antiferromagnetic order tends to encourage gap opening, producing Os moments of 0.3 μ_B.

To include in the modeling the effect of the observed Os moment, we have

adopted the constrained atomic moment method as implemented in the *abinit* code [171]. This method proceeds not by specifying a value for U for the Os 5d orbitals, but by fixing the spin moment by applying an intra-atomic Zeeman field determined self-consistently; both magnitude and direction can be specified separately for any atom. Magnitudes of 0.8 μ_B and 0.5 μ_B have been studied; the latter value represents the ordered component expected of a 0.8 μ_B local (C-W) moment. Bandgaps of 0.25 eV and larger were obtained, depending weakly on the imposed moment but strongly on the magnetic alignment (the larger ones were for AFM order). The resulting orbital moments are minor, only a few hundredths of 1 μ_B, independent of the chosen direction of spin. These results do not fit that of a Mott insulator: there is no robust local moment, and Hubbard U is not needed to open a gap and has little effect on the size of the gap. Thus our model rationalizes the observations of a narrow transport gap and small magnetic moment in $Li_{2.15}Os_{0.85}O_3$.

Due to intermixing of Li on the Os honeycomb lattice, we have made an initial study of the effect of intermixing, by replacing 25% of the Os sublattice by Li while keeping the Li sublattice intact. The Os moments are fixed with magnitude 0.8 μ_B and oriented along separate (111) axes to mimic disordered moments. The resulting band structure, shown in Figure 6.15, illustrates the flat individual bands that arise, and that a very small gap exists or is imminent, depending on details of the calculations. The bands are not significantly different in appearance from those of Li_2OsO_3.

We now focus on the effect of Li substitution on the remaining Os ions. This
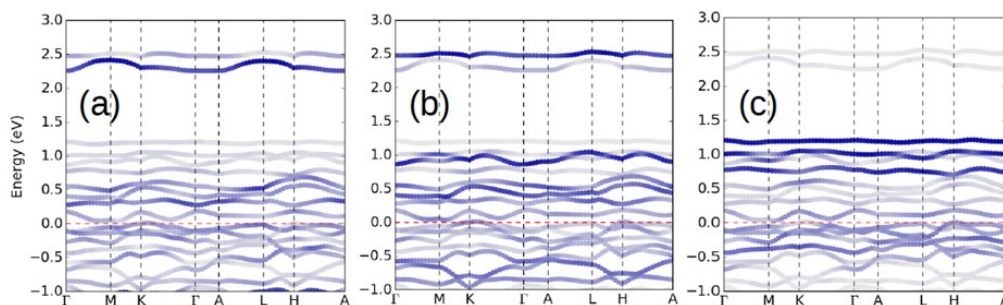
Figure 6.15: Plot of bands in the Os t_{2g} region of 25% Li-substituted Li_2OsO_3 on the Os honeycomb sublattice, with energy zero (horizontal red dashed line) denoting the gap region. The fatbands plots emphasize the Os 5d character on (a) the Os[0] site with no Li neighbor, (b) the Os[1] site with one Li neighbor, and (c) the Os[2] site with two Li neighbors. While Os[0] and Os[1] show some differences, Os[2] is qualitatively different.

25% replacement results in three Os sites, denoted by Os[j] which has j Li neighbors, j = 0, 1, or 2. The formal valences of Os in this $Li_2(Li_{1/4}Os_{3/4})O_3$ structure should average to 5+. The periodicity leaves Os[0]-Os[1] chains and comparatively isolated Os[2] ions, which in addition to two Li neighbors the Os neighbor is at a long Os-Os separation. The spectral distribution of Os[2] in Figure 6.15 is substantially different from the other two, more representative of a lower oxidation state. While simple electron count indicates that Li substitution must oxidize some Os ions, having two Li neighbors strongly affects the formal valence of the Os ion.

This modeling illustrates that the Os valence is sensitive not only to the total charge available, but also to the local environment. Different valence states carry different moments, and sensitivity to the local environment suggests that variation of exchange constants promotes a frustration of magnetic order. Note in Figure 6.15 that the spectral distributions of 5d weight are significantly different for Os[0]

and Os[1], while that of Os[2] is less weight in the occupied bands. This implication then is that of one Os(4+) ions and two Os(5+) ion, with an average valence of 4.67 consistent with spectroscopic evidence on our samples. More of a specific nature cannot be concluded because the Os moments were constrained (to be equal), whereas those of different valence states would not be equal.

6.4   Summary

We have presented the first example of Os on a honeycomb structure, $Li_{2.15(3)}Os_{0.85(3)}O_3$, and have characterized it with atomic, structural, and magneto-thermal probes. The Os ions have an average valence state of +4.7 and large site disorder exists in the honeycomb layers. This compound is a narrow band gap semiconductor. The magnetic susceptibility and specific heat present a picture in which the effective Os moment is reduced to a value well below that expected from the valence-state measurements, which suggests that the valence electrons are on the verge of itineracy, a conclusion supported by our density functional theory calculations. These results strongly suggest that spin orbit coupling of Os is playing an important role in the collective electronic behavior of this honeycomb system, and that further studies of osmates on frustrating lattices are warranted.

6.5   Methods

6.5.1   Synthesis and Structure Characterization

Stoichiometric amounts of Li_2CO_3 and OsO_2 (synthesized from osmium metal - see below) were intimately ground, pressed into a pellet, loaded into an alumina crucible, and fired in a tube furnace at 700 C under Argon flow. Firing was repeated to 850 C with 50 C increments, grinding the sample before each firing. Each firing was performed under argon flow. The OsO_2 sample was synthesized by first placing a known amount thin layer of osmium metal in an alumina crucible. The crucible was then placed in an atmosphere controlled quartz tube furnace setup. Argon gas flow was introduced for approximately 20 minutes. The quartz tube setup was then sealed and vacuum out the argon atmosphere to $\sim$0.05 MPa below atmospheric pressure. A stoichiometric amount of O_2 gas was introduced based on the relative pressure change. The resulting tube furnace setup was then slowly fired to $\sim$600 C for $\sim$3 hours. Phase analysis of the powder samples was performed by X-ray diffraction using a Rigaku MiniFlex II diffractometer with Cu Kα radiation and a graphite monochromator for the diffracted beam. Time of Flight (TOF) neutron diffraction measurements were collected at ORNL NOMAD BL-1B SNS beamline. X-ray absorption spectroscopy measurements were carried out at beamline 4-ID-D of the Advanced Photon Source at Argonne National Laboratory using a transmission geometry. Reference samples for valence determination included Os metal, $Os^{4+}O_2$ and $Sr_2FeOs^{5+}O_6$ [177].

6.5.2 Electronic and Thermal Properties

The Seebeck coefficient and electrical conductivity data (350 K – 600 K) were collected on an ULVAC ZEM-3 under a helium atmosphere. Magnetization measurements (2 K - 300 K) were obtained with a Quantum Design MPMS. Resistivity, $\rho(T)$, (200 K - 350 K) and specific heat, $C(T)$, data (2 K - 30 K) were obtained using a Quantum Design PPMS. Magnetic ac-susceptibility data down to 0.1 K were obtained in a ^{3}He-^{4}He dilution refrigerator with thermal contact to the mixing chamber made via a copper wire bundle bonded to the sample with Stycast 1266 epoxy. Data were obtained at 143 Hz and with an excitation current low enough to eliminate heating from the coils.

6.5.3 Theoretical Methods

We use the open-source package ABINIT [53] to perform electronic calculations, with the generalized gradient approximation (GGA) [54] for the semilocal exchange-correlation functional and the projector augmented wave method (PAW) [174] for core electrons. A Hubbard U repulsive interaction was applied with magnitude as indicated, Hund's J_H = 0.4 eV was applied, on the Os 5d orbitals [175]. A mesh of 9x5x9 was used for k-sampling and 500 eV for energy cutoff. The constrained atomic spin moment on Os method [176] was used in some calculations to fix moments at or near the observed value. Constraints are managed by the use of Lagrangian multipliers, imposed with constraint parameters; the input parameter $\lambda = 1.0$ was used [172].

Chapter 7: Unraveling the Mixed Valence Picture of the Double Perovskites $Ba_{2-x}La_xYIrO_6$

7.1 Abstract

The interest in perovskites can be attributed to their wide array of properties, which in turn derives from their compositional and structural flexibility. The framework of the $A_2MM'O_6$ double perovskite containing $4d/5d$ elements with strong spin-orbit coupling (SOC) are of interest for the exploration of quantum magnetism. In such systems, the interplay between the electron localizing tendencies of SOC and the delocalizing effects of the large spatial extent of the $4d/5d$ orbitals has the potential to combine with electronic correlations to produce unusual states. The motivation to study $Ba_{2-x}La_xYIrO_6$ is twofold: (1) to investigate a mixed $5d^4/5d^5$ iridate perovskite with noncubic symmetry and with iridium as the sole magnetic ion, and (2) to elucidate the influence of local environment on the magnetism in such systems. As shown by the structural refinements presented, $a^0a^0a^0$ ($Fm\bar{3}m$) $\rightarrow a^0b^-b^-$ ($I2/m$) octahedral distortion of the YO_6-IrO_6 rock-salt framework occurs with increasing x to account for the incorporation of smaller La^{3+} radii. From the magnetic susceptibility measurements, deviations from the proposed mixed valence picture are observed, not only for $x = 0.2$, but also on approaching $x = 0.8$. For $x = 0.2$, χ_{VV} is larger than found for $x = 0$.

Publication based on this chapter:

1. Wallace, M.K.; LaBarre, P.G.; Svadlenak, S.; Ramirez, A.P.; Subramanian, M.A; Unraveling the Mixed Valence Picture of the Double Perovskites $Ba_{2-x}La_xYIrO_6$, *in progress*, (2019).

7.2   Introduction

The prevalence of perovskites can be elucidated by the compositional and structural flexibility of the corresponding structure. Because of this inherent flexibility, an array of properties have been reported, with numerous examples where substitution of one or more of the cations can considerably impact structure and properties [178–184]. The double perovskite $A_2MM'O_6$ structure can be described as a close packed AO_3 arrangement with $\frac{1}{4}$ of the octahedral sites filled with M/M' metals, forming a network of corner shared MO_6-$M'O_6$ octahedra with A cations residing in 12-coordinated sites (Figure 7.1).
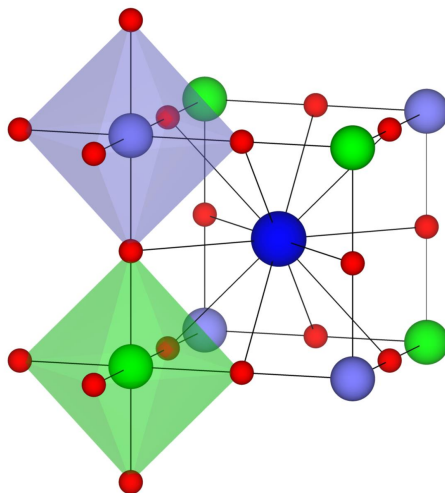
Figure 7.1: The ideal cubic $A_2MM'O_6$ double perovskite with blue, green/purple, and red representing A-site, M/M'- site, and oxygen, respectively.

Depending on the relative charge, size, and electronegativity differences, the M-site arrangement can be disordered or ordered with possible octahedral distortions

throughout the MO_6-M'O_6 octahedral lattice [178–181,185]. The framework of the A_2MM'O_6 double perovskite containing $4d/5d$ elements with strong spin-orbit coupling (SOC) are of interest for the exploration of exotic states [182, 183, 186–189]. Effects due to crystal field, SOC, and electronic correlations can have a strong influence on the electronic states. Of recent interest for topological materials are perovskites where SOC is large enough to influence the electronic band structure. Iridates are the most widely studied perovskites with Iridium frequently in a 4+ oxidation ($5d^5$) state [187,190,191], resulting in a $s = \frac{1}{2}$ Kramers doublet. Systems with such $5d^5$ ground states have been predicted to possess anisotropic exchange interactions, a key ingredient of the Kitaev model of quantum spin liquid [192]. In contrast, $5d^4$ iridates should yield a nonmagnetic ground state with total angular momentum $J = 0$ and a higher energy triplet which gives rise to van Vleck paramagnetism [193]. Thus, Ba_2YIrO_6 is expected to be nonmagnetic. The observed small magnetic moment of Ba_2YIrO_6 advocates a non-magnetic state with impurity spins [194–196]. Recent work by Kataev et al, has verified that the magnetism of Ba_2YIrO_6 is solely due to a few percent of Ir^{4+} and Ir^{6+} magnetic defects while the regular Ir^{5+} sites remain nonmagnetic, thus confirming the existence of a non-magnetic $5d^4$ ground state [186]. There are a few reports that endorse the influence of noncubic symmetry on the magnetism of $5d^4$ iridate perovskites [197,198]. The argument of local environment influencing the SOC, however, is unclear as the spin-orbit Hamiltonian is defined by the fixed term $(1/r)(\delta V/\delta r)$, with V as the nuclear Coulombic potential and r representing the radial position of the electron. Recent work by Khaliullin speculate $J_{eff} \neq 0$ in $5d^4$ iridates can be achieved if the

superexchange (SE) interaction energy is on the order of the SOC [193]. The SOC for Ir^{5+} is 540 meV [199]. To our knowledge, $5d^4$ iridates with SE large enough to overpower such a large SOC has not been observed. The motivation to study $Ba_{2-x}La_xYIrO_6$ is twofold: (1) to investigate a mixed $5d^4/5d^5$ iridate perovskite with noncubic symmetry and with iridium as the only magnetic ion, and (2) to elucidate the influence of local environment on the magnetism in such systems. As shown by the structural refinements presented, $a^0a^0a^0$ ($Fm\bar{3}m$) $\rightarrow$ $a^0b^-b^-$ ($I2/m$) octahedral distortion of the YO_6-IrO_6 rock-salt framework occurs with increasing x to account for the incorporation of smaller La^{3+} radii. From the magnetic susceptibility measurements, deviations from the proposed mixed valence picture are observed, not only for $x = 0.2$, but also on approaching $x = 0.8$. For $x = 0.2$, χ_{VV} is larger than found for $x = 0$.

7.3 Experimental

Stoichiometric amounts of $BaCO_3$, IrO_2, La_2O_3, and Y_2O_3 were intimately ground, pressed into a pellet, loaded onto an alumina crucible, and fired in air at 900 C for 6 hours and then at 1200-1250 C, 12 hour firings each with intermediate grindings. Both La_2O_3 and Y_2O_3 were preheated at 800 C for 12 hrs. X-ray diffraction (XRD) were collected using a Rigaku MiniFlex II diffractometer with Cu K_α radiation and a graphite monochromator for the diffracted beam. The samples were loaded onto an oriented Si single-crystal sample holder (MTI Corporation). Diffraction patterns were collected with a fixed-time scan rate of 0.02^0 step^{-1}

and 4.0 s step^{-1} from 10 to 110^0 2θ. Time of Flight (TOF) neutron diffraction measurements were collected at Oak Ridge National Laboratory POWGEN BL-11A SNS beamline. The Seebeck coefficient and electrical conductivity data (350 K – 600 K) were collected on an ULVAC ZEM-3 under a helium atmosphere. Magnetization measurements (2K - 300 K) were obtained with a Quantum Design MPMS. Resistivity, ρ(T), (200K - 350 K) were obtained using a Quantum Design PPMS.

7.4   Results

7.4.1   Structure

A combination of powder XRD and TOF neutron diffraction were used establish the most appropriate space group for each $Ba_{2-x}La_xYIrO_6$ and to refine atomic structures for $x{=}0$ and $x{=}0.6$ samples. Figure 7.2 shows XRD patterns of $Ba_{2-x}La_xYIrO_6$ ($0 \leq x \leq 0.6$) samples. A small presence of La_2O_3 impurity phase exists for $x \leq 0.6$. Trace Y_2O_3 impurity phase was detected in the diffraction pattern upon magnification for all samples. With increasing La^{3+} content x from 0 to 0.6, $Fm\bar{3}m \rightarrow I4/m \rightarrow I2/m$ space group transformations occur with La^{3+} solubility limit close to $x{=}0.6$ (Figure 7.3). The $A_2MM'O_6$ rock salt M-site ordered double perovskite of $a^0a^0a^0$ ($Fm\bar{3}m$), $a^0a^0c^-$ ($I4/m$), and $a^0b^-b^-$ ($I2/m$) Glazer tilt systems are illustrated in Figure 7.4.

As shown in Figure 3, cell edges decrease with increasing La^{3+}, concurrent to
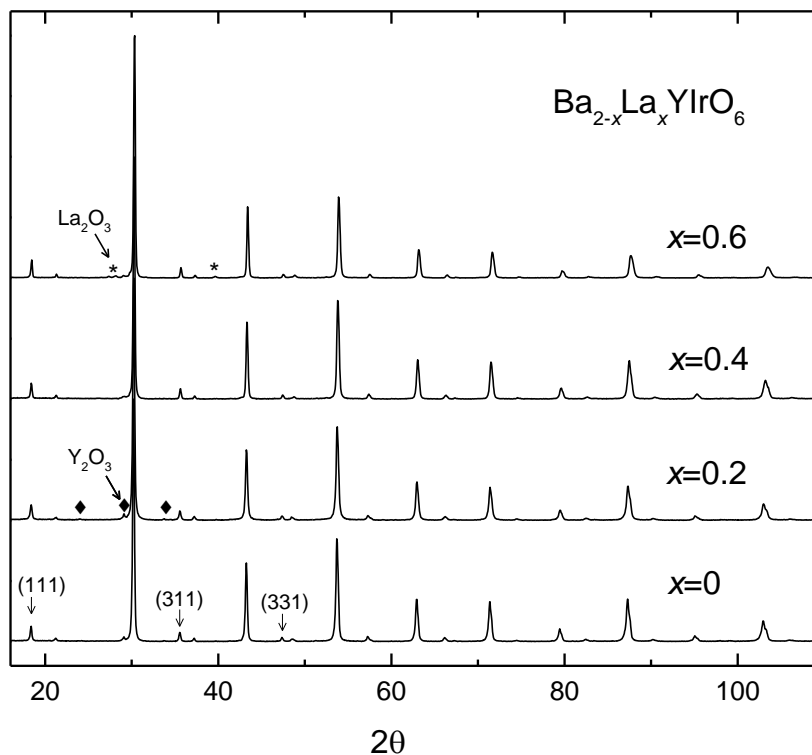
Figure 7.2: XRD patterns of $Ba_{2-x}La_xYIrO_6$ ($0 \leq x \leq 0.6$) samples shown from 15-110^0 2θ. A small presence of La_2O_3 impurity exists for $x \leq 0.6$ samples (asterisks). Trace Y_2O_3 impurity phase was detected in the diffraction pattern upon magnification for all samples (diamonds).

the ionic radii difference between Ba^{2+} and La^{3+} (1.61 Å versus 1.36 Å, respectively [200,201]. Deviation from the linear decrease of the a and b axis from $x=0.4$ to $x=0.6$ nominal samples can be attributed to the transformation to a Glaser 2-tilt distorted monoclinic structure. For Ba_2YIrO_6, both powder XRD and TOF neutron refinements reveal an ideal cubic perovskite with rock salt 1:1 B-site ordering ($Fm\bar{3}m$), consistent with other work, tolerance factor ($\tau=0.98$), and the
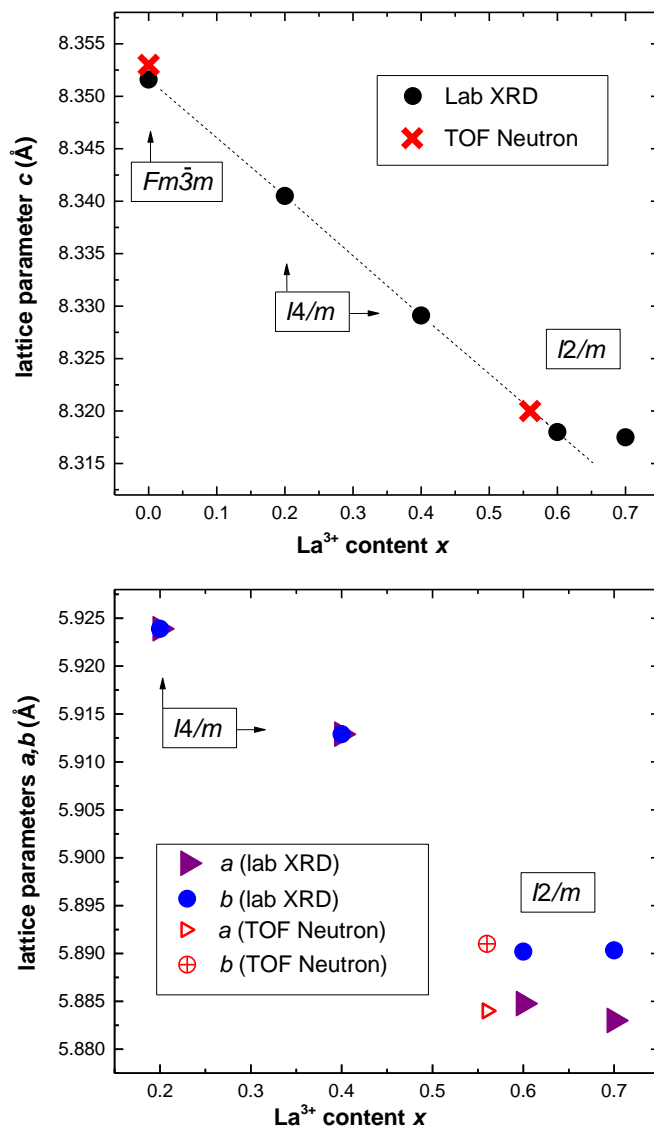
Figure 7.3: Cell edges a, b, and c vs La^{3+} content x in $Ba_{2-x}La_xYIrO_6$. Lab XRD cell parameters are plotted by nominal La^{3+} content x. TOF neutron cell parameters are plotted by refined La^{3+} content $x=0.56$.

Fm$\bar{3}$m ($a^0a^0a^0$) *I4/m* ($a^0a^0c^-$) *I2/m* ($a^0b^-b^-$)
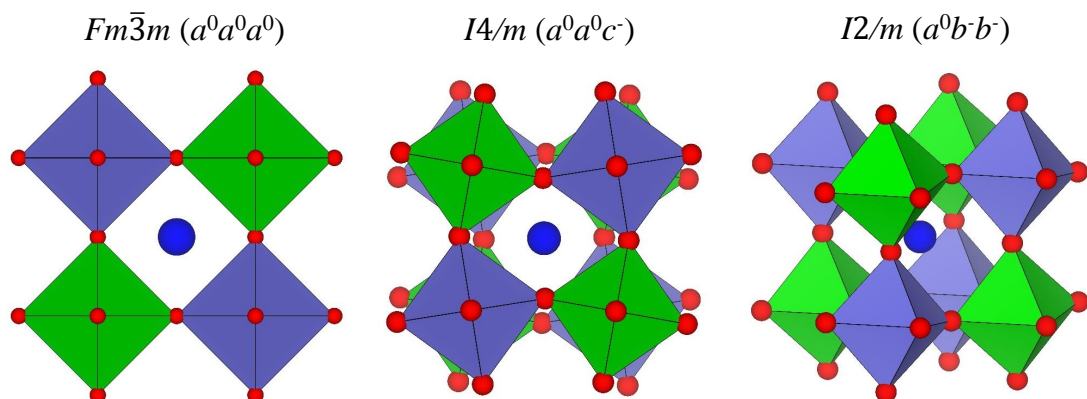
Figure 7.4: Illustration of $A_2MM'O_6$ rock salt M-site ordered double perovskite structure looking down the c-axis of $a^0a^0a^0$ (*Fm$\bar{3}$m*), $a^0a^0c^-$ (*I4/m*), and a-b plane of $a^0b^-b^-$ (*I2/m*) tilt systems. Here, A-site cations are represented as blue spheres and M/M' cations reside separately within the green and purple polyhedral sites.

common knowledge of M-site ordering influenced by corresponding size and charge difference [178–181, 184, 202, 203]. Metal 1:1 rock salt M-site ordering is shown by the presence of the (111), (311), and (331) peaks at 18.5^0, 35.5^0, and 47.5^0 2θ respectively (Figure 7.2). With increasing La^{3+} content, XRD peak shapes and positions within 70 - 110^0 2θ prove difficult to refine with $Fm\bar{3}m$ and suggest lower-symmetry structures. By substituting Ba^{2+} with the smaller radii of La^{3+} (1.61 Å versus 1.36 Å, respectively) [200, 201], octahedral tilting to accommodate the smaller A-site cation is conceivable, hence lower-symmetry structures will result. Several previous analyses report the space-group symmetries that result from the combination of octahedral tilting and octahedral-site cation ordering [204–206]. Neutron diffraction is ideal to establish this condition as oxygen has a coherent

neutron scattering length comparable to heavier atoms [207]. In addition, the neutron scattering lengths of Ba, La, Y, and Ir are each distinctive [207].

Additional reflections representing monoclinic doublets such as (110) and (002) are not present, eliminating 3-tilt distorted space-group symmetries [180, 205, 206]. Space-group symmetries associated to Glaser 1- and 2-tilt systems for 1:1 rock salt ordered double perovskites were therefore investigated [204–206]. For nominal composition $Ba_{1.4}La_{0.6}YIrO_6$, space-group symmetry was refined to be $I2/m$. Resulting TOF Neutron refinements are shown in Figure 7.5. Refined cell parameters and atomic information are presented in Tables 7.1 and 7.2.

The resulting refined compositions are $Ba_2Y_{0.955(8)}IrO_{5.964(2)}$ and $Ba_{1.442(4)}La_{0.558(4)}$ $Y_{0.953(2)}IrO_{5.952(8)}$. Occupancy refinements indicate that the iridium sites are fully occupied. For Ba_2YIrO_6, barium site occupancy was refined to be 1. The lanthanum content was refined to be slightly less than the expected x=0.6. This is consistent with the small presence of La_2O_3 impurity. A small presence of yttrium and oxygen vacancies exist for both systems. Attempts of refining iridium in the yttrium site proved unsuccessful as iridium occupancy was refined to 0. Though 1:1 stoichiometric amounts of Y:Ir were used in the synthesis, the refined yttrium occupancy is considered reasonable as a small presence of Y_2O_3 impurity is formed during the synthesis. Small presence of oxygen vacancies are common with perovskite systems. The A-site, Y, and Ir thermal parameters, U, are considered reasonable and consistent between both samples. A-site U are larger than Y/Ir U, consistent with similar systems [178–180, 184]. A larger cation residing in a 12-coordinated environment is expected to possess a larger U. For $Fm\bar{3}m$ sam-
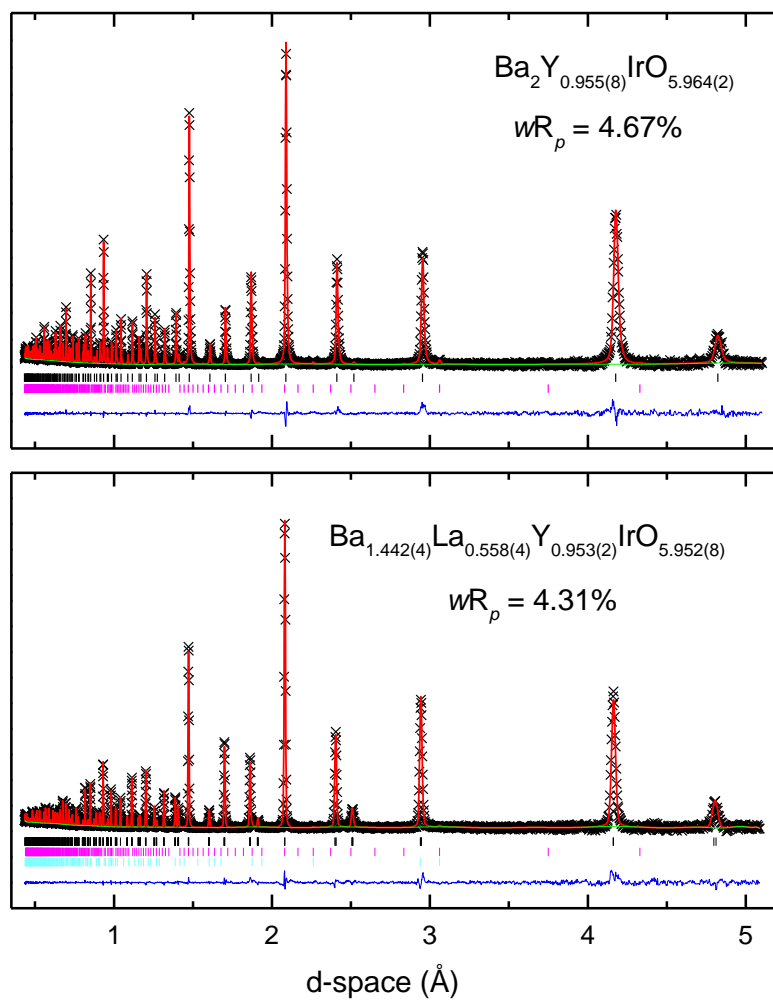
Figure 7.5: TOF Neutron refinement of nominal compositions Ba_2YIrO_6 (top) and $Ba_{1.4}La_{0.6}YIrO_6$ (bottom). Observed (black crosses) and calculated (solid red line) profiles, background (green), and difference curve (I_{obs}-I_{calc}) (blue) are shown for each refinement. The vertical bars indicate the expected reflection positions with black, pink, and teal representing $Ba_{2-x}La_xYIrO_6$, Y_2O_3 ($Ia\bar{3}$), and La_2O_3 ($P3\bar{m}1$) phases respectively. Resulting stoichiometric identities and wR_p are represented.

Table 7.1: Rietveld refinement results of TOF Neutron diffraction data for nominal compositions Ba_2YIrO_6 and $Ba_{1.4}La_{0.6}YIrO_6^{a-c}$.

Composition	$Ba_2Y_{0.955(8)}IrO_{5.964(2)}$	$Ba_{1.442(4)}La_{0.558(4)}Y_{0.953(2)}IrO_{5.952(8)}$
space group	$Fm\bar{3}m$	$I2/m$
R_{wp} (%)	4.67	4.31
a (Å)	8.35293(2)	5.88434(2)
b (Å)	-	5.89065(2)
c (Å)	-	8.32105(3)
β (deg)	-	90.1738(2)
V (Å^3)	582.795(2)	288.426(3)
A x	-	0.4966(9)
A z	-	0.2578(6)
Ba $occ.$	1	0.721(2)
La $occ.$	-	0.279(2)
A U_{iso} (Å^2)	0.00422(2)	0.00638(3)
Y U_{iso} (Å^2)	0.00117(2)	0.0014(5)
Ir U_{iso} (Å^2)	0.00118(2)	0.00175(3)
Y $occ.$	0.955(8)	0.953(2)
O1 x	0.26164(5)	-0.0264(2)
O1 y	-	0
O1 z	-	0.2606(6)
O1 $occ.$	0.994(4)	1
U_{11} (O1) (Å^2)	0.00229(2)	0.0287(3)
U_{22} (O1) (Å^2)	0.00802(1)	0.0193(2)
U_{33} (O1) (Å^2)	0.00802(1)	0.00654(2)
O2 x	-	0.2544(8)
O2 y	-	0.2676(6)
O2 z	-	0.0243(4)
O2 $occ.$	-	0.988(2)
U_{11} (O2) (Å^2)	-	0.0221(2)
U_{22} (O2) (Å^2)	-	0.0127(1)
U_{33} (O2) (Å^2)	-	0.00283(2)

a) TOF Neutron diffraction data collected at POWGEN BL-11A (room temperature).

b) For $Fm\bar{3}m$, crystal structure refined in space group with A(Ba) at $8c$ (1/4,1/4,1/4),Y at $4a$ (0,0,0),Ir at $4b$ (1/2,1/2,1/2), and O1 at $24e$ (x,0,0) sites, respectively.

c) For $I2/m$, crystal structure refined in space group with A(Ba/La) at $4i$ (x,0,z), Y at $2a$ (0,0,0), Ir at $2d$ (0,0,1/2), O1 at $4i$ (x,0,z), and O2 at $8j$ (x,y,z) sites, respectively.

Table 7.2: Resulting BVS, bond distances and respective angles from refined TOF Neutron diffraction data for nominal compositions Ba_2YIrO_6 and $Ba_{1.4}La_{0.6}YIrO_6^{a-c}$.

Composition	$Ba_2Y_{0.955(8)}IrO_{5.964(2)}$	$Ba_{1.442(4)}La_{0.558(4)}Y_{0.953(2)}IrO_{5.952(8)}$
A BVS	1.95	2.01
Y BVS	3.39	3.69
Ir BVS	5.18	4.53
O1 BVS	2.01	1.86
O2 BVS	-	2.00
Y-O1 (Å)	2.2102(4)	2.174(6)
Y-O2 (Å)	-	2.183(4)
Ir-O1 (Å)	1.9662(4)	1.998(5)
Ir-O2 (Å)	-	2.001(4)
$A_{avg.}$ (Å)	2.9557(2)	2.947(5)
Y-O1-Ir (deg)	180	171.4(4)
Y-O2-Ir (deg)	180	168.48(4)

a) TOF Neutron diffraction data collected at POWGEN BL-11A (room temperature).

b) For $Fm\bar{3}m$, crystal structure refined in space group with A(Ba) at $8c$ (1/4,1/4,1/4),Y at $4a$ (0,0,0),Ir at $4b$ (1/2,1/2,1/2), and O1 at $24e$ (x,0,0) sites, respectively.

c) For $I2/m$, crystal structure refined in space group with A(Ba/La) at $4i$ (x,0,z), Y at $2a$ (0,0,0), Ir at $2d$ (0,0,1/2), O1 at $4i$ (x,0,z), and O2 at $8j$ (x,y,z) sites, respectively.

ple, oxygen thermal parameters show disk-like ellipsoids, analogous to other corner shared octahedral systems. Oxygen U are slightly larger and more oval for $I2/m$ sample, congruent with Glaser 2-tilt systems to accommodate the smaller A-site cation. For $I2/m$ sample, the [001] octahedral tilt angles for yttrium and iridium are approximately 4.3^0, consistent with other reported $I2/m$ double perovskite systems [178–180, 184]. When comparing the average A-O bond distance, a slight reduction is observed with the incorporation of La^{3+} (Table 7.2). A portion of the $Ba_2Y_{0.955(8)}IrO_{5.964(2)}$ ($Fm\bar{3}m$) and $Ba_{1.442(4)}La_{0.558(4)}Y_{0.953(2)}IrO_{5.952(8)}$ ($I2/m$) unit cells from TOF neutron refinements are illustrated in Figure 7.6. Bond valence sums (BVS) were calculated and are reported in Table 7.2. Oxygen BVS are all close to 2. For the mixed A-(Ba^{2+}/La^{3+}) and mixed iridium charge (Ir^{5+}/Ir^{4+}) sites, BVS were calculated using the weighted average of the corresponding bond valance parameters. Such BVS values are analogous to what would be expected for iridium and A-site oxidation states based on refined composition. The yttrium cation, however, is observed to be over-bonded with BVS=3.39 for x=0 and BVS=3.69 for x=0.56 (Table 7.2). Attempts of fixing the yttrium occupancy to 1 makes an insignificant difference to the Y-O bond distances, and an overall increase in wR_p of the refinement is observed. Other known work on Ba_2YIrO_6 also reveal yttrium being over-bonded with similar reported BVS [184]. For a cubic double perovskite system, if the tolerance factor (τ) is equal to 1.0, the A-O and B-O bonds can adopt their ideal lengths in the cubic structure [178,208,209]. When $\tau <$ 1, the perovskite structure can compensate for the cation size mismatch by tilting the MO_6 octahedra and/or by distorting the ideal bond lengths [178,208,210,211].

Both tilting and bond length alteration can take place simultaneously to alleviate strain induced by cation size mismatch [178, 208]. If τ is only marginally less than 1 (τ=0.98 for Ba_2YIrO_6), small structural strain tends to be relieved by a change of bond lengths, instead of octahedral tilting [178, 208]. Comparable observations have been reported in other similar perovskite systems [184, 208, 210–215].

7.4.2   Transport and Magnetic Properties

Temperature dependent resistivity and Seebeck measurements from 300–600 Kelvin for $0 \leq x \leq 0.6$ samples are shown in Figure 7.7. Low temperature $\rho(T)$ data from 75-300 Kelvin are shown in Figure 7.8. All samples are semiconducting. The reported electrical properties are consistent with previous reports [194].

With increasing La^{3+} content, the conductivity of the material increases and becomes n-type. The development of $Ir^{4+/5+}$ sites with increasing La^{3+} content is projected to decrease the Hubbard U energy, thus empowering electron hopping. Low temperature transport measurements were analyzed using the general formula for variable range hopping (VRH) $\rho=\rho_0\exp((T_0/T)^{(1/(d+1))})$ where d is the dimensionality, and ρ_0 and T_0 are fitting parameters. The χ^2 of the fits for all compounds were minimized at $d = 3$. The differential activation energy was determined by differentiating $\ln(\rho)$ with respect to $(k_BT)^{-1}$ (Figure 7.8). An increase in the activation energy is observed with increasing temperature due to decreased hopping distance and increased energy difference between sites. With increasing La^{3+} content, the activation energy does decrease overall with the largest reduc-
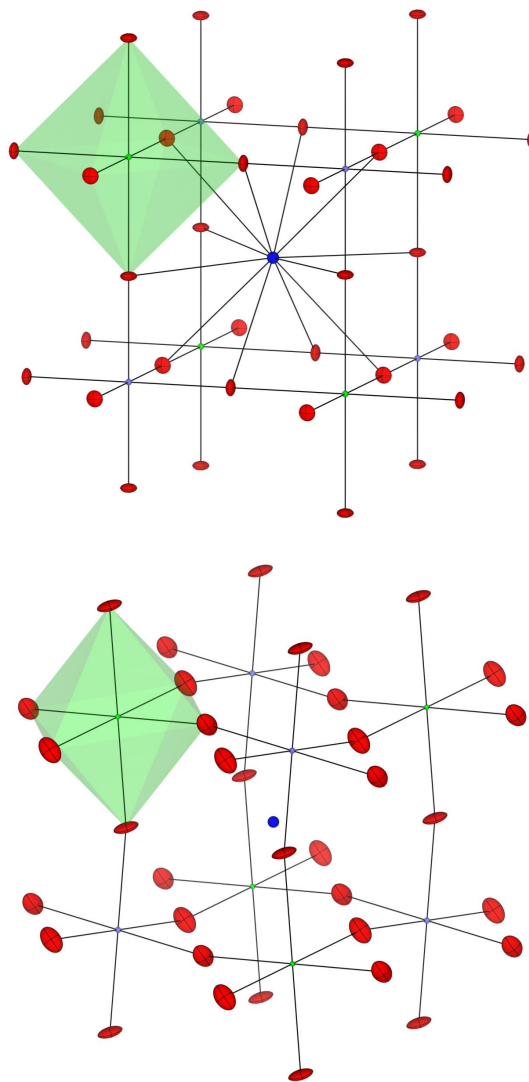
Figure 7.6: A portion of the $Ba_2Y_{0.955(8)}IrO_{5.964(2)}$ $(Fm\bar{3}m)$ and $Ba_{1.442(4)}La_{0.558(4)}Y_{0.953(2)}IrO_{5.952(8)}$ $(I2/m)$ unit cells from TOF neutron refinements with barium-lanthanum, yttrium, iridium, and oxygen thermal ellipsoids represented as blue, green, purple, and red respectively.
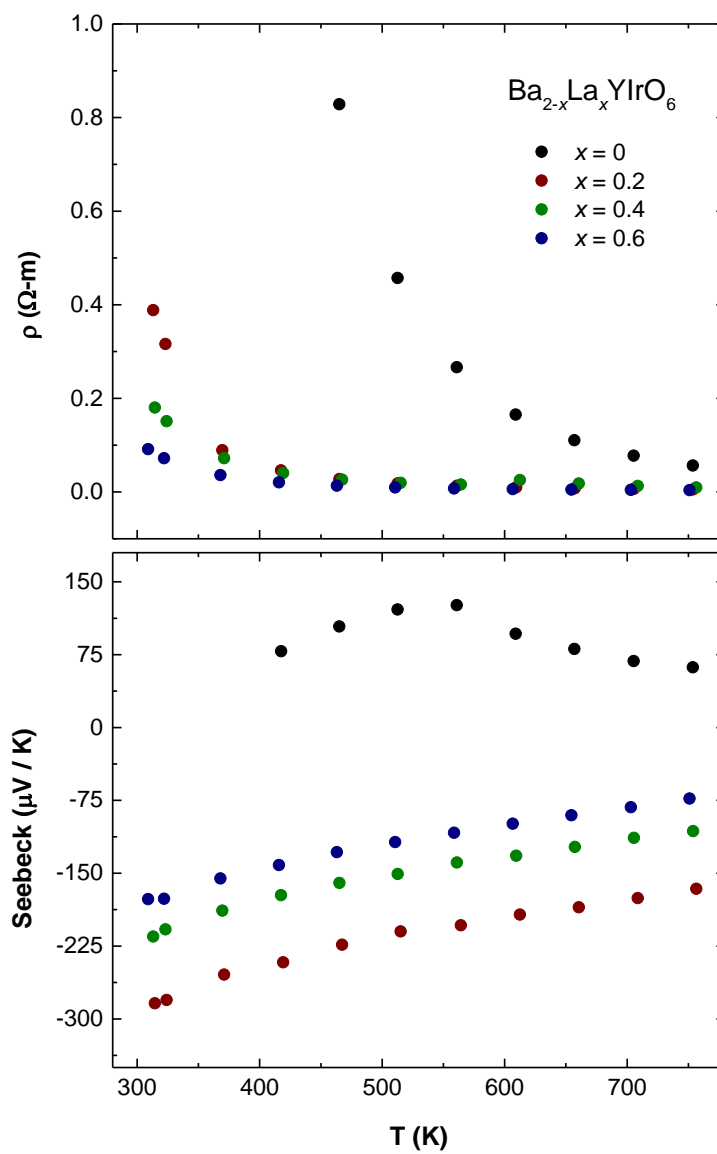
Figure 7.7: Temperature dependent resistivity (top) and Seebeck coefficient data (bottom) of $Ba_{2-x}La_xYIrO_6$ samples ($0 \leq x \leq 0.6$) from 300 to 600 K.
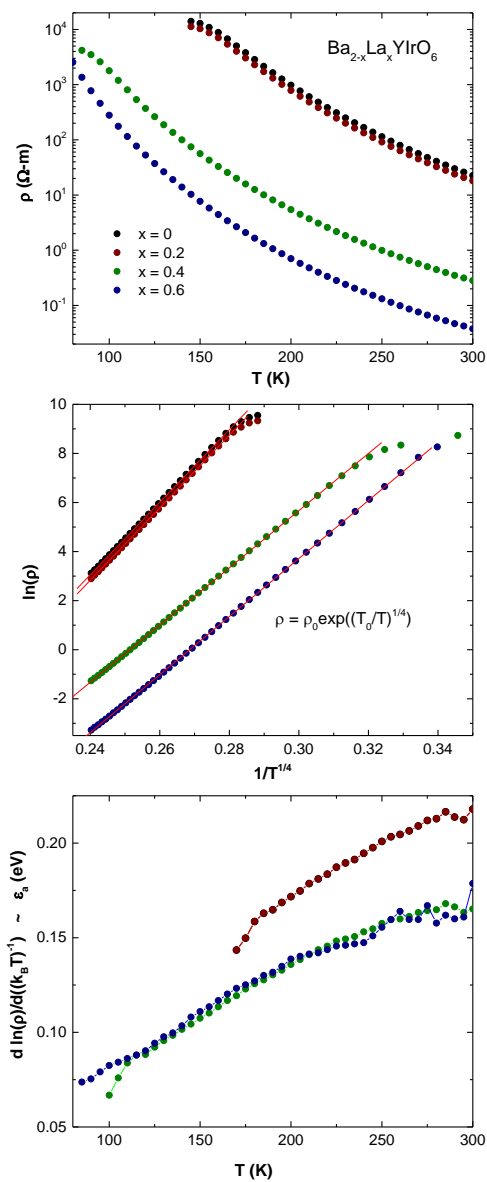
Figure 7.8: Temperature dependent, low temperature resistivity plots (top/middle) for $Ba_{2-x}La_xYIrO_6$ samples ($0 \leq x \leq 0.6$) and the differential activation energy determined by differentiating $\ln(\rho)$ with respect to $(k_BT)^{-1}$ (bottom) from 75 to 300 K.

tion going from $x=0.2$ to $x=0.4$. The magnetic susceptibility χ (H = 0.5 T) was measured for $0 \leq x \leq 0.8$ samples and shows the combined effects of a Curie-Weiss effective moment (μ_{eff}) presumably originating from Ir^{4+} and a van Vleck temperature independent paramagnetism (χ_{VV}), which is known for Ir^{5+}. In Figure 7.9 are shown the data with χ_{VV} subtracted, and then multiplied by T, along with fits to a Curie-Weiss form. For $x=0$ and 0.6 nominal samples, a small bump exists in the magnetic susceptibility at 55 K. A small presence of a second phase, undetectable with XRD, is likely the cause. The 5M BaIrO$_3$ phase is known to have a ferromagnetic transition at $\sim$55 K [216].

The value of χ_{VV} used for each x is that which, after subtraction from χ(T), produces the best fit to a Curie-Weiss form, yielding μ_{eff} values of 0.304, 0.577, 0.883, 1.001, and 1.071 μ_B for $x = 0$, 0.2, 0.4, 0.6, and 0.8 respectively. We test the assumption that x tunes between 100% d^4 for x $= 0$ to 80% d^5 for $x = 0.8$ in Figure 7.10. Here we plot the fraction of Ir^{4+} moments that would give rise to the μ_{eff} values, assuming a moment of 1.73 μ_B for each Ir^{4+}. Also plotted is the obtained χ_{VV}(x) divided by the $x = 0$ value which, for a simple mixed valence situation, would range from 1.0 for $x = 0$ to 0.2 for $x = 0.8$. Clearly, we see deviations from this mixed valence picture, not only for $x = 0.2$, but also on approaching $x = 0.8$. The $x = 0$ sum is 1 by construction. For $x = 0.2$, χ_{VV} is larger than found for $x = 0$. For $x = 0$, χ_{VV} is expected to be the largest as this compound is nominally all Ir^{5+}. The presence of oxygen vacancies might account for the deviations in the mixed valence picture. Because the neutron scattering length for oxygen is comparable to most metals [207], oxygen occupancy refinement is
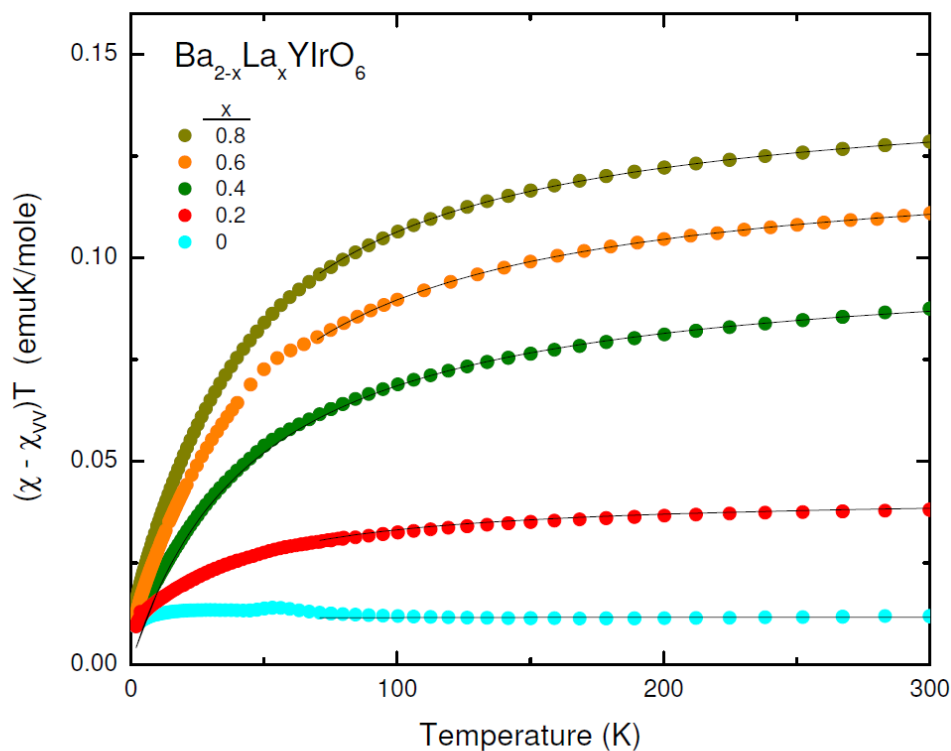
Figure 7.9: Magnetic susceptibility χ (H = 0.5 T) measured for $0 \leq x \leq 0.8$ samples are shown with χ_{VV} subtracted, and then multiplied by T, along with fits to a Curie-Weiss form.

accurate with neutron refinements. Our reported neutron refinements reveal an oxygen occupancy of 0.994(4) and 0.988(2) for $x=0$ and $x=0.6$ nominal samples, respectively (Table 7.1). Such a small presence of vacancies clearly cannot explain such deviations in the mixed valence picture. Because all samples were synthesized under the same condition, it is unlikely $x=0.2$ and 0.4 nominal samples possess

a greater presence of oxygen vacancies and therefore likely does not elucidate the mixed valence picture. Work by Kataev et al reveal a few percent of Ir^{6+} magnetic defects in Ba_2YIrO_6, determined by ESR spectroscopy [186]. Deviation from the expected simple $Ir^{4+/5+}$ mixed valence state might exist for $x > 0$ samples due to the presence of Ir^{6+} magnetic defects. Thus, studies with ESR spectroscopy might be able to clarify the observed mixed valence picture.

7.5   Summary

The motivation to study $Ba_{2-x}La_xYIrO_6$ was to elucidate the influence of noncubic symmetry on the electronic and magnetic properties of such iridate perovskites. With increasing La^{3+} content, the conductivity of the material increases and becomes n-type. The development of $Ir^{4+/5+}$ sites with increasing La^{3+} content is projected to decrease the Hubbard U energy, thus empowering electron hopping. As shown by the structural refinements presented, $a^0a^0a^0$ ($Fm\bar{3}m$) $\rightarrow a^0b^-b^-$ ($I2/m$) octahedral distortion of the YO_6-IrO_6 rock-salt framework occurs with increasing x to account for the incorporation of smaller La^{3+} radii. From the magnetic susceptibility measurements, deviations from the proposed mixed valence picture are observed, not only for $x = 0.2$, but also on approaching $x = 0.8$. For $x = 0.2$, χ_{VV} is larger than found for $x = 0$.
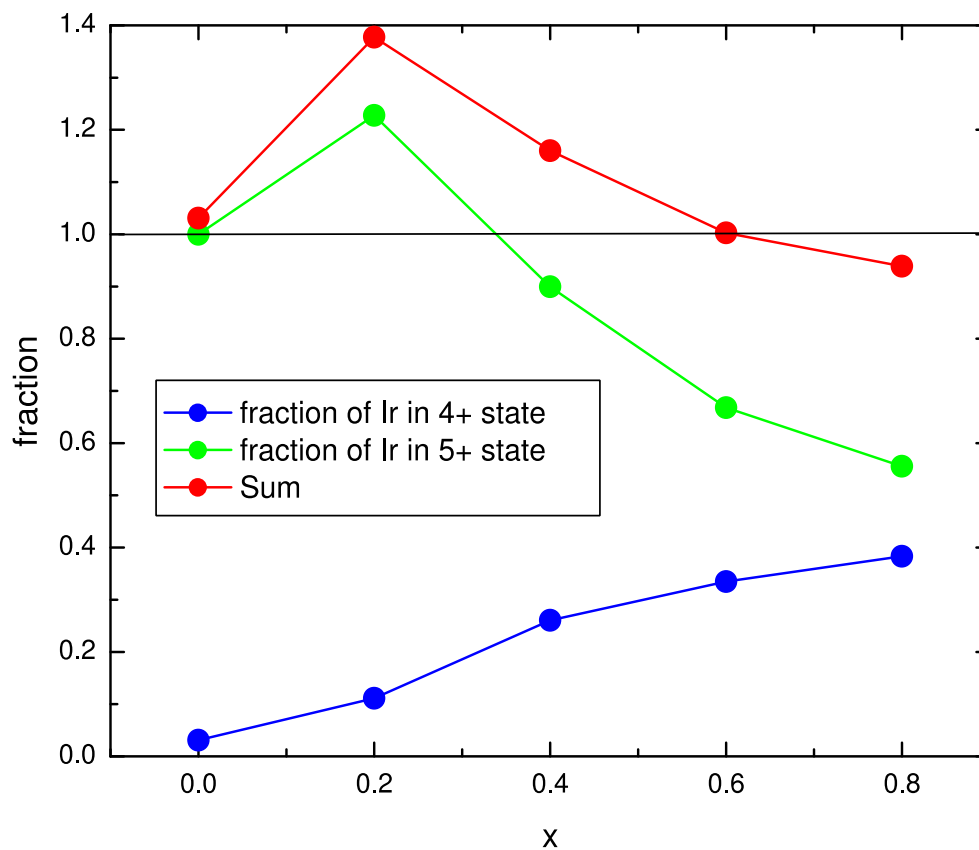
Figure 7.10: Blue symbols – Variation of the inferred density of $s = \frac{1}{2}$ spins expressed as a fraction of the total Ir concentration versus x in $Ba_{2-x}La_xYIrO_6$. Green symbols – Variation of Van Vleck temperature independent susceptibility expressed as a fraction of the value obtained at $x = 0$ versus x. Red symbols – the sum of the $s = \frac{1}{2}$ fraction and van Vleck spin fraction versus x.

Chapter 8: Structural and Electronic Properties of Cu[Ir$_{1.5}$Cu$_{0.5}$]O$_4$ Spinel

8.1 Abstract

Frustrated systems populated with large spin-orbit coupled (SOC) ions are an ideal setting for the exploration of exotic states. Among the known frustrated frameworks, the spinel structure has been extensively investigated. Though many spinel systems with $3d/4d$ elements exist, to our knowledge, an Iridium based spinel oxide has not been reported. Most spinel oxides are known to be insulating and only two, LiV$_2$O$_4$ and LiTi$_2$O$_4$, are reported as conducting. A frustrated mixed valence system that is metallic and exhibits large SOC is scarce, and if a metallic spinel is close to a correlation driven metal-insulator transition, a novel interplay between the charge carriers and the frustrated spin degree of freedom is anticipated. Here we present the first Iridate spinel: Cu[Ir$_{1.498(1)}$Cu$_{0.502(1)}$]O$_4$. Synchrotron XRD refinements reveal a face-centered cubic structure with space group $Fd\bar{3}m$. Electrical properties reveal a metallic state within 50~600 K range with a Kondo-effect at T<50 K.

 Publication based on this chapter:

1. M.K. Wallace, P.G. LaBarre, J. Telser, A.P. Ramirez, M.A. Subramanian, Structural and Electronic Properties of Cu[Ir$_{1.5}$Cu$_{0.5}$]O$_4$ Spinel, *in progress*, (2019).

8.2 Introduction

Frustrated systems populated with large spin-orbit coupled (SOC) ions are an ideal setting for the exploration of exotic states. Among the known frustrated frameworks, the spinel structure has been extensively investigated. The general formula for a spinel is $[A_{1-\gamma}M_\gamma]^{tet}[M_{2-\gamma}A_\gamma]^{oct}O_4$, where γ represents the fraction of M and A cations on the tetrahedral and octahedral sites, respectively. The M_2O_4 octahedral network forms a rock salt structure with alternate octahedral sites occupied by the M-cations. The A-cation occupies 1/8 of the tetrahedral sites with all four neighboring octahedral sites empty. One of the unique features of the spinel structure is that the M-cations form a sub-lattice of corner-shared tetrahedra and the A-cations form a diamond sublattice (Figure 8.1).

If the sublattice framework is populated with magnetic ions, strong magnetic frustration can occur. Though many spinel systems exist with $3d/4d$ elements, to our knowledge, an Iridium based spinel oxide has not been reported. The SOC for iridium is 540 meV [217]. A spinel framework populated by M-ions with SOC comparable to iridium is not known. The SOC of iridium is large enough to influence the electronic states. Iridates are the most widely studied with Iridium frequently in a 4+ oxidation ($5d^5$) state [218–220], resulting in a $s = \frac{1}{2}$ Kramers doublet. Various systems with such $5d^5$ ground states have been predicted to possess anisotropic exchange interactions, a key ingredient of the Kitaev model of quantum spin liquid [221]. Most spinel oxides are known to be insulating and only two spinel oxides, LiV_2O_4 and $LiTi_2O_4$, are reported as conducting [222]. A frus-
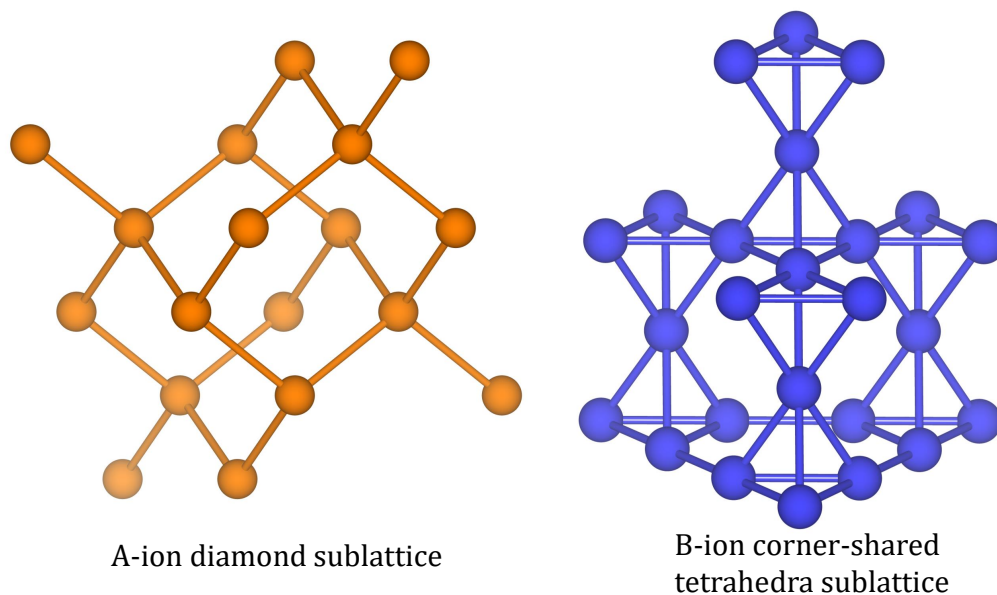
Figure 8.1: The A-ions form a diamond sublattice and the B-ions form a sublattice of corner-shared tetrahedra within the spinel structure.

trated mixed valence system that is metallic and exhibits large SOC is scarce, and if a metallic spinel is close to a correlation driven metal-insulator transition, a novel interplay between the charge carriers and the frustrated spin degree of freedom is anticipated. Here we present the first Iridate spinel: $Cu[Ir_{1.498(1)}Cu_{0.502(1)}]O_4$. Synchrotron XRD refinements reveal a face-centered cubic structure with space group $Fd\bar{3}m$. Electrical properties reveal a metallic state within 50~600 K range with a Kondo-effect at T<50 K.

8.3 Experimental

Polycrystalline $Cu[Ir_{1.498(1)}Cu_{0.502(1)}]O_4$ was prepared via the synthesis of the hyper-kagome structure $Na_4Ir_3O_8$ and then an ion-flux exchange approach using CuCl. The compounds Na_2CO_3 and IrO_2 with the correct stoichiometric ratio ($Na_4Ir_3O_8$) were ground and pressed into 10 mm diameter pellets. The resulting pellet was fired at 750 C for 16 hrs, ground, and then reheated to 1000 C for 18 hrs before being quenched using a water bath. The resulting hyper-kagome $Na_4Ir_3O_8$ sample was mixed with molar excess of CuCl and then fired at 450 C under an argon flow. The sample was then washed with a dilute nitric acid solution to remove remaining NaCl and excess CuCl and Cu metal. Phase analysis of powder samples was performed by X-ray diffraction using a Rigaku MiniFlex II diffractometer with Cu K_α radiation and a graphite monochromator for the diffracted beam. Synchrotron X-ray Diffraction (Advanced Photon Source 11-BM) was collected at room temperature (λ=0.412833 Å, $2\theta < 50$). The principal thermoelectric properties; the Seebeck coefficient (S), electrical conductivity (σ), and thermal conductivity (k) were measured from 300~600K. The Seebeck coefficient and electrical conductivity data was collected on an ULVAC ZEM-3 under a helium atmosphere. Low-temperature (5-300 K) magnetization measurements were obtained with a Quantum Design MPMS and resistivity (50-300 K) measurements were obtained using a Quantum Design PPMS.

8.4   Results

Powder X-ray diffraction pattern of $Cu[Ir_{1.498(1)}Cu_{0.502(1)}]O_4$ reveals face-centered cubic structure with space group $Fd\bar{3}m$ (Figure 8.2). Trace IrO_2 impurity phase was detected in the diffraction pattern upon magnification (Figure 8.2, asterisk symbol).
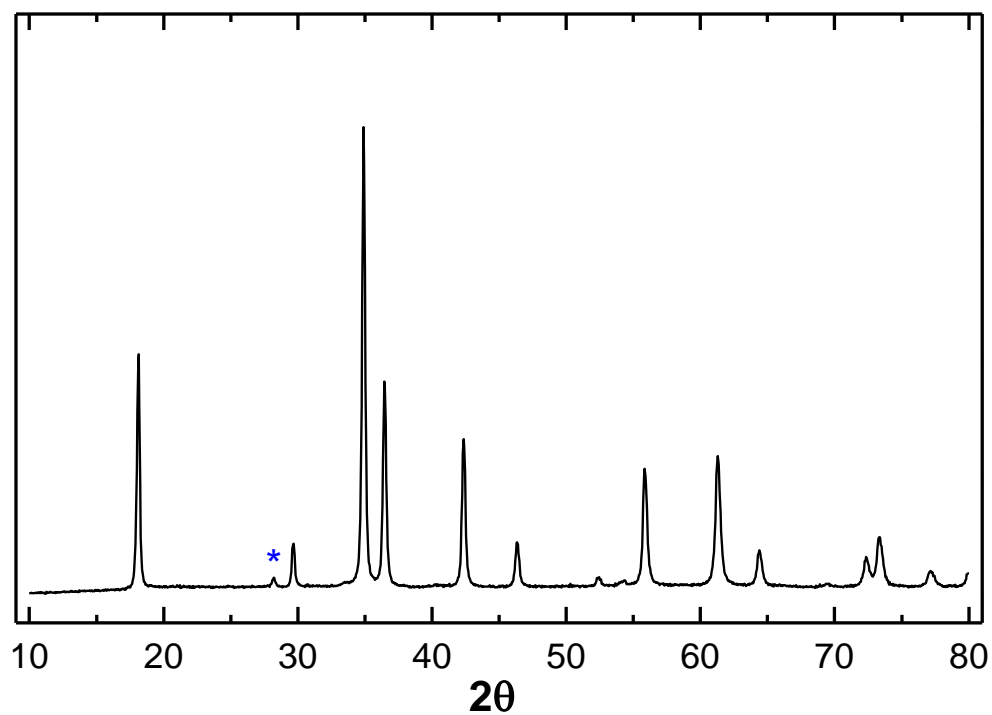
Figure 8.2: Powder XRD pattern of $Cu[Ir_{1.5}Cu_{0.5}]O_4$ sample. Blue asterisk symbol indicates a small presence of IrO_2 impurity phase.

To determine the crystal structure, Rietveld refinements were performed on

synchrotron XRD data collected at APS 11bm beamline (λ=0.412833 Å) using the GSAS program. Room temperature synchrotron XRD was collected up to 50 2θ. A pseudo-Voigt peak shape profile was chosen, and parameters refined to obtain the best fit to the collected data. The space group was refined to be $Fd\bar{3}m$. Trace IrO_2 impurity phase was detected in the diffraction pattern upon magnification. Resulting synchrotron XRD Rietveld refinement for $Cu[Ir_{1.498(1)}Cu_{0.502(1)}]O_4$ is shown in Figure 8.3.
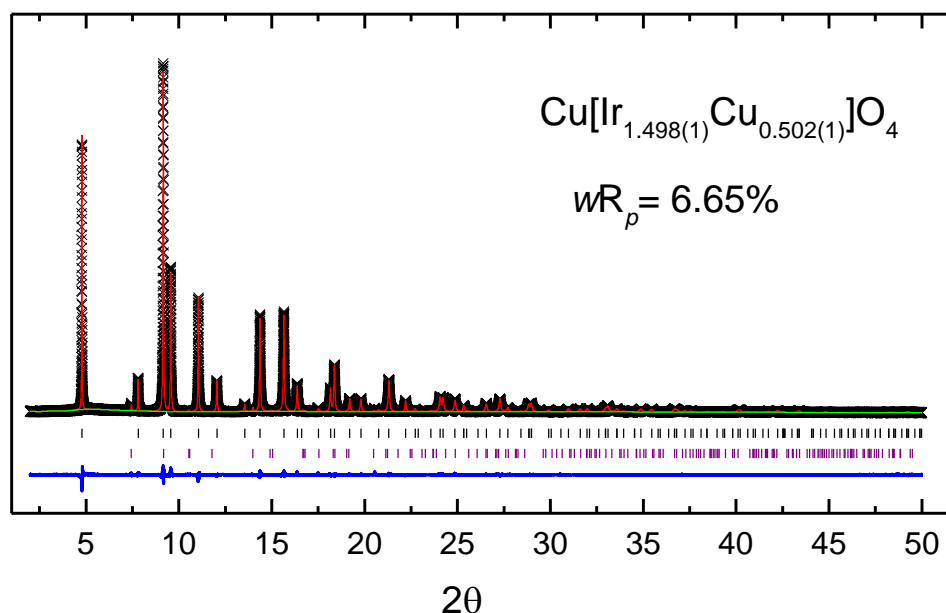
Figure 8.3: Synchrotron Rietveld refinement of $Cu[Ir_{1.5}Cu_{0.5}]O_4$ sample at room temperature (λ=0.412833 Å). Observed (black crosses) and calculated (solid red line) profiles, background (green), and difference curve (I_{obs} - I_{calc}) (blue) are shown. The vertical bars indicate the expected reflection positions for spinel ($Fd\bar{3}m$) phase (black) and IrO_2 impurity phase (purple). Resulting stoichiometric identity and wR_p are represented.

The detailed results are given in Table 8.1. Refined lattice parameters are in

accordance of $CuRh_2O_4$ normal spinel ($Fd\bar{3}m$) [223].

From the refined parameters provided in Table 8.1, the tetrahedral $8a$ site was refined to be occupied by copper with an occupancy of 1. Iridium is too large for a tetrahedral site and any addition of Iridium in the $8a$ site proved not stable in the refinement. Refinement of sodium in the tetrahedral $8a$ site or neighboring empty $16c$ octahedral sites also were not stable with the occupancy refining to zero. Incorporation of copper on the octahedral $16d$ site did result in an overall more stable refinement. The resulting $16d$ refined occupancies reveal 75% of the respective site occupied by iridium with the remaining 25% occupied by copper. The $A_4M_3O_8$ hyper-kagome edge shared octahedral framework is analogous to the spinel framework, except 1/4 of the edge shared octahedral sites are occupied by the A-cation (compared to all 1/2 of the octahedral sites occupied by M in the normal AM_2O_4 spinel structure). In addition, molar excess CuCl was used in the ion-exchange process. Thus, Na-Cu exchange resulting in 25% of the $16d$ site occupied by copper is considered logical. Refinements were performed with Na^+ occupying the $16d$ site, however, such refinements were proven to not be stable. If we assume Cu residing on the tetrahedral $8a$ site has an oxidation state of 1+ (d^{10}) and Cu occupying the octahedral $16d$ site has an oxidation state of 2+ (d^9), the overall charge of the refined stoichiometric identity (assuming Ir^{4+}) equates to zero. Any alternate combinations of $Cu^{1+/2+}$ in the tetrahedral/octahedral sites results in the overall charge of the refined stoichiometric identity not equating to zero (assuming Ir^{4+}). In addition, calculated BVS match best with the expected oxidation states if Cu^+ is assumed for the tetrahedral $8a$ site and Cu^{2+} for the

Table 8.1: Rietveld refinement results of synchrotron XRD diffraction data for $Cu[Ir_{1.498(1)}Cu_{0.502(1)}]O_4^{a,b}$.

Composition	$Cu[Ir_{1.498(1)}Cu_{0.502(1)}]O_4$
Space group	$Fd\bar{3}m$
wR_p (%)	6.65
$a=b=c$ (Å)	8.57619(1)
vol (Å^3)	630.788(1)
O x, y, z	0.26068(9)
Cu($8a$) occ.	1.003(2)
Ir($16d$) occ.	0.7490(2)
Cu($16d$) occ.	0.2510(2)
Cu($8a$) U_{iso}	0.01636(2)
Cu/Ir($16d$) U_{iso}	0.009581(3)
O U_{iso}	0.02051(2)
Cu$^+$($8a$) BVS	1.04
Ir^{4+}/Cu^{2+}($16d$) BVS	3.40
O BVS	1.95
Cu(tet.)-O (Å)	2.0155(1)
Cu/Ir(oct.)-O (Å)	2.0565(7)
O-Cu(tet.)-O (^{o})	109.47120(1)
O-Cu/Ir(oct.)-O (^{o})	95.22(4) / 84.78(4)

a) Synchrotron XRD diffraction data collected at APS 11-BM (room temperature).

b) For $Fd\bar{3}m$, AM$_2$O$_4$ crystal structure refined in space group with A(Cu) at $8a$ (1/8,1/8,1/8), M(Cu/Ir) at $16d$ (1/2,1/2,1/2), and O at $32e$ (x,x,x) sites.

octahedral 16d site (Table 8.1 and Table 8.2).

Based on the crystal field stabilization energy (CFSE), Cu^+ (d^{10}) has no preference for tetrahedral or octahedral sites and because of the relatively small ionic size, tetrahedral site would be preferred. From CFSE, the Jahn-teller active Cu^{2+} (d^9) would prefer an octahedral site and would also suggest a non-cubic system. Lower symmetry space groups, such as $I41/amd$ were investigated to account for the possible Jahn-teller distortion of Cu^{2+} on the octahedral 16d site. Such lower symmetry space groups require additional hkl peaks which were not present in the synchrotron XRD data, suggesting the higher symmetry $Fd\bar{3}m$ which account for all peaks. Because 75% of the octahedral 16d site is occupied by Ir^{4+}, which is not considered Jahn-teller active, cubic $Fd\bar{3}m$ is considered reasonable.

Temperature dependent resistivity and Seebeck measurements from 300–600 Kelvin for the $Cu[Ir_{1.498(1)}Cu_{0.502(1)}]O_4$ sample are shown in Figure 8.4. Low temperature $\rho(T)$ data from 5-300 Kelvin are shown in Figure 8.5. Electrical properties reveal a metallic state within 50~600 K range with a Kondo-effect at T<50 K.

8.5   Summary

If a metallic spinel is close to a correlation driven metal-insulator transition, a novel interplay between the charge carriers and the frustrated spin degree of freedom is anticipated. Synchrotron XRD refinements reveal a face-centered cubic structure with space group $Fd\bar{3}m$. Electrical properties reveal a metallic state within 50~600 K range with a Kondo-effect at T<50 K.

Table 8.2: A list of calculated bond valence sums (BVS) for each element in $Cu[Ir_{1.498(1)}Cu_{0.502(1)}]O_4$ based on the assigned oxidation state of copper. The overall charge of the refined stoichiometric identity is calculated based on the assigned oxidation states of Cu and Ir. The Resulting BVS are compared to the expected oxidation state (Exp. ox.) and the difference between BVS and Exp. ox. is calculated (Δ)

	BVS	Exp. ox.	Δ
Cu^{1+} (tet.)	1.04	1	0.04
Ir^{4+}/Cu^{2+} (oct.)	3.396	3.498	0.102
O (tet.)	1.95	2	0.05
	overall charge $= + 0.004$		

	BVS	Exp. ox.	Δ
Cu^{1+} (tet.)	1.12	1	0.12
Ir^{4+}/Cu^{1+} (oct.)	3.066	3.247	0.181
O (tet.)	1.784	2	0.216
	overall charge $= +0.506$		

	BVS	Exp. ox.	Δ
Cu^{2+} (tet.)	1.51	2	0.49
Ir^{4+}/Cu^{2+} (oct.)	3.396	3.498	0.102
O (tet.)	2.08	2	0.08
	overall charge $= - 0.996$		

	BVS	Exp. ox.	Δ
Cu^{2+} (tet.)	1.51	2	0.49
Ir^{4+}/Cu^{1+} (oct.)	3.066	3.247	0.181
O (tet.)	1.911	2	0.089
	overall charge $= 0.494$		
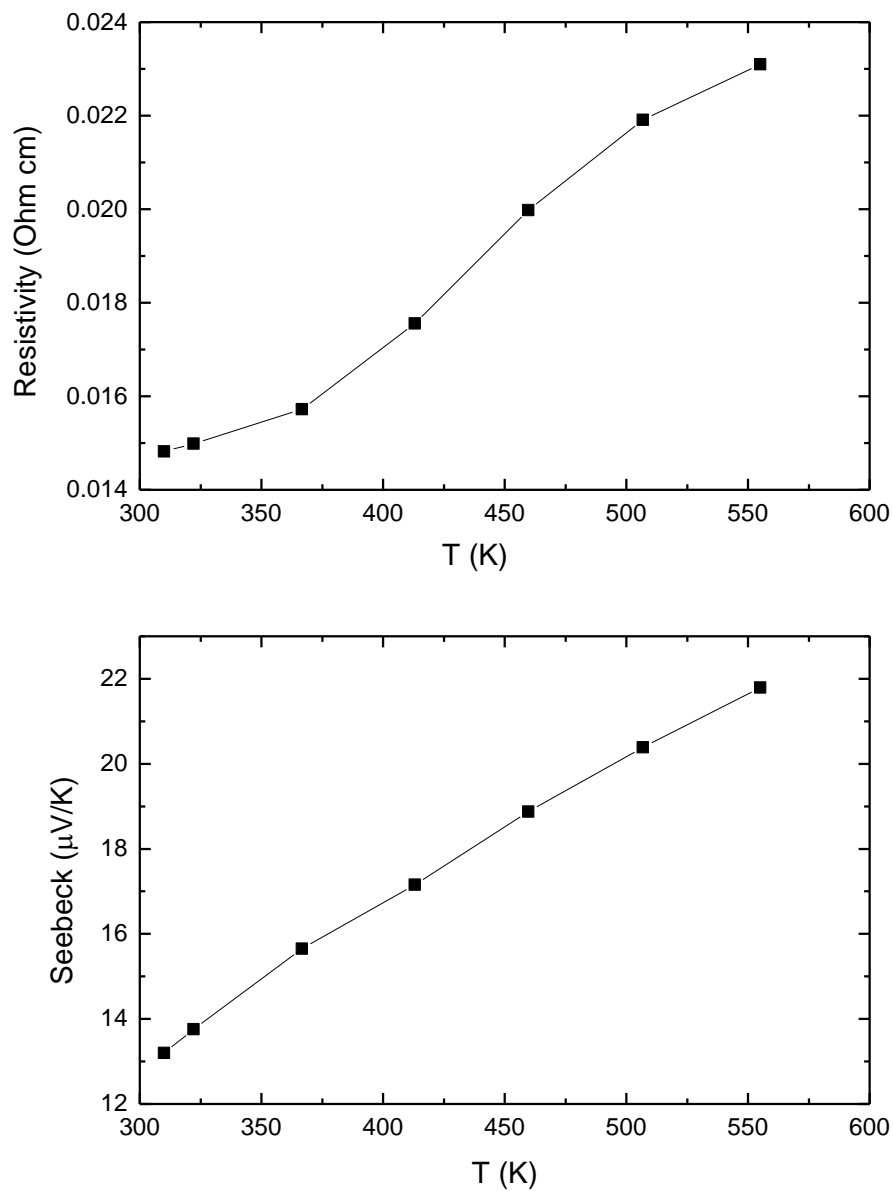
Figure 8.4: Temperature dependent resistivity (top) and Seebeck coefficient data (bottom) of $Cu[Ir_{1.498(1)}Cu_{0.502(1)}]O_4$ from 300 to 600 K.
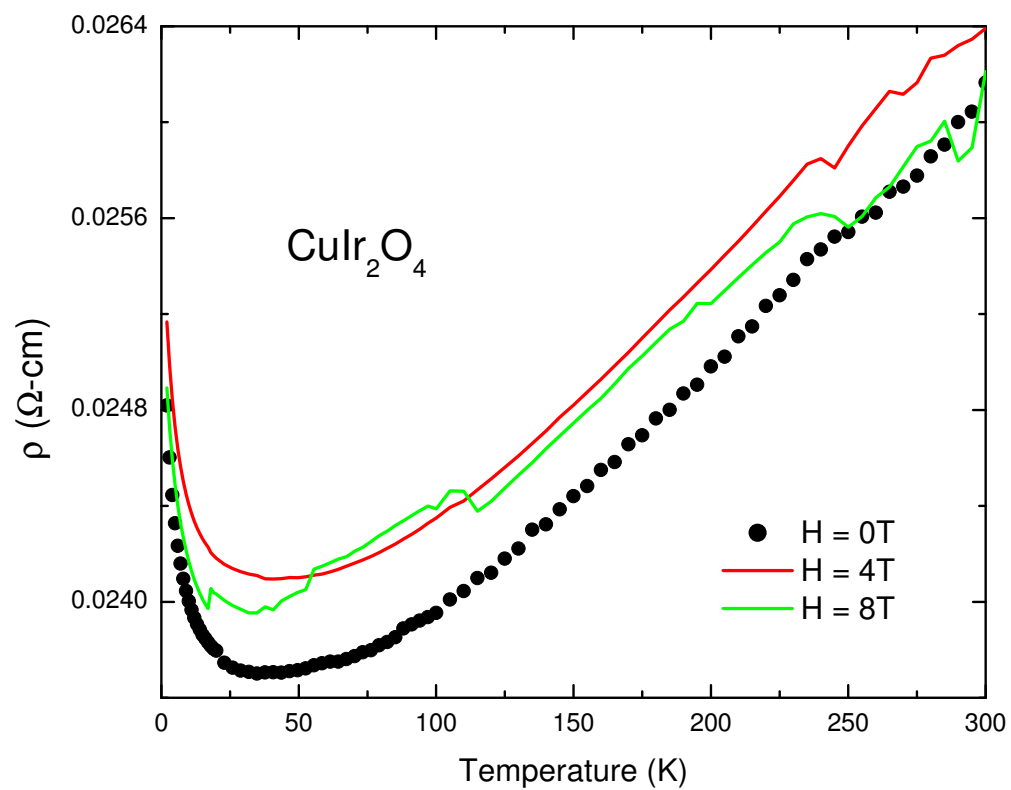
Figure 8.5: Temperature dependent low-temperature resistivity of $Cu[Ir_{1.498(1)}Cu_{0.502(1)}]O_4$ from 5 to 300 K.

Chapter 9: Structural, Electronic, and Thermal Properties of Indium-Filled $In_xIr_4Sb_{12}$ Skutterudites

9.1 Abstract

The "phonon-glass/electron-crystal" approach has been implemented through incorporation of "rattlers" into skutterudite void sites to increase phonon scattering and thus increase the thermoelectric efficiency. Indium filled $IrSb_3$ skutterudites are reported for the first time. Polycrystalline samples of $In_xIr_4Sb_{12}$ ($0 \leq x \leq 0.2$) were prepared by solid-state reaction under a gas mixture of 5% H_2 and 95% Ar. The solubility limit of $In_xIr_4Sb_{12}$ was found to be close to 0.18. Synchrotron X-ray diffraction refinements reveal all $In_xIr_4Sb_{12}$ phases crystallized in body-centered cubic structure (space group: $Im\bar{3}$) with 8% antimony site vacancy and with indium partially occupying the $16f$ site. Unlike known rattler filled skutterudites, under synthetic conditions employed, indium filling in $IrSb_3$ significantly increases the electrical resistivity and decreases the Seebeck coefficient (n-type) while reducing the thermal conductivity by 30%. The resultant power factor offsets the decrease in total thermal conductivity giving rise to a substantial decrease in ZT. Principal thermoelectric properties of $In_xM_4Sb_{12}$ (M = Co, Rh, Ir) phases are compared. As iridium is a $5d$ transition metal, zero field cooled (ZFC) magnetization were performed to unravel the effect of spin-orbit interaction on the electronic properties.

These results serve to advance the understanding of filled skutterudites, and provide additional insight on the less explored smaller "rattlers" and their influence on key thermoelectric properties.

Publication based on this chapter:

1. M.K. Wallace, J. Li, and M.A. Subramanian, Structural, electronic, and thermal properties of indium-filled $In_x Ir_4 Sb_{12}$ skutterudites, *Solid State Sciences*, 80:170-177, 2018.

9.2   Introduction

Because of the unique structure and recognized ability to tune key transport properties, skutterudites are known to be strong thermoelectric candidates. The skutterudites are one well known class of Zintl compounds. As shown in Figure 9.1, the skutterudite crystal structure can be described in two ways: (a) a repeated corner-sharing MX_6 arrangement with two M_4X_{12} formula units and two large empty cages per unit cell, or (b) an open cage like structure of cube-connecting M atoms with three fourths of the void sites filled with X_4 Zintl polyanions, where M is a transition metal atom (M = Fe, Co, Rh, or Ir) and X is a pnictogen atom (X = P, As or Sb). The general formula is MX_3 with cubic space group $Im\bar{3}$. The M cations occupy the $8c$ (1/4, 1/4, 1/4) site and the X anions occupy the $24g$ (0, y, z) site with $y \sim 0.15$ and $z \sim 0.34$.

The thermoelectric performance of a material is characterized by the thermoelectric figure of merit, $ZT = \frac{\sigma S^2 T}{K}$, where S is the Seebeck coefficient, σ is the electrical conductivity, T is the effective temperature, and K is the summation of the lattice and electronic components of the total thermal conductivity ($K_L + K_e$) (Chapter 3.3) [224–226]. An increase in thermoelectric performance corresponds to an increase in the ZT value. There are several approaches to optimize ZT such as nanostructuring techniques, alloying, and transition metal/pnictogen-site doping (Chapter 3.4) [225–229]. Another method to maximize ZT is by filling the unoccupied empty cages within M cube framework (Figure 9.1) with an ion. The empty cages can be filled by an ion A, leading to the formula $A_y M_4 X_{12}$ with y ≤
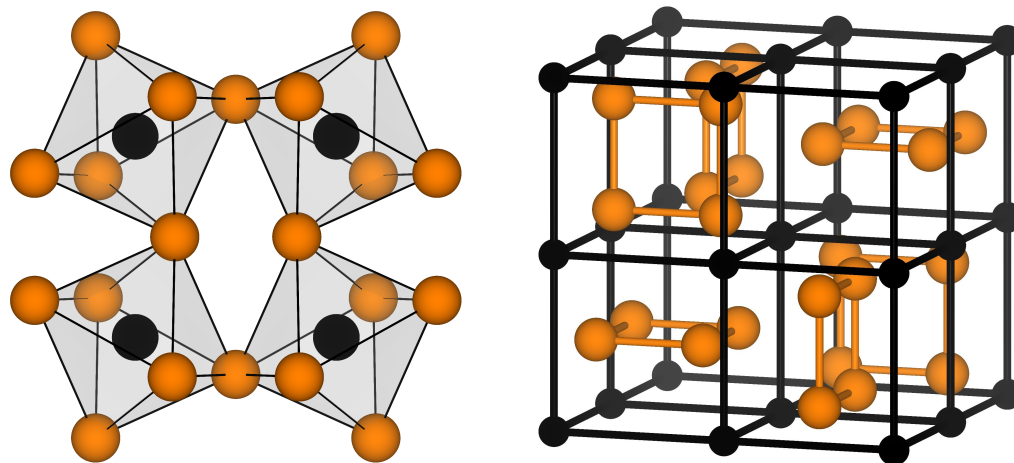
Figure 9.1: Skutterudite crystal structure shown as (a) a repeated corner-sharing MX_6 arrangement and (b) cube-forming M atoms with three fourths of the void sites filled with X_4 Zintl polyanions.

1. Because of the large size difference between the corresponding filler atom and void site, the filler atom can conceivably act as an independent oscillator and thus dampen the thermal phonon conductivity and decrease the total thermal conductivity (Chapter 3.4.1) [230–232]. Filling skuterudite voids can also influence the electrical conductivity, albeit the effect is usually negligible with respect to the decrease in total thermal conductivity [225, 230–232]. Though there is much work regarding the use of rare earth, alkali earth, or IVA group elements to fill the voids of various skuterudite structures, little work on indium filled skutterudites have been achieved [224–233]. The $IrSb_3$-based skutterudite compounds have shown potential for thermoelectric applications due to high Hall mobility [234–236]. Though many rare earth and alkali earth filled $IrSb_3$ have been reported, to our knowledge,

investigation of indium filled $In_xIr_4Sb_{12}$ has not been addressed. It is suggested a smaller filler atom can possess greater rattler displacement, and thus enhance dampening of the lattice thermal conductivity [237, 238]. This corresponding enhancement is observed for indium filled $In_xCo_4Sb_{12}$ showing an overall increase in ZT [232]. Yet for $In_xIr_4Sb_{12}$, with increasing indium content, the observed increase in electrical resistivity outweighs the decrease in total thermal conductivity, revealing a significant reduction in ZT. With the prospect of new science and technology of topological insulators (TI), systems with strong spin-orbit coupling (SOC) are of great interest within the solid state science community [239]. Strong SOC systems have shown to exhibit many unconventional properties that challenge existing theory. Heavy metal alloys are of interest to better understand TI behavior. Iridium has one of the strongest SOC among magnetic d-electron elements [240]. In addition, certain indium based metal alloys reveal promising SOC behavior, supporting TI behavior [241–243]. There has been much theoretical work on potential TI heavy metal based skutterudite candidates [244–246]. Yet, key physical properties that address the prospect of topologically insulating behavior for metal alloy systems are lacking. Principal thermoelectric properties, zero field cooled (ZFC) magnetization, and structure properties are presented for indium filled $In_xIr_4Sb_{12}$.

9.3 Results and Discussion

9.3.1 Structural Properties

Powder X-ray diffraction patterns reveal all $In_xIr_4Sb_{12}$ (x $\leq$ 0.2) in a body-centered cubic structure with space group $Im\bar{3}$ (Figure 9.2). For $In_xIr_4Sb_{12}$ samples where x > 0.1, trace InSb, $IrSb_2$ and Sb impurity phases were detected in the diffraction pattern upon magnification (Figure 9.2, asterisk symbol). As shown in Figure 9.3, lattice variation with indium filling fraction indicates a minor increase in the cell edge and an indium solubility limit of approximately x = 0.18, which was also observed for $In_xRh_4Sb_{12}$ and $In_xCo_4Sb_{12}$ [232, 237]. The obtained lattice parameters are in accordance with previous work on $IrSb_3$, $In_xRh_4Sb_{12}$ and $In_xCo_4Sb_{12}$ [232, 234, 235, 237].

To determine the crystal structure, Rietveld refinements were performed on synchrotron XRD data collected at APS 11bm beamline (λ = 0.412731 Å) using the GSAS program. Room temperature synchrotron XRD was collected up to 50º 2θ for x = 0, 0.1, and 0.15 and 70º 2θ for x = 0.1 nominal samples. Synchrotron XRD scans for x = 0 and 0.1 nominal samples show no presence of impurities (small existence of $IrSb_2$ and Sb phases in x = 0.15). A pseudo-Voigt peak shape profile was chosen and parameters refined to obtain the best fit to the collected data. For all systems, the space group was refined to be $Im\bar{3}$. Resulting synchrotron XRD Rietveld refinements for nominal compositions $IrSb_3$ and $In_{0.1}Ir_4Sb_{12}$ collected at room temperature and 100 K are shown in Figure 9.4. The detailed results are given in Table 9.1.
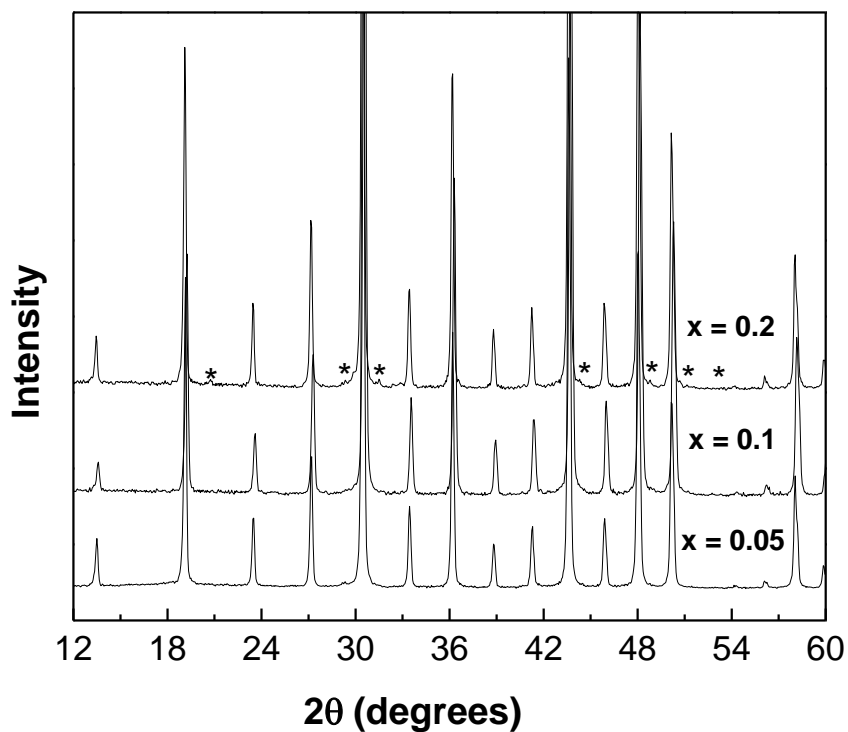
Figure 9.2: XRD patterns of $In_xIr_4Sb_{12}$ ($x = 0.05$, 0.1 and 0.2) samples. Asterisk symbols indicate small presence of $IrSb_2$, $InSb$, and Sb impurity phases.

To successfully refine the indium in the structure, room temperature and low temperature (T = 100 K) synchrotron XRD data were collected up to 70° 2θ for nominal $In_{0.1}Ir_4Sb_{12}$ sample, and the refined crystal structure is shown in Figure 9.5. At both room temperature and 100 K, indium was refined to partially occupy the $16f$ position with stoichiometric identity $In_{0.088}Ir_4Sb_{11.04}$.

All known skutterudite systems report filler ions in the $2a$ position, center of the
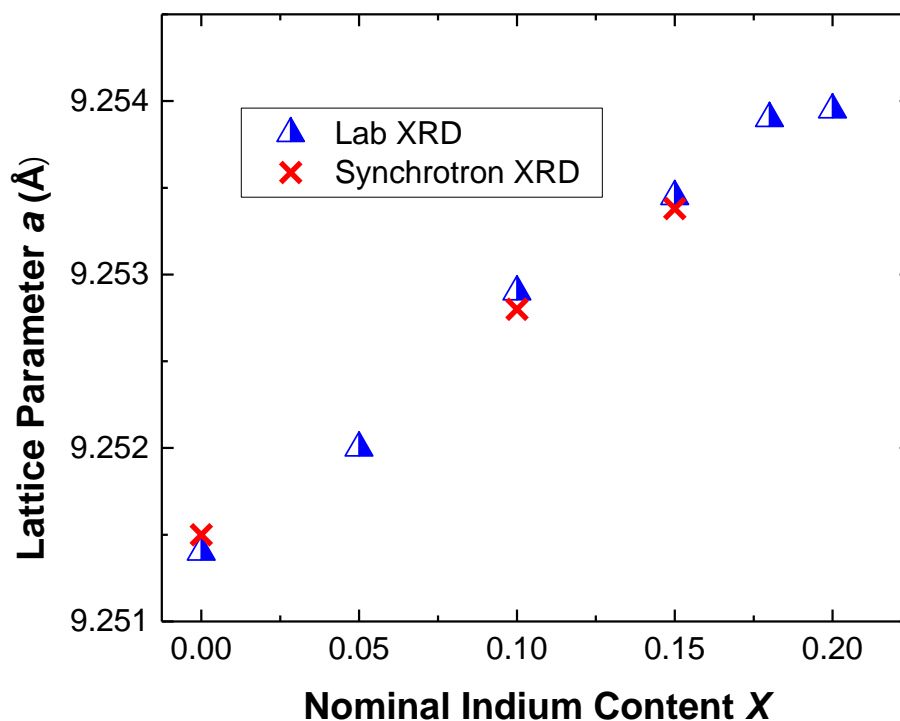
Figure 9.3: Cubic cell edge a vs nominal indium content x in $In_xIr_4Sb_{12}$.

void site [225, 226, 230, 232, 233, 237, 247, 248]. Our refinement of indium in the $2a$ position was unsuccessful as the occupancy refined to zero with unrealistic thermal parameters. Nonetheless moving indium along the [111] direction to the adjacent $16f$ site resulted in reasonable values for the refined occupancy and isotropic U_{iso}. The displacement of indium from the ideal $2a$ site is ≤ 1.15 Å. Indium occupation of the void site was confirmed by its extremely large thermal displacement parameter as compared to Ir and Sb. The magnitude of U_{iso} for indium at room temperature

Table 9.1: Rietveld refinement results of Synchrotron data for nominal compositions $IrSb_3$ and $In_{0.1}Ir_4Sb_{12}$ collected at room temperature and 100 K.[a,b]

Composition	$IrSb_3$	$In_{0.1}Ir_4Sb_{12}$ (RT)	$In_{0.1}Ir_4Sb_{12}$ (100 K)
R_{wp} (%)	7.31	6.79	6.93
a = b = c (Å)	9.25159(2)	9.25237(2)	9.24287(2)
V (Å^3)	791.862(3)	792.063(3)	789.625(3)
Sb, y	0.34030(2)	0.34024(2)	0.34035(2)
Sb, z	0.15315(2)	0.15331(2)	0.15323(2)
In, x	-	0.0707(2)	0.0722(1)
Sb Occ.	0.9321(5)	0.9193(5)	0.9183(5)
In Occ.	-	0.011(1)	0.011(1)
Ir U_{iso} (Å^2)	0.00297(2)	0.00342(1)	0.00150(1)
Sb U_{iso} (Å^2)	0.00517(8)	0.00578(7)	0.00376(6)
In U_{iso} (Å^2)	-	0.17(2)	0.018(3)
Refined FOR.	$IrSb_{2.793}$	$In_{0.088}Ir_4Sb_{11.04}$	$In_{0.088}Ir_4Sb_{11.04}$
Ir–Sb × 6 (Å)	2.61731(7)	2.61684(7)	2.61473(7)
Ir–In × 8 (Å)	-	2.87(4)	2.847(2)
In–In × 12 (Å)	-	1.31(4)	1.334(2)
Sb–Ir–Sb × 3 (°)	95.098(7)	95.102(7)	95.116(7)
Sb–Ir–Sb × 3 (°)	84.902(7)	84.898(7)	84.884(7)

a) Synchrotron data collected at APS 11bm beamline, $\lambda = 0.412731$ Å.

b) Crystal structure refined in space group $Im\bar{3}$ with Ir at $8c$ $(\frac{1}{4}, \frac{1}{4}, \frac{1}{4})$, In at $16f$ (x, x, x) and Sb at $24g$ $(0, y, z)$ sites, respectively.

is about ten times larger than that at 100 K due to exaggerated thermal motion at higher temperatures. The isotropic thermal parameter of Ir was found to be smaller as compared to Sb, consistent with other skutterudite systems. Iridium site $(8c)$ is fully occupied with no detectable vacancies observed for $IrSb_3$ and $In_{0.1}Ir_4Sb_{12}$ nominal samples. Antimony occupancy refinements, however, always show $\sim 8\%$ vacancy at $24g$ site (Table 9.1). Attempts of refining the structure by including antimony in other available crystallographic positions were not successful, and no
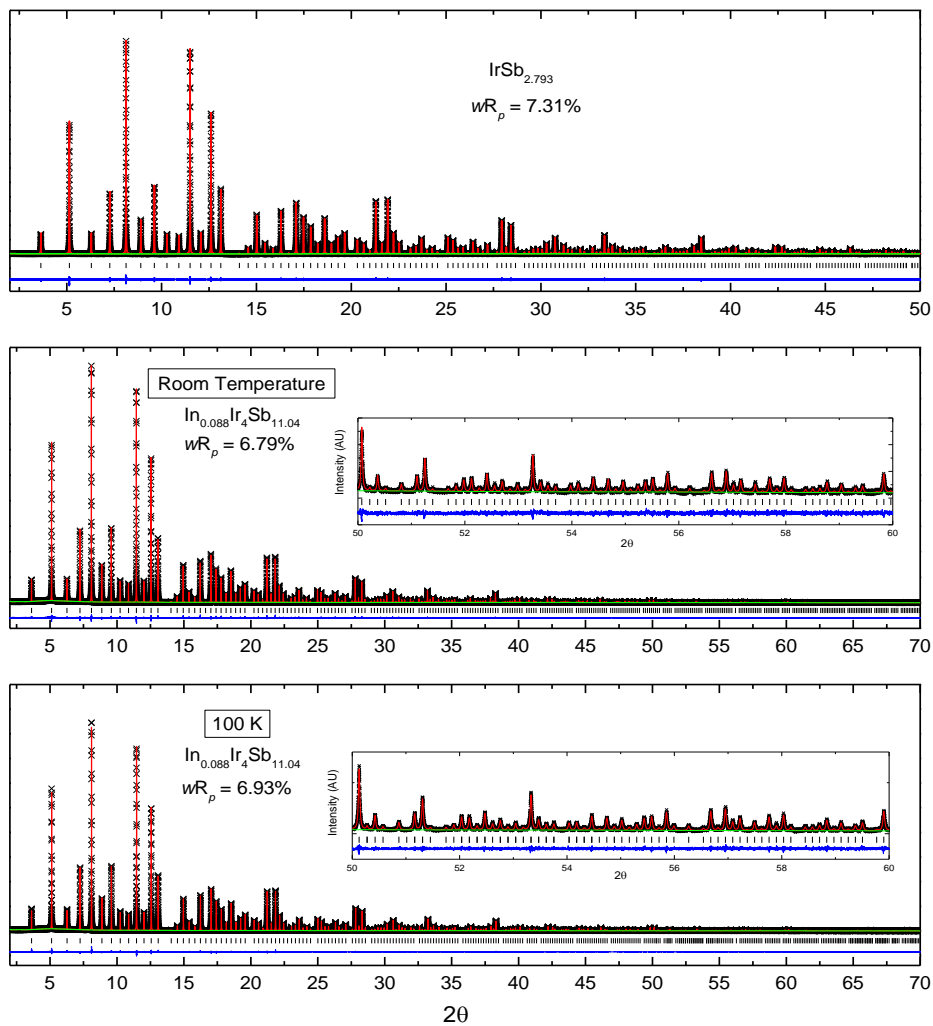
Figure 9.4: Synchrotron Rietveld refinement of nominal compositions $IrSb_3$ (top) and $In_{0.1}Ir_4Sb_{12}$ at room temperature (middle) and T = 100 K (bottom) (λ = 0.412731 Å). Observed (black crosses) and calculated (solid red line) profiles, background (green), and difference curve (I_{obs} - I_{calc}) (blue) are shown for each refinement. The vertical bars indicate the expected reflection positions. Resulting stoichiometric identities and wR_p are represented.

indium was found at Ir site.
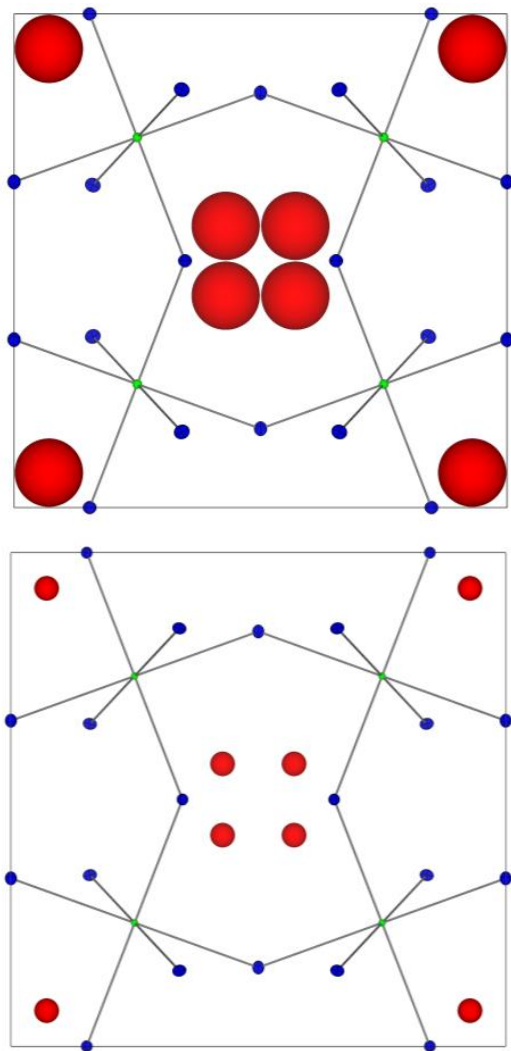
Figure 9.5: The $In_{0.088}Ir_4Sb_{11.04}$ unit cell illustrated down the c-axis from room temperature (top) and 100 K (bottom) synchrotron XRD refinements with iridium, antimony, and indium thermal ellipsoids as green, blue, and red respectively.

There are few reported systems with antimony vacancies [249, 250] and we acknowledge that ~8% vacancy is greater than such reported systems. This in part could be explained on the synthesis as antimony vapor was used to account for antimony loss in the sample and/or the covalency of iridium-antimony to allow chemical stability despite the slight reduction in the Zintl electron count. The uncommon movement of indium away from the center of the void site is likely associated with the resulting asymmetric bonding environment induced by Sb vacancies as well as the larger void size due to Ir. The influence of indium incorporation on cell dimensions, bond distances and angles are not significant.

9.3.2   Electrical Properties

Temperature dependent Resistivity measurements and Seebeck measurements of $In_xIr_4Sb_{12}$ ($0 \leq x \leq 0.2$) from 300-600 Kelvin are shown in Figure 9.6 and Figure 9.7. Unfilled $IrSb_3$ is metallic [234, 235, 251], and indium filled $In_xIr_4Sb_{12}$ samples are semiconductors (Figure 9.6). The activation energies (E_a) for each sample were extracted using $\sigma = \sigma_0\exp(E_a/k_BT)$ and are listed in Table 9.2.

Table 9.2: Activation energy for $In_xIr_4Sb_{12}$.

x	E_a (meV)
0.05	218.6
0.1	216.6
0.15	106.8
0.18	105.8
0.2	91.8
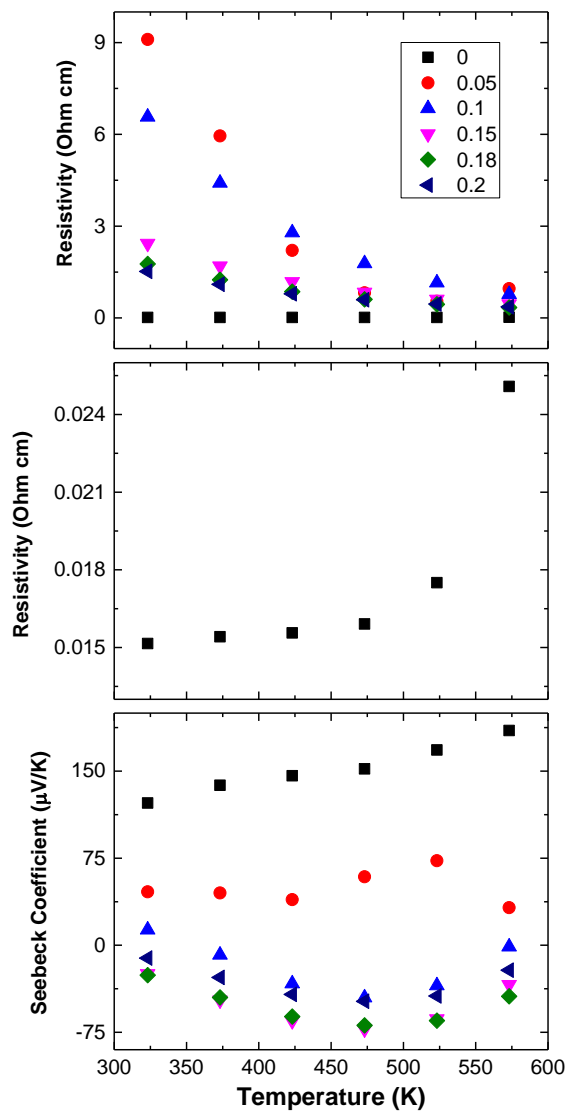
Figure 9.6: Temperature dependent resistivity (top/middle) and Seebeck coefficient data (bottom) of $In_xIr_4Sb_{12}$ samples ($0 \leq x \leq 0.2$) from 300 to 600 K.

As indicated by the Resistivity measurements (Figures 9.6 and 9.7), from x = 0.05 to 0.2, a decrease in E_a is observed. With increasing indium content, $In_xIr_4Sb_{12}$ samples undergo a transition from primarily p-type to n-type semiconductors (Figure 9.6). These trends are in parallel with published work on unfilled $IrSb_3$ and lanthanum filled $La_xIr_4Sb_{12}$ [234–236]. Because of the smaller void-site radius of $In_xCo_4Sb_{12}$ relative to $In_xIr_4Sb_{12}$, the indium contribution to the charge carrier in $In_xIr_4Sb_{12}$ should be insignificant compared to $In_xCo_4Sb_{12}$ [232]. Contrary to $In_xRh_4Sb_{12}$ [237] an increase in indium content reveals a distinct trend in the Seebeck measurements for $In_xIr_4Sb_{12}$.

Temperature dependent thermal conductivity data of $In_xIr_4Sb_{12}$ ($0 \leq x \leq 0.2$) from 300-600 K are shown in Figure 9.8. The lattice thermal conductivity was calculated from $K_l = K_t - K_e$, where K_t is the total thermal conductivity and K_e is the electronic thermal conductivity. The electronic thermal conductivities were determined using the Wiedemann-Franz law, $K_e = L\sigma T$, where the Lorentz number, L, of 2.00×10^8 V^2 K^2 was used [232, 237]. For all $In_xIr_4Sb_{12}$ samples, both the total and the lattice component of the thermal conductivity decrease with increasing temperature. With increasing indium content, the thermal conductivity decreases (Figure 9.8), consistent with indium filled $In_xRh_4Sb_{12}$ [237] and with the recognized presumption of the "rattling effect". From $x = 0$ to $x = 0.2$, K_t decreases approximately 30% across temperature range, similar to $La_xIr_4Sb_{12}$ and $In_xRh_4Sb_{12}$ [235,237]. For $In_xRh_4Sb_{12}$, at higher temperatures, thermal conductivity becomes independent of indium content. This is attributed to the contribution of bipolar thermal diffusion (k_{BP}) [237].
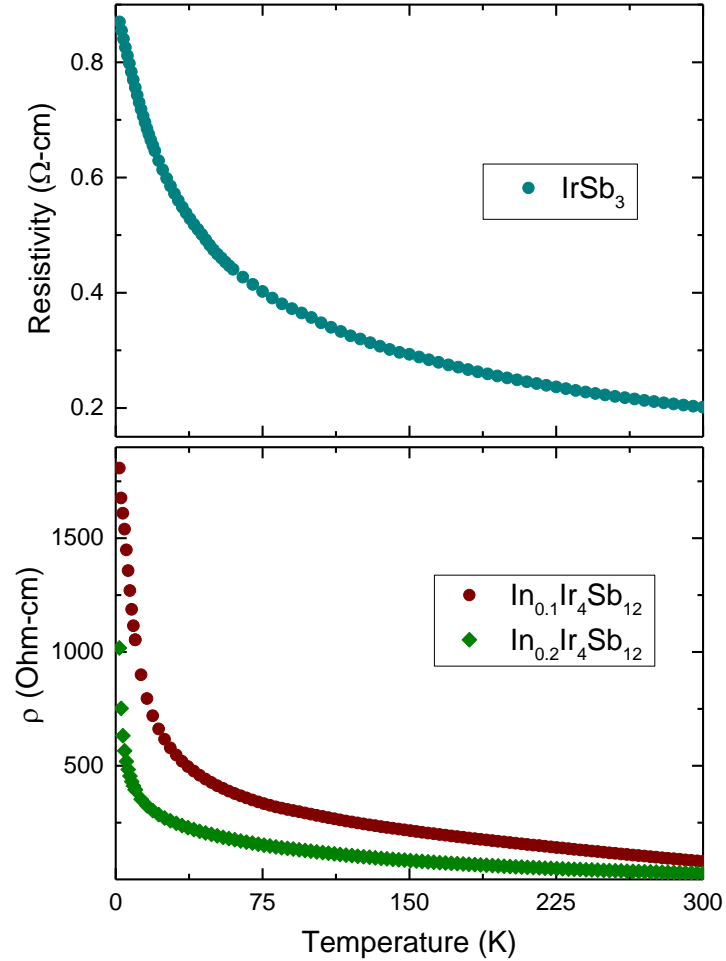
Figure 9.7: Temperature dependent, low temperature resistivity plots for $In_xIr_4Sb_{12}$ samples ($x = 0$, 0.1, and 0.2).

Conversely, effect of k_{BP} is not obvious for indium filled $In_xIr_4Sb_{12}$ ($0 \leq x \leq 0.2$) within 300-600 K temperature range. Bipolar thermal diffusion typically occurs in lightly doped small band-gap semiconductors and when there is reasonable
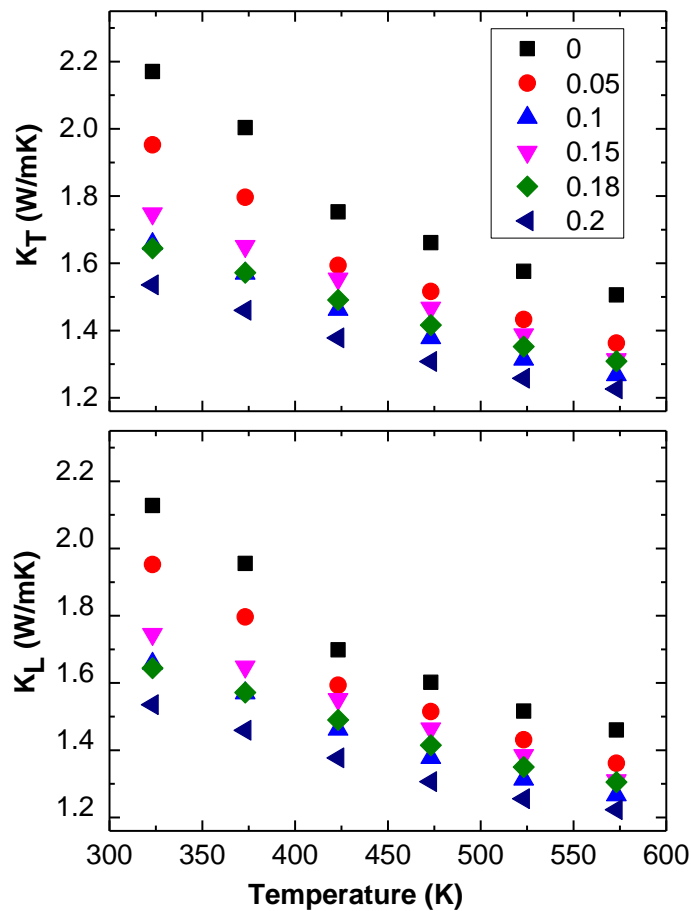
Figure 9.8: Temperature dependent total (top) and lattice thermal conductivity (bottom) of $In_xIr_4Sb_{12}$ samples ($0 \leq x \leq 0.2$) from 300 to 600 K.

contribution to the total electrical conductivity by both charge carriers [252, 253]. Though the Seebeck properties (Figure 9.6) would perhaps indicate the possibility of slight k_{BP} contribution at higher temperatures, higher resistivity relative to $In_xRh_4Sb_{12}$ would suggest otherwise. For $In_xRh_4Sb_{12}$, contribution of k_{BP} was

in part attributed to the disparity between hole and electron mobility [237]. It is known that large spin-orbit interaction influences electron and hole transport properties [254]. Zero-Field cooled magnetic susceptibility χ(T) was measured for $In_xIr_4Sb_{12}$($x = 0$ and 0.2 shown) (Figure 9.9). For all samples, χ(T) is small and nearly temperature independent above 50 K. Unfilled $IrSb_3$ exhibits diamagnetic behavior (consistent with Larmor diamagnetism), with the exception of a weak "Curie tail" at low temperatures due to the common presence of impurity spins (Figure 9.9) [255, 256]. A group 9 metal for an unfilled BX_3 skutterudite has a +3 charge, and therefore an electronic configuration of nd^6 [255]. Thus, for unfilled $IrSb_3$ (Ir^{3+} - filled t_{2g} band and an empty e_g band), diamagnetic behavior is undisputed.

With the increase of indium, below 50 K, the magnetic susceptibility appears temperature dependent (Figure 9.9). It could be argued that small inclusions of defect free spin 1/2 Ir ions could explain the magnetic susceptibility below $\sim$50 K for $In_{0.2}Ir_4Sb_{12}$. This was suggested for $In_xRh_4Sb_{12}$ [256]. It is possible that the observed increase in χ(T) (compared to $In_xRh_4Sb_{12}$ [256]) cannot be attributed alone to the small presence of defect spin 1/2 Ir ions. In addition, because of the on-site coulomb repulsion energy for $5d$ transition metals compared to $4d$ transition metals [257], iridium charge modification is conceivable. Temperature dependent thermoelectric figure of merit, ZT, values of $In_xIr_4Sb_{12}$ samples ($0 \leq x \leq 0.2$) are revealed in Figure 9.10. Though there is a decrease in total thermal conductivity with increasing indium content, the corresponding large increase in resistivity outweighs the prior and thus dictates the thermoelectric figure of merit, ZT. For
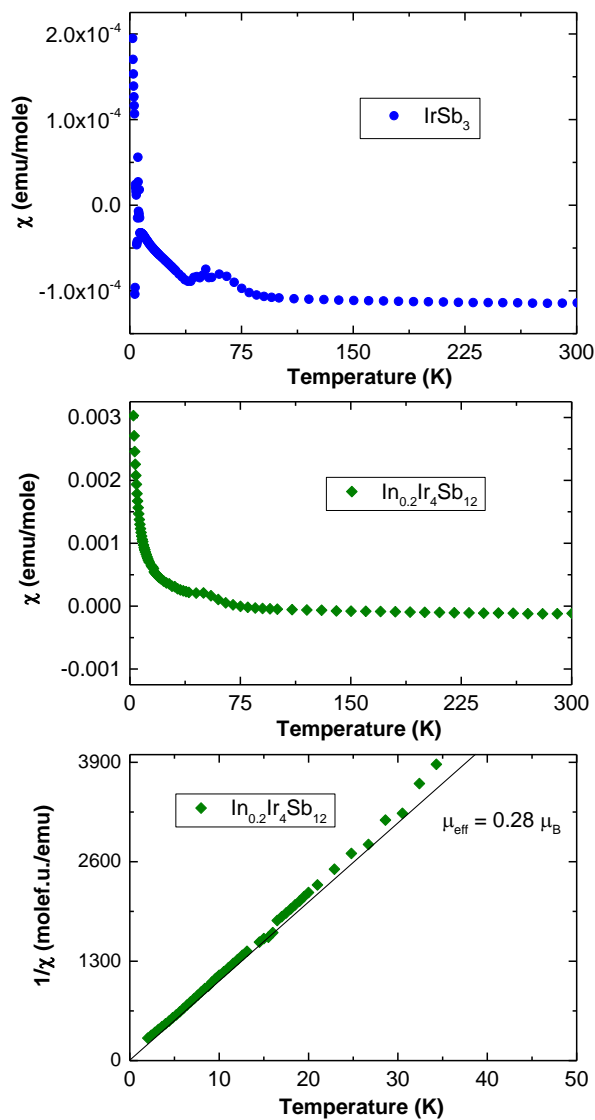
Figure 9.9: Zero-Field cooled magnetic susceptibility plots for $In_xIr_4Sb_{12}$ ($x = 0$ and 0.2) and inverse magnetic susceptibility plot for $In_xIr_4Sb_{12}$ ($x = 0.2$).

$In_xRh_4Sb_{12}$, increase in electrical resistivity also outweighs the corresponding decrease in total thermal conductivity, revealing an overall decrease in ZT [237]. The observed decrease in ZT for $In_xRh_4Sb_{12}$, however, is not as severe ($\sim$10 fold decrease). This is not the case for $In_xCo_4Sb_{12}$ and other light-element filling skuterudite systems have been proven to enhance TE performance by improving electrical transport properties and decreasing the total thermal conductivity [232, 258–261]. As thermoelectric properties of semiconductors are closely related to their electronic band structure, it is likely the large increase in resistivity can be explained by the electronic structure in relation to the contiguity of the $16f$ indium occupying the relatively large icosahedron. Electronic band structure studies of such indium filled $IrSb_3$ are therefore warranted.

Table 9.3 reveals electrical and thermal values of $In_xM_4Sb_{12}$, (M = Ir, Rh, and Co) at approximately 575 K for the x > 0 sample possessing the highest ZT. The samples presented in Table 9.3 all had the same synthesis with similar pellet densities [232, 237].

Table 9.3: $In_xM_4Sb_{12}$, (M = Ir, Rh, or Co) at approximately 575 K for $x > 0$ sample possessing the highest ZT [158,163].

	$In_xIr_4Sb_{12}$	$In_xRh_4Sb_{12}$	$In_xCo_4Sb_{12}$
x	0.18	0.05	0.3
R (Ohm cm)	0.341	$1.25x10^{-3}$	$2.4x10^{-3}$
S (V/K)	-44	55	-267
K_T (W/mK)	1.31	2.5	2.08
ZT	$2.42x10^{-4}$	0.11	1.19
Reference		232	237

For $In_{0.3}Co_4Sb_{12}$, the ZT value is primarily attributed to the large negative
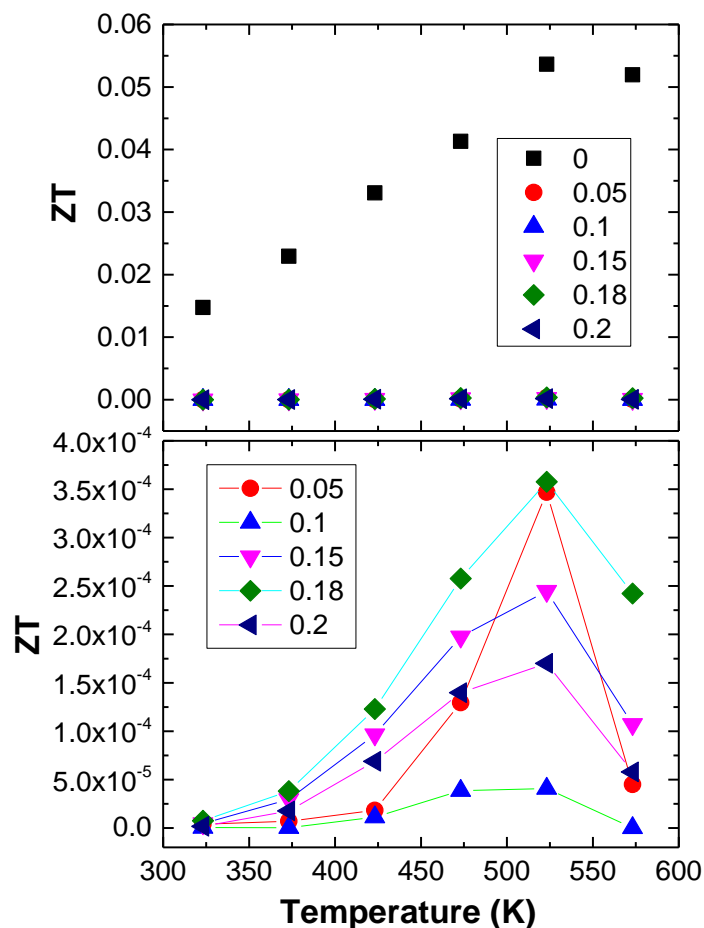
Figure 9.10: Resulting thermoelectric figure of merit, ZT, values of $In_xIr_4Sb_{12}$ samples ($0 \leq x \leq 0.2$) shown from 300-600 K.

Seebeck coefficient. For $In_xRh_4Sb_{12}$, though measured resistivity is desirable, large total thermal conductivity and small Seebeck coefficient characterize the insignificant ZT value. Of the three compared skutterudites, $In_xIr_4Sb_{12}$ samples reveal the smallest total thermal conductivity. For $In_xCo_4Sb_{12}$, K_t increases with in-

creasing x, and as discussed previously, K_t for $\text{In}_x\text{Rh}_4\text{Sb}_{12}$ becomes independent of indium content at higher temperature due to the contribution of bipolar thermal diffusion (k_{BP}) [232, 237]. From the ZT values alone (Figure 9.10), $\text{In}_x\text{Ir}_4\text{Sb}_{12}$ skutterudite clearly is not a thermoelectric candidate. However, the effect of indium on decreasing the total thermal conductivity as well as possible spin-orbit coupling effects of iridium on electronic and thermal parameters suggest indium filled iridium-rhodium-cobalt antimony alloy-based skutterudite system as a fundamentally intriguing research avenue.

9.4 Investigation of Indium Filled Rhodium-Iridium-Antimonide Skutterudites

Indium filled $\text{In}_x\text{Rh}_{4-y}\text{Co}_y\text{Sb}_{12}$ for $x = 0$ and 0.1 has been investigated [262]. For $\text{In}_{0.1}\text{Rh}_{4-y}\text{Co}_y\text{Sb}_{12}$, the increased thermal conductivity combined with diminishing Seebeck coefficients at elevated temperatures results in ZT values much lower than indium-filled $\text{In}_{0.1}\text{Co}_4\text{Sb}_{12}$ sample. However, for unfilled $\text{Co}_{4-y}\text{Rh}_y\text{Sb}_{12}$, ZT increases with increasing rhodium content. While rhodium substitution reduces the thermal conductivity of unfilled compositions, indium-filled samples exhibit bipolar thermal conductivity with increasing rhodium content [262]. Thermal and electrical properties of $\text{In}_{0.15}\text{Ir}_{4-y}\text{Rh}_y\text{Sb}_{12}$ ($y = 0$, 1, 2, 3, and 4) are compared in Figure 9.11 and 9.12.

As discussed, for $\text{In}_x\text{Rh}_4\text{Sb}_{12}$, although measured resistivity is desirable, large total thermal conductivity and small Seebeck coefficient characterize the insignif-
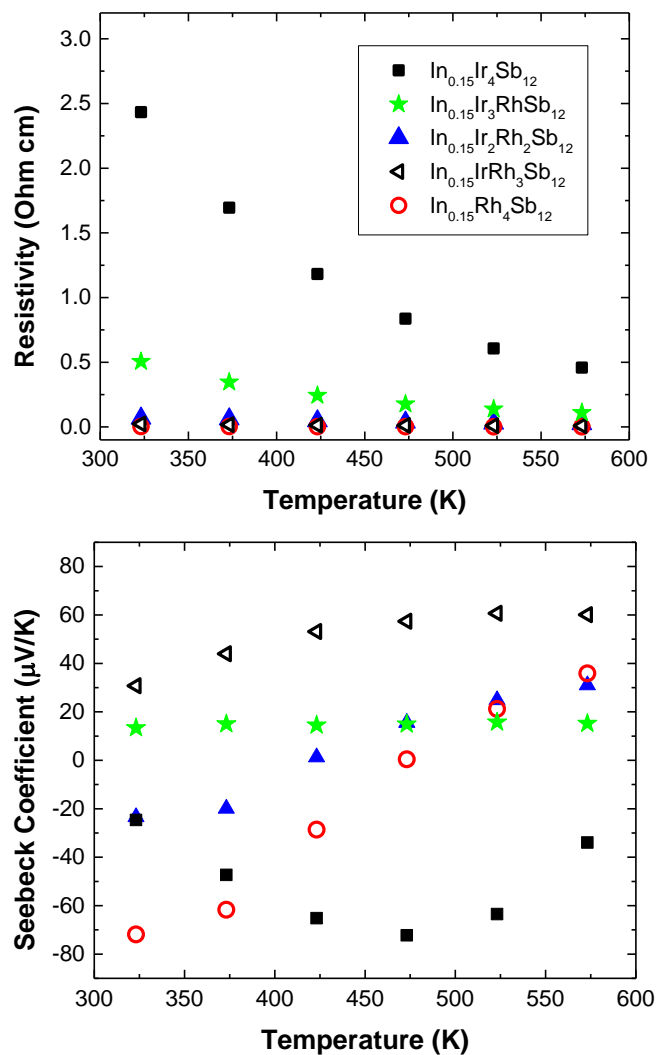
Figure 9.11: Temperature dependent resistivity (top) and Seebeck coefficient data (bottom) of $In_{0.15}Ir_{4-y}Rh_ySb_{12}$ samples ($0 \leq y \leq 1$) from 300 to 600 K.

icant ZT value and $In_xIr_4Sb_{12}$ samples reveal the smallest total thermal conductivity relative to Co and Rh versions (Table 9.3). With increasing y for

$In_{0.15}Ir_{4-y}Rh_ySb_{12}$, resistivity dramatically decreases. The total thermal conductivity remains small for nearly all $In_{0.15}Ir_{4-y}Rh_ySb_{12}$ (with the exception of $In_{0.15}Rh_4Sb_{12}$) (Figure 9.12). For $In_{0.15}Ir_2Rh_2Sb_{12}$, the Seebeck coefficient and resistivity are both similar to $In_{0.15}Rh_4Sb_{12}$, and the total thermal conductivity equates to $In_{0.15}Ir_4Sb_{12}$, resulting in ZT approximately three times greater than $In_{0.15}Rh_4Sb_{12}$ at higher temperatures (Figure 9.12). Yet, because the magnitude of the Seebeck remains small compared to $In_xCo_4Sb_{12}$ [9], a high ZT is not obtained.

Because $IrSb_3$ cell parameter is larger than $RhSb_3$ [237], it is conceivable a larger void site for the same filler atom would enhance dampening of the lattice thermal conductivity. This prediction is observed when comparing the total thermal conductivities of $In_{0.1}Ir_4Sb_{12}$ and $In_{0.1}Rh_4Sb_{12}$ (Figure 9.12). The trends shown in Figures 9.11 and 9.12 reveal that the electrical and thermal properties can be tuned for $In_{0.15}Ir_{4-y}Rh_ySb_{12}$ mirroring the behavior of $In_{0.15}Rh_4Sb_{12}$ ($y < 0.5$) or $In_{0.15}Ir_4Sb_{12}$ ($y < 0.5$). A solid solution of iridium, rhodium, and cobalt was investigated, however, synthesizing samples under similar conditions resulted in separate Ir/Rh and Co skutterudite phases.

9.5 Summary

The work presented on indium filled $In_xIr_4Sb_{12}$ skutterudites highlights trends in key thermoelectric properties that are atypical to the "phonon-glass/electron-crystal" approach. Unlike known "rattler" filled skutterudites which show an increase in ZT with increasing "rattler" concentration, a substantial decrease in ZT
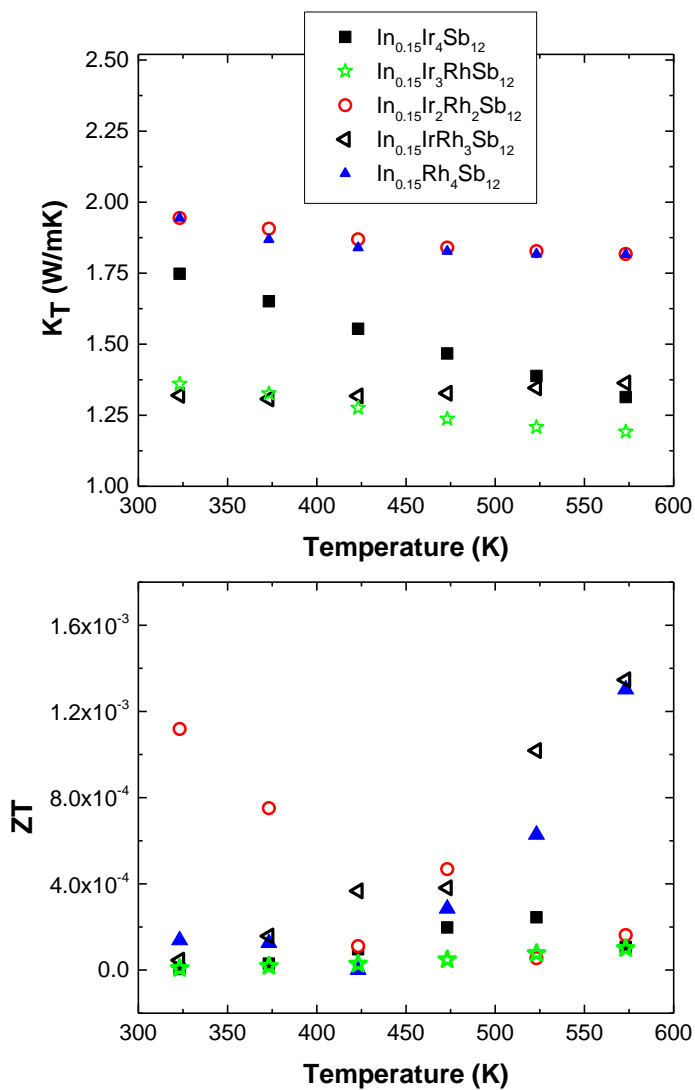
Figure 9.12: Temperature dependent total thermal conductivity (top) and resulting thermoelectric figure of merit, ZT, values of $In_{0.15}Ir_{4-y}Rh_ySb_{12}$ samples ($0 \leq y \leq 1$) (bottom) from 300 to 600 K.

with addition of indium is observed. This is credited to the substantial increase in electrical resistivity and decrease in the Seebeck coefficient with indium con-

tent. Synchrotron X-ray diffraction refinements reveal $\sim$8% antimony vacancy and indium partially occupying the $16f$ site. As thermoelectric properties of semiconductors are closely related to their electronic band structure, it is likely the large increase in resistivity can be explained by the electronic structure in relation to indium occupying the $16f$ position in the large icosahedron void site and/or antimony vacancies. Electronic band structure studies and further structure and thermoelectric property analysis of indium filled $IrSb_3$ under high pressure synthesis conditions are therefore warranted.

9.6 Methods

9.6.1 Synthesis

Polycrystalline samples of $In_xIr_4Sb_{12}$ ($0 \leq x \leq 0.2$) were prepared by standard solid-state reaction. The elements 99.999% In powder (Aldrich), 99.5% Ir powder (Aldrich), and 99.9% Sb powder (Strem) were thoroughly mixed in air in an agate mortar. The powders were loaded into alumina crucibles and reacted in a tube furnace at 610 °C for 4 h under a constant flow of antimony vapor and 95/5 N_2/H_2 gas. The samples were then ground and light-pressed into 10 mm diameter pellets and conventionally sintered at 610 °C for 4 h, followed by 675 °C for 4 h under a constant flow of 95/5 N_2/H_2 gas. The resultant sintered pellets were approximately 65% of the theoretical density.

9.6.2 Structure Determination

Phase analysis of powder samples was performed by X-ray diffraction using a Rigaku MiniFlex II diffractometer with Cu K_α radiation and a graphite monochromator for the diffracted beam. Lattice parameters were calculated by LeBail fit using KCl ($Fm\bar{3}m$) as an internal standard. Synchrotron X-ray Diffraction (Advanced Photon Source 11-BM) was collected for $In_xIr_4Sb_{12}$ (x = 0, 0.1, and 0.15) samples at room temperature (λ=0.412731 Å, $2\theta \leq 50$) along with T = 100 K for x = 0.1 sample ($2\theta \leq$70).

9.6.3 Electrical Properties

The principal thermoelectric properties; the Seebeck coefficient (S) electrical conductivity (σ) and thermal conductivity (K) were measured from 300-600 K. The Seebeck coefficient and electrical conductivity data was collected on an ULVAC ZEM-3 under a helium atmosphere. Thermal diffusivity (α) was measured on a Netzsch LFA 457 Micro Flash under flowing N_2. Low-temperature (2-300 K) magnetization measurements were obtained with a Quantum Design MPMS and resistivity (50-300 K) measurements were obtained using a Quantum Design PPMS.

Bibliography

[1] A.R. West. *Solid State Chemistry and its Applications*. Wiley, 2014.

[2] L.E. Smart and E.A. Moore. *Solid State Chemistry: An Introduction*. CRC Press, 2016.

[3] C. Hammond. *The Basics of Crystallography and Diffraction*. Oxford, 2016.

[4] G.E. Bacon. *The Basics of Crystallography and Diffraction*. Elsevier, 1966.

[5] H.E. Taylor. *Inductively Coupled Plasma-Mass Spectrometry : Practices And Techniques*. Elsevier, 2000.

[6] G.H. Jeffery et al. *Quantitative Chemical Analysis*. Bath Press, 1989.

[7] C.S. Schnor and M.C. Ridgeway. *X-Ray Absorption Spectroscopy Of Semiconductors*. Springer, 2016.

[8] G. Grosso. *Solid State Physics*. Elsevier, 2000.

[9] J.D. Tilley. *Understanding Solids*. Wiley, 2013.

[10] P.A. Cox. *Transition Metal Oxides*. Oxford, 1992.

[11] A.F. Orchard. *Magnetochemistry*. Oxford, 2003.

[12] Quantum Design. Physical Property Measurement System Hardware Manual. `https://web.njit.edu/~tyson/PPMS_Documents/PPMS_Manual/1070-150%20Rev.%20B5%20PQ%20%20PPMS%20Hardware.pdf`, 2003.

[13] Mike Micelfresh. Fundamentals of Magnetism and Magnetic Measurements-Featuring Quantum Design's Magnetic Measurement Property Measurement System. `https://www.mrl.ucsb.edu/sites/default/files/mrl_docs/instruments/fundamentals.pdf`, 1994.

[14] Quantum Design. Physical Property Measurement System AC Measurement System (ACMS) Option User's Manual. `https://web.njit.edu/~tyson/PPMS_Documents/PPMS_Manual/1084-100%20C1%20ACMS%20manual.pdf`, 2003.

[15] Quantum Design. Physical Property Measurement System Heat Capacity Option User's Manual. `https://www.mrl.ucsb.edu/sites/default/files/mrl_docs/instruments/hcapPPMS.pdf`, 2003.

[16] Netzch. LFA 457 MicroFlash Laser Flash Apparatus. `https://www.netzsch-thermal-analysis.com/us/products-solutions/thermal-diffusivity-conductivity/lfa-457-microflash/`, 2018.

[17] K.A. Borup et al. Measuring thermoelectric transport properties of materials. *Energy Environ. Sci.,*, 8:423, 2015.

[18] ULVAC. Zem-3 series. `http://www.ulvac.com/components/Thermal-Instruments/Thermoelectric-Testers/ZEM-3-Series`, 2018.

[19] C.P. Slichter. *Principles of Magnetic Resonanace*. Springer, 1961.

[20] D. Goldfarb and S. Stoll. *EPR Spectroscopy: Fundamentals and Methods*. Wiley, 2018.

[21] S. Fuchs et al. Unraveling the Nature of Magnetism of the $5d^4$ Double Perovskite Ba_2YIrO_6. *Physical Review Letters*, 120:237204, 2018.

[22] P. Gast et al. EPR interactions - *g*-anisotropy. *eMagRes*, 5:1435, 2016.

[23] The ABINIT Group. Abinit software. `https://www.abinit.org/`, 2019.

[24] D. Pesin and L. Balents. Mott physics and band topology in materials with strong spin–orbit interaction. *Nat. Phys.*, 6:376–381, 2010.

[25] W. Witczak–Krempa, G. Chen, Y.B. Kim, and L. Balents. Correlated Quantum Phenomena in the Strong Spin–Orbit Regime. *Annu. Rev. Condens. Matter Phys.*, 5:57–82, 2014.

[26] P.A. Cox. *Transition Metal Oxides*. Oxford, 1992.

[27] W.J. Duffin. *Electricity and magnetism*. McGraw-Hill, 1990.

[28] B.J. Kim et al. Novel $J_{eff} = 1/2$ Mott State Induced by Relativistic Spin–Orbit Coupling in Sr_2IrO_4. *Phys. Rev. Lett.*, 101:076402, 2008.

[29] J.W. Kim et al. Dimensionality Driven Spin–Flop Transition in Layered Iridates. *Phys. Rev. Lett.*, 109:037204, 2012.

[30] G. Jackeli and G. Khaliullin. Mott Insulators in the Strong Spin-Orbit Coupling Limit: From Heisenberg to a Quantum Compass and Kitaev Models. *Phys. Rev. Lett.*, 102:017205, 2008.

[31] G.L. Stamokostas and G.A. Fiete. Mixing of t_{2g}-e_g orbitals in 4d and 5d transition metal oxides. *Phys. Rev. B.*, 97:085150, 2018.

[32] A.R. Makintosh and O.K. Andersen. *Electrons at the Fermi Surface*. M. Springford, 1980.

[33] M. Hermanns, I. Kimchi, and J. Knolle. Physics of the Kitaev model: fractionalization, dynamical correlations, and material connections. *Annu. Rev. Condens. Matter Phys.*, 9:17–33, 2018.

[34] J. Chaloupka, G. Jackeli, and G. Khaliullin. Kitaev-Heisenberg Model on a Honeycomb Lattice: Possible Exotic Phases in Iridium Oxides A_2IrO_3. *Phys. Rev. Lett.*, 105:027204, 2010.

[35] J. Knolle, D.L. Kovrizhin, J.T. Chalker, and R. Moessner. Dynamics of a two-dimensional quantum spin liquid: signatures of emergent Majorana fermions and fluxes. *Phys. Rev. Lett.*, 112:207203, 2014.

[36] P.W. Anderson. Resonating valence bonds: A new kind of insulator? *Mater. Res. Bull.*, 8:153–160, 1973.

[37] M.F. Collins. *Magnetic critical scattering*. Oxford University Press, 1989.

[38] P.W. Anderson. The Resonating Valence Bond State in La_2CuO_4 and Superconductivity. *Science*, 235:1196–1198, 1987.

[39] S.M. Hayden et al. Sin dynamics in the two-dimensional antiferromagnetic La_2CuO_4. *Phys. Rev. B.*, 42:10220, 1990.

[40] P.W. Anderson. The spin-1/2 Heisenberg antiferromagnet on a square lattice and its application to the cuprous oxides. *Review of Modern Physics*, 63:1–62, 1991.

[41] A. Kitaev. Anyons in an exactly solved model and beyond. *Annals of Physics*, 321:2–111, 2006.

[42] G. Jackeli and G. Khaliullin. Mott Insulators in the Strong Spin-Orbit Coupling Limit: From Heisenberg to a Quantum Compass and Kitaev Models. *Phys. Rev. Lett.*, 102:017205, 2009.

[43] M.K. Wallace et al. Local Moment Instability of Os in Honeycomb $Li_{2.15}Os_{0.85}O_3$. *Sci. Rep.*, 8:6605, 2018.

[44] A. Banerjee et al. Neutron scattering in the proximate quantum spin liquid α-$RuCl_3$. *Science*, 356:1055–1059, 2017.

[45] M. Abramchuk et al. Cu_2IrO_3: A New Magnetically Frustrated Honeycomb Iridate. *J. Am. Chem. Soc.*, 139:15371–15376, 2017.

[46] P. Mendels et al. Quantum Magnetism in the Paratacamite Family: Towards an Ideal Kagomé Lattice. *Phys. Rev. Lett.*, 98:077204, 2006.

[47] X. Liu et al. Long-range magnetic ordering in Na_2IrO_3. *Physical Review B*, 83:220403, 2011.

[48] J. Van–Kranendonk and J.H. Van–Vleck. Spin Waves. *Reviews of Modern Physics*, 23:1–23, 2014.

[49] M.R. Norman. Herbertsmithite and the search for the quantum spin liquid . *Reviews of Modern Physics*, 88:1–14, 2016.

[50] M. Mourigal et al. Fractional spinon excitations in the quantum Heisenberg antiferromagnetic chain. *Nat. Phys.*, 9:435–441, 2013.

[51] G.E. Granroth. Opportunities in Inelastic Neutron Scattering at Oak Ridge National Laboratory. *Am. Phys. Soc. 74th Annu. Meet. Southeast. Sect.*, 1:8–10, 2007.

[52] G.E. Granroth. Inelastic Neutron Scattering Signal from Deconfined Spinons in a Fractionalized Antiferromagnet. *International Journal of Modern Physics B*, 17:2821–2838, 2003.

[53] J.S. Helton et al. Spin Dynamics of the Spin-1/2 Kagome Lattice Antiferromagnet $ZnCu_3(OH)_6Cl_2$. *Physical Review Letters*, 98:107204, 2007.

[54] T.D. Ladd et al. Quantum Computers. *Nature*, 464:45–53, 2010.

[55] A. Kitaev. Fault-tolerant quantum computation by anyons. *Annals of Physics*, 303:2–30, 2003.

[56] L. Balents. Spin liquids in frustrated magnets. *Annals of Physics*, 464:199–208, 2010.

[57] Q. Xiao-Liang and Z. Shou-Cheng. Topological insulators and superconductors. *Rev. Mod. Phys.*, 83:1057–1110, 2011.

[58] R. Joynt and R.E. Prange. Conditions for the quantum Hall effect. *Phys. Rev. B.*, 29:3303–3317, 1984.

[59] M.Z. Hasan and C.L. Kane. Colloquium: Topological insulators. *Rev. Mod. Phys.*, 82:3045–3067, 2010.

[60] B.A. Bernevig, T.L. Hughes, and S.C. Zhang. Quantum spin Hall effect and topological phase transition in HgTe quantum wells. *Science*, 314:1757–1761, 2006.

[61] D. Hsieh et al. A topological Dirac insulator in a quantum spin Hall phase. *Nature*, 452:970–974, 2008.

[62] F.D.M. Haldane. Model for a Quantum Hall Effect without Landau Levels: Condensed-Matter Realization of the "Parity Anomaly". *Phys. Rev. Lett.*, 61:2015–2018, 1988.

[63] A. Shitade et al. Quantum Spin Hall Effect in a Transition Metal Oxide Na_2IrO_3. *Phys. Rev. Lett.*, 102:256403, 2009.

[64] H.S. Kim, C.H. Kim, H. Jeong, H. Jin, and J. Yu. Strain-induced topological insulator phase and effective magnetic interactions in Li_2IrO_3. *Phys. Rev. Lett.*, 87:165117, 2013.

[65] N.P. Armitage, E.J. Mele, and A. Vishwanath. Weyl and Dirac semimetals in three-dimensional solids. *Review of Modern Physics*, 90:015001, 2018.

[66] M. Sato and Y. Ando. Topological superconductors: a review. *Rep. Prog. Phys.*, 80:076501, 2017.

[67] L. Yang, Z.G. Chen, M.S. Dargusch, and J. Zou. High Performance Thermoelectric Materials: Progress and Their Applications. *Advanced Energy Materials*, 8:1701797, 2018.

[68] T.M. Tritt and M.A. Subramanian. Thermoelectric materials, phenomena, and applications: A bird' s eye view. *MRS Bull*, 31:188–198, 2006.

[69] T. Zhu et al. Compromise and Synergy in High-Efficiency Thermoelectric Materials. *Adv. Mater.*, 29:1605884, 2017.

[70] M. Hamid Elsheikh et al. A review on thermoelectric renewable energy: Principle parameters that affect their performance. *Renew. Sustain. Energy Rev.*, 30:337–355, 2014.

[71] Z.G. Chen, G. Han, L. Yang, L. Cheng, and J. Zou. Nanostructured thermoelectric materials: Current research and future challenge. *Prog. Nat. Sci. Mater. Int.*, 22:535–549, 2013.

[72] M. Rull–Bravo et al. Skutterudites as thermoelectric materials: Revisited. *RSC Adv.*, 5:41653–41667, 2015.

[73] A. Elarusi, A. Attar, and H. Lee. Analysis and experimental investigation of optimum design of thermoelectric cooling/heating system for car seat climate control (cscc). *J. Electron. Mater.*, 47:1131–1321, 2018.

[74] JPL Cal Tech. Jet propulsion laboratory thermoelectric science and engineering web site. `http://www.its.caltech.edu/01jsnyder/thermoelectrics/`, 2018.

[75] M. Newhall. Jet propulsion laboratory thermoelectric science and engineering web site. `https://www.energy.gov/articles/history-nuclear-power-space`, 2015.

[76] T.C. Holgate et al. Increasing the efficiency of the multi–mission radioisotope thermoelectric generator. *J. Electron. Mater.*, 44:1814–1821, 2015.

[77] H. Mamur et al. A review on bismuth telluride (Bi_2Te_3) nanostructure for thermoelectric applications. *Renewable and Sustainable Energy Reviews*, 82:4159–4169, 2018.

[78] L.D. Zhao et al. Ultralow thermal conductivity and high thermoelectric figure of merit in snse crystals. *J. Electron. Mater.*, 508:373–377, 2014.

[79] G.S. Nolas, D.T. Morelli, and T.M. Tritt. Skutterudties: A Phonon-Glass-Electron Crystal Approach to Advanced Thermoelectric Energy Conversion Applications. *Annual Review of Material Science*, 29:88–116, 1999.

[80] Y. Pei et al. High thermoelectric figure of merit in heavy hole dominated PbTe. *En. Env. Sci.*, 4:2085–2089, 2011.

[81] Y. Pei, A.D. Lalonde, H. Wang, and G.J. Snyder. Low effective mass leading to high thermoelectric performance broader context. *En. Env. Sci.*, 7:7963–7969, 2012.

[82] M. Hong, Z.G. Chen, Y. Pei, L. Yang, and J. Zou. Limit of ZT enhancement in rocksalt structured chalcogenides by band convergence. *Phys. Rev. B.*, 94:161201, 2016.

[83] L. Yang, Z.G. Chen, M. Hong, G. Han, and J. Zou. Enhanced Thermoelectric Performance of Nanostructured Bi_2Te_3 through Significant Phonon Scattering. *ACS Appl. Mater. Interfaces*, 7:23694–23699, 2015.

[84] L. Yang et al. High-performance thermoelectric Cu_2Se nanoplates through nanostructure engineering. *Nano Energy*, 16:367–374, 2015.

[85] J.R. Szczech, J.M. Higgins, and S. Jin. Enhancement of the thermoelectric properties in nanoscale and nanostructured materials. *J. Mater. Chem.*, 21:4037–4055, 2011.

[86] X.W. Wang et al. Enhanced thermoelectric figure of merit in nanostructured *n*-type silicon germanium bulk alloy. *Appl. Phys. Lett.*, 93:1–4, 2008.

[87] T. Mori. Novel principles and nanostructuring methods for enhanced thermoelectrics. *Small*, 13:1–10, 2017.

[88] J. Eilertsen, J. Li, S. Rouvimov, and M.A. Subramanian. Thermoelectric properties of indium–filled $In_xRh_4Sb_{12}$ skutterudites. *J. Alloys Compd.*, 509:6289–6295, 2011.

[89] M.K. Wallace, J. Li, and M.A. Subramanian. Structural, electronic, and thermal properties of indium–filled $In_xIr_4Sb_{12}$ skutterudites. *Solid State Sci.*, 80:170–177, 2018.

[90] H. Tao, H. Jiazhong, D. Rosenfeld, and M.A. Subramanian. Thermoelectric properties of indium-filled skutterudites. *Chem. Mat.*, 18:759–762, 2006.

[91] H. Luo et al. A large family of filled skutterudites stabilized by electron count. *Nat. Comm.*, 6:6489, 2015.

[92] B.C. Sales et al. Filled skutterudite antimonides: Electron crystals and phonon glasses. *Phys. Rev. B*, 56:15081–15089, 1997.

[93] J. Breger et al. High-resolution X-ray diffraction, DIFFaX, NMR and first principles study of disorder in the Li_2MnO_3–$Li[Ni_{1/2}Mn_{1/2}]O_2$ solid solution. *J. Solid State Chem.*, 178:2575–2585, 2005.

[94] G. Blasse. *Crystal Chemistry and Some Magnetic Properties of Mixed Metal Oxides with Spinel Structure.* Thesis, 1964.

[95] S. Vasala and M. Karppinen. $A_2B'B''O_6$ perovskites: A review. *Prog. Solid State Chem.*, 43:1–36, 2015.

[96] M.T. Anderson, K.B. Greenwood, G.A. Taylor, and K.R. Poeppelmeier. B-cation arrangements in double perovskites. *Prog. Solid State Chem.*, 22:197–233, 1993.

[97] R.H. Mitchell. *Perovskites: Modern and Ancient.* Almaz Press Inc., 2002.

[98] G. King and P.M. Woodward. Cation ordering in perovskites. *J. Mater. Chem.*, 20:5785, 2010.

[99] J. Flynn, J. Li, A.W. Sleight, A.P. Ramirez, and M.A. Subramanian. Structure and Properties of Ir-Containing Oxides with Large Spin–Orbit Coupling: $Ba_2In_{2-x}Ir_xO_{5+\delta}$. *Inorganic Chemistry*, 55:2748–2754, 2016.

[100] J. Flynn, J. Li, A. P. Ramirez, and M.A. Subramanian. The effect of iridium oxidation state on the electronic properties of perovskite-type solid solutions: $Ba_{2-x}La_xInIrO_6$ and $BaLaIn_{1-y}Ca_yIrO_6$. *Journal of Solid State Chemistry*, 247:53–59, 2017.

[101] B. Ranjbar et al. Structural and Magnetic Properties of the Iridium Double Perovskites $Ba_{2-x}Sr_xYIrO_6$. *Inorganic Chemistry*, 54:10468–10476, 2015.

[102] L. Clark et al. Two-dimensional spin liquid behaviour in the triangular-honeycomb antiferromagnet $TbInO_3$. *Nature Physics*, 9:1–8, 2019.

[103] H. Jun, S.H. Rhim, and A.J. Freeman. Topological Oxide Insulator in Cubic Perovskite Structure. *Scientific Reports*, 1651:1–5, 2013.

[104] J. Carter, V. Shankar, M. Ahsan-Zeb, and H. Kee. Semimetal and Topological Insulator in Perovskite Iridates. *Physical Review B*, 85:115105, 2012.

[105] P. Abbamonte et al. A structural probe of the doped holes in cuprate super-conductors. *Science*, 297:581, 2002.

[106] C.C. Torardi, M.A. Subramanian, J. Gopalakrishnan, and A.W. Sleight. Alkali-metal substituted La_2CuO_4: Structures of $La_{2-x}M_xCuO_4$ (M = Na, K;x 0.2). *Phys. C Supercond.*, 158:465–470, 1989.

[107] N.D. Shinn et al. $La_2CuO_{4+\delta}$: A superconducting superoxide. *Synth. Met.*, 29:709–714, 1989.

[108] B.J. Kim et al. Phase-Sensitive Observation of a Spin-Orbital Mott State in Sr_2IrO_4. *Science*, 323:1329, 2009.

[109] M. Azuma, S. Kaimori, and M.. Takano. High-Pressure Synthesis and Magnetic Properties of Layered Double Perovskites Ln_2CuMO_6 (Ln = La, Pr, Nd, and Sm; M = Sn and Zr). *Chemistry of Materials*, 10:3124–3130, 1998.

[110] P.M. Woodward et al. Influence of Cation Size on the Structural Features of $Ln_{1/2}A_{1/2}MnO_3$ Perovskites at Room Temperature. *Chemistry of Materials*, 10:3652–3665, 1998.

[111] R.B. Macquart, Q. Zhou, and B.J. Kennedy. Structural investigation of Sr_2LiReO_6. Evidence for a continuous tetragonal–cubic phase transition. *J. Solid State Chem*, 182:1691–1693, 2009.

[112] L. Pauling. The Principles Determining The Structure Of Complex Ionic Crystals. *J. Am. Chem. Soc.*, 51:1010–1026, 1929.

[113] A.M. Glazer. The classification of tilted octahedra in perovskites. *Acta Crystallogr. Sect. B Struct. Crystallogr. Cryst. Chem.*, 28:3384–3392, 1972.

[114] P.M. Woodward. Octahedral Tilting in Perovskites. I. Geometrical Considerations. *Acta Crystallogr. Sect. B Struct. Crystallogr. Cryst. Chem.*, 53:32–43, 1997.

[115] T. Nagai, M. Sugiyama, M. Sando, and K. Niihara. Structural Changes in $Ba(Sr_{1/3}Ta_{2/3})O_3$-Type Perovskite Compounds upon Tilting of Oxygen Octahedra. *Jpn. J. Appl. Phys.*, 36:1146–1153, 1997.

[116] V.F. Sears. Neutron scattering lengths and cross sections. *Neutron News*, 3:29–37, 1992.

[117] S. Kauzlarich. *Chemistry, structure, and bonding of Zintl phases and ions (chemistry of metal clusters)*. New York, 1996.

[118] W. Schmidt, R. Berthelot, L. Etienne, A. Wattiaux, and M.A. Subramanian. Synthesis and characterization of O_3-$Na_3LiFeSbO_6$: A new honeycomb ordered layered oxide. *Mater. Res. Bull.*, 50:292–296, 2014.

[119] L. Sandhya Kumari, M.K Wallace, J.T. Barnes, B. Tong, A.P. Ramirez, and M.A. Subramanian. Charge transfer instability in a mixed Ir/Rh honeycomb lattice in $Li_2Ir_{1x}Rh_xO_3$ solid solution. *Solid State Sci.*, 61:232–238, 2016.

[120] G. Khaliullin. Excitonic magnetism in van vleck-type d^4 mott insulators. *Physical Review Letters*, 111:197201, 2013.

[121] A. Kitaev. Anyons in an exactly solved model and beyond. *Annals of Physics*, 321:2–111, 2006.

[122] I. Felner and I.M. Bradari. The magnetic behavior of Li_2MO_3 (M = Mn, Ru and Ir) and $Li_2(Mn_{1-x}Ru_x)O_3$. *Physica B: Condensed Matter*, 311:195–199, 2002.

[123] A.P. James and J.B. Goodenough. Structure and bonding in Li_2MoO_3 and $Li_{2-x}MoO_3$ ($0 \leq x \leq 1.7$). *Journal of Solid State Chemistry*, 76:87–96, 1988.

[124] S. Lee et al. Antiferromagnetic ordering in Li_2MnO_3 single crystals with a two-dimensional honeycomb lattice. *Journal of Physics: Condensed Matter*, 24:456004, 2012.

[125] J.C. Wang et al. Lattice-tuned magnetism of $Ru^{4+}(4d^4)$ ions in single-crystals of the layered honeycomb ruthenates: Li_2RuO_3 and Na_2RuO_3. *Phys. Rev. B.*, 90:161110, 2014.

[126] J. Breger et al. High-resolution X-Ray diffraction, DIFFAX, NMR and first principles study of disorder in the Li_2MnO_3-$Li[Ni_{1/2}Mn_{1/2}]O_2$ solid solution. *J. Solid State Chem.*, 178:2575–2585, 2005.

[127] W. Schmidt, R. Berthelot, L. Etienne, A. Wattiaux, and M.A. Subramanian. Synthesis and characterization of O_3-$Na_3LiFeSbO_6$: A new honeycomb ordered layered oxide. *Mater. Res. Bull.*, 50:292–296, 2014.

[128] Z. Lu and J.R. Dahn. Effects of stacking fault defects on the X-ray diffraction patterns of T_2 , O_2 , and O_6 structure $Li_{2/3}[Co_xNi_{1/3-x}Mn_{2/3}]O_2$. *Chemistry of Materials*, 13:2078–2083, 2001.

[129] L. Torres-Castro, M.A. Abreu-Sepulveda, R.S. Katiyar, and A. Manivannan. Electrochemical investigations on the effect of Mg-substitution in Li_2MnO_3 cathode. *Journal of the Electrochemical Society*, 164:A1464–A1473, 2017.

[130] J.L. Hodeau, M. Marezio, A. Santoro, and R.S. Roth. Neutron profile refinement of the structures of Li_2SnO_3 and Li_2ZrO_3. *Journal of Solid State Chemistry*, 45:170–179, 1982.

[131] S. Manni et al. Effect of isoelectronic doping on honeycomb lattice iridate A_2IrO_3. *Phys. Rev. B.*, 89:1–7, 2014.

[132] Y. Singh and P. Gegenwart. Antiferromagnetic mott insulating state in single crystals of the honeycomb lattice material. *Phys. Rev. B.*, 82:1–7, 2010.

[133] E. Mccalla et al. Visualization of O-O peroxo-like dimers in high-capacity layered oxides for li-ion batteries. *Science*, 350:1516–1521, 2015.

[134] S. Okada et al. Cathode characteristics of layered rocksalt oxide, Li_2PtO_3. *Electrochim. Acta.*, 45:329–334, 1999.

[135] Y.V. Baklanova et al. Photo- and radioluminescence of lithium hafnate Li_2HfO_3. *Optical Materials*, 34:1037–1041, 2012.

[136] H. Kobayashi et al. Structure, and magnetic and electrochemical properties of layered oxides, Li_2IrO_3. *J. Mater. Chem.*, 13:957–962, 2003.

[137] Sandhya L. Kumari, M.K. Wallace, J.T. Barnes, B. Tong, A.P. Ramirez, and M.A Subramanian. Charge transfer instability in a mixed Ir/Rh honeycomb lattice in $Li_2Ir_{1-x}Rh_xO_3$ solid solution. *Solid State Sciences*, 61:232–238, 2016.

[138] S. Yogesh et al. Relevance of the heisenberg-kitaev model for the honeycomb lattice iridates A_2IrO_3. *Phys. Rev. Lett.*, 108:127203, 2012.

[139] Y. Singh and P. Gegenwart. Antiferromagnetic mott insulating state in single crystals of the honeycomb lattice material, Na_2IrO_3. *Phys. Rev. B.*, 82:064412, 2010.

[140] T. Takayama, A. Kato, R. Dinnebier, J. Nuss, and H. Takagi. Hyper-honeycomb iridate β-Li_2IrO_3 as a platform for kitaev magnetism. *Phys. Rev. Lett.*, 114:077202, 2015.

[141] A. Banerjee et al. Neutron scattering in the proximate quantum spin liquid α-$RuCl_3$. *Science*, 356:1055–1059, 2017.

[142] A.P. Ramirez. Strongly geometrically frustrated magnets. *Ann. Rev, Mater. Sci.*, 24:453–480, 1994.

[143] A R. Makintosh and O K. Andersen. *Electrons at the Fermi Surface*, volume 149. M. Springford, 1980.

[144] Z.K. Heiba and K. El-Sayed. Structural and anisotropic thermal expansion correlation of Li_2ZrO_3 at different temperatures. *Journal of Applied Crystallography*, 35:634–636, 2002.

[145] V. Jansen and R.Z. Hoppe. Zur kenntnis der nacl-strukturfamilie: Neue untersuchungen an Li_2MnO_3. *Anorg. Allg. Chem.*, 397:279, 1973.

[146] A. Boulineau, L. Croguennec, C. Delmas, and F. Weill. Reinvestigation of Li_2MnO_3 structure: Electron diffraction and high resolution TEM. *Journal of Applied Crystallography*, 21:4216–4222, 2009.

[147] S.J. Hibble, I.D. Fawcett, and A.C. Hannon. Structure of two disordered molybdates, $Li_2Mo^{IV}O_3$ and $Li_4Mo_3^{IV}O_8$, from total neutron scattering. *Acta Crystallographica*, B53:604–612, 1997.

[148] M.J. O'Malley, H. Verweij, and P.M. Woodward. Structure and properties of ordered Li_2IrO_3 and Li_2PtO_3. *Journal of Solid State Chemistry*, 181:1803–1809, 2008.

[149] M.J. O'Malley and P.M. Woodward. *A Structural, Bonding, and Properties Study of the Ordered Rock Salt Structures, Li_2MO_3 (M = Ru, Ir, Pt)*. Dissertation Thesis, Ohio State University, 2009.

[150] V.M. Katukuri et al. Strong magnetic frustration and anti-site disorder causing spin-glass behavior in honeycomb Li_2RhO_3. *Scientific Reports*, 5:14718, 2018.

[151] Hechang Lei, Wei-Guo Yin, Zhicheng Zhong, and Hideo Hosono. Structural, magnetic, and electrical properties of $Li_2Ir_{1-x}Ru_xO_3$. *Physical Review B*, 89:020409, 2014.

[152] A.C. Larson and R.B. Von-Dreele. General structure analysis system (GSAS). *Los Alamos National Laboratory Report*, page 86–748, 1994.

[153] B.H. Toby. EXPGUI, a graphical user interface for GSAS. *Journal of Applied Crystallography*, 34:210–213, 2001.

[154] M.J. Treacy, J.M. Newsam, and M.W. Deem. A general recursion method for calculating diffracted intensities from crystals containing planar faults. *Proc. R. Soc. Lond. Ser. A*, 433:499, 1991.

[155] D.C. Wallace and T.M. McQueen. New honeycomb iridium(v) oxides: $NaIrO_3$ and $Sr_3CaIr_2O_9$. *Dalton Trans*, 44:20344, 2015.

[156] D.C. Wallace, C.M. Brown, and T.M. McQueen. Evolution of magnetism in $Na_{1-\delta}(Na_{1-x}Mg_x)Ir_2O_6$ the series of honeycomb iridates. *Journal of Solid State Chemistry*, 224:28–35, 2015.

[157] B. Sebastian et al. Solution of the heavily stacking faulted crystal structure of the honeycomb iridate $H_3LiIr_2O_6$. *Dalton Trans*, 46:15216, 2017.

[158] G. van-der Laan and B.T. Thole. Local probe for spin-orbit interaction. *Physical Review Letters*, 60:1977, 1988.

[159] G. van-der Laan and B.T. Thole. Orbital magnetism and spin-orbit effects in the electronic structure of $BaIrO_3$. *Physical Review Letters*, 105:216407, 2010.

[160] J.S. Helton et al. Spin Dynamics of the Spin-1/2 Kagome Lattice Antiferromagnet $ZnCu_3(OH)_6Cl_2$. *Physical Review Letters*, 98:107204, 2007.

[161] M.A. Laguna-Marco et al. Orbital magnetism and spin-orbit effects in the electronic structure of $BaIrO_3$. *Physical Review Letters*, 105:216407, 2010.

[162] S. Gangopadhyay and W.E. Pickett. Interplay between spin-orbit coupling and strong correlation effects: Comparison of the three osmate double perovskites Ba_2AOsO_6 (A=Na, Ca, Y). *Physical Review B*, 93:155126, 2016.

[163] I.I. Mazin et al. Na_2IrO_3 as a molecular orbital crystal. *Phys. Rev. Lett.*, 109:197201, 2012.

[164] Y. Singh et al. Relevance of the heisenberg-kitaev model for the honeycomb lattice iridates A_2IrO_3. *Phys. Rev. Lett.*, 108:127203, 2012.

[165] I.I. Mazin et al. Origin of the insulating state in honeycomb iridates and rhodates. *Phys. Rev. B.*, 88:035115, 2013.

[166] Y. Yamaji et al. First-principles study of the honeycomb-lattice iridates Na_2IrO_3 in the presence of strong spin orbit interaction and electronic correlations. *Phys. Rev. lett.*, 113:107201, 2014.

[167] S. Nishimoto et al. Strongly frustrated triangular spin lattice emerging from triplet dimer formation in honeycomb Li_2IrO_3. *Nat. Commun.*, 7:10273, 2016.

[168] K. Hu, F. Wang, and J. Feng. First-principles study of the magnetic structure of Na_2IrO_3. *Phys. Rev. Lett.*, 115:167204, 2015.

[169] M. Kim, B.H. Kim, and B.I. Min. Insulating nature of Na_2IrO_3: Mott-type or slater-type. *Phys. Rev. B*, 93:195135, 2016.

[170] Y. Li, S.M. Winter, H.O. Jeschke, and R. Valenti. Electronic excitations in gamma-Li_2IrO_3. *Phys. Rev. B*, 95:045129, 2017.

[171] X. Gonze, S.M. Winter, H.O. Jeschke, R. Valenti, S.M. Winter, H.O. Jeschke, and R. Valenti. Abinit: first-principles approach to materials and nanosystem properties. *Comp. Phys. Commun.*, 180:2582, 2009.

[172] X. Gonze et al. Recent developments in the ABINIT software package. *Computer Phys. Comm.*, 205:106, 2016.

[173] J.P. Perdew, K. Burke, and M. Ernzerhof. Generalized gradient approximation made simple. *Phys. Rev. Lett.*, 77:3865, 1996.

[174] M. Torrent, F. Jollet, F. Bottin, G. Zerah, and X. Gonze. Implementation of the projector augmented-wave method in the ABINIT code. *Comput. Mat. Science*, 42:337, 2008.

[175] B. Amadon, F. Jollet, and M. Torrent. Gamma and beta cerium: LDA+U calculations of ground-state parameters. *Phys. Rev. B.*, 77:155104, 2008.

[176] D.D. ORegna and G. Teobaldi. Optimization of constrained density functional theory. *Phys. Rev.*, 94:035159, 2016.

[177] L.I. Veiga et al. Fragility of ferromagnetic double exchange interactions and pressure tuning of magnetism in 3d—5d double perovskite Sr_2FeOsO_6. *Physical Review B*, 91:235135, 2015.

[178] S. Vasala and M. Karppinen. $A_2B'B''O_6$ perovskites: A review. *Progress in solid state chemistry*, 43:1–36, 2015.

[179] M.T. Anderson, K.B. Greenwood, G.A. Taylor, and K.R. Poeppelmeier. B-cation arrangements in double perovskites. *Progress in solid state chemistry*, 22:197–233, 1993.

[180] R.H. Mitchell. *Perovskites: Modern and Ancient*. Almaz Press Inc., 2002.

[181] G. King and P.M. Woodward. Cation ordering in perovskites. *Journal of Materials Chemistry*, 20:5785–5796, 2010.

[182] J. Flynn, J. Li, A.W. Sleight, A.P. Ramirez, and M.A. Subramanian. Structure and properties of Ir-containing oxides with large spin-orbit coupling: $Ba_2In_{2-x}Ir_xO_{5+\delta}$. *Inorganic Chemistry*, 55:2748–2754, 2016.

[183] J. Flynn, J. Li, A.P. Ramirez, and M.A. Subramanian. The effect of iridium oxidation state on the electronic properties of perovskite-type solid solutions: $Ba_{2-x}La_xInIrO_6$ and $BaLaIn_{1-y}Ca_yIrO_6$. *Journal of Solid State Chemistry*, 247:53–59, 2017.

[184] B. Ranjbar, E. Reynolds, P. Kayser, and B.J. Kennedy. Structural and Magnetic Properties of the Iridium Double Perovskites $Ba_{2x}Sr_xYIrO_6$. *Inorganic Chemistry*, 54:10468–10476, 2015.

[185] A.M. Glazer. The Classification of Tilted Octahedra in Perovskites. *Acta Crystallographica Section B*, 28:3384–3392, 1972.

[186] S. Fuchs et al. Unraveling the Nature of Magnetism of the $5d^4$ Double Perovskite Ba_2YIrO_6. *Physical Review Letters*, 120:237204, 2018.

[187] W. Witczak-Krempa, G. Chen, Y.B. Kim, and L. Balents. Correlated Quantum Phenomena in the Strong Spin-Orbit Regime. *Annual Review of Condensed Matter Physics*, 5:57, 2014.

[188] A. Aczel et al. Highly anisotropic exchange interactions of $j_{eff} = 1/2$ iridium moments on the fcc lattice in La_2BIrO_6 (B = Mg, Zn). *Physical Review B*, 93:214426, 2016.

[189] V.I. Azarov, R.R. Gayasov, Y.N. Joshi, and S.S. Churilov. The Sixth Spectrum of Iridium (Ir VI): Determination of the $5d^4$, $5d^36s$ and $5d^36p$ Configurations. *Physica Scripta*, 64:295–313, 2001.

[190] B.J. Kim et al. Novel $J_{eff}=1/2$ Mott State Induced by Relativistic Spin-Orbit Coupling in Sr_2IrO_4. *Physical Review Letters*, 101:076402, 2008.

[191] J.W. Kim et al. Dimensionality Driven Spin-Flop Transition in Layered Iridates. *Physical Review Letters*, 109:037204, 2012.

[192] G. Jackeli and G. Khaliullin. Mott Insulators in the Strong Spin-Orbit Coupling Limit: From Heisenberg to a Quantum Compass and Kitaev Models. *Physical Review Letters*, 102:017205, 2009.

[193] G. Khaliullin. Excitonic Magnetism in Van Vleck–type d^4 Mott Insulators. *Physical Review Letters*, 111:197201, 2013.

[194] T. Dey et al. Ba_2YIrO_6: A cubic double perovskite material with Ir^{5+} ions. *Physical Review B*, 93:014434, 2016.

[195] Q. Chen et al. Magnetism out of antisite disorder in the J=0 compound Ba_2YIrO_6. *Physical Review B*, 96:144423, 2017.

[196] F. Hammerath et al. Diluted paramagnetic impurities in nonmagnetic Ba_2YIrO_6. *Physical Review B*, 96:165108, 2017.

[197] J.E. Page et al. Doped Sr_2FeIrO_6-Phase Separation and a $J_{eff} \neq 0$ State for Ir^{5+}. *Inorganic Chemistry*, 96:10303–10311, 2017.

[198] G. Cao et al. Novel Magnetism of $Ir^{5+}(5d^4)$ Ions in the Double Perovskite Sr_2YIrO_6. *Physical Review Letters*, 112:056402, 2014.

[199] A.R. Makintosh and O.K. Andersen. *Electrons at the Fermi Surface*. Springford, 1980.

[200] R.D. Shannon and C.T. Prewitt. Effective ionic radii in oxides and fluorides. *Acta Crystallographica Section B*, 25:925, 1969.

[201] R.D. Shannon. Revised effective ionic radii and systematic studies of inter-atomic distances in halides and chalcogenides. *Acta Crystallographica Section A*, 32:751–767, 1976.

[202] T. Dey et al. Ba_2YIrO_6: A cubic double perovskite material with Ir^{5+} ions. *Physical Review B*, 93:014434, 2016.

[203] A. Nag et al. Origin of magnetic moments and presence of a resonating valence bond state in Ba_2YIrO_6. *Physical Review B*, 98:014431, 2018.

[204] M.V. Talanov, V.B. Shirokov, and V.M. Talanov. Anion order in perovskites: a group-theoretical analysis. *Acta Crystallographica Section A*, 72:222–235, 2016.

[205] O. Bock and U. Muller. Symmetry relationships in variants of the perovskite type. *Acta Crystallographica Section B*, 58:594–606, 2002.

[206] P.M. Woodward. Octahedral Tilting in Perovskites. I. Geometrical Considerations. *Acta Crystallographica Section B*, 53:32–43, 1997.

[207] V.F. Sears. Neutron scattering lengths and cross sections. *Neutron News*, 3:29–37, 1992.

[208] I.D. Brown. Recent Developments in the Methods and Applications of the Bond Valence Model. *Chemical Reviews*, 109:6881, 2009.

[209] R.D. Shannon. Revised Effective Ionic Radii and Systematic Studies of Interatomie Distances in Halides and Chaleogenides. *Acta Crystallographica Section A*, 32:751–767, 1976.

[210] B.E. Day et al. Structures of ordered tungsten- or molybdenum-containing quaternary perovskite oxides. *Journal of Solid State Chemistry*, 185:107–116, 2012.

[211] P.J. Saines, B.J. Kennedy, and M.M. Elcombe. Structural phase transitions and crystal chemistry of the series Ba_2LnBO_6 (Ln=lanthanide and B=Nb^{5+} or Sb^{5+}). *Journal of Solid State Chemistry*, 180:401–409, 2007.

[212] V. Ting, Y. Liu, R.L. Withers, and E. Krausz. An electron diffraction and bond valence sum study of the space group symmetries and structures of the photocatalytic 1:1 ordered A_2InNbO_6 double perovskites (A=Ca^{2+}, Sr^{2+}, Ba^{2+}). *Journal of Solid State Chemistry*, 177:979–986, 2004.

[213] A.K. Prodjosantoso, Q. Zhou, and B.J. Kennedy. Synchrotron X-ray diffraction study of the $Ba_{1x}SrSnO_3$ solid solution. *Journal of Solid State Chemistry*, 200:241–245, 2013.

[214] M.C. Knapp and P.M. Woodward. A-site cation ordering in $AABBO_6$ perovskites. *Journal of Solid State Chemistry*, 179:1076–1085, 2006.

[215] C. Bernuy-Lopez et al. $Sr_2MgMoO_{6-\delta}$: Structure, Phase Stability, and Cation Site Order Control of Reduction. *Chemistry of Materials*, 19:1035–1043, 2007.

[216] J.G. Zhao, L.X. Yang, Y. Yu, F.Y. Li, R.C. Yu, and C.Q. Jin. Physical properties of the 5M $BaIrO_3$: A new weak ferromagnetic iridate synthesized under high pressure. *Solid State Communications*, 150:36–39, 2010.

[217] A.R. Makintosh and O.K. Andersen. *Electrons at the Fermi Surface*. Springford, 1980.

[218] W. Witczak-Krempa, G. Chen, Y.B. Kim, and L. Balents. Correlated Quantum Phenomena in the Strong Spin-Orbit Regime. *Annual Review of Condensed Matter Physics*, 5:57, 2014.

[219] B.J. Kim et al. Novel J_{eff}=1/2 Mott State Induced by Relativistic Spin-Orbit Coupling in Sr_2IrO_4. *Physical Review Letters*, 101:076402, 2008.

[220] J.W. Kim et al. Dimensionality Driven Spin-Flop Transition in Layered Iridates. *Physical Review Letters*, 109:037204, 2012.

[221] G. Jackeli and G. Khaliullin. Mott Insulators in the Strong Spin-Orbit Coupling Limit: From Heisenberg to a Quantum Compass and Kitaev Models. *Physical Review Letters*, 102:017205, 2009.

[222] C. Urano et al. LiV_2O_4 Spinel as a Heavy-Mass Fermi Liquid: Anomalous Transport and Role of Geometrical Frustration. *Physical Review Letters*, 85:1052, 2000.

[223] B.J. Kennedy and B.A. Hunter. Phase Transformation in $CuRh_2O_4$: A Powder Neutron Diffraction Study. *Materials Research Bulliten*, 34:135–143, 1999.

[224] T.M. Tritt and M.A. Subramanian. Thermoelectric Materials, Phenomena, and Applications: A Bird' s Eye View. *MRS Bull*, 31:188–198, 2006.

[225] M. Rull-Bravo, A. Moure, J.F. Fernandez, and M. Martin-Gonzalez. Skutterudites as thermoelectric materials: revisited. *RSC Advances*, 5:41653–41667, 2015.

[226] M.H. Elsheikh et al. A review on thermoelectric renewable energy: Principle parameters that affect their performance. *Renewable and Sustainable Energy Reviews*, 30:337–355, 2014.

[227] J.R. Szczech, J.M. Higgins, and S. Jin. Enhancement of the thermoelectric properties in nanoscale and nanostructured materials. *Journal of Materials Chemistry*, 21:4037–4055, 2011.

[228] X.W. Wang et al. Enhanced thermoelectric figure of merit in nanostructured *n*-type silicon germanium bulk alloy. *Applied Physics Letters*, 93:193121, 2008.

[229] T. Mori. Novel Principles and Nanostructuring Methods for Enhanced Thermoelectrics. *Small*, 13:1702013, 2017.

[230] B.C. Sales, D. Mandrus, B.C. Chakoumakos, V. Keppens, and J.R. Thompson. Filled skutterudite antimonides: Electron crystals and phonon glasses. *Physical Review B*, 56:15081, 1997.

[231] B.C. Sales, B.C. Chakoumakos, and D. Mandrus. Thermoelectric properties of thallium-filled skutterudites. *Physical Review B*, 61:2475, 2000.

[232] T. He, J. Chen, H.D. Rosenfeld, and M.A. Subramanian. Thermoelectric properties of indium-filled skutterudites. *Chemistry of Materials*, 18:759–762, 2006.

[233] E. Visnow et al. On the True Indium Content of In-Filled Skutterudites. *Inorganic Chemistry*, 54:7818–7827, 2015.

[234] S.W. Kim, Y. Kimura, and Y. Mishima. Effects of Doping on the High-Temperature Thermoelectric Properties of $IrSb_3$ Skutterudite Compounds. *Journal of Electronic Materials*, 32:1141–1147, 2003.

[235] S.W. Kim, Y. Kimura, and Y. Mishima. Effect of Partial La Filling on High-Temperature Thermoelectric Properties of $IrSb_3$-Based Skutterudite Compounds. *Journal of Electronic Materials*, 33:1156–1160, 2004.

[236] T.M. Tritt, G.S. Nolas, G.A. Slack, A.C. Ehrlich, D.J. Gillespie, and J.L. Cohn. Low-temperature transport properties of the filled and unfilled $IrSb_3$ Skutterudite System. *Journal of Applied Physics Letters*, 79:8412–8418, 1996.

[237] J. Eilertsen, J. Li, S. Rouvimov, and M.A. Subramanian. Thermoelectric properties of indium-filled $In_xRh_4Sb_{12}$ skutterudites. *Journal of Alloys and Compounds*, 509:6289–6295, 2011.

[238] O.M. Loevvik and O. Prytz. Density-functional band-structure calculations for La-, Y-, and Sc-filled CoP_3-based skutterudite structures. *Physical Review B*, 70:195119–195119, 2004.

[239] Xiao-Liang Qi and Shou-Cheng Zhang. Topological insulators and superconductors. *Reviews of Modern Physics*, 83:1057–1110, 2011.

[240] A R. Makintosh and O.K. Andersen. *Electrons at the Fermi Surface*, volume 149. M. Springford, 1980.

[241] Ashish C.G. and Sheng Y.W. Routes to probe Bismuth induced strong-coupling superconductivity in bimetallic BiIn alloys. *Scientific Reports*, 7:9442, 2017.

[242] Z. Ruidan et al. Indium Substitution Effect on the Topological Crystalline Insulator Family $(Pb_{1-x}Sn_x)_{1-y}In_yTe$: Topological and Superconducting Properties. *Crystals*, 7:55, 2017.

[243] Q. Liu, X. Zhang, L.B. Abdalla, and A. Zunger. Transforming Common III–V and II–VI Semiconductor Compounds into Topological Heterostructures: The Case of CdTe/InSb Superlattices. *Advanced Functional Materials*, 26:3259–3267, 2016.

[244] B. Yan, L. Muchler, Q. Xiao-Liang, Z. Shou-Cheng, and C. Felser. Topological insulators in filled skutterudites. *Physical Review B*, 85:165125, 2012.

[245] M. Yang, Liu, and Wu-Ming. The d-p band-inversion topological insulator in bismuth-based skutterudites. *Scientific Reports*, 4:5131, 2014.

[246] V. Pardo, J.C. Smith, and W.E. Pickett. Linear bands, zero-momentum Weyl semimetal, and topological transition in skutterudite-structure pnictides. *Physical Review B*, 85:214531, 2012.

[247] T. Keiber and F. Bridges. Modeling correlated motion in filled skutterudites. *Physical Review B*, 92:1–10, 2015.

[248] D. Cao et al. Evidence for rattling behavior of the filler atom (L) in the filled skutterudites LT_4X_{12} (L=Ce,Eu,Yb; T=Fe,Ru; X=P,Sb) from EXAFS studies. *Physical Review B*, 70:1–11, 2004.

[249] W.Y. Zhao, C.L. Dong, P. Wei, W. Guan, L.S. Liu, P.C. Zhai, X.F. Tang, and Q.J. Zhang. Synthesis and high temperature transport properties of barium and indium double-filled skutterudites $Ba_xIn_yCo_4Sb_{12-z}$. *Journal of Applied Physics*, 102:1–6, 2007.

[250] C. Chongze-Hu et al. Effects of partial La filling and Sb vacancy defects on $CoSb_3$ skutterudites. *Physical Review B*, 95:165204, 2017.

[251] K. Koga, K. Akai, K. Oshiro, and M. Matsuura. Electronic structure and optical properties of binary skutterudite antimonides. *Physical Review B*, 71:155119, 2005.

[252] S. Wang, J. Yang, T. Toll, J. Yang, W. Zhang, and X. Tang. Electronic structure and optical properties of binary skutterudite antimonides. *Scientific Reports*, 5:10136, 2015.

[253] X. Shi, W. Zhang, L.D. Chen, and J. Yang. Filling Fraction Limit for Intrinsic Voids in Crystals: Doping in Skutterudites. *Physical Review Letters*, 95:185503, 2005.

[254] R. Winkler. *Spin–Orbit Coupling Effects in Two-Dimensional Electron and Hole Systems*, volume 191. Springer, 2003.

[255] H. Luo et al. A large family of filled skutterudites stabilized by electron count. *Nature Communications*, 6:6489, 2015.

[256] J. Trinh. *Low temperature properties of strong spin-orbit systems*, volume 1. Thesis, UC Santa Cruz, 2016.

[257] I.I. Mazin, S. Manni, K. Foyevtsova, H.O. Jeschke, and P. Gegenwart. Origin of the insulating state in honeycomb iridates and rhodates. *Physical Review B*, 88:035115, 2013.

[258] Y.Z. Pei, J. Yang, L.D. Chen, W. Zhang, J.R. Salvador, and J. Yang. Improving thermoelectric performance of caged compounds through light-element Filling. *Applied Physics Letters*, 95:042101, 2009.

[259] X. Shi et al. Band Structure Engineering and Thermoelectric Properties of Charge-Compensated Filled Skutterudites. *Scientific Reports*, 5:14641, 2015.

[260] Y.Z. Pei, L.D. Chen, W. Zhang, X. Shi, S.Q. Bai, X.Y. Zhao, Z.G. Mei, and X.Y. Li. Synthesis and thermoelectric properties of $K_yCo_4Sb_{12}$. *Applied Physics Letters*, 89:221107, 2006.

[261] W. Leithe-Jasper et al. Ferromagnetic Ordering in Alkali-Metal Iron Antimonides: $NaFe_4Sb_{12}$ and KFe_4Sb_{12}. *Applied Physics Letters*, 91:037208, 2003.

[262] J. Eilertsen, R. Berthelot, A.W. Sleight, and M. A. Subramanian. Structure and transport behavior of In-filled cobalt rhodium antimonide skutterudites. *Journal of Solid State Chemistry*, 190:238–245, 2012.

APPENDICES

Appendix A: Charge Transfer Instability in a Mixed Ir/Rh Honeycomb Lattice in $Li_2Ir_{1-x}Rh_xO_3$ Solid Solution

A.1 Abstract

The solid solution series $Li_2Ir_{1-x}Rh_xO_3$ is synthesized for several values of x between 0 and 1. The compounds possess a monoclinic layered structure (space group $C2/m$) throughout the solid solution range with the lattice constants following Vegard's relationship. Magnetization and resistivity data below room temperature are presented. The effective magnetic moment (μ_{eff}) is reduced below the value obtained by interpolating between the end-members, presumably due to nearest neighbor charge exchange leading to non-magnetic Ir^{5+}/Rh^{3+} pairs. Surprisingly, the degree of reduction of eff cannot be explained by a random mixture of Ir and Rh and, in particular, is strongly asymmetric around $x = 0.5$. This anomalous moment reduction possibly results from the difference in on-site Coulomb repulsion between Ir and Rh ions.

Publication based on this chapter:

1. L.S. Kumari, M.K. Wallace, J.T. Barnes, B. Tong, A.P. Ramirez, and M.A. Subramanian. Charge transfer instability in a mixed Ir/Rh honeycomb lattice in $Li_2Ir_{1-x}Rh_xO_3$ solid solution. *Solid State Sci.*, 61:232-238, 2016.

A.2   Introduction

With the prospect of new science and technology in topological insulators, systems with strong spin-orbit coupling (SOC) are of great interest within the solid state science community. Through numerous studies, strong SOC systems have been shown to exhibit many unconventional properties that challenge existing theory. In particular, many A_2MO_3 "honeycomb" layered oxides where A is an alkali atom and M is a 4d or 5d element, show unique electronic and magnetic properties indicative of SOC [1-10]. These properties also reflect the lamellar structure, composed of alternating layers of pure Li and mixed LiM_2 units in a cubic-close-packed oxide array [11]. The LiM_2 layers are composed of a hexagonal network of edge sharing MO_6 octahedra where a single Li^+ ion occupies the centers of the resulting hexagons (Figure A.1).

The honeycomb lattice iridates A_2IrO_3 (A = Li, Na) are especially important since Ir has the strongest SOC among magnetic d-electron elements and these materials have been proposed alternatively as candidates for either topologically insulating or Kitaev quantum spin liquid states [12,13]. For Li_2IrO_3, three different polytypes are known. In α-Li_2IrO_3, edge-sharing IrO_6 octahedra form a simple two-dimensional (2D) honeycomb layered structure [11]. For β-and γ-Li_2IrO_3, however, the edge shared IrO_6 octahedra form three dimensional (3D) connected arrangement [14,15]. Specifically, these Li_2MO_3 polytypes are Li_2MnO_3-type ($C2/m$) and Li_2SnO_3-type ($C2/c$) with the difference being the stacking of the LiM_2 layers along the c-axis (Figure A.2) [16]. There has been some controversy in the lit-
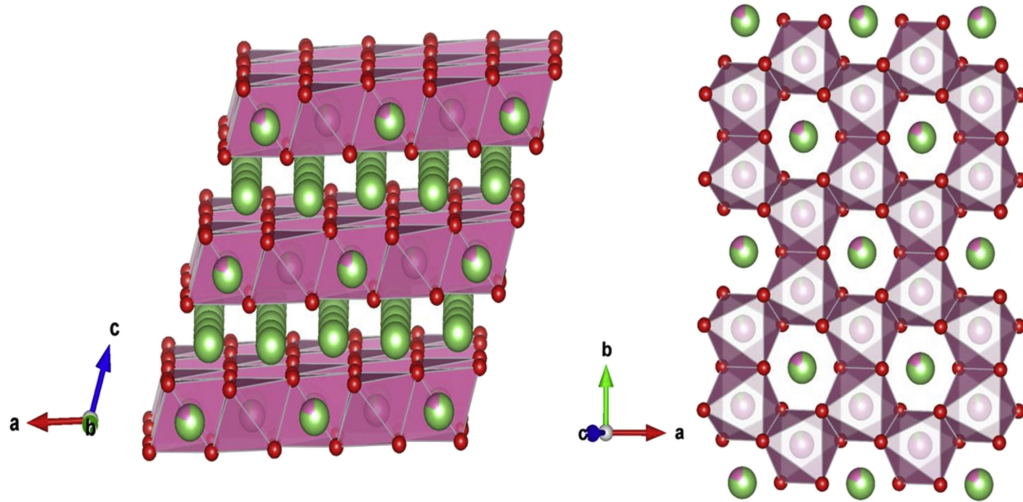
Figure A.1: (a) Li_2MO_3 (M = Ir, Rh) structure as alternating layers of Li^+ and LiM_2 and (b) LiM_2 layer where MO_6 octahedra form the honeycomb like lattice. Green, pink and red spheres represent lithium, metal, and oxygen atoms respectively.

erature regarding the space group of Li_2IrO_3, particularly between $C2/c$ ($Z = 8$) symmetry or $C2/m$ ($Z = 4$) symmetry [8,11]. Recent work, confirmed in the present study, shows that higher symmetry $C2/m$ is the appropriate space group for Li_2IrO_3 [11,17]. It is known that Li_2IrO_3 is electrically insulating with an effective magnetic moment $\mu_{eff} = 1.83$ μ_B and an antiferromagnetically ordered state below 15 K [17,18]. This behavior has been described as that of a Mott insulator with magnetism of a Heisenberg-Kitaev interaction arising from SOC [18]. The isoelectronic $4d^5$ honeycomb compound Li_2RhO_3 which crystallizes in the $C2/m$ structure has been explored, and is also found to be an insulator [19,20]. Long range magnetic order was not observed in this system but the susceptibility displays a frequency-dependent feature consistent with a spin glass state below a

freezing temperature, $T_f = 5$ K [21]. Since the Weiss temperature, θ_W, is 50K, the ratio θ_W/T_f of roughly 10 suggests strong geometrical frustration, although the presence of stacking faults, discussed below introduces a random component to the mean field. While the isoelectronic and isostructural honeycomb iridates and rhodates are both insulators, the analogous comparison of the square-lattice systems Sr_2IrO_4 and Sr_2RhO_4, shows a transition from insulating to metallic ground state [22,23]. The absence of such a transition in the honeycomb systems has been suggested to result from the combined effect of (i) quasi-molecular orbitals, which effect a band insulator, and (ii) the interplay between SOC and Coulomb correlations [20]. An important difference between the Ir and Rh honeycomb systems is a change of μ_{eff}, from 1.83 μ_B in the large-SOC Li_2IrO_3 [18] to 2.2 μ_B in Li_2RhO_3 [20]. In the present work, we study the solid solution series $Li_2Ir_{1-x}Rh_xO_3$, in particular to examine the change in both μ_{eff} as well as charge transport across the series. We find a strong moment reduction on the Rh-rich side of the series, which supports the notion that on-site Coulomb energy in the Rh-rich compounds plays an important role in charge localization.

A.3   Experimental

Polycrystalline samples of $Li_2Ir_{1-x}Rh_xO_3$ ($x = 0$, 0.2, 0.4, 0.5, 0.6, 0.8 and 1) were prepared by intimately mixing and grinding stoichiometric amounts of Li_2CO_3 (Sigma, 99.8%), IrO_2 and Rh_2O_3 (Matthey, 99.99%) in an agate mortar. The Li_2CO_3 was dried at 120 C overnight, and the IrO_2 was obtained by decomposing
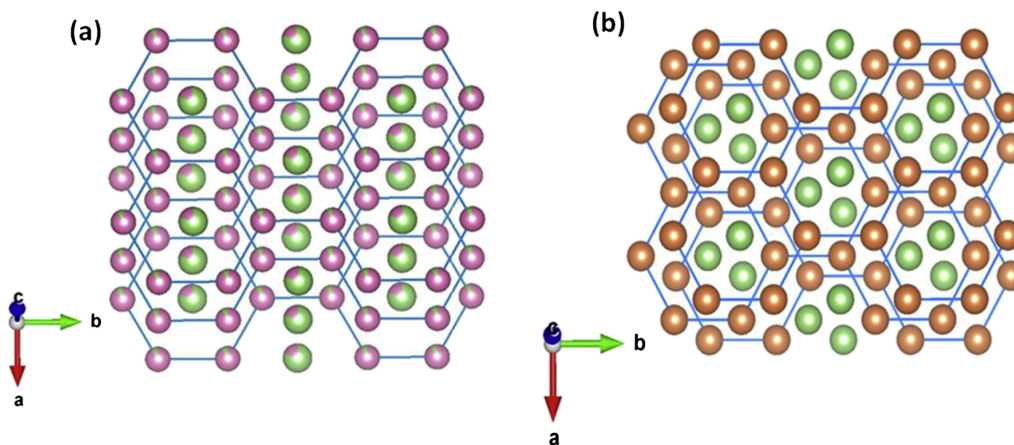
Figure A.2:   Stacking of LiM$_2$ layers in (a) Li$_2$MnO$_3$- type ($C2/m$) and (b) Li$_2$SnO$_3$-type ($C2/c$) structure when viewed along the c-axis. Green, purple and orange spheres represent lithium, manganese and tin atoms respectively. Oxygen atoms are omitted for clarity.

IrCl$_3$ (Alfa Aesar, 99.9%) at 750 C for 10 h under air flow. For all synthesis processes, 5% excess Li$_2$CO$_3$ was added to compensate for high temperature lithium volatility. The samples were then pelletized and sintered in oxygen flow at 950 C for 24 h for all samples except Li$_2$RhO$_3$ which was sintered at 850 C for 24 h with intermittent grinding. All samples were black in color. X-ray diffraction (XRD) characterization was done on a Rigaku Miniflex II diffractometer using Cu K$_\alpha$ radiation and a graphite monochromator. Seebeck and resistivity measurements were performed at high temperatures (300–800 K) on an ULVACRIKO ZEM 3 under a static helium atmosphere. Low-temperature (5–300 K) magnetization measurements were obtained with a Quantum Design MPMS and resistivity (50–300 K) measurements were obtained using a Quantum Design PPMS.

A.4   Results and Discussion

A.4.1   Structural Properties

Polycrystalline samples of complete solid solution between Li_2IrO_3 and Li_2RhO_3 were successfully synthesized. Figure A.3(a) shows the XRD patterns of the samples crystallizing in monoclinic layered structure with space group $C2/m$. The a-, b- and c-lattice parameters decrease marginally with increasing x in $Li_2Ir_{1-x}Rh_xO_3$ as shown in Figure A.3(b). This trend is expected given the small difference in ionic radii between Ir^{4+} (0.625) and Rh^{4+} (0.60) [24]. Figure A.4(a,b) shows changes in the β angle and the unit cell volume as a function of x. It is noticed that the reflections in the XRD patterns are very weak between 2θ of 19^0 and 33^0, a region where stacking faults affect the intensity of the hkl reflections and create an asymmetric broadening of the affected reflections. With the exception of Li_2IrO_3, the Le-Bail refinement clearly does not fit the broad asymmetrical peaks within the 2θ region 19–33^0 (Figure A.3).

Refining the $Ir(4g)$–$Li(2a)$ site occupancies did not improve the fit to these asymmetric broad peaks [11]. The broadness of these peaks in this region for other honeycomb layered structures has been attributed also to the existence of stacking faults [16,25,26]. A structure with less peak broadening in the specific stacking fault 2θ region with an increase in temperature is observed for Li_2IrO_3, while the best structurally ordered sample was obtained at 850 C in oxygen atmosphere for Li_2RhO_3.

In order to evaluate the degree of stacking faults of $Li_2Ir_{1-x}Rh_xO_3$ in a quan-
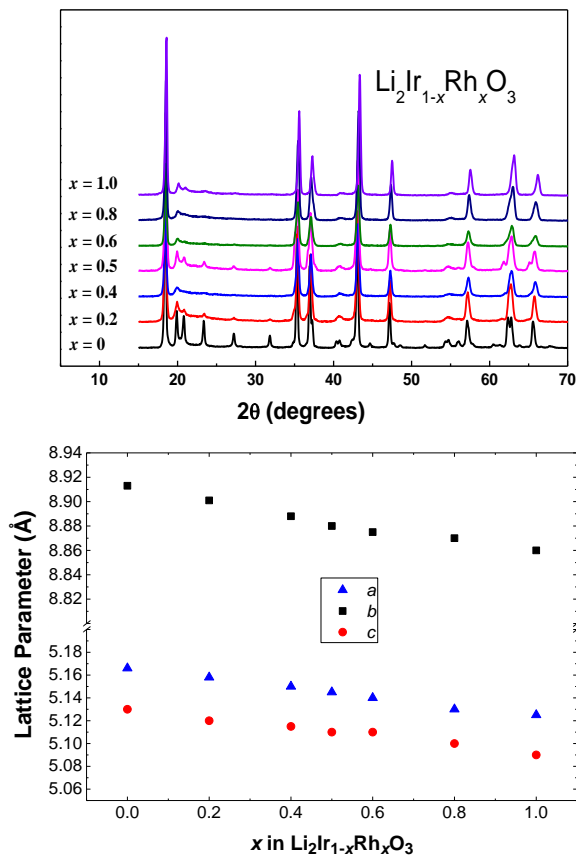
Figure A.3: (a) Powder XRD patterns and (b) lattice parameters for x=0–1 in $Li_2Ir_{1-x}Rh_xO_3$.

titative manner, the DIFFaX software was employed [27] and a model similar to that used by Breger et al. was applied [16]. The DIFFaX software requires the cell axes to be defined such that the c-axis is perpendicular to the fault direction, resulting with a new idealized unit cell. Thus, a hexagonal unit cell with $a_{hex}=a_{C2/m}$ and $c_{hex}=c_{C2/m}\cos(\beta_{C2/m}-90)$ was implemented and individual honeycomb metal oxide layers were defined. As discussed by Breger et. al., in order to replicate
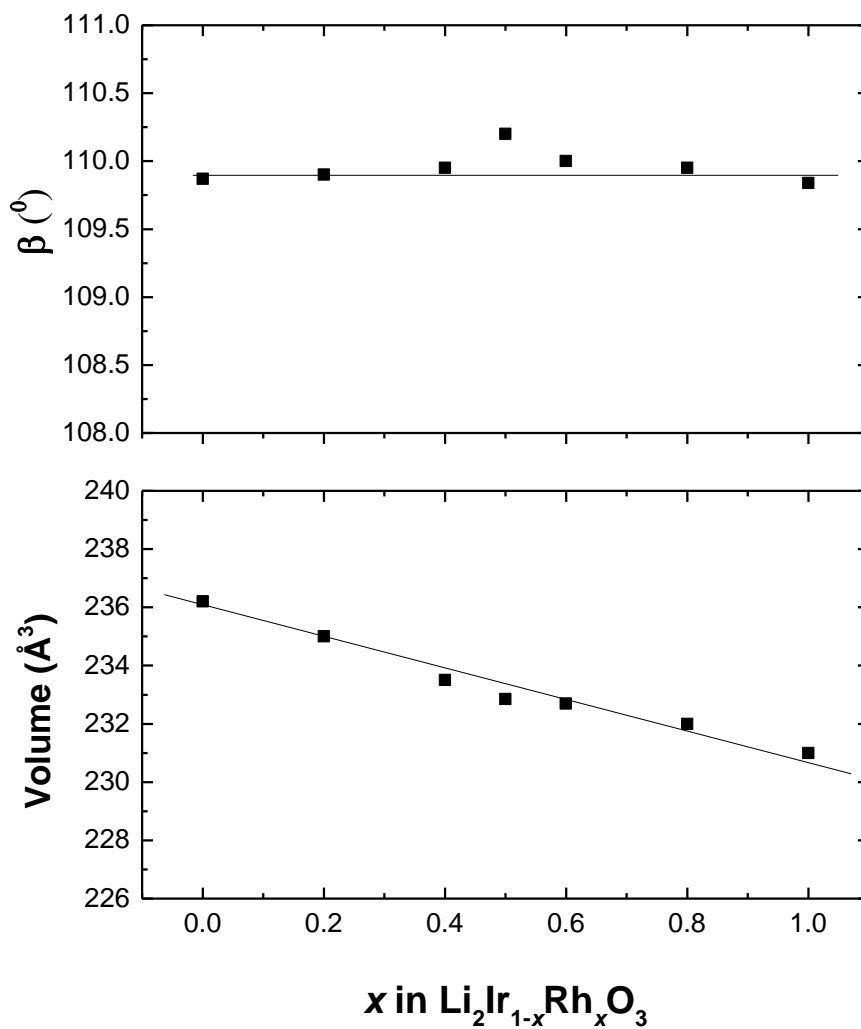
Figure A.4: (a) The β angle and (b) Cell volume as a function of x in $\text{Li}_2\text{Ir}_{1-x}\text{Rh}_x\text{O}_3$.

the $\text{A}_1\text{B}_1\text{C}_1$ stacking sequence of Li_2IrO_3 ($C2/m$), the honeycomb metal oxide layers were characterized by the $[1/3,0,1]$ transition vector (α_1). The rotation of the stacking direction by 120^0 and 240^0 was described by the transition vectors

[2/3,2/3,1] and [0,1/3,1] (α_2 and α_3). Probabilities were assigned to each of the three transition vectors, with $\alpha_1 + \alpha_2 + \alpha_3 = 1$. For the latter two transition vectors, there was no tangible difference in the model when varying the contribution for a given total stacking fault probability. Thus for the models presented, the assumption $\alpha_2 = \alpha_3$ was implemented. Figure A.5 reveals a comparison of XRD patterns in the 2θ region 19–33^0 among the different compounds $Li_2Ir_{1-x}Rh_xO_3$ ($x = 0$, 0.5 and 1) (blue line), along with simulated DIFFaX best fit XRD patterns with corresponding stacking fault percentages (red line). These simulated XRD patterns supports the conjecture that the asymmetrical broadness of the peaks is due to the presence of stacking faults. As expected, a higher density of stacking faults is estimated for the honeycomb Li_2RhO_3 (30%) compared to Li_2IrO_3 (5%).

A.4.2   Electrical Properties

The magnetic susceptibility $\chi(T)$, was measured for in a magnetic field of H = 0.5T. Both Li_2IrO_3 and Li_2RhO_3 display paramagnetic behavior above 50 K [8,21]. Figure A.6 shows the magnetic susceptibility for the series as function of temperature. The behavior of the end members is consistent with previous results that show deviations in Curie-Weiss behavior indicative of antiferromagnetic interaction at 15 K for Li_2IrO_3 and spin freezing 6 K for Li_2RhO_3 [18,21]. The inverse susceptibility, $1/\chi(T)$ is fit by the Curie-Weiss form, $\chi = C/(T-\theta) - \chi_{vv}$, where C is the Curie constant, θ is the Weiss constant and χ_{vv} a van Vleck temperature independent term. The μ_{eff}, values reported here were obtained by selecting, for each x, a
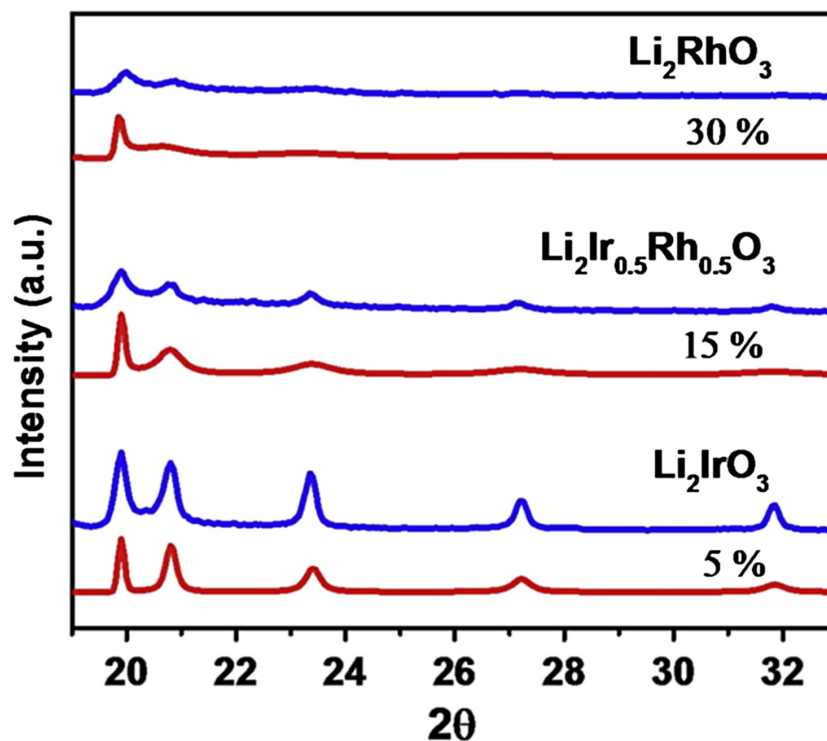
Figure A.5: DIFFaX simulated (red line) and experimental powder XRD patterns (blue line) for $Li_2Ir_{1-x}Rh_xO_3$ ($x = 0$, 0.5 and 1.0) in the region $2\theta = 19–33^0$.

χ_{vv} that provides the smallest sum of the variances (χ^2) for a linear fit to $1/\chi(\text{T})$. Resulting fits between 100 and 300 K yields μ_{eff} values of $1.87\mu_B$ for Li_2IrO_3 and $2.03 \mu_B$ for Li_2RhO_3 (Figure A.6b). These values of μ_{eff} are close to the expected spin only μ_{eff} value for Ir (IV) and Rh (IV) in octahedral coordination ($1.73 \mu_B$), with the differences being attributable to SOC through the g-factor. We see that μ_{eff} decreases with increasing Rh concentration until the region $0.5 < \text{x} < 0.8$ and then increases to $2.03 \mu_B$ for $x = 1$ (Figure A.7(a)). The θ values are 35.0 K and 57.7 K for Li_2IrO_3 and Li_2RhO_3 respectively which indicate antiferromagnetic interactions, consistent with a Curie-Weiss analysis for T > 100 K. Thus, the Ir-Rh

solid solutions show systematic paramagnetic behavior and the AFM transition in Li_2IrO_3 is suppressed quickly by Rh substitution over the entire measurement region.
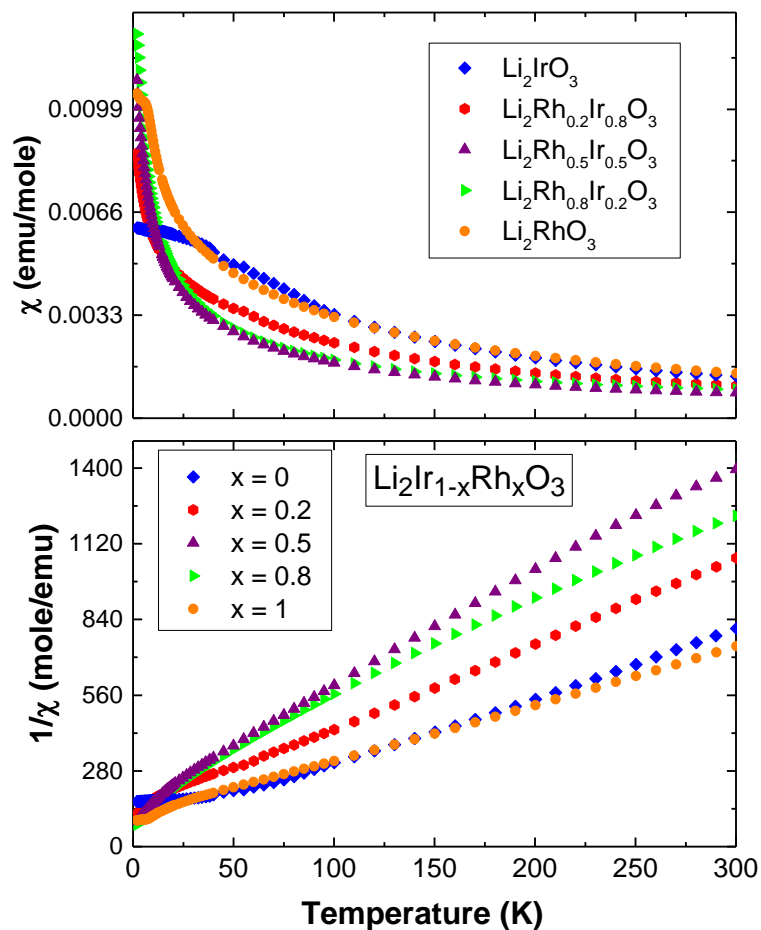
Figure A.6: Temperature dependence of magnetic susceptibility (χ) plot (top) and inverse magnetic susceptibility ($1/\chi$) plot (bottom) for $Li_2Ir_{1-x}Rh_xO_3$ ($x = 0$, 0.2, 0.5, 0.8 and 1.0).

A reduced moment is difficult to explain if one assumes a random spatial config-

uration of only Ir^{4+} and Rh^{4+} ions, since i) the local environment does not change over the series, and ii) the spin-spin interaction, as derived from the Weiss constants is too small to cause an effective moment reduction above 100 K. As noted in Rh-dilution studies of the square lattice system Sr_2IrO_4, however [28,29], Ir can be readily stabilized in the pentavalent configuration (Ir^{5+}) and Rh in the trivalent configuration (Rh^{3+}), both of which are non-magnetic. Thus it is possible for the $Li_2Ir_{1-x}Rh_xO_3$ solid solution members to have a lower effective moment and still maintain ionic charge balance if a fraction of Ir^{4+} ions transfers an electron to a neighboring Rh^{4+} ion, resulting in a Ir^{5+}/Rh^{3+} pair. The driving force for such a charge transfer (CT) mechanism might be the different on-site Coulomb repulsion energy U, which is 3–4 eV for 4d metals, about twice that found for 5d metals [20]. Since the honeycomb lattice is bipartite, full magnetic compensation at x = 0.5 is possible if the site occupancy is perfectly ordered. Away from $x = 0.5$, and for maximum magnetic compensation, a lower limit for the effective moment is $\mu_{eff}=\sqrt{1-2y}\mu_m$, where y is the fraction of the total that are minority spins ($y = x$ or (1-x) for x < or >0.5 respectively and μ_m is the effective moment of the majority ion. For $x<$ 0.5, $\mu_m = \mu_{eff}(Ir^{4+}) = 1.86\ \mu_B$ and for $x>$ 0.5, $\mu_m = \mu_{eff}\ (Rh^{4+}) = 2.03\ \mu_B$. This lower limit is plotted in Figure A.7(a). Clearly, the observed μ_{eff} show only partial compensation, indicating that randomness is important for determining the number of uncompensated magnetic ions. In order to estimate $\mu_{eff}(x)$ we construct a simple model in which the sites of a 13 x 13 honeycomb lattice are randomly occupied by (1-x) Ir^{4+} and x Rh^{4+} ions. We then step through the lattice and identify Ir^{4+}/Rh^{4+} nearest neighbor pairs, which are

assumed to undergo CT and become non-magnetic. If more than one pair can be formed, we randomly select one of them. The value of μ_{eff} is obtained by first counting the resulting unpaired atoms and assigning them the appropriate moment, either Ir^{4+} or Rh^{4+}. The effective moment in this "unscreened" model is then given by $\mu_{us}=[z_{Ir}\mu_{Ir^{4+}}^2+z_{Rh}\mu_{Rh^{4+}}^2]^{1/2}$, where z_{Ir} and z_{Rh} is the fraction of free Ir and Rh moments respectively. Simulations are performed for different starting configurations, and different ratios of Ir and Rh, and the uncertainty in μ_{eff} derived from the resulting spread of μ_{us} values. As shown in Figure A.7, μ_{us} obtained by this method is greater than the maximum pairing assumption at all x, as expected. In addition, μ_{us} is approximately symmetric about $x = 0.5$, with the small asymmetry arising from the slightly different μ_{eff} values for Ir^{4+} and Rh^{4+}. A much larger asymmetry is displayed by the observed μ_{eff} values, discussed next.

As seen in Figure A.7(a), the measured μ_{eff} is larger than μ_{us} for $x < 0.5$, and smaller than μ_{us} for $x > 0.5$. Thus, in the Ir-rich phase the CT mechanism leading to Ir^{4+}/Rh^{3+} pairs seems to be screened, fewer CT pairs thus formed, and the density of residual magnetic moments is larger than expected in the unscreened scenario.

The source of such screening is not obvious, but may lie in the spin-orbit splitting of the Ir^{4+} six-fold t_{2g} multiplet, which is larger than in Rh, thus providing a barrier for charge transfer. As x increases towards 0.5, μ_{eff} approaches μ_{us}. As mentioned above, however, the number of stacking faults becomes substantial for x > 0.5. It is also likely that concurrently, the density of anti-site defects, in which Rh ions exchange places with Li, also becomes substantial. While the
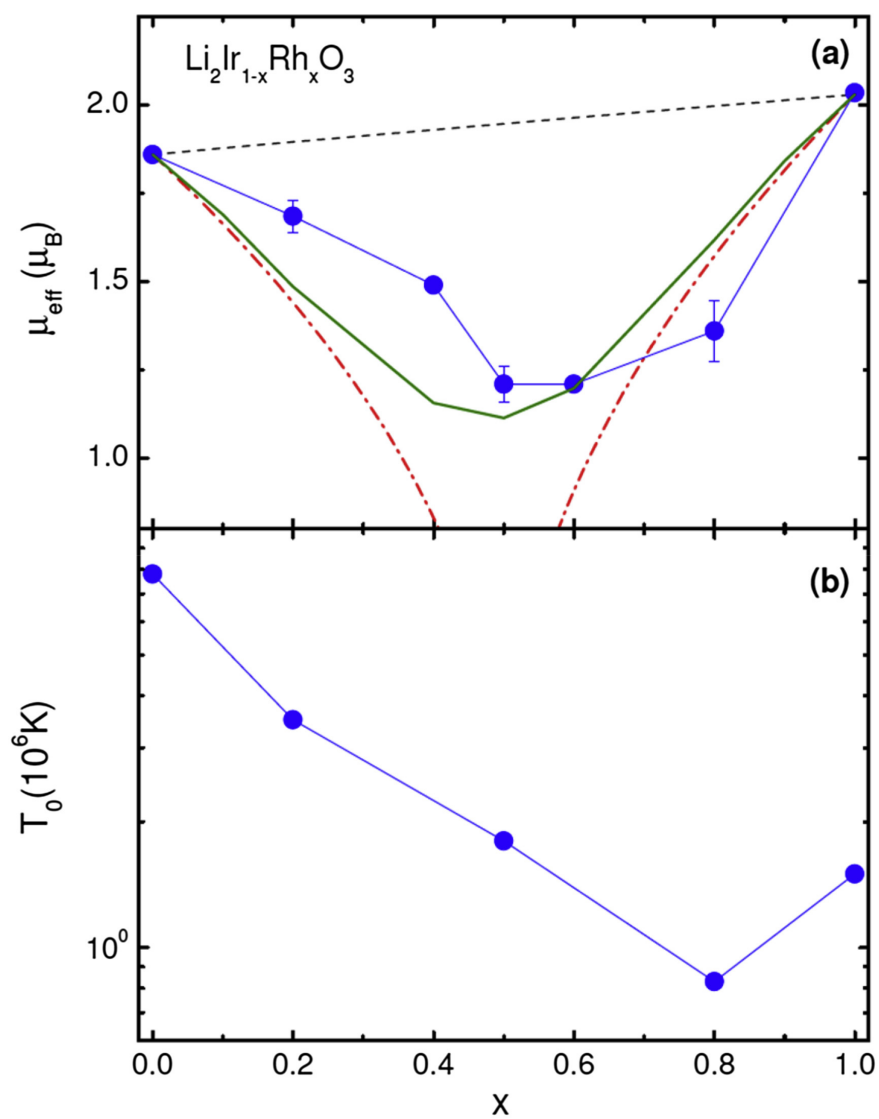
Figure A.7: (a) Variation of effective moment, μ_{eff}, with x in $Li_2Ir_{1-x}Rh_xO_3$ (solid blue circles). Models of μ_{eff} variation discussed in the text are simple interpolation (dashed black line), charge-transfer between Ir^{4+}/Rh^{4+} pairs in an ordered lattice (dashed-dot red line) and unscreened random charge-transfer, μ_{us} (solid green line). (b) The variation of the characteristic temperature, T_0, in a 2D variable range hopping model with x. Lines are drawn to guide the eye.

Li environment is octahedral, similar to the Ir or Rh environment, and as such the moment would be preserved, such an effect would work in opposition to the CT mechanism since it would reduce the number of nearest neighbor Ir^{4+}/Rh^{4+} pairs. For x > 0.5, μ_{eff} is smaller than μ_{us}, which cannot be explained solely with local moments. We know, however, that μ_{eff} of Li_2RhO_3 is well-explained by local moments, which has been interpreted to result from the combination of quasi-molecular orbitals and large onsite U, as discussed by Mazin et al. [20]. A possible explanation for the reduction in μ_{eff} for x > 0.5 might lie in an enhanced charge mobility since delocalization correlates with reduced local moment. Such an "over-screened" CT process is reflected in resistivity, $\rho(T)$,which is reduced for $0.5 < x < 1.0$, as discussed next.

Low temperature $\rho(T)$, data for the compounds $x = 0$, 0.2, 0.5, 0.8 and 1.0 are shown in Figure A.8(a). The room temperature values for the two end members are in reasonable agreement with previous experimental results [17,19,21] and $\rho(T)$, is semiconductor-like over the entire range of measurement. The $\rho(T)$, data for Li_2RhO_3 is consistent with results of Luo et al. but is, not surprisingly, an order of magnitude greater than the high-frequency (>1 MHz) results of Todorova et al. [19,21]. Previous transport studies on related honeycomb systems explained $\rho(T)$, in terms of 3D variable range hopping (VRH) for Na_2IrO_3 [1] and Li_2RhO_3 [21], and 2D VRH for the $Li_2Ir_{1-x}Ru_xO_3$ [17]. We analyzed our data using the general formula for VRH ($\rho=\rho_0\exp[(T_0/T)^{(1/(d+1))}]$) where d is the dimensionality, and ρ_0 and T_0 are fitting parameters. We found that the reduced χ^2 of the fits for all compounds except $x = 0.8$ were minimized at $d = 2$, supporting the notion of

transport mainly within the honeycomb lattice.
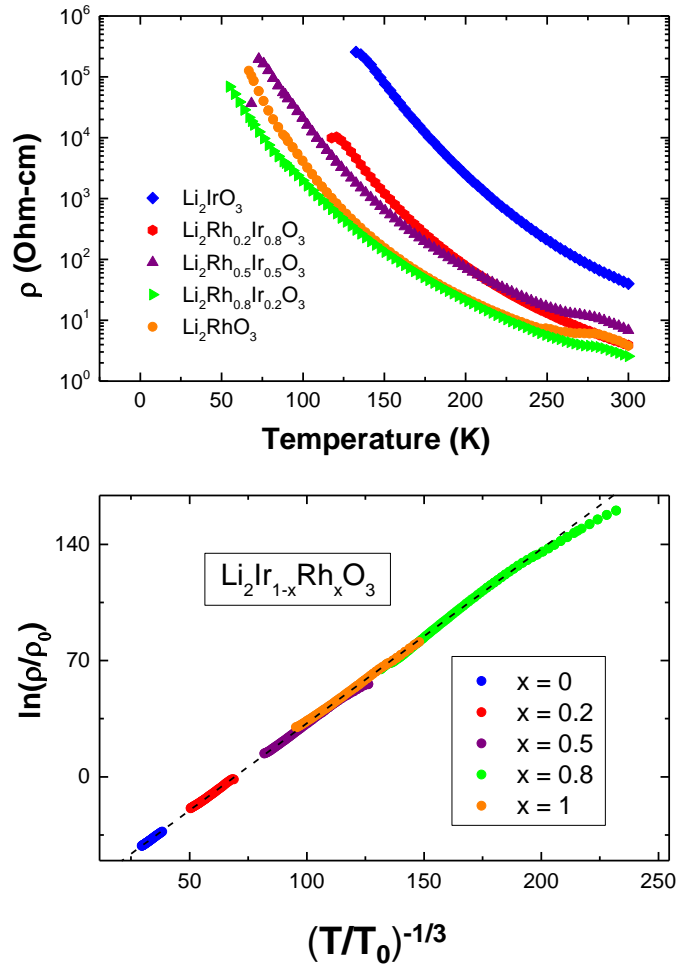
Figure A.8: Temperature-dependent, low-temperature resistivity plot (top) and 2D VRH plot for $Li_2Ir_{1-x}Rh_xO_3$ ($x = 0, 0.2, 0.5, 0.8$ and 1.0) (bottom).

The T_0 and ρ_0, values obtained from these fits for each sample are listed in Table A.1. In Figure A.8(b) we show the resistivity data for all samples collapsed onto a $d = 2$ VRH model. While the agreement is generally very good, the $x =$

0.8 compound deviates significantly from VRH behavior in a manner that suggests a temperature-independent conduction channel in parallel with the 2D channel. Given the large number of stacking faults on the Rh-rich side of the series, it is possible that the related anti-site disorder [30] along with the lower U of Ir combine to create such a channel. High temperature resistivity and Seebeck coefficients for $x = 0$, 0.2, 0.5, 0.8 and 1.0 are shown in Figure A.9. All samples are observed to be p-type semiconductors. However a transition from n-type to p-type is expected for Li_2RhO_3 as observed by the negative S for it at room temperature suggesting carriers of both signs which is temperature dependent [31]. We note the large value of S found for $x = 1$, which suggests that the on-site Coulomb energy, suspected as a contributor to the small moments in the intermediate-x range, is playing a substantial role in charge transport.

Table A.1: The fitting parameters T_0 and ρ_0 for $Li_2Ir_{1-x}Rh_xO_3$ ($x = 0$, 0.2, 0.5, 0.8 and 1.0).

Composition	T_0(K)	ρ_0 (Ohm-cm)
x = 0	7.80×10^7	3.75×10^{-11}
x = 0.2	3.51×10^7	1.79×10^{-9}
x = 0.5	1.84×10^7	1.23×10^{-7}
x = 0.8	9.16×10^5	5.35×10^{-7}
x = 1.0	1.50×10^7	7.31×10^{-8}
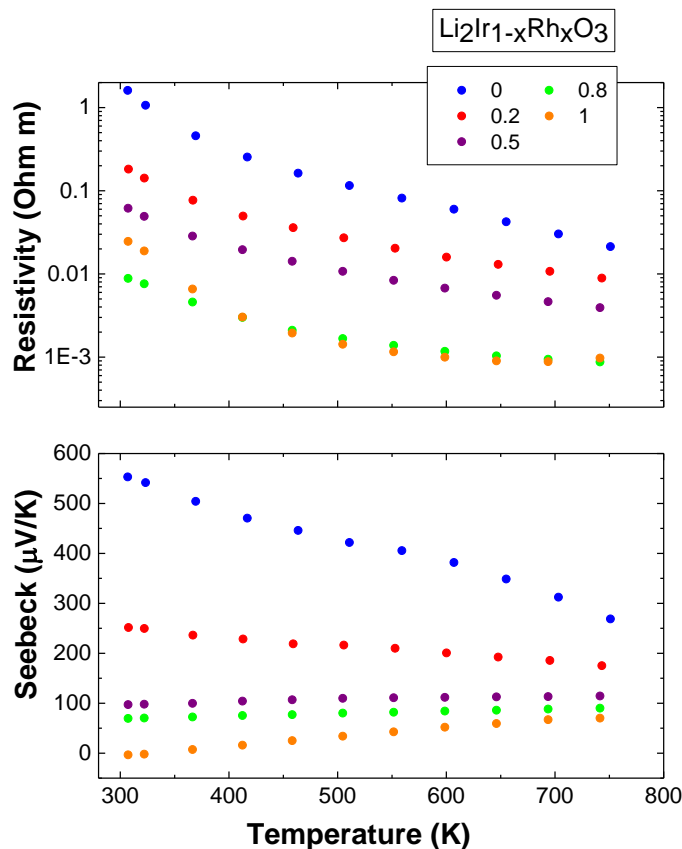
Figure A.9: (a) Temperature dependent, high temperature resistivity and (b) Seebeck coefficient plot for $Li_2Ir_{1-x}Rh_xO_3$ ($x = 0$, 0.2, 0.5, 0.8 and 1.0).

A.5 Summary

We have synthesized the solid solution series $Li_2Ir_{1-x}Rh_xO_3$ and studied it using magnetic and transport probes. We find a marked reduction of the effective moment over the entire range of dilution. This moment reduction is understood to arise from several factors: a charge transfer process between Ir^{4+}/Rh^{4+} pairs leading to nonmagnetic Ir^{5+}/Rh^{3+} pairs; large spin orbit splitting of the t_{2g} multiplet

on the Ir-rich side of the series; and large onsite U on the Rh-rich side of the series. Anti-site mixing may play a role in reducing the number of charge transfer processes. Apart from the complication introduced by anti-site mixing, the present study illuminates some of the issues associated with controlling the valence state in heavy d-element compounds. First, related to the high oxidation states of these $j = 1/2$ species, stable neighboring oxidation states are often found, and can be induced by the doping process itself. Second, the tendency towards itineracy is balanced not only by the onsite U, but also by SOC. Finally, the combined effects of small-U Ir and large-U Rh can have dramatic consequences for transport in these systems.

A.6   TOF Neutron Diffraction Refinements (not in manuscript)

Time of Flight (TOF) neutron diffraction measurements for $Li_{2-x}Ir_{1-x}Rh_xO_3$ samples were collected at Oak Ridge National Laboratory POWGEN BL-11A SNS beamline. Rietveld refinement of $Li_2Ir_{0.2}Rh_{0.8}O_3$ nominal composition sample is shown in Figure A.10. A pseudo-Voigt peak shape profile was chosen and parameters refined to obtain the best fitt to the collected data. The space group was refined to be $C2/m$, with lattice dimensions $a = 5.135$ Å, $b = 8.871$ Å, $c = 5.112$ Å, and $\beta = 109.92^0$. Rietveld refinement shows a $wR_p = 3.19\%$. The atomic coordinates, occupancies, and isotropic displacement parameters are represented in Table A.2. For $C2/m$ there are two unique atomic positions to describe describe the Li and Ir/Rh sites within the $Li(Ir/Rh)_2$ layer. Shown in Table A.2,

corresponding sites are labeled as $4g$ and $2a$ wyckoff sites. If no Li-M site disorder existed within the LiM$_2$ layer, only Ir/Rh($4g$) and Li($2a$) would exist, with the Ir/Rh($4g$) site describing the honeycomb ring. As shown from Table A.2 occupancies, a small percentage ($\approx$13%) of Li-M site disorder exists within the Li(Ir/Rh)$_2$ layer. As shown by the $2d$ and $4h$ refined occupancies, no Ir/Rh was detected within the Li-layers. The stoichiometry derived from occupancy refinements is Li$_2$Ir$_{0.203}$Rh$_{0.797}$O$_3$.
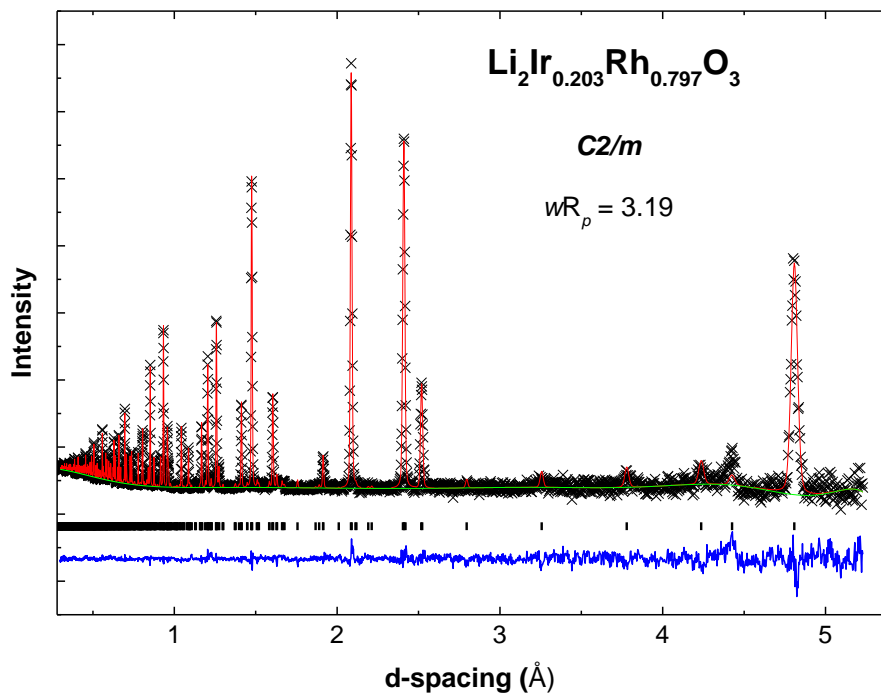
Figure A.10: TOF Neutron refinement of nominal composition $Li_2Ir_{0.2}Rh_{0.8}O_3$. Observed (black crosses) and calculated (solid red line) profiles, background (green), and difference curve (I_{obs} - I_{calc}) (blue) are shown for each refinement. The vertical bars indicate the expected reflection positions with black representing $Li_2Ir_{0.2}Rh_{0.8}O_3$ $C2/m$. Resulting stoichiometric identities and wRp are represented.

	Wyckoff	x	y	z	occ	U_{iso}
Rh^{+4}	$4g$	0	0.3321(4)	0	0.73(5)	0.0014(2)
Li^{+1}	$4g$	0	0.3321(4)	0	0.13(5)	0.0014(2)
Ir^{+4}	$4g$	0	0.3321(4)	0	0.13(5)	0.0014(2)
Li^{+1}	$2a$	0	0	0	0.73(5)	0.0020(2)
Ir^{+4}	$2a$	0	0	0	0.13(5)	0.0020(2)
Rh^{+4}	$2a$	0	0	0	0.13(5)	0.0020(2)
Li^{+1}	$2d$	0	0.5	0.5	1	0.0021(2)
Li^{+1}	$4h$	0	0.8112(1)	0.5	1	0.0042(2)
O^{2-}	$8j$	0.2501(6)	0.3292(8)	0.7663(5)	1	0.0066(9)
O^{2-}	$8j$	0.2674(8)	0	0.7665(2)	1	0.0082(3)

Table A.2: Atomic coordinates, occupancies and isotropic displacement parameters obtained from Rietveld refinement ($C2/m$) of TOF Neutron (Oak Ridge POWGEN BL-11A SNS) diffraction data.

References

1. Y. Singh, P. Gegenwart, *Phys. Rev. B* 82 (2010) 1-7.

2. S. Manni, S. Choi, I.I. Mazin, R. Coldea, H.O. Jeschke, R. Valenti, et al., *Phys. Rev. B* 89 (1-7) (2014) 245113.

3. E. Mccalla, A.M. Abakumov, D. Foix, E.J. Berg, G. Rousse, M. Doublet, et al., *Science* 350 (2015) 1516-1521.

4. S. Okada, J. Yamaki, K. Asakura, H. Ohtsuka, H. Arai, S. Tobishima, et al., *Electrochim. Acta* 45 (1999) 329-334.

5. I. Felner, I.M. Bradaric, *Phys. B Condens. Mater.* 311 (2002) 195-199.

6. A.C.W.P. James, J.B. Goodenough, *J. Solid State Chem.* 76 (1988) 87-96.

7. Y.V. Baklanova, .V. Ishchenko, .. Denisova, L.G. Maksimova, B.V. Shulgin, V.. Pustovarov, et al., *Opt. Mater.* 34 (2012) 1037-1041.

8. H. Kobayashi, M. Tabuchi, M. Shikano, H. Kageyama, R. Kanno, *J. Mater. Chem.* 13 (2003) 957-962.

9. A. Sinha, S.R. Nair, P.K. Sinha, *J. Nucl. Mater.* 399 (2010) 162-166.

10. M.I. Pantyukhina, V.P. Obrosov, A.P. Stepanov, *Crystallogr. Rep.* 49 (2004) 676-679.

11. M.J. O'Malley, H. Verweij, P.M. Woodward, *J. Solid State Chem.* 181 (2008) 1803-1809.

12. A. Biffin, R.D. Johnson, S. Choi, F. Freund, S. Manni, A. Bombardi, et al., *Phys. Rev. B* 90 (1-14) (2014) 205116.

13. S.C. Williams, R.D. Johnson, F. Freund, S. Choi, A. Jesche, I. Kimchi, et al., *Phys. Chem.* 93 (1-13) (2016) 195158.

14. K.A. Modic, T.E. Smidt, I. Kimchi, N.P. Breznay, A. Biffin, S. Choi, et al., *Nat. Commun.* 5 (2014) 1-6.

15. T. Takayama, A. Kato, R. Dinnebier, J. Nuss, H. Kono, L.S.I. Veiga, et al., *Phys. Rev. Lett.* 114 (1-5) (2015) 077202.

16. J. Breger, M. Jiang, N. Dupre, Y.S. Meng, Y. Shao-Horn, Gerbrand Ceder, et al., *J. Solid State Chem.* 178 (2005) 2575-2585.

17. H. Lei, W. Yin, Z. Zhong, H. Hosono, *Phys. Rev. B* 89 (1-5) (2014) 020409.

18. Y. Singh, S. Manni, J. Reuther, T. Berlijn, R. Thomale, W. Ku, et al., *Phys. Rev. Lett.* 108 (1-5) (2012) 127203.

19. V. Todorova, M. Jansen, Z. Anorg, *Allg. Chem.* 637 (2011) 37-40.

20. I.I. Mazin, S. Manni, K. Foyevtsova, H.O. Jeschke, P. Gegenwart, *Phys. Rev. B* 88 (1-7) (2013) 035115.

21. Y. Luo, C. Cao, B. Si, Y. Li, J. Bao, H. Guo, *Phys. Rev. B* 87 (1-6) (2013) 161121.

22. N.S. Kini, A.M. Strydom, H.S. Jeevan, C. Geibel, S. Ramakrishnan, *J. Phys. Condens. Mater.* 18 (2006) 8205-8216.

23. R.S. Perry, F. Baumberger, L. Balicas, N. Kikugawa, N.J.C. Ingle, A. Rost, et al., *New J. Phys.* 8 (2006) 1-14.

24. R.D. Shannon, *Acta Cryst.* A32 (1976) 751-767.

25. W. Schmidt, R. Berthelot, L. Etienne, A. Wattiaux, M.A. Subramanian, *Matter. Res. Bull.* 50 (2014) 292-296.

26. Z. Lu, J.R. Dahn, *Chem.* 13 (2001) 2078-2083.

27. M.M.J. Treacy, J.M. Newsam, M.W. Deem, in: A443, *Proc. Roy.Soc.,* London, 1991.

28. Y. Klein, I. Terasaki, *J. Phys. Condens. Mater* 20 (2008) 295201-295205.

29. Y. Klein, I. Terasaki, *J. Electron. Mater.* 38 (2009) 1331-1336.

30. V.M. Katukuri, S. Nishimoto, I. Rousochatzakis, H. Stoll, J. van den Brink, L. Hozoi, *Sci. Rep.* 5 (1-7) (2015) 14718.

31. J. Flynn, J. Li, A.W. Sleight, A.P. Ramirez, M.A. Subramanian, *Inorg. Chem.* 55 (2016) 2748-2754.

Appendix B: DIFFaX input file

```
1   INSTRUMENTAL
2   X–Ray
3   1.541
4   PSEUDO–VOIGT  0.1  −0.036  0.009  0.6  TRIM
5   STRUCTURAL
6   5.1839  5.1839  4.8037  120.0
7   UNKNOWN
8   9
9   infinite
10
11  LAYER 1
12  None
13  Ir4+ 2 1/9 5/9 0 2.0 1.0
14  Ir4+ 2 4/9 2/9 0 2.0 1.0
15  Li1+ 1 7/9 8/9 0 2.0 1.0
16  O 2− 3 1/9 8/9 1/4 2.0 1.0
17  O 2− 3 4/9 5/9 1/4 2.0 1.0
18  O 2− 3 7/9 2/9 1/4 2.0 1.0
19  Li1+ 1 1/9 2/9 1/2 2.0 1.0
20  Li1+ 1 4/9 8/9 1/2 2.0 1.0
21  Li1+ 1 7/9 5/9 1/2 2.0 1.0
22  O 2− 3 1/9 5/9 3/4 2.0 1.0
23  O 2− 3 4/9 2/9 3/4 2.0 1.0
```

```
24  O 2-  3  7/9  8/9  3/4  2.0  1.0
25  LAYER  2  =  1
26  LAYER  3  =  1
27  LAYER  4  =  1
28  LAYER  5  =  1
29  LAYER  6  =  1
30  LAYER  7  =  1
31  LAYER  8  =  1
32  LAYER  9  =  1
33
34  STACKING
35   recursive  {Statistical  ensemble}
36   infinite  {Infinite  number  of  layers}
37
38  TRANSITIONS
39
40  {Transitions - layer  1}
41  0.0000  0/3  0/3  1.0  {layer  1  to  layer  1}
42  0.0000  1/3  2/3  1.0  {layer  1  to  layer  2}
43  0.0000  2/3  1/3  1.0  {layer  1  to  layer  3}
44  0.7000  1/3  0/3  1.0  {layer  1  to  layer  4}
45  0.1500  2/3  2/3  1.0  {layer  1  to  layer  5}
46  0.1500  0/3  1/3  1.0  {layer  1  to  layer  6}
47  0.0000  1/3  1/3  1.0  {layer  1  to  layer  7}
48  0.0000  2/3  0/3  1.0  {layer  1  to  layer  8}
49  0.0000  0/3  2/3  1.0  {layer  1  to  layer  9}
50
```

```
51  {Transitions − layer 2}
52  0.0000 2/3 1/3 1.0 {layer 2 to layer 1}
53  0.0000 0/3 0/3 1.0 {layer 2 to layer 2}
54  0.0000 1/3 2/3 1.0 {layer 2 to layer 3}
55  0.1500 0/3 1/3 1.0 {layer 2 to layer 4}
56  0.7000 1/3 0/3 1.0 {layer 2 to layer 5}
57  0.1500 2/3 2/3 1.0 {layer 2 to layer 6}
58  0.0000 0/3 2/3 1.0 {layer 2 to layer 7}
59  0.0000 1/3 1/3 1.0 {layer 2 to layer 8}
60  0.0000 2/3 0/3 1.0 {layer 2 to layer 9}
61
62  {Transitions − layer 3}
63  0.0000 1/3 2/3 1.0 {layer 3 to layer 1}
64  0.0000 2/3 1/3 1.0 {layer 3 to layer 2}
65  0.0000 0/3 0/3 1.0 {layer 3 to layer 3}
66  0.1500 2/3 2/3 1.0 {layer 3 to layer 4}
67  0.1500 0/3 1/3 1.0 {layer 3 to layer 5}
68  0.7000 1/3 0/3 1.0 {layer 3 to layer 6}
69  0.0000 2/3 0/3 1.0 {layer 3 to layer 7}
70  0.0000 0/3 2/3 1.0 {layer 3 to layer 8}
71  0.0000 1/3 1/3 1.0 {layer 3 to layer 9}
72
73  {Transitions − layer 4}
74  0.0000 2/3 0/3 1.0 {layer 4 to layer 1}
75  0.0000 0/3 2/3 1.0 {layer 4 to layer 2}
76  0.0000 1/3 1/3 1.0 {layer 4 to layer 3}
77  0.0000 0/3 0/3 1.0 {layer 4 to layer 4}
```

```
78   0.0000  1/3  2/3  1.0  {layer 4 to layer 5}
79   0.0000  2/3  1/3  1.0  {layer 4 to layer 6}
80   0.1500  0/3  1/3  1.0  {layer 4 to layer 7}
81   0.7000  1/3  0/3  1.0  {layer 4 to layer 8}
82   0.1500  2/3  2/3  1.0  {layer 4 to layer 9}
83
84   {Transitions − layer 5}
85   0.0000  1/3  1/3  1.0  {layer 5 to layer 1}
86   0.0000  2/3  0/3  1.0  {layer 5 to layer 2}
87   0.0000  0/3  2/3  1.0  {layer 5 to layer 3}
88   0.0000  2/3  1/3  1.0  {layer 5 to layer 4}
89   0.0000  0/3  0/3  1.0  {layer 5 to layer 5}
90   0.0000  1/3  2/3  1.0  {layer 5 to layer 6}
91   0.1500  2/3  2/3  1.0  {layer 5 to layer 7}
92   0.1500  0/3  1/3  1.0  {layer 5 to layer 8}
93   0.7000  1/3  0/3  1.0  {layer 5 to layer 9}
94
95   {Transitions − layer 6}
96   0.0000  0/3  2/3  1.0  {layer 6 to layer 1}
97   0.0000  1/3  1/3  1.0  {layer 6 to layer 2}
98   0.0000  2/3  0/3  1.0  {layer 6 to layer 3}
99   0.0000  1/3  2/3  1.0  {layer 6 to layer 4}
100  0.0000  2/3  1/3  1.0  {layer 6 to layer 5}
101  0.0000  0/3  0/3  1.0  {layer 6 to layer 6}
102  0.7000  1/3  0/3  1.0  {layer 6 to layer 7}
103  0.1500  2/3  2/3  1.0  {layer 6 to layer 8}
104  0.1500  0/3  1/3  1.0  {layer 6 to layer 9}
```

```
105
106  {Transitions − layer 7}
107  0.1500 2/3 2/3 1.0 {layer 7 to layer 1}
108  0.1500 0/3 1/3 1.0 {layer 7 to layer 2}
109  0.7000 1/3 0/3 1.0 {layer 7 to layer 3}
110  0.0000 0/3 2/3 1.0 {layer 7 to layer 4}
111  0.0000 1/3 1/3 1.0 {layer 7 to layer 5}
112  0.0000 2/3 0/3 1.0 {layer 7 to layer 6}
113  0.0000 0/3 0/3 1.0 {layer 7 to layer 7}
114  0.0000 1/3 2/3 1.0 {layer 7 to layer 8}
115  0.0000 2/3 1/3 1.0 {layer 7 to layer 9}
116
117  {Transitions − layer 8}
118  0.7000 1/3 0/3 1.0 {layer 8 to layer 1}
119  0.1500 2/3 2/3 1.0 {layer 8 to layer 2}
120  0.1500 0/3 1/3 1.0 {layer 8 to layer 3}
121  0.0000 2/3 0/3 1.0 {layer 8 to layer 4}
122  0.0000 0/3 2/3 1.0 {layer 8 to layer 5}
123  0.0000 1/3 1/3 1.0 {layer 8 to layer 6}
124  0.0000 2/3 1/3 1.0 {layer 8 to layer 7}
125  0.0000 0/3 0/3 1.0 {layer 8 to layer 8}
126  0.0000 1/3 2/3 1.0 {layer 8 to layer 9}
127
128  {Transitions − layer 9}
129  0.1500 0/3 1/3 1.0 {layer 9 to layer 1}
130  0.7000 1/3 0/3 1.0 {layer 9 to layer 2}
131  0.1500 2/3 2/3 1.0 {layer 9 to layer 3}
```

```
132  0.0000 1/3 1/3 1.0 {layer 9 to layer 4}
133  0.0000 2/3 0/3 1.0 {layer 9 to layer 5}
134  0.0000 0/3 2/3 1.0 {layer 9 to layer 6}
135  0.0000 1/3 2/3 1.0 {layer 9 to layer 7}
136  0.0000 2/3 1/3 1.0 {layer 9 to layer 8}
137  0.0000 0/3 0/3 1.0 {layer 9 to layer 9}
```

Appendix C: FAULTS input file

```
1   TITLE
2   FAULTS TEST
3
4   INSTRUMENTAL AND SIZE BROADENING
5   !Type Of Radiation
6    Radiation        X–Ray
7   !                 lambda1     lambda2     ratio
8    Wavelength       1.5418      0.0         0.0
9   !instrumental aberrations      zero        sycos       sysin
10   Aberrations                   0.0000      0.0000      0.0000
11                                 0.00        0.00        0.00
12  !instr. broadening    u           v           w           x           Dg          Dl
13   Pseudo−Voigt    0.106138   −0.039704   0.086296    0.063275    579.26
          459.87  TRIM
14   0.0 0.0 0.0 0.0 0.0 0.0 (0.01 0.01 0.01 0.01 100.0 100.0 )
15  STRUCTURAL
16  !a b c gamma
17  Cell   5.123851     5.061555    23.928276          60.00
18        0.0 0.0 0.0 0.0 ( 0.01 0.01 0.1 0.1 )
19
20  ! FullProf Studio commands
21   FST_CMD SEQ 3 1 2 3
22
```

```
23  ! Laue symmetry
24  Symm   none
25  ! number of layer types
26  nlayers 5
27  ! layer width
28  Lwidth infinite
29
30
31  LAYER 1
32  NONE
33  ! Atom name number x y z Biso Occ
34  Atom Li1+ 1 0.85163 0.85163 0.0 1.125 1.0
35       0.0 0.0 0.0 0.0 ( 0.1 0.1 0.1 0.1)
36  Atom Li1+ 2 0.17643 0.17643 0.0 1.125 1.0
37       0.0 0.0 0.0 0.0 ( 0.1 0.1 0.1 0.1)
38  Atom Li1+ 2 0.5 0.5 0.0 5.125 1.0
39       0.0 0.0 0.0 0.0 ( 0.1 0.1 0.1 0.1)
40  Atom O2- 3  0.17724   0.85246   0.04989 1.125 1.0
41       0.0 0.0 0.0 0.0 ( 0.1 0.1 0.1 0.1)
42  Atom O2- 4  0.50000   0.17724   0.04989 1.125 1.0
43       0.0 0.0 0.0 0.0 ( 0.1 0.1 0.1 0.1)
44  Atom O2- 5 0.85164   0.50246   0.04989 1.125 1.0
45       0.0 0.0 0.0 0.0 ( 0.1 0.1 0.1 0.1)
46  Atom Os4+ 6 0.51833 0.85163 0.0952496 5.125 1.0
47       0.0 0.0 0.0 0.0 ( 0.1 0.1 0.1 0.1)
48  Atom Os4+ 7 0.84313 0.17643 0.0952496 5.125 1.0
49       0.0 0.0 0.0 0.0 ( 0.1 0.1 0.1 0.1)
```

```
50  Atom  Li1+  8  0.16749  0.50083  0.0952496  1.125  1.0
51          0.0  0.0  0.0  0.0  (  0.1  0.1  0.1  0.1)
52  Atom  O2−   9  0.50000     0.50000     0.14936  1.125  1.0
53                 0.0  0.0  0.0  0.0  (  0.1  0.1  0.1  0.1)
54  Atom  O2−  10  0.17724     0.17724     0.14936  1.125  1.0
55                 0.0  0.0  0.0  0.0  (  0.1  0.1  0.1  0.1)
56  Atom  O2−  11  0.85244     0.85244     0.14936  1.125  1.0
57               0.0  0.0  0.0  0.0  (  0.1  0.1  0.1  0.1)
58
59
60
61  LAYER  2  =  1
62    LSYM    none
63
64  LAYER  3  =  1
65    LSYM    none
66
67  LAYER  4  =  1
68    LSYM    none
69
70  LAYER  5  =  1
71    LSYM    none
72
73
74    STACKING
75  ! stacking  typ
76     Recursive
```

```
77  !number of layers
78    infinite
79
80  TRANSITIONS
81
82  !layer 1 to layer 1
83   LT 0.0  0.0  0.0  0.0
84       0.0  0.0  0.0  0.0  ( 0.3  0.1  0.1  0.1)
85  !layer 1 to layer 2
86   LT 1.0  −0.6666 0.0  1/5
87       0.0  0.0  0.0  0.0  ( 0.3  0.1  0.1  0.1)
88  !layer 1 to layer 3
89   LT 0.0  −0.333 0.0  0.333
90       0.0  0.0  0.0  0.0  ( 0.3  0.1  0.1  0.1)
91  !layer 1 to layer 4
92   LT 0.0  0.0  0.0  0.0
93       0.0  0.0  0.0  0.0  ( 0.3  0.1  0.1  0.1)
94  !layer 1 to layer 5
95   LT 0.0  0.0  0.0  0.0
96       0.0  0.0  0.0  0.0  ( 0.3  0.1  0.1  0.1)
97
98  !layer 2 to layer 1
99   LT 0.0  0.0  0.3333 0.33333
100      0.0  0.0  0.0  0.0  ( 0.1  0.1  0.1  0.1)
101 !layer 2 to layer 2
102  LT 0.0  0.0  0.0  0.0
103      0.0  0.0  0.0  0.0  ( 0.3  0.1  0.1  0.1)
```

```
104  ! layer 2 to layer 3
105   LT 1.0 −0.6666 0.0 1/5
106      0.0 0.0 0.0 0.0 ( 0.3 0.1 0.1 0.1)
107  ! layer 2 to layer 4
108   LT 0.0 0.0 0.0 0.0
109      0.0 0.0 0.0 0.0 ( 0.3 0.1 0.1 0.1)
110  ! layer 2 to layer 5
111   LT 0.0 0.0 0.0 0.0
112      0.0 0.0 0.0 0.0 ( 0.3 0.1 0.1 0.1)
113
114  ! layer 3 to layer 1
115   LT 0.0 −0.3333 0.0 0.3333
116      0.0 0.0 0.0 0.0 ( 0.1 0.1 0.1 0.1)
117  ! layer 3 to layer 2
118   LT 0.0 0.0 0.3333 0.33333
119      0.0 0.0 0.0 0.0 ( 0.3 0.1 0.1 0.1)
120  ! layer 3 to layer 3
121   LT 0.0 −0.333 0.0 0.333
122      0.0 0.0 0.0 0.0 ( 0.3 0.1 0.1 0.1)
123  ! layer 3 to layer 4
124   LT 1.0 −0.6666 0.0 1/5
125      0.0 0.0 0.0 0.0 ( 0.3 0.1 0.1 0.1)
126  ! layer 3 to layer 5
127   LT 0.0 −0.333 0.0 0.333
128      0.0 0.0 0.0 0.0 ( 0.3 0.1 0.1 0.1)
129
130  ! layer 4 to layer 1
```

```
131   LT  0.0  −0.3333  0.0  0.3333
132        0.0  0.0  0.0  0.0  (  0.1  0.1  0.1  0.1)
133   !layer 4 to layer 2
134   LT  0.0  0.0  0.3333  0.33333
135        0.0  0.0  0.0  0.0  (  0.3  0.1  0.1  0.1)
136   !layer 4 to layer 3
137   LT  0.0  −0.333  0.0  0.333
138        0.0  0.0  0.0  0.0  (  0.3  0.1  0.1  0.1)
139   !layer 4 to layer 4
140   LT  0.0  −0.333  0.0  0.333
141        0.0  0.0  0.0  0.0  (  0.3  0.1  0.1  0.1)
142   !layer 4 to layer 5
143   LT  1.0  −0.6666  0.0  1/5
144        0.0  0.0  0.0  0.0  (  0.3  0.1  0.1  0.1)
145
146   !layer 5 to layer 1
147   LT  1.0  −0.6666  0.0  1.0
148        0.0  0.0  0.0  0.0  (  0.1  0.1  0.1  0.1)
149   !layer 5 to layer 2
150   LT  0.0  0.0  0.3333  0.33333
151        0.0  0.0  0.0  0.0  (  0.3  0.1  0.1  0.1)
152   !layer 5 to layer 3
153   LT  0.0  −0.333  0.0  0.333
154        0.0  0.0  0.0  0.0  (  0.3  0.1  0.1  0.1)
155   !layer 5 to layer 4
156   LT  0.0  −0.6666  0.0  1/5
157        0.0  0.0  0.0  0.0  (  0.3  0.1  0.1  0.1)
```

```
158  ! layer 5 to layer 5
159   LT 0.0  −0.333  0.0  0.333
160      0.0  0.0  0.0  0.0  ( 0.3  0.1  0.1  0.1)
161  CALCULATION
162   LMA
163   Corrmax     30
164   Maxfun      2400
165   Tol         0.100000E−04
166   Nprint      0
167  ! Replace_Files
168
169   Experimental
170  ! Filename                    Scale factor     code
171   FILE        Li2OsO32.dat   0.001      0.00
172   Excluded_Regions 0
173   FFORMAT free
174  ! Linear interpolation
175   Bgrinter   background3.bgr
```

Appendix D: Programs

Programs to mitigate certain tasks have been sought after in the Functional Materials Research Group. Four programs were written in Python and converted to windows executable programs (author: Max Wallace). The "MAS TOOLBAR" was created to host the four programs (Figure D.1) (author: Max Wallace).
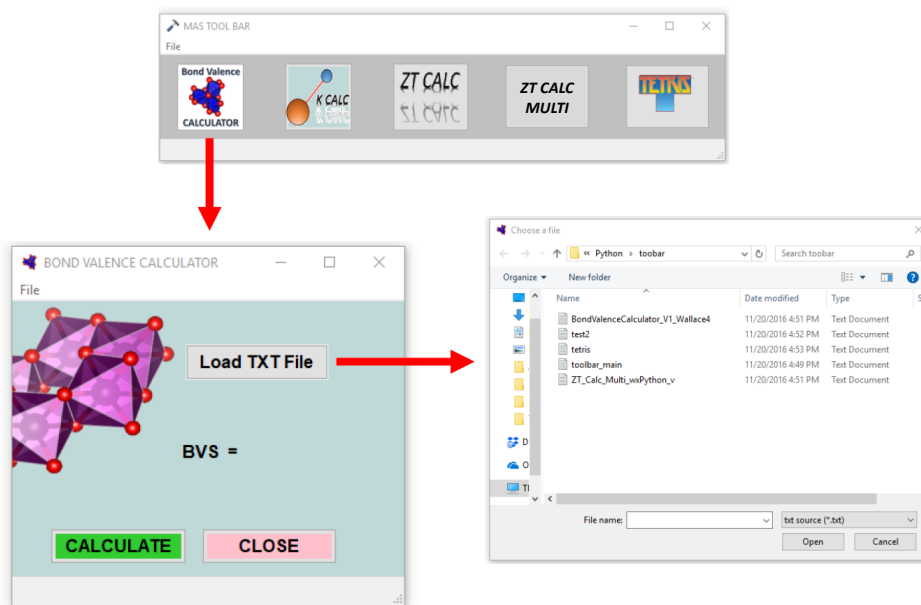
Figure D.1: The "MAS TOOLBAR" with the following programs: Bond Valence Calculator, K-Calc, ZT Calc, ZT Calc MULTI, and Tetris.

A brief definition of each of the four programs is provided in Table D.1. Python code for "ZT Calc MULTI" and "K-Calc" are provided below.

Table D.1: Brief description of programs written by Max Wallace

Bond Valence Calculator: Used to calculate the bond valence sum (BVS) around each metal atom in a compound. The BVS can be compared to the expected oxidation state of that atom. The bond valence is used to validate newly determined crystal structures.
K-Calc: Calculates the dielectric constant of a compound using the Clausius-Mossotti relation. The Clausius-Mossotti relation connects polarizability to dielectric permittivity.
ZT Calc: Calculates the Figure of Merit (ZT) of a thermoelectric material. The electrical conductivity, Seebeck value, and total thermal conductivity values must be known.
ZT Calc MULTI: compiles the raw data collected from the laser flash instrument (thermal diffusion) and ZEM instrument (electrical conductivity and Seebeck) into a single excel spreadsheet with raw data, corrected data and calculated ZT for each temperature for a given sample.

D.1 ZT CALC MULTI

```python
import re
import math
import wx.lib.platebtn as platebutton
import wx
import os
import sys
import csv


class Example(wx.Frame):

    def __init__(self, *args, **kw):
        super(Example, self).__init__(*args, **kw)
```

```
14
15            self.InitUI()
16
17
18        def InitUI(self):
19
20            pnl = wx.Panel(self)
21            #font = self.GetFont()
22            #font.SetPointSize(12)
23            #self.SetFont(font)
24            font = wx.Font(12, wx.DECORATIVE, wx.NORMAL, wx.BOLD)
25            self.SetFont(font)
26            #loc = wx.IconLocation(r'bv_icon.ico', 0)
27            #self.SetIcon(wx.IconFromLocation(loc))
28
29
30            wx.StaticText(self, label='',
31            pos=(20,20))
32            #wx.StaticText(self, label='Name of Text File = ', pos=(34,
                  40))
33            #wx.StaticText(self, label='BVS  = ', pos=(157, 130))
34
35
36            self.f = wx.StaticText(self, label='', pos=(200, 150))
37            self.y = wx.StaticText(self, label='', pos=(270, 129))
38            #self.sc1 = wx.TextCtrl(self, value='', pos=(180, 34), size
                  =(130, -1))
```

```python
39
40
41            # Setting up the menu
42           file_menu = wx.Menu()
43
44          # A Statusbar in the bottom of the window
45           self.CreateStatusBar()
46
47          # wx.ID_ABOUT and wx.ID_EXIT are standard IDs provided
48          # by wxWidgets.
49          #file_menu.Append(wx.ID_ABOUT, '&About',
50                           #'Information about this application')
51          # Creating the menubar
52          menu_bar = wx.MenuBar()
53
54          m_about = file_menu.Append(wx.ID_ABOUT, "&About", "
                 Information about this program")
55           self.Bind(wx.EVT_MENU, self.OnAbout, m_about)
56
57          # Adding the 'file_menu' to the menu bar
58          menu_bar.Append(file_menu, '&File')
59
60          # Adding the menu bar to the frame content
61           self.SetMenuBar(menu_bar)
62           self.Show()
63
64          btn = wx.Button(self, label='CALCULATE', pos=(120, 90))
```

```python
btn1 = wx.Button(self, label='Load TXT File', pos=(120, 30))
#btn2 = wx.Button(self, label='Export as CSV file?', pos=(70,
        150))
btn.SetBackgroundColour('lime green')

btn.SetFocus()
btn1.SetFocus()
#cbtn = wx.Button(self, label='CLOSE', pos=(90, 210))
#cbtn.SetBackgroundColour('pink')


btn.Bind(wx.EVT_BUTTON, self.OnCompute)
btn1.Bind(wx.EVT_BUTTON, self.OnLoad)
#cbtn.Bind(wx.EVT_BUTTON, self.OnClose)
#btn2.Bind(wx.EVT_BUTTON, self.OnExport)

self.SetSize((400, 400))
self.SetTitle('ZT CALCULATOR MULTI')
self.Centre()
self.Show(True)

self.panel = wx.Panel(self)
self.SetBackgroundColour('light blue')

imageFile = 'test.png'
png = wx.Image(imageFile, wx.BITMAP_TYPE_ANY).ConvertToBitmap
        ()
```

```
90              wx.StaticBitmap(self, -1, png, (10, 155), (png.GetWidth(),
                    png.GetHeight()))

91

92

93         def OnAbout(self, event):

94

95

96             description = """

97         Just load desired txt file (try 'Example.txt' file)

98             and click CALCULATE

99

100            -> Can be used...

101

102            -> txt file example {

103

104

105

106

107                                }

108

109                    [ Description of txt file ]

110

111            """

112

113            info = wx.AboutDialogInfo()

114            info.SetName('ZT CALCULATOR MULTI')

115            info.SetVersion('""all out of bubble gum" edition')
```

```
116            info.SetDescription(description)

117            info.SetCopyright('(C) 2016 Max W')

118

119            wx.AboutBox(info)

120

121

122        def OnLoad(self, e):

123

124            wildcard = "txt source (*.txt)|*.txt|" \
125            "All files (*.*)|*.*"
126            dlg = wx.FileDialog(self, "Choose a file", os.getcwd(), "",
                    wildcard, wx.OPEN)
127            if dlg.ShowModal() == wx.ID_OK:
128                self.filename=dlg.GetFilename()
129                self.dirname=dlg.GetDirectory()

130

131            dlg.Destroy()

132

133

134        #def OnClose(self, e):

135

136        #    self.Close(True)

137

138

139        def OnCompute(self, e):

140

141                answer = self.filename
```

```python
142             fin=open(answer,'r')
143             L1list = fin.readline()
144             L2list = fin.readline()
145             L3list = fin.readline()
146             L4list = fin.readline()
147             L5list = fin.readline()
148             L6list = fin.readline()
149             L7list = fin.readline()
150             L8list = fin.readline()
151             L9list = fin.readline()
152             x = str(L1list.split())
153             num = int (L2list)
154             D = float(L3list)
155             SHC = float(L4list)
156             L = float(L5list)
157
158             if num == 6:
159
160                 T1, T2, T3, T4, T5, T6 =  L6list.split()
161                 T1, T2, T3, T4, T5, T6 = [float(T1), float(T2),
                        float(T3), float(T4), float(T5), float(T6)]
162
163                 SC1, SC2, SC3, SC4, SC5, SC6 = L7list.split()
164                 SC1, SC2, SC3, SC4, SC5, SC6 = [float(SC1), float
                        (SC2), float(SC3), float(SC4), float(SC5),
                        float(SC6)]
165
```

```
166          TD1, TD2, TD3, TD4, TD5, TD6 = L8list.split()
167          TD1, TD2, TD3, TD4, TD5, TD6 = [float(TD1), float
                 (TD2), float(TD3), float(TD4), float(TD5),
                 float(TD6)]
168
169          R1, R2, R3, R4, R5, R6 = L9list.split()
170          R1, R2, R3, R4, R5, R6 = [float(R1), float(R2),
                 float(R3), float(R4), float(R5), float(R6)]
171
172          Kt1 = float((TD1)*D*(1.0/(1000.0**2.0))
                 *(1.0/1000.0)*(100.0**3.0)*SHC)
173          Ke1 = float((1/R1)*L*T1)
174          Kl1 = float(Kt1-Ke1)
175          ZT1 = float((T1*(SC1**2)*(1/Kt1)*(1/R1)))
176
177          Kt2 = float(TD2*D*(1.0/(1000.0**2.0))
                 *(1.0/1000.0)*(100.0**3.0)*SHC)
178          Ke2 = float((1/R2)*L*T2)
179          Kl2 = float(Kt2-Ke2)
180          ZT2 = float(T2*(SC2**2)*(1/Kt2)*(1/R2))
181
182          Kt3 = float(TD3*D*(1.0/(1000.0**2.0))
                 *(1.0/1000.0)*(100.0**3.0)*SHC)
183          Ke3 = float((1/R3)*L*T3)
184          Kl3 = float(Kt3-Ke3)
185          ZT3 = float(T3*(SC3**2)*(1/Kt3)*(1/R3))
186
```

```python
187             Kt4 = float(TD4*D*(1.0/(1000.0**2.0))
                    *(1.0/1000.0)*(100.0**3.0)*SHC)
188             Ke4 = float((1/R4)*L*T4)
189             Kl4 = float(Kt4-Ke4)
190             ZT4 = float(T4*(SC2**2)*(1/Kt4)*(1/R4))
191
192             Kt5 = float(TD5*D*(1.0/(1000.0**2.0))
                    *(1.0/1000.0)*(100.0**3.0)*SHC)
193             Ke5 = float((1/R5)*L*T5)
194             Kl5 = float(Kt5-Ke5)
195             ZT5 = float(T5*(SC5**2)*(1/Kt5)*(1/R5))
196
197             Kt6 = float(TD6*D*(1.0/(1000.0**2.0))
                    *(1.0/1000.0)*(100.0**3.0)*SHC)
198             Ke6 = float((1/R6)*L*T6)
199             Kl6 = float(Kt6-Ke6)
200             ZT6 = float(T6*(SC6**2)*(1/Kt6)*(1/R6))
201
202             print("Resulting Kt values (W/mK) : ")
203             print(Kt1)
204             print(Kt2)
205             print(Kt3)
206             print(Kt4)
207             print(Kt5)
208             print(Kt6)
209             print ("")
210             print("Resulting Ke values (W) : ")
```

```
211                    print(Ke1)
212                    print(Ke2)
213                    print(Ke3)
214                    print(Ke4)
215                    print(Ke5)
216                    print(Ke6)
217                    print ("")
218                    print("Resulting Kl values (W/mK)-W : ")
219                    print(Kl1)
220                    print(Kl2)
221                    print(Kl3)
222                    print(Kl4)
223                    print(Kl5)
224                    print(Kl6)
225                    print("")
226                    print("Resulting ZT values : ")
227                    print(ZT1)
228                    print(ZT2)
229                    print(ZT3)
230                    print(ZT4)
231                    print(ZT5)
232                    print(ZT6)
233                    print ("")
234                    print ("")
235                    print ("Export as CSV file? (y/n)")
236                    answer = raw_input()
237                    if answer == "y":
```

```
238
239                        with open(str(x) +'.csv', 'w') as csvfile:
240                            fieldnames = ['Density (g/cm^3)','
                                    specific heat capacity (J/kg*K)','
                                    Lorentz number (V^2/K)','Temperature (
                                    K)', 'Seebeck Coefficients (V/K)', '
                                    Thermal Diffusivity (mm^2/sec)', '
                                    Resistivity(Ohm * m)', 'Total Thermal
                                    Conductivity (W/mK)', 'Electronic
                                    Thermal Conductivity (W)','Lattice
                                    Thermal Conductivity (W/mK)', 'ZT' ]
241                            writer = csv.DictWriter(csvfile,
                                    fieldnames=fieldnames)
242                            writer.writeheader()
243                            writer.writerow({'Density (g/cm^3)': str(
                                    D), 'specific heat capacity (J/kg*K)':
                                     str(SHC), 'Lorentz number (V^2/K)':
                                    str(L)})
244                            writer.writerow({'Temperature (K)': str(
                                    T1), 'Seebeck Coefficients (V/K)': str
                                    (SC1), 'Thermal Diffusivity (mm^2/sec)
                                    ': str(TD1), 'Total Thermal
                                    Conductivity (W/mK)': str(Kt1), '
                                    Resistivity(Ohm * m)': str(R1),'
                                    Electronic Thermal Conductivity (W)':
                                    str(Ke1), 'Lattice Thermal
                                    Conductivity (W/mK)': str(Kl1),'ZT':
```

```
                                  str(ZT1)})
245    writer.writerow({'Temperature (K)': str(
           T2),'Seebeck Coefficients (V/K)': str(
           SC2), 'Thermal Diffusivity (mm^2/sec)'
           : str(TD2), 'Total Thermal
           Conductivity (W/mK)': str(Kt2),'
           Resistivity(Ohm * m)': str(R2),'
           Electronic Thermal Conductivity (W)':
           str(Ke2), 'Lattice Thermal
           Conductivity (W/mK)': str(Kl2),'ZT':
           str(ZT2)})
246    writer.writerow({'Temperature (K)': str(
           T3),'Seebeck Coefficients (V/K)': str(
           SC3),'Thermal Diffusivity (mm^2/sec)':
            str(TD3), 'Total Thermal Conductivity
            (W/mK)': str(Kt3),'Resistivity(Ohm *
           m)': str(R3),'Electronic Thermal
           Conductivity (W)': str(Ke3), 'Lattice
           Thermal Conductivity (W/mK)': str(Kl3)
           ,'ZT': str(ZT3)})
247    writer.writerow({'Temperature (K)': str(
           T4), 'Seebeck Coefficients (V/K)': str
           (SC4),'Thermal Diffusivity (mm^2/sec)'
           : str(TD4),'Total Thermal Conductivity
            (W/mK)': str(Kt4),'Resistivity(Ohm *
           m)': str(R4),'Electronic Thermal
           Conductivity (W)': str(Ke4), 'Lattice
```

```
                                    Thermal Conductivity (W/mK)':str(Kl4),
                                    'ZT': str(ZT4)})
248                            writer.writerow({'Temperature (K)': str(
                                    T5), 'Seebeck Coefficients (V/K)': str
                                    (SC5),'Thermal Diffusivity (mm^2/sec)'
                                    : str(TD5), 'Total Thermal
                                    Conductivity (W/mK)': str(Kt5),'
                                    Resistivity(Ohm * m)': str(R5),'
                                    Electronic Thermal Conductivity (W)':
                                    str(Ke5), 'Lattice Thermal
                                    Conductivity (W/mK)':str(Kl5),'ZT':
                                    str(ZT5)})
249                            writer.writerow({'Temperature (K)': str(
                                    T6), 'Seebeck Coefficients (V/K)': str
                                    (SC6),'Thermal Diffusivity (mm^2/sec)'
                                    : str(TD6), 'Total Thermal
                                    Conductivity (W/mK)': str(Kt6),'
                                    Resistivity(Ohm * m)': str(R6),'
                                    Electronic Thermal Conductivity (W)':
                                    str(Ke6), 'Lattice Thermal
                                    Conductivity (W/mK)':str(Kl6),'ZT':
                                    str(ZT6)})
250
251                            imageFile = 'laser5.gif'
252                            png = wx.Image(imageFile, wx.
                                    BITMAP_TYPE_ANY).ConvertToBitmap()
```

```
253                                   wx.StaticBitmap(self, -1, png, (125, 205)
                                          , (png.GetWidth(), png.GetHeight()))
254
255                                   imageFile = 'folder.gif'
256                                   png = wx.Image(imageFile, wx.
                                          BITMAP_TYPE_ANY).ConvertToBitmap()
257                                   wx.StaticBitmap(self, -1, png, (240, 180)
                                          , (png.GetWidth(), png.GetHeight()))
258
259
260
261                                   self.f.SetLabel("ZT CALC MULTI file")
262 def main():
263
264     ex = wx.App()
265     Example(None)
266     ex.MainLoop()
267
268
269 if __name__ == '__main__':
270     main()
```

D.2   K CALC

```
1
```

```python
import wx
import re
import sys
import wx.lib.platebtn as platebutton


class Example(wx.Frame):

    def __init__(self, *args, **kw):
        super(Example, self).__init__(*args, **kw)

        self.InitUI()


    def InitUI(self):

        pnl = wx.Panel(self)
        font = self.GetFont()
        font.SetPointSize(12)
        self.SetFont(font)
        loc = wx.IconLocation(r'animal_hamster_csW_icon.ico', 0)
        self.SetIcon(wx.IconFromLocation(loc))

        wx.StaticText(self, label='',
        pos=(20,20))
        wx.StaticText(self, label='Molecular Formula = ', pos=(25,
            40))
```

```python
27              wx.StaticText(self, label='Unit Cell Volume / Z = ', pos=(20,
                    80))
28              wx.StaticText(self, label='K = ', pos=(80, 150))
29
30
31          self.f = wx.StaticText(self, label='', pos=(150, 150))
32          self.sc1 = wx.TextCtrl(self, value='', pos=(180, 35), size
                =(110, -1))
33
34          self.volume = wx.StaticText(self, label='', pos=(150, 150))
35          self.sc2 = wx.TextCtrl(self, value='', pos=(180, 75), size
                =(60, -1))
36
37           # Setting up the menu
38          file_menu = wx.Menu()
39
40          # A Statusbar in the bottom of the window
41           self.CreateStatusBar()
42
43          # wx.ID_ABOUT and wx.ID_EXIT are standard IDs provided
44          # by wxWidgets.
45          #file_menu.Append(wx.ID_ABOUT, '&About',
46                          #'Information about this application')
47          # Creating the menubar
48          menu_bar = wx.MenuBar()
49
```

```
50          m_about = file_menu.Append(wx.ID_ABOUT, "&About", "
                Information about this program")
51          self.Bind(wx.EVT_MENU, self.OnAbout, m_about)
52
53          # Adding the 'file_menu' to the menu bar
54          menu_bar.Append(file_menu, '&File')
55
56          # Adding the menu bar to the frame content
57          self.SetMenuBar(menu_bar)
58          self.Show()
59
60          btn = wx.Button(self, label='Compute', pos=(45, 210))
61          btn.SetFocus()
62          cbtn = wx.Button(self, label='Close', pos=(165, 210))
63
64          btn.Bind(wx.EVT_BUTTON, self.OnCompute)
65          cbtn.Bind(wx.EVT_BUTTON, self.OnClose)
66
67          self.SetSize((340, 340))
68          self.SetTitle('K CALCULATOR')
69          self.Centre()
70          self.Show(True)
71
72          self.panel = wx.Panel(self)
73          self.SetBackgroundColour('light blue')
74
75      def OnAbout(self, event):
```

```python
76
77            description = """ 'K CALC '... blah  blah ...
78                """
79            info = wx.AboutDialogInfo()
80            info.SetName('K CALC')
81            info.SetVersion('1.0')
82            info.SetDescription(description)
83            info.SetCopyright('(C) 2016 Max W.')
84
85            wx.AboutBox(info)
86
87        def OnClose(self, e):
88
89            self.Close(True)
90
91        def OnCompute(self, e):
92            f = self.sc1.GetValue()
93            #volume = self.sc.GetValue()
94            #cels = round((volume - 32) * 5 / 9.0, 2)
95            #self.volume.SetLabel(str(cels))
96            pol = {
97
98            # WARNING: VALUES LISTED BELOW ARE ATOMIC WEIGHTS #
99            "H": 1.0079, "He": 4.0026, "Li": 1.20, "Be": 0.19,
100           "B": 0.05, "O": 2.01, "F": 18.998,
101           "Ne": 20.180, "Na": 2.990, "Mg": 24.305, "Al": 26.982,
102           "Si": 28.086, "P": 30.974, "S": 32.065, "Cl": 35.453,
```

```
103        "Ar": 39.948, "K": 39.098, "Ca": 40.078, "Sc": 44.956,
104        "Ti": 47.867, "V": 50.942, "Cr": 51.996, "Mn": 54.938,
105        "Fe": 55.845, "Co": 58.933, "Ni": 58.693, "Cu": 63.546,
106        "Zn": 65.39, "Ga": 69.723, "Ge": 72.61, "As": 74.922,
107        "Se":78.96, "Br": 79.904, "Kr": 83.80, "Rb": 85.468, "Sr":
               87.62,
108        "Y": 88.906, "Zr": 91.224, "Nb": 92.906, "Mo": 95.94,
109        "Tc": 97.61, "Ru": 101.07, "Rh": 102.91, "Pd": 106.42,
110        "Ag": 107.87, "Cd": 112.41, "In": 114.82, "Sn": 118.71,
111        "Sb": 121.76, "Te": 127.60, "I": 126.90, "Xe": 131.29,
112        "Cs": 132.91, "Ba": 137.33, "La": 138.91, "Ce": 140.12,
113        "Pr": 140.91, "Nd": 144.24, "Pm": 145.0, "Sm": 150.36, "Eu":
               151.96,
114        "Gd": 157.25, "Tb": 158.93, "Dy": 162.50, "Ho": 164.93, "Er":
               167.26,
115        "Tm": 168.93, "Yb": 173.04, "Lu": 174.97, "Hf": 178.49, "Ta":
               180.95,
116        "W": 183.84, "Re": 186.21, "Os": 190.23, "Ir": 192.22, "Pt":
               196.08,
117        "Au": 196.08, "Hg": 200.59, "Tl": 204.38, "Pb": 207.2, "Bi":
               208.98,
118        "Po": 209.0, "At": 210.0, "Rn": 222.0, "Fr": 223.0, "Ra":
               226.0,
119        "Ac": 227.0, "Th": 232.04, "Pa": 231.04, "U": 238.03, "Np":
               237.0,
120        "Pu": 244.0, "Am": 243.0, "Cm": 247.0, "Bk": 247.0, "Cf":
               251.0, "Es": 252.0,
```

```
121          "Fm" :  257.0 ,  "Md" :  258.0 ,  "No" :  259.0 ,  "Lr" :  262.0 ,  "Rf" :
                261.0 ,  "Db" :  262.0 ,
122          "Sg" :  266.0 ,  "Bh" :  264.0 ,  "Hs" :  269.0 ,  "Mt" :  268.0  }
123
124      def  find_closing_paren ( tokens ) :
125
126          count  =  0
127          for  index ,  tok  in  enumerate ( tokens ) :
128              if  tok  ==  ' ) ' :
129                  count  -=  1
130                  if  count  ==  0:
131                      return  index
132              elif  tok  ==  ' ( ' :
133                  count  +=  1
134          raise  ValueError ( 'unmatched  parentheses ' )
135
136      def  parse ( tokens ,  stack ) :
137          if  len ( tokens )  ==  0:
138              return  sum ( stack )
139          tok  =  tokens [ 0 ]
140          if  tok  ==  ' ( ' :
141              end  =  find_closing_paren ( tokens )
142              stack . append ( parse ( tokens [1: end ] ,  [ ] ) )
143              return  parse ( tokens [ end  +  1 : ] ,  stack )
144          elif  tok . isdigit ( ) :
145              stack [ -1 ]  *=  int ( tok )
146          else :
```

```
147                       stack.append(pol[tok])
148                 return parse(tokens[1:], stack)
149
150                 if True:
151
152                     tokens2 = re.findall(r'[A-Z][a-z]*|\d+|\(|\)', f)
153
154             tokens2 = re.findall(r'[A-Z][a-z]*|\d+|\(|\)', f)
155             volume = self.sc2.GetValue()
156             answer = round(3*float(volume)+8*3.1415*float(parse(tokens2,
                     [])))/(3*float(volume)-4*3.1415*float(parse(tokens2, []))))
157             self.volume.SetLabel(str(answer))
158
159 def main():
160
161     ex = wx.App()
162     Example(None)
163     ex.MainLoop()
164
165
166 if __name__ == '__main__':
167     main()
```